MITIGATION OF MICROGRID INTERACTIONS ON PROTECTION SYSTEMS IN UTILITY NETWORKS

A Thesis

Submitted to the College of Graduate and Postdoctoral Studies

In Partial Fulfillment of the Requirements

For the Degree of Doctor of Philosophy

In the Department of Electrical and Computer Engineering

University of Saskatchewan

Saskatoon, Saskatchewan

By

Keaton A. Wheeler

PERMISSION TO USE

In presenting this thesis/dissertation in partial fulfillment of the requirements for a Postgraduate degree from the University of Saskatchewan, I agree that the Libraries of this University may make it freely available for inspection. I further agree that permission for copying of this thesis/dissertation in any manner, in whole or in part, for scholarly purposes may be granted by the professor or professors who supervised my thesis/dissertation work or, in their absence, by the Head of the Department or the Dean of the College in which my thesis work was done. It is understood that any copying or publication or use of this thesis/dissertation or parts thereof for financial gain shall not be allowed without my written permission. It is also understood that due recognition shall be given to me and to the University of Saskatchewan in any scholarly use which may be made of any material in my thesis/dissertation.

Request for permission to copy or to make any other use of the material in this thesis in whole or part should be addressed to:

Head of the Department of Electrical and Computer Engineering
57 Campus Drive
University of Saskatchewan
Saskatoon, Saskatchewan S7N 5A9 Canada

OR

Dean
College of Graduate and Postdoctoral Studies
University of Saskatchewan
116 Thorvaldson Building, 110 Science Place
Saskatoon, Saskatchewan S7N 5C9 Canada

ABSTRACT

This thesis presents novel schemes and techniques to overcome the difficulties associated with the integration of distributed generation (DG) and microgrids in the context of existing short circuit characteristics and protection infrastructure adequacy. One such inadequacy is associated with the loss of coordination (LOC) in existing protection infrastructure, with disruption to an expected sequence between utility reclosers and fuses. This thesis aims to offer solutions to these issues, allowing for DG sources and microgrids to be integrated into utility distribution networks without significant effect on existing protection infrastructure.

The integration of DG units into radial distribution networks can result in LOC between upstream reclosers and downstream fuses. To overcome this issue a novel reclosing scheme is proposed whereby a control unit, variable load bank and dedicated recloser are integrated at the point of common coupling (PCC) between the DG unit and the network. This scheme works by receiving a control signal from the distribution network head-end recloser via a communication channel to signal the detection of a fault. Post fault detection, in conjunction with the DG current exceeding pre-specified pick up levels, the control unit disconnects the DG unit from the network to a transfer impedance. This transfer allows the DG unit to continue to supply the transfer impedance at the pre-fault load sharing condition, without the requirement for a shut down. This causes the DG unit to maintain its pre-fault speed and frequency, resulting in a fast reconnection time once the system fault is cleared by the existing protection infrastructure. The scheme is also compared to another potential method, namely fault current limiters (FCLs).

To address the possibility of communication failure in the novel reclosing scheme, a fault detection technique is proposed based on measurements of the rate of change of current output by DG sources. The rate of change of current (ROCOC) is measured over a specified time window to generate a fault detection signal when the ROCOC exceeds specified pickup values.

A hybrid adaptive overcurrent and differential protection scheme is proposed to protect microgrids that operate in both grid and islanded modes. Differential relays are utilized for feeder backbones and buses while adaptive overcurrent relays are concurrently used for load points. The hybrid approach is to reduce both infrastructure upgrade requirements and setting

computation complexity, whilst also addressing the potential lack of coordination when differing protection mechanisms are merged. The proposed scheme is validated through multiple time-domain simulations while the microgrid is in both grid and islanded modes of operation.

A smart protection scheme is then proposed to predict and mitigate the short circuit contribution of a microgrid to a utility fault at a magnitude below the LOC limit. The scheme utilizes polynomial regression analysis (PRA) and particle swarm optimization (PSO) in conjunction with a directional element of a relay to allow for partial continual microgrid connection during utility faults. The directional element specifies the direction of short circuit current flow, only allowing the scheme's operation when the microgrid current is flowing to the utility. The PRA and PSO utilize wind speed, irradiance and operating conditions of synchronous machine based (SM-based) generators to determine the short circuit contributions to utility faults from plants and units within the microgrid. The predictions are used to minimize generation source disconnection to reduce the microgrid short circuit contribution to below the LOC limit dictated by the utility network allowing for the original utility coordination to be maintained.

Finally, a case study is offered to demonstrate the capacity of every approach to mitigate microgrid short circuit contributions while restoring pre-fault operating conditions shortly after fault clearance by utility protection infrastructure. In this thesis, all case studies have been conducted using realistic distribution network and microgrid designs and settings, ensuring the efficacy of the proposed approaches. Time-domain simulations are carried out on these test benchmark models within the EMTP-RV software environment for validation purposes.

ACKNOWLEDGEMENTS

Foremost, I would like to express my sincere gratitude to my supervisor Dr. Sherif O. Faried. This thesis would not have been possible without your continuous support, enthusiasm and guidance. Your mentorship has nurtured a passion and motivation for problem solving.

The dedication and patience of my soon- to- be wife, Renae Zook, has been greatly appreciated. Renae, thank you for travelling the journey with me: all the frustrations, disappointments and difficulties associated with this thesis have been shared challenges. Thank you for your support and constant encouragement while I pursued my dreams. This thesis would not have been possible without your sacrifices and I will be forever grateful.

I would also like to express my appreciation to my parents, sister and friends for their encouragement and support. Special thanks go to my mother, Colleen Wheeler, for helping me with the editing of this thesis.

I would also like to thank Dr. Mohamed Elsamahy for his support throughout the duration of this research. Your advice has been valued during my academic and professional journey.

TABLE OF CONTENTS

LIST OF TABLES

LIST OF FIGURES

LIST OF ABBREVIATIONS

DER	Distributed energy resource
DG	Distributed generation
PV	Photovoltaic
RCA	Relay characteristic angle
HV	High voltage
LV	Low voltage
PSO	Particle swarm optimization
FCL	Fault current limiter
MMT	Minimum melting time
TCT	Total clearing time
TCC	Time current characteristic
PCC	Point of common coupling
AC	Alternating current
DC	Direct current
DFIG	Doubly fed induction generator
BTB	Back to back
PWM	Pulse width modulated
VSC	Voltage source converter
MPPT	Maximum power point tracker
VSI	Voltage source inverter
MPPT	Maximum power point tracker
R	Resistance
L	Inductance
C	Capacitance
A	Amperes
V	Volts
CT	Current transformer
VA	Volt ampere
VAR	Volt ampere reactive

W	Watts
RMS	Root mean square
CCU	Central control unit
R/T	Receiver/transmitter
DG-RC	DG recloser
TBCB	Thyristor-based circuit breaker
LOC	Loss of coordination
SM	Synchronous machine
RD	DG recloser
SFCL	Superconducting fault current limiter
ROCOC	Rate of change of current
RD-Mod	Modified DG recloser
PRA	Polynomial regression analysis

1. INTRODUCTION

1.1 Distributed Generation and Microgrids

The development of renewable technology and ideological shifts has prompted a distinct increase in consumer energy demands, resulting in operational and behavioral changes in the electrical grid. Electrical utilities globally face the challenge of sourcing new methods and technologies to accommodate this increased demand. One method of increasing supply capacity is through employing distributed energy resources (DERs), also known as distributed generation (DG), whereby power is supplied locally to the load to reduce strain on existing sources [1].

Since load centers are capable of installing local generation, the inclusion of DG sources has attracted increased attention from utilities and the public. In part this can be attributed to the fact that these DG sources (such as biogas generators, wind turbines and solar photovoltaic (PV) panels) have the capability to generate grid quality power. This practice, although advantageous, introduces unique challenges. One such challenge is ameliorating undesired functionality changes in protective devices resulting from the DG unit's capability to shift operational behaviors of the grid locally in existing infrastructure [2]-[8].

An interesting proposed solution that has emerged recently is the concept of the microgrid [3]-[10]. A microgrid can be expressed as a low or medium voltage network that contains a small cluster of local loads in conjunction with DG sources and storage devices [6]. Microgrids are capable of two modes of operation; grid connected and islanded [6]. Both are controllable to enable modification of operational characteristics. This close source generation by DGs in the microgrid context has numerous advantages, including transmission reduction loss and prevention of network congestion. Additionally, local DGs and controllable loads reduce the probability of supply interruption for end-of-line infrastructure, due to the capability of reversion to islanded operation of the microgrid during severe grid fault conditions [5].

It is typical for DERs to be classed as either traditional (diesel or gas fueled generators) or non-traditional (renewable energy generators). Generators such as low speed turbines, diesel engines and micro-turbines are some examples of traditional sources. It is common for micro-turbines to be used, as they are efficient and have the capacity to operate using multiple fuel sources. In general, traditional generation sources are synchronous machine based [2].

Non-traditional DERs are typically used in reference to renewable energy sources or electrochemical devices such as fuel cells. The non-traditional sources that have been attracted the most attention are renewables such as wind turbines and PV panels [11]. Due to the introduction of green initiatives [12] and public demand, wind and solar PV generation have been increasingly employed for wide scale integration by governments and utilities.

1.1.1 Interconnection of Distributed Resources

Interconnection occurs when DERs are connected to the main network. In order for interconnection to occur, the scheme will require components such as a collector feeder and an inter-connecting transformer. This is depicted in Figure 1.1 [8].

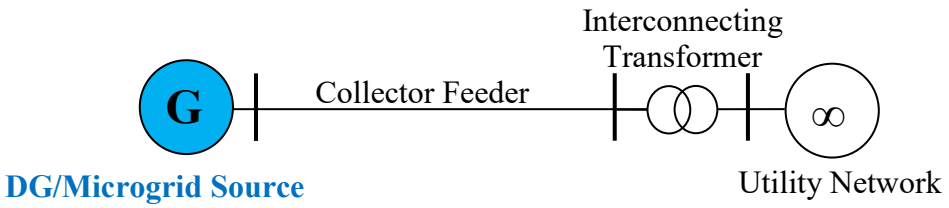

Figure 1.1: A typical DG interconnecting scheme.

Table 1.1: Advantages and disadvantages of interconnecting transformers.

Low Voltage Side	High Voltage Side	Disadvantages	Advantages
Delta	Delta	Supplies network from ungrounded source even if utility breaker trips.	Provides no fault current for a ground fault on the HV side of the transformer. Main network breakers will not react to ground faults on the LV side of the transformer.
Ground-Wye	Delta		
Delta	Wye		
Delta	Ground-Wye	Provides an unwanted ground current for network faults.	Main network breakers will not react to ground faults on the LV side of the transformer. No overvoltages for faults on main feeder.
Ground-Wye	Ground-Wye	Allows main feeder relaying to respond to ground faults on the LV side.	No overvoltages for ground faults on main feeder if the DG source is grounded.

An important component of interconnection is the transformer; however each type comes with advantages and disadvantages. Currently there are five connections that are most commonly used: the advantages and disadvantages are summarized in Table 1.1.

There is no universal agreement amongst utilities about the most effective connection type [13], but a range of utilities have specified preferences for DG interconnection in relation to DG size.

SaskPower specifically has two regulations based on DG source size, namely smaller or greater than 100 kW in generating capacity [14]. For DG sources that contribute less than 100kW the utility side is required to be wye-grounded, with the DG/Microgrid side to be wye-grounded or wye-ungrounded. For a DG size greater than 100 kW SaskPower requires that the source not contribute to the ground current, to avoid affecting the main feeder ground protection coordination. For greater than 100 kW in size the interconnection transformer can be one of two connection types:

- Delta on the utility side with a wye-ground connection on the LV side.
- Wye-grounded on the utility side with a wye-grounded or wye-ungrounded connection on the LV side. For the wye-grounded connection the DG generator must be delta connected.

1.2 Power System Protection

Power system protection is defined as “the science, skill and art of applying and setting relays and/or fuses to provide maximum sensitivity to faults and undesirable conditions, but to avoid their operation on all permissible or tolerable conditions” [15] - [16]. Modern protection schemes attempt to remove only faulted sections from the network, while requiring the protective device closest to the short circuit to operate before devices that are further away [15]-[18].

1.2.1 Protection Coordination of Radial Distribution Networks

In a radial distribution network it is common for a recloser to be connected at the head-end of a designated feeder to allow for attempts at temporary fault clearing. If a recloser operates but short circuit current is still flowing, the fuse will melt and remove the source of the fault from the network. This sequence is termed a ‘fuse saving scheme’ [17]. For successful

implementation of fuse saving schemes in distribution networks, both the minimum and maximum short circuit currents experienced by each component must be known in order to allow for protective device coordination. The head end recloser is required to be placed below the fuse's minimum melting time (MMT) curve since it has a fast operating characteristic curve. In contrast, the slow operating characteristic curve of the head end recloser is placed above the fuse's total clearing time (TCT) curve. This coordination ensures that the head end recloser will operate for a temporary fault before the fuse melts, allowing for an attempt at fault self-clearing. Increases in DG penetration on the network can result in downstream devices such as fuses, experiencing higher short circuit levels than upstream devices (reclosers). As a result of the alterations in short circuit behavior, there is potential that the efficacy of existing protection coordination will be compromised, yielding unexpected performance. This scheme can be depicted graphically via Figure 1.2.

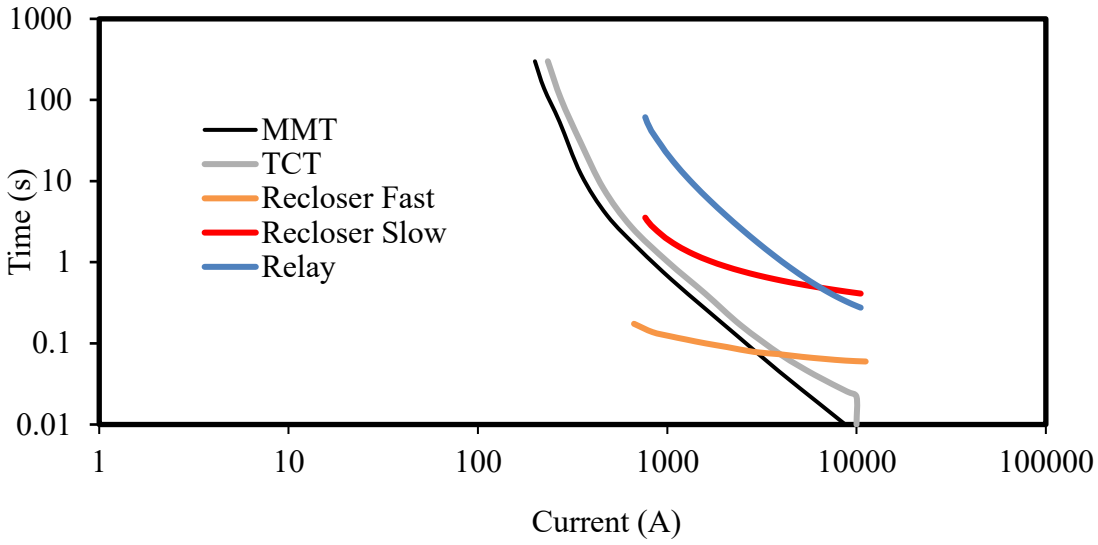

Figure 1.2: Typical characteristic curves for protection coordination in radial distribution networks.

1.2.2 Directional Protection Coordination

Directional relays are designed to operate for faults that are present in one direction only [17], and are necessary when fault current is multidirectional in nature. This type of protection is classified as 'directional' since operation is dependent on the relative direction of current compared to voltage.

In directional protection, the system voltage is always taken as the point of reference [17]. The operation of directional relays is best explained through examples. In Figure 1.3, B21 is required to operate for fault currents that are in the direction of bus two to bus one. The current flowing from bus two to bus one will lag the voltage at bus two by approximately 90 degrees; since transmission/distribution line characteristics are typically mostly reactive [19]. For fault currents that are in the direction from bus one to bus two, the current will lead the voltage at bus two by approximately 90 degrees. As depicted in Figure 1.3, B21 is required to trip for faults flowing from bus two to bus one and block the tripping mechanism for faults flowing from bus one to bus two. This operational concept can be explained diagrammatically as well mathematically and is depicted in Figure 1.4 and Equations 1.1 and 1.2.

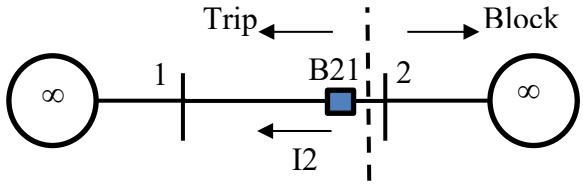

Figure 1.3: Sample system with a directional relay.

$$\theta_{min} > \theta_{op} > \theta_{\max}: Trip \tag{1.1}$$

$$\theta_{min} < \theta_{op} < \theta_{\max}: Block \tag{1.2}$$

where θ_{op} is the phase angle of the current through the relay with respect to the polarizing phasor voltage (in this case $V2_{LL}$).

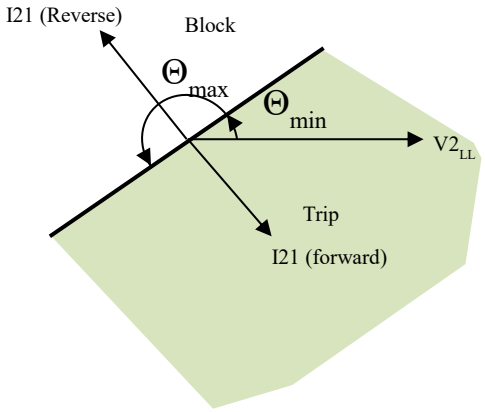

Figure 1.4: Sample directional relay operational characteristic.

For directional relays there are two important parameters that require determination: relay connection angle and relay characteristic angle.

1.2.2.1 Relay Connection Angle

The relay connection angle can be defined as the angle between the current applied to the relay and the phase voltage applied at system unity power factor [19].

When applying the polarizing voltage to the relay, two common connection methods are utilized: 30 degree and 90 degree connections [19]. For the 30 degree connection, the angle of phase A (ABC reference frame) is energized by the current of phase A and the line voltage V_{AC}. Similarly, the angle of phase B is energized by the current of phase B and the line voltage $V_{BA,}$ and the angle of phase C is energized by the current of phase C and the line voltage V_{CB}. This connection method is designed to develop maximum torque of the relay when the current and voltage are in phase, which occurs when the system phase angle is at 30 degrees.

For the 90 degree connection, the angle of phase A (ABC reference frame) is energized by the current of phase A and the line voltage V_{BC}. Similarly, the angle of phase B is energized by the current of phase B and the line voltage $V_{CA,}$ and the angle of phase C is energized by the current of phase C and the line voltage V_{AB}. This connection method is designed to develop maximum torque of the relay when the current leads the voltage by 45 degrees. For all fault types, the phase angle of the connection method is well below 90 degrees; hence this connection will perform better in most circumstances [19]. The weakness of the 90 degree connection angle is it is not able to operate correctly for very small values of current and voltage delivered to the relay.

1.2.2.2 Relay Characteristic Angle

The relay characteristic angle (RCA) can be defined as the angle by which the current applied to the relay must be displaced from the polarizing voltage (line to line voltage) when applied to the relay to produce maximum operational sensitivity (digital) or maximum torque (induction) [19]. In Equations 1.1 and 1.2, the RCA is θ_{min}. θ_{max} is 180 degrees more than θ_{min}. The standard relay connection angles and RCAs can be summarized as:

- 90 degree connection with 30 degree (leading) RCA for plain feeders with the zero sequence source (e.g. delta (HV)/ Wye-grounded (LV) transformer connection).
- 90 degree connection with 45 degree (leading) RCA for feeders with the zero

sequence source in front of the relay (e.g. transformer feeders).

1.3 Microgrids

Microgrids have the capability to operate in AC (AC microgrid) or DC (DC microgrid) systems [11]. In the case of AC microgrids, the network is connected to the utility through power transformers with directly-connected AC loads. For DC loads in the AC microgrid, power electronic inverters are required for network connection. DC microgrids have increasingly been considered for implementation [20] since they have several advantages: they do not require synchronization with the AC utility and are compatible with most DG source coupling interfaces, hence reduction of conversion losses.

Although microgrids offer a feasible solution to the issue of integration of DGs, they also introduce challenges from a system operational perspective. In low voltage distribution level networks, protection systems are generically divided into protective zones in the network (overhead lines and cables) and in apparatus classification (buses, transformers, generators, loads.) [5]. Traditionally, distribution networks are designed on the basis of large fault currents with radial (unidirectional) characteristic power flow [3]. The introduction of DERs into standalone or microgrid contexts yields potential for degradation of this common characteristic, especially in older classical networks.

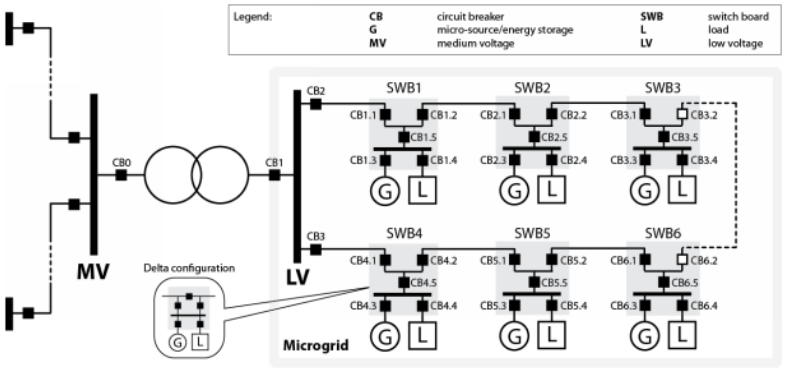

Figure 1.5: A typical microgrid layout.

One key operational constraint associated with microgrids is the requirement for internal protection infrastructure to have the capability for quick responses to both grid connected and microgrid faults. In the case where a grid fault occurs, the microgrid must not affect the utility

protection scheme so as to allow for reliable and efficient clearing. In the case of a microgrid fault, the smallest portion of the microgrid must be sectionalized to allow for continued normal operation [5]. A typical microgrid configuration is demonstrated in Figure 1.5.

Another issue associated with microgrids is the insufficient level of fault current contributed by DG sources. During a fault on the utility grid, if the microgrid maintains full connection then the short circuit contribution from the utility source may reduce to such a level that existing overcurrent devices malfunction in their operation [4]. In contrast, during the microgrid islanded mode the DG sources may provide insufficient levels of short circuit current to allow for overcurrent fault detection and clearing mechanisms to operate. This is particularly prevalent in inverter based DGs as they are equipped with current limiting devices to prevent overload currents on individual components [4].

The requirement for the microgrid to have the capacity for topological change also introduces the issue of selectivity and sensitivity of overcurrent relays. The protective devices employed in the microgrid and network must have the capability to discriminate between grid and internal microgrid faults [4].

1.4 Polynomial Regression Analysis

Polynomial regression is a well- documented method of approximating data sets when inputs can be variable [21]. In order to generate a polynomial equation associated with a dataset, the least squares method is commonly used. A generic form of the polynomial can be expressed as:

$$y = a_k x^k + \cdots + a_1 x + a_0 + \varepsilon, k = N - 1 \tag{1.3}$$

Where the maximum order of the polynomial k is dictated by the number of data points N. Following a set of matrix equations will allow for the coefficients of the polynomial to be determined. This matrix equation can be expressed generically by:

$$\begin{bmatrix} N & \sum_{i=1}^{N} x_i & \cdots & \sum_{i=1}^{N} x_i^k \\ \sum_{i=1}^{N} x_i & \sum_{i=1}^{N} x_i^2 & \cdots & \sum_{i=1}^{N} x_i^{k+1} \\ \vdots & \vdots & \ddots & \vdots \\ \sum_{i=1}^{N} x_i^k & \sum_{i=1}^{N} x_i^{k+1} & \cdots & \sum_{i=1}^{N} x_i^{2k} \end{bmatrix} \begin{bmatrix} a_0 \\ a_1 \\ \vdots \\ a_k \end{bmatrix} = \begin{bmatrix} \sum_{i=1}^{N} y_i \\ \sum_{i=1}^{N} x_i y_i \\ \vdots \\ \sum_{i=1}^{N} x_i^k y_i \end{bmatrix} \tag{1.4}$$

By solving Equation 1.4 for a set of N data points in the form (x_i, y_i), a polynomial of order k

or less can be found. In the case of a polynomial of degree 2, at least 3 data points would be required. The set of matrix equations to be solved would then be expressed as:

$$\begin{bmatrix} N & \sum_{i=1}^{N} x_i & \sum_{i=1}^{N} x_i^2 \\ \sum_{i=1}^{N} x_i & \sum_{i=1}^{N} x_i^2 & \sum_{i=1}^{N} x_i^3 \\ \sum_{i=1}^{N} x_i^2 & \sum_{i=1}^{N} x_i^3 & \sum_{i=1}^{N} x_i^4 \end{bmatrix} \begin{bmatrix} a_0 \\ a_1 \\ a_2 \end{bmatrix} = \begin{bmatrix} \sum_{i=1}^{N} y_i \\ \sum_{i=1}^{N} x_i y_i \\ \sum_{i=1}^{N} x_i^2 y_i \end{bmatrix} \tag{1.5}$$

1.5 Particle Swarm Optimization

Particle swarm optimization (PSO) is a population-based stochastic optimization technique developed by Kennedy and Eberhart in 1995 [22]. The method was inspired by bird flocking and fish schooling and involves the use of "particles" which present a candidate solution. The algorithm then generates the optimal solution based on a multitude of criteria. PSO and genetic algorithm (GA) techniques have recently been applied to power systems contexts and have yielded impressive results however, GAs have been shown to converge prematurely. This has led to PSO being adopted as a potential optimization technique for power systems in the future.

PSO operates on the premise of three simple behaviors: separation (to avoid overcrowding), alignment and cohesion (move toward the average position of local path). Each particle will adjust speed dynamically in a fashion that is dependent on the experiences of other particles and itself. This adjustment is modified according to current position, current velocity, difference between the current position and the particle's best position and the difference between the current position and the best of all the particles [22].

In PSO the population has particles that can represent possible solutions. Each particle is an n-dimensional real valued vector with n being the number of optimized parameters [23].

The PSO algorithm can be explained in the following set of steps [23]:

1. Initialization
    a. Set the time counter at *n*.
    b. Create t particles and generate random initial velocities for each particle.
    c. Evaluate each particle's position according to an objective function. Use each individual particle's value for the objective function as the best particle solution (p_{best}) and use the best value from every particle as the global best solution (g_{best}).

d. Set the initial weighted value of inertia which is used to control the impact of previous velocity on current velocity of each particle.

2. Update the time counter, $n=n+1$.
3. Update the inertia weight using the equation:

$$\omega_n = \alpha\omega_{n-1} \tag{1.6}$$

where α is a decrement constant smaller than one (a typical value is 0.98 as used in this thesis [12]) and ω_n is the inertia coefficient (typically ω_0 is equal to 1 [23]).

4. Update the velocity using the equation:

$$v_{n+1}^i = \omega_n v_n^i + c_1 r_1 \left(p_{best} - x_n^i\right) + c_2 r_2 \left(g_{best} - x_n^i\right) \tag{1.7}$$

where v_{n+1}^i is the velocity of particle i for iteration $n+1$, x_n^i is the position of particle i for iteration n, c_1 and c_2 are positive constants typically equal to two as in this thesis [23] while r_1 and r_2 are uniformly distributed random numbers in the range from zero to one.

a. The first component of the equation represents the inertia. Inertia influences the particle to move in the same direction as its current velocity.
b. The second component represents personal influence which improves the individual particle's performance and also makes the particle move toward a previous solution if it performed better.
c. The third component of the equation represents social influence which makes the particle move toward the best neighboring particle's solution.

5. Using the new velocities of each particle through use of Equation 1.7, update each particle's position according to:

$$x_{n+1}^i = x_n^i + v_{n+1}^i \tag{1.8}$$

6. Evaluate each particle's position according to an objective function. Compare each individual particle to its previous best solution. If the current position is better than the previous best (p_{best}) then update it, otherwise use the previous best solution. Compare every individual particle to the previous global best (g_{best}). If one particle

has a better solution than the previous global best then update it, otherwise use the previous best solution.

7. The algorithm terminates if any of the following conditions are met:
    a. The number of iterations since the last change in best solution is greater than a pre-determined number of iterations.
    b. The number of iterations has reached a pre-determined maximum

PSO has several advantages over other optimization techniques namely [24]:

1. PSO is a population-based search algorithm. This means that local minima's are less likely to trap the algorithm.
2. The use of the objective function guides the search for the best solution.
3. PSO algorithms are more robust and flexible as they make use of probabilistic transitional tools.
4. PSO algorithms typically will not converge prematurely, enhancing the search capability.
5. The end solution does not rely on initial population selection.
6. PSO algorithms converge to an optimal solution regardless of starting position in the search space.

1.6 Fault Current Limiters

Fault current limiters (FCLs) limit the amount of short circuit current that is allowed to flow into a power network, enabling continual operation of systems despite faulted conditions [25]. FCLs are series devices that have very low impedances (near zero) during steady state system operation (normal mode) but rapidly introduce high impedance into the protected line to restrain the short circuit current (superconducting mode) to a desirable level during fault conditions [26].

FCLs can be classified into quench, non-quench and composite types, depending on their operating characteristics. Quench FCLs can be resistive, inductive or hybrid and act to limit the fault level through control of the conversion between the normal and superconducting states. Non-quench type FCLs can be iron core, bridge or active types, and control the fault level by controlling the conductor current. Composite type FCLs combines the principles of the quench and non-quench types [27].

An alternate type of FCL is known as the resonant FCL. The resonant FCL, as the name suggests, is a component that utilizes a series resonant circuit in a system to limit the short circuit level during fault conditions. For resonant FCLs, the short circuit current increases gradually, (as opposed to instantaneously) during a fault condition; the effect being that the fault can be interrupted at a lower magnitude, preventing damage to the system [28]-[29].

1.7 Research Objective and Scope of the Thesis

Although DERs and microgrids have undeniable advantages they also introduce their own challenges. Present literature demonstrates that the field of DG and microgrid protection is still emerging as a key topic for researchers, with rarely more than an idea being presented on a scheme, as opposed to methods with tangible evidence of feasibility. Following the introduction of the microgrid concept for DG source integration, there is a growing need for feasible protective solutions for implementation. The main objective of this research is to determine the feasibility of a novel reclosing method in conjunction with a prediction method coupled with a protection scheme to allow for integration of DG sources and microgrids. These objectives are able to be accomplished through the following five stages:

1. Investigation of the use of a reclosing scheme to aid in mitigation of DG effects on existing utility protection infrastructure. This will allow for the integration of DG units into distribution networks without loss of coordination between reclosers and fuses.
2. Comparing the reclosing scheme with another method, namely fault current limiters. Comparison with FCLs will demonstrate the efficacy of the proposed approach in stage 1 for cases where an FCL may not work in mitigation of DG unit short circuit contributions while the proposed scheme does, justifying it's use.
3. Creation of a fault detection technique to enable the novel reclosing scheme to operate without the requirement of a communication link. This will remove the requirement for the communication link that will be outlined in stage 1, making the novel reclosing scheme more robust.
4. Creation of a smart protection scheme for a microgrid integrated into a distribution network. This protection scheme is to be developed to handle the drastic changes in short circuit current between grid and islanded modes of operation for microgrids.

5. Implementation of a PSO controller that uses polynomial regression to predict short circuit currents present in a microgrid. This controller will then be able to identify sources that are yielding a negative effect on existing network protection infrastructure. This will allow for generator short circuit contributions to be identified and mitigated preventing loss of coordination between the distribution network protection infrastructures.

This thesis is organized into seven chapters, a list of references section and appendices.

Chapter 1 introduces the fundamentals of protection coordination, generation source interconnection, microgrids, polynomial regression analysis and particle swarm optimization. Objectives are also presented.

In Chapter 2, the systems under study are introduced along with the details associated with the modelling of individual components.

Chapter 3 outlines the approach for the reclosing scheme used to mitigate DG effects on existing network protection. In addition, this chapter demonstrates the comparison of the method with FCLs. Case studies are presented for validation purposes.

Chapter 4 presents the approach for detecting faults within the distribution network without the need for communication links. An analysis of these results, with supporting case studies, is also presented.

Chapter 5 presents a hybrid adaptive overcurrent and differential protection scheme to be used in microgrids that are integrated into the utility network. Case studies with results are presented.

Chapter 6 presents a smart protection scheme which utilizes polynomial regression in conjunction with PSO to mitigate microgrid short circuit effects on the existing protection infrastructure in distribution networks. Combined case studies are discussed, with results demonstrated.

Chapter 7 summarizes the research described in this thesis and presents conclusions.

2. MODELING OF POWER SYSTEMS FOR DISTRIBUTED GENERATION AND MICROGRID INTEGRATION STUDIES

2.1 Introduction

This chapter presents the system and microgrid that are utilized in the investigations conducted in this thesis. Details of the protection settings, models and individual components are also provided.

2.2 System under Study

2.2.1 Distribution Network

The distribution network used during the investigations in this thesis is presented in Figure 2.1. The system is a modified representation of an actual network currently being used in the province of Saskatchewan, Canada. It comprises of a connection to the utility (modeled as a constant voltage source behind an impedance) through a double grounded wye substation transformer. The substation serves two 25 kV feeders which share a point of common coupling (PCC). A two ohm series reactor is placed after the substation to limit the highest short circuit current to less than 6100 A. There are six loads in the network which represent lateral feeders. Each load is protected via a fuse (F1 to F6). The system loads are characterized as: constant impedance loads (L1, L2 and L4), constant power loads (L3), and composite loads (L5 and L6). In addition to the fuses, each feeder is protected by an individual head-end recloser (RE1 and RE2) with a relay connected in the substation as a backup. Further detail on loads, components and conductors are presented in Appendix A.

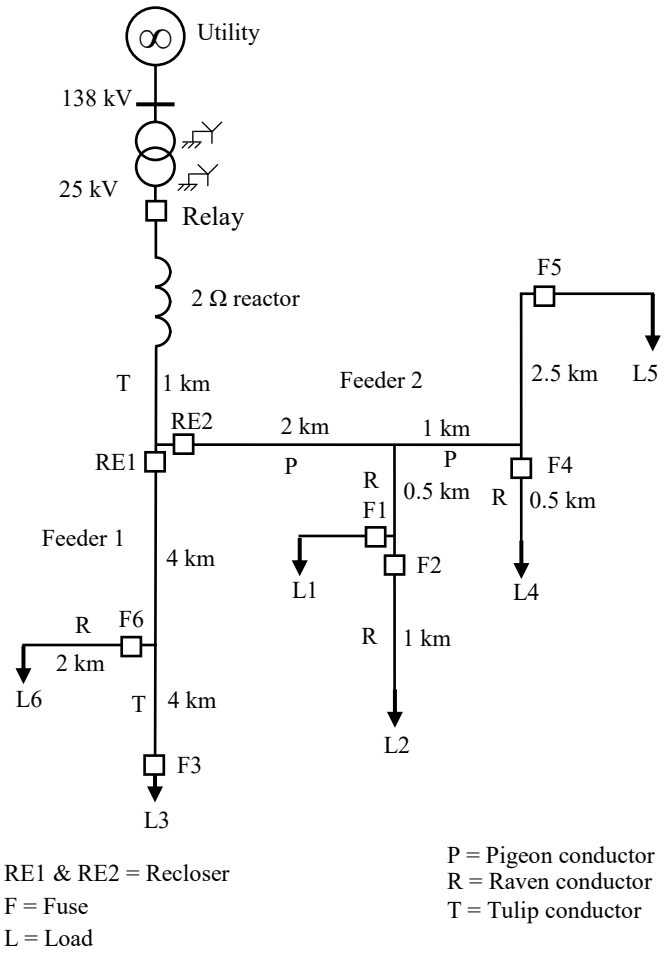

Figure 2.1: Single line diagram of the typical system under study.

2.2.2 Protection Coordination Paths

As per Figure 2.1, all loads are fuse protected, with each individual feeder utilizing a head-end recloser. As a result, there are six coordination paths each with a relay-recloser-fuse scheme. The coordination paths are shown in Figures 2.2 to 2.4.

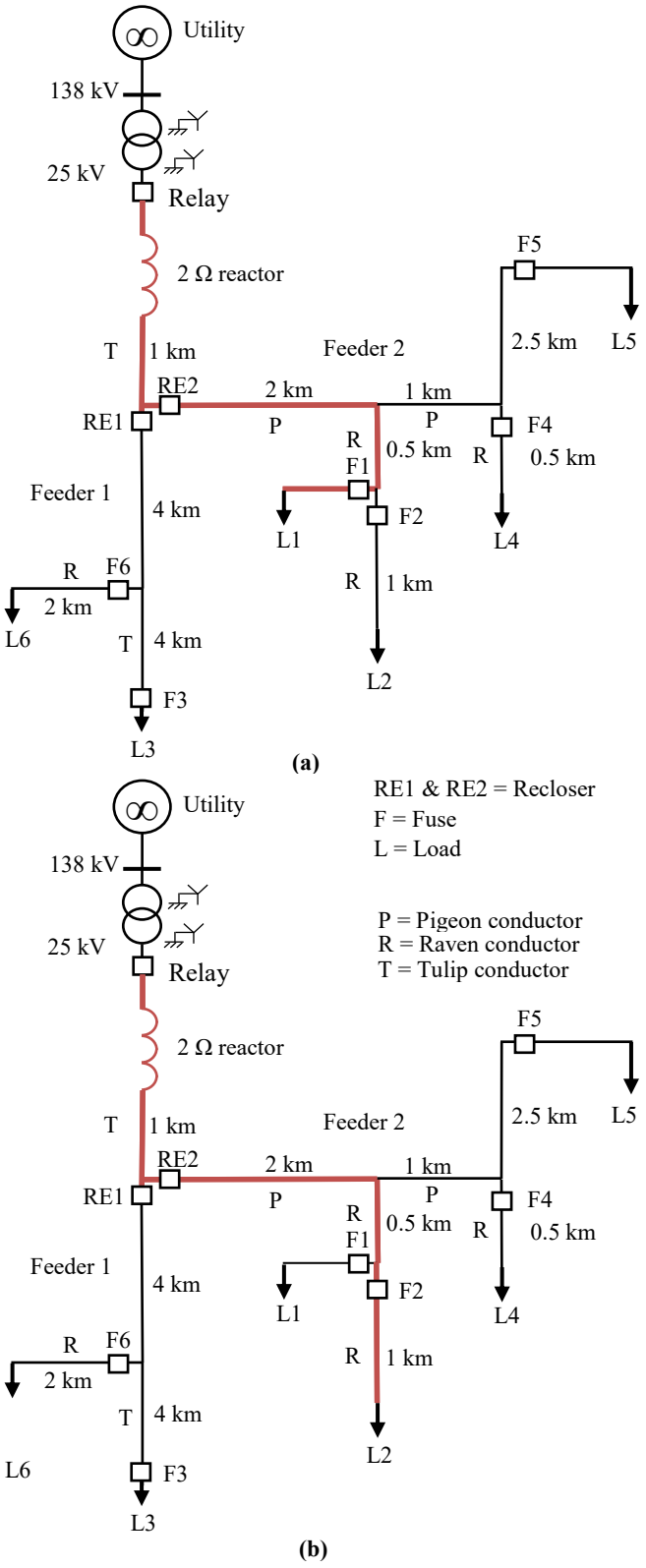

Figure 2.2: Single line diagram of the: (a) load 1 coordination path, (b) load 2 coordination path.

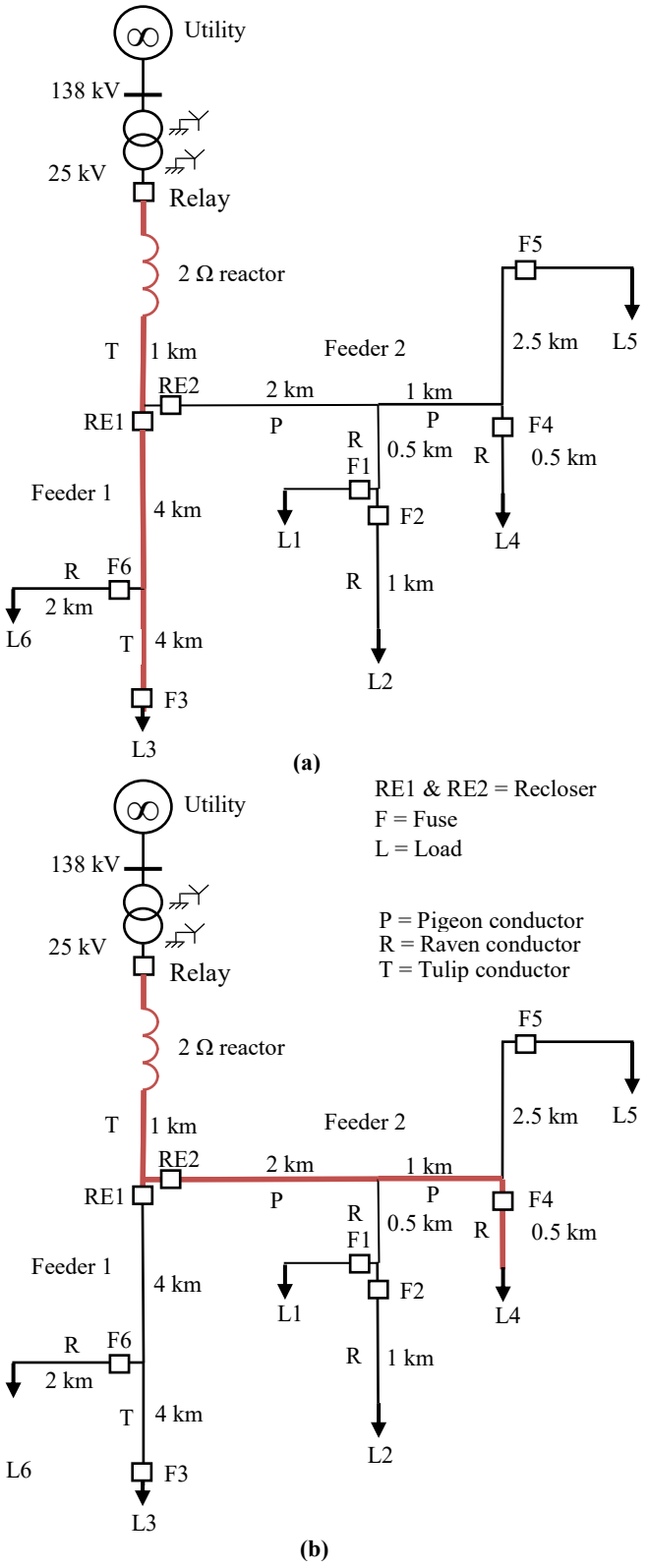

Figure 2.3: Single line diagram of the: (a) load 3 coordination path, (b) load 4 coordination path.

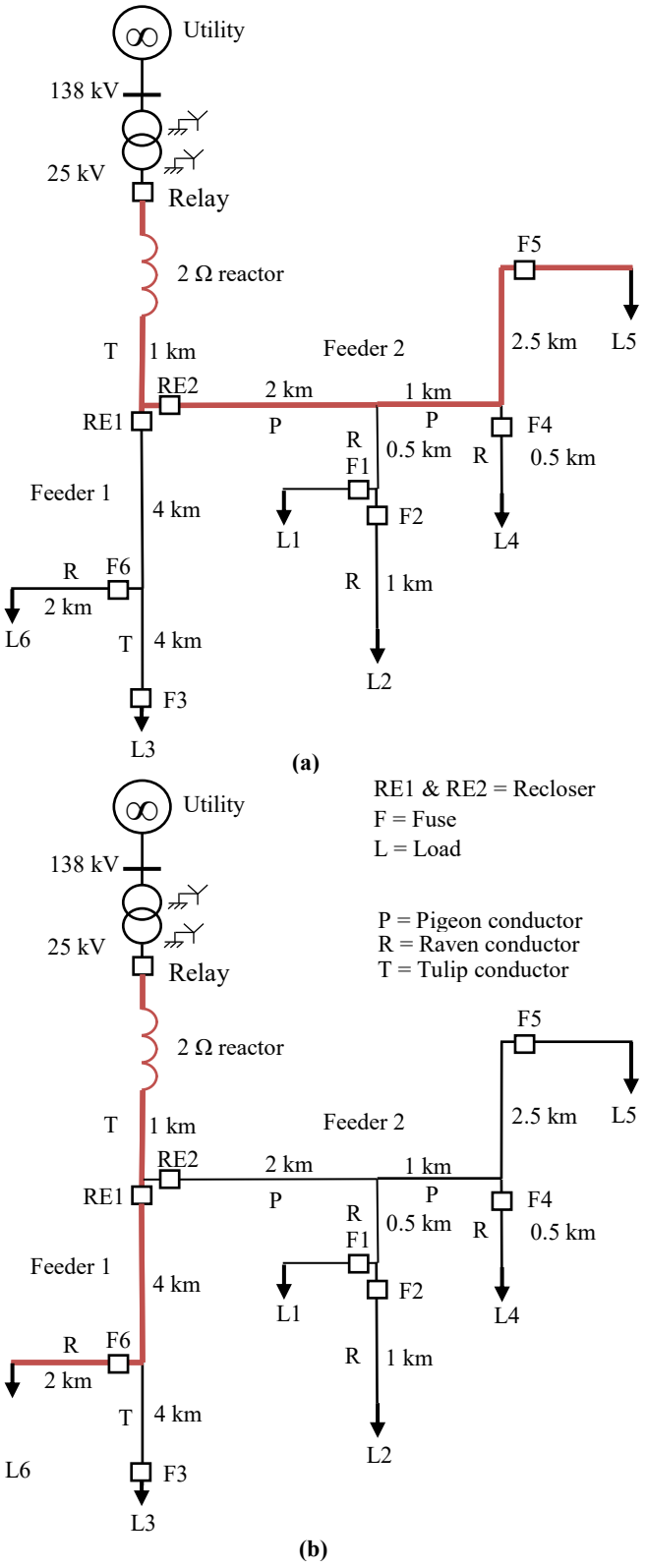

Figure 2.4: Single line diagram of the: (a) load 5 coordination path, (b) load 6 coordination path.

2.2.3 Protection Settings

2.2.3.1 Utility to Load 1 Coordination Settings

As per Figure 2.1 (a), this coordination path extends through feeder 2 to load 1 and includes the substation relay, RE2 recloser and the fuse F1. The recommended rating of this fuse is selected through the use of Equation 2.1 [30].

$$I = \frac{S_{load}}{\sqrt{3} \times V_{LL}} \times Multiplying\ factor \tag{2.1}$$

For the fuse, a multiplying factor of 1.75 is used [31].

This gives a recommended rating of:

$$I = \frac{10^6}{\sqrt{3} \times 25000} \times 1.75 = 40.4\ \text{A}$$

Using S&C SM-4 and SM-5 slow distribution fuses [32], an S&C 40E should be adequate.

For the recloser, multiplying factors for the phase and ground settings are 1.5 and 0.75 respectively [30]. Feeder 2 has loads 1, 2, 4 and 5 equating to an overall load of 9 MVA. As such the RE2 recloser rating can be expressed as:

$$I = \frac{9 \times 10^6}{\sqrt{3} \times 25000} \times 1.5 = 311.8\ \text{A}$$

The nearest standard recloser rating that is adequate is 400 A [15].

The ground trip setting is given as:

$$I = \frac{9 \times 10^6}{\sqrt{3} \times 25000} \times 0.75 = 155.9\ \text{A}$$

The nearest standard recloser rating that is adequate is 200 A [15].

The substation relay is not always used in distribution networks. As such, it was excluded from the studies conducted in this thesis.

The head end recloser is required to coordinate with the downstream fuse to achieve a fuse-saving scheme. For this condition to be realized, the recloser fast time current characteristic (TCC) needs to be able to operate faster than the fuse for the most severe short circuit currents

present within the network. The short circuit current for the network is given in Appendix B. The maximum phase current that is experienced by F1 is 4229 A while RE2 experiences 4244 A. In order for fuse-saving schemes to be realized, it is recommended that the upstream recloser fast clearing time be at least 75% lower than the downstream fuses MMT. In addition, the recloser slow clearing time should be at least double the fuses TCT [17]. For F1, if a 40E fuse were to be selected, the MMT would be 0.0401 seconds. This is faster than any of the standard fast clearing curves for an ABB PCD2000 Recloser [33]. As such, F1 can be increased to be a 175E fuse. As a result, the recloser RE2 fast TCC was selected to be ANSI INV INST-1 with a trip setting of 400 A. For the maximum short circuit case (a three-phase fault), this yields a trip time of 0.0762 seconds while F1 has an MMT of 0.1094 seconds. The RE2 slow TCC was selected to be the ANSI INV-2 curve. For the minimum short circuit case (a line-to-line fault), this yields a trip time of 0.576 seconds for a short circuit current of 3748 A while F1 has a TCT of 0.171 seconds for a short circuit current of 3670 A.

The ground settings can be found in a similar way. The maximum short circuit current (linne-to-line-to-ground fault) experienced by F1 is 4141 A while RE2 experiences 4162 A. The RE2 fast ground TCC was selected to be ANSI INV INST-4 with a trip setting of 210 A. This means for a short circuit current of 4162 A the clearing time of RE2 is 0.0814 seconds. In contrast, the MMT of F1 for a short circuit current of 4141 A is 0.1368 seconds. The RE2 slow TCC was selected to be ANSI LTVI-1. For the minimum short circuit case (single line-to-ground fault), this yields a trip time of 0.868 seconds for a short circuit current of 3421 A while F1 has a TCT of 0.2052 seconds for a short circuit current of 3399 A.

2.2.3.2 Utility to Load 2, 4, 5 Coordination Settings

As per Figure 2.1 (b), Figure 2.3 (b) and Figure 2.4 (a) this coordination path extends through feeder 2 to load 2, 4 and 5 including the RE2 recloser and the fuses F2, F4 and F5. The fuse sizes are selected in a similar way to Section 2.2.3.1. From short circuit analysis results given in Appendix B, the fuse size selected for F2, F4 and F5 was the S&C 150E. Results with tripping times, MMTs and TCTs are given in Appendix B.

2.2.3.3 Utility to Load 3 and 6 Coordination Settings

As per Figure 2.3 (a) and Figure 2.4 (b) this coordination path extends through feeder 1 to loads 3 and 6 including the RE1 recloser and the fuses F3 and F6. The fuse sizes were selected in a similar way to Section 2.2.3.1. From short circuit analysis results given in Appendix B, the fuse size selected for F3 and F6 was the S&C 125E. Results with tripping times, MMTs and TCTs are given in Appendix B.

For the recloser, Feeder 1 has loads 3 and 6 equating to an overall load of 7 MVA. As such the RE2 recloser rating can be expressed as:

$$I = \frac{7 \times 10^6}{\sqrt{3} \times 25000} \times 1.5 = 242.5 \text{ A}$$

The nearest standard recloser rating that is adequate is 280 A [15].

The ground trip setting is given as:

$$I = \frac{7 \times 10^6}{\sqrt{3} \times 25000} \times 0.75 = 121.24 \text{ A}$$

The nearest standard recloser rating that is adequate is 200 A [15].

The maximum phase current that is experienced by F3 or F6 is 3077 A while RE1 experiences 3090 A (three-phase fault). The recloser RE1 fast TCC was selected to be ANSI INV INST-1 with a trip setting of 280 A. In contrast the RE1 slow TCC was selected to be ANSI INV-2. Similarly for the ground settings, the maximum ground short circuit current experienced by F3 or F6 is 2939 A (line-to-line-to-ground fault). As a result the ground fast TCC curve was selected to be ANSI INV INST-4 while the slow TCC curve was selected to be ANSI LTEI-1.

2.2.4 The Microgrid

The microgrid used in the investigations of this thesis in an adaptation of a model depicted in reference [34]. The network is connected to the utility via an interconnecting line at the point of common coupling (PCC). The voltage of the network is 13.8 kV. The microgrid consists of six main buses each with a DG source and a load. The microgrid consists of two separate feeders. Loads 1, 2, 4 and 5 are all operating at 0.2 MW while loads 3 and 6 are operating at 0.1 MW. At each load there is a protective breaker. In addition, each bus has three breakers while each line has a breaker on each end. It should be noted that the breaker protecting

the load point is also used for the load bus (i.e. it can be tripped due to a fault on the load or on the load bus). Details of the protection system are discussed in Chapter 5 of this thesis. Further detail on loads, components and conductors are presented in Appendix A.

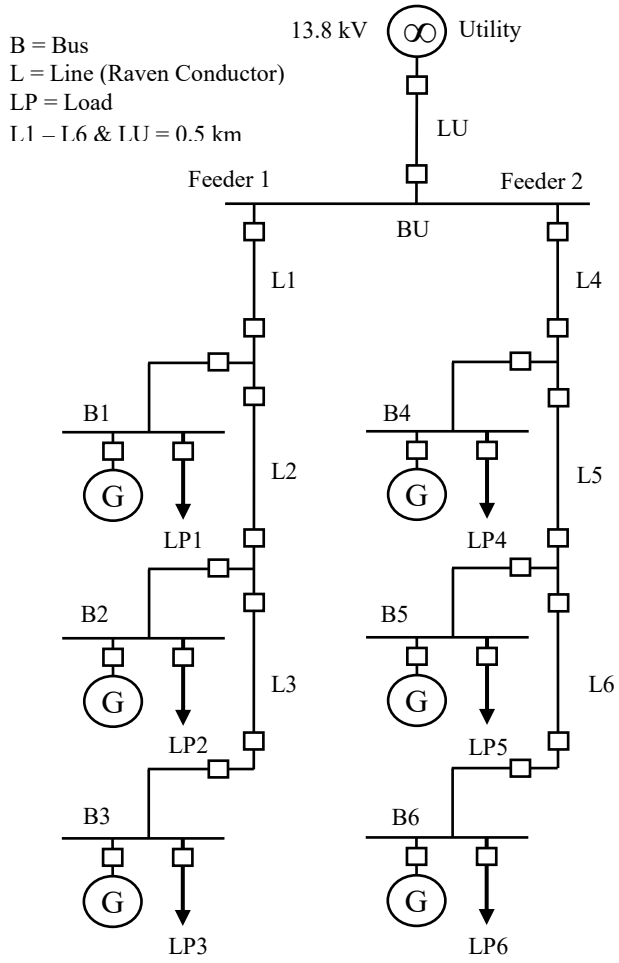

Figure 2.5: Single line diagram of the microgrid under study.

2.3 Power System Modeling

2.3.1 Modeling of Distribution Lines

Transmission and distribution lines can be defined by one of three categories based on their length [15]:

1. Short lines: lines smaller than 80 km.
2. Medium lines: lines equal to or longer than 80 km but smaller than 240 km.
3. Long lines: lines longer than 240 km.

In the EMTP-RV software environment, there are multiple types of distribution line models each with their own characteristics. These can be described as such:

1. Beregon/Steady State Model: this is the traditional nominal PI model of conductors. In this model the admittance and impedance are input for a specific frequency. As a result this model is limited to applications where the frequency is expected to fluctuate at a negligible level. Studies such as relay coordination and short circuit analysis are suitable for this type of line application [35].
2. Frequency Dependent Model: in this model the parameters of the line are frequency dependent. The parameters are calculated at multiple frequencies in addition to being dependent on transmission tower configurations. This model is accurate in the majority of studies but is typically limited to transmission line applications where tower configurations are known [35].
3. PI Model: The PI model in EMTP-RV requires the steady state impedances based on a fixed frequency be input to allow for the load flow to be solved. In time-domain simulations the model is able to re-evaluate the impedance of the line based on changes in frequency in real-time. This model is suitable for applications where tower configurations are unknown but steady state data is available.

Considering that the longest lines in the distribution networks under study are 6.5 kilometers and short circuit time-domain simulations are required, the PI model was selected for use in this thesis. This model can be represented visually by Figure 2.6 [15].

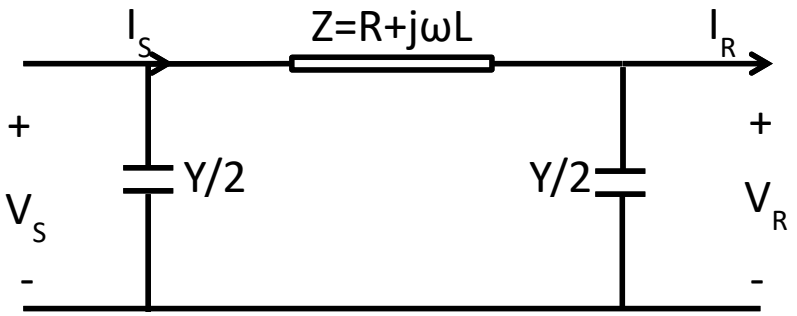

Figure 2.6: The PI model for distribution lines.

where

- V_S is the sending voltage (V)
- V_R is the receiving voltage (V)
- I_S is the sending current (A)
- I_R is the receiving current (A)
- Y is the total shunt admittance (S)
- Z is the total series impedance (Ω)

When modelling distribution lines in the PI model it is important to obtain the sequence impedance data. Positive sequence components comprise of three phasors that have identical magnitude but are displaced by 120 degree spacing. The phasors rotate in the same direction as the phasors in the network. It is very common for the negative sequence components to be the same as the positive, with the phasors rotating in the reverse order. The zero sequence components are three in phase equal magnitude phasors that rotate in the same direction as the positive sequence phasors. The key difference between positive/negative sequence and zero sequence components is that the magnetic fields that create the positive/negative sequence are different to that of the zero sequence. In the context of single circuit overhead lines, the zero sequence impedance can be up to 3.5 times the positive. In the context of single circuit underground cables, the zero sequence can be between 3 and 5 times larger than the positive for triplex core cables [36] - [37]. In this thesis, the cable data is taken from an actual system with field measured impedances. Cable impedances are given in Appendix A.

2.3.2 Modeling of transformers

The three-phase transformer model used in EMTP-RV comprises of three single-phase transformers. The transformer leakage and magnetizing reactances are accounted for.

2.3.3 Modeling of system loads

System loads can be modeled by Equations 2.2 and 2.3 [38]

$$P_{Load} = P_0 \left(\frac{V}{V_0}\right)^a \tag{2.2}$$

$$Q_{Load} = Q_0 \left(\frac{V}{V_0}\right)^b \tag{2.3}$$

where

P_{Load} = real load power at V

Q_{Load} = reactive load power at V

a = real load constant equal to the slope $\frac{dP}{dV}$

b = reactive load constant equal to the slope $\frac{dQ}{dV}$

V_0 = initial voltage

V = current voltage

From Equations 2.2 and 2.3, load types can be classed into multiple categories:

1. Constant Power Loads: have a fixed active and reactive power demand regardless of the voltage level. Constants *a* and *b* in Equations 2.2 and 2.3 are both zero. Examples of this type of load are induction motors and tap changing transformers.
2. Constant Current Loads: have a power demand that is proportional to the voltage. Constants *a* and *b* in Equations 2.2 and 2.3 are both one. An example of this type of load is the thyristor application drive.
3. Constant Impedance Loads: have a power demand that is proportional to the square of the voltage. Constants *a* and *b* in Equations 2.2 and 2.3 are both two. Examples of this type are residential and commercial loads.
4. Composite System Loads: have combinations of the other three load types. The constant '*a*' usually ranges between 0.5 and 1.8 while '*b*' usually ranges between 1.5 and 6.

2.3.4 Modeling of the synchronous generator

In a conventional synchronous machine, the stator circuit consisting of a three phase winding is responsible for generating a magneto motive force. The field winding, located on the rotor, is excited by a DC voltage. The synchronous machine model can be represented in the equations below and the d-q reference frame given in Figure 2.7. The convention adopted for the signs of the voltages and currents in the equations below is that *v* is the impressed voltage at the terminals, and the direction of positive current *i* corresponds to generation [39].

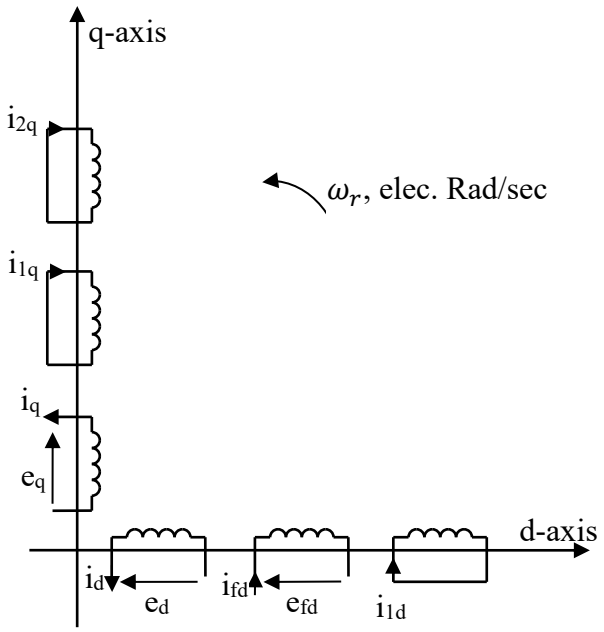

Figure 2.7: Modeling of the synchronous machine in the d-q reference frame.

With time t expressed in seconds, the angular velocity ω expressed in rad/s ($\omega_0 = 377 rad/\text{sec}$) and the other quantities expressed in per unit, the stator equations become:

$$e_d = \frac{1}{\omega_0}\frac{d\Psi_d}{dt} - \frac{\omega}{\omega_0}\Psi_q - R_a i_d \tag{2.4}$$

$$e_q = \frac{1}{\omega_0}\frac{d\Psi_q}{dt} + \frac{\omega}{\omega_0}\Psi_d - R_a i_q \tag{2.5}$$

The rotor equations:

$$e_{fd} = \frac{1}{\omega_0}\frac{d\Psi_{fd}}{dt} + R_{fd} i_{fd} \tag{2.6}$$

$$0 = \frac{1}{\omega_0}\frac{d\Psi_{1d}}{dt} + R_{1d} i_{1d} \tag{2.7}$$

$$0 = \frac{1}{\omega_0}\frac{d\Psi_{1q}}{dt} + R_{1q} i_{1q} \tag{2.8}$$

$$0 = \frac{1}{\omega_0}\frac{d\Psi_{2q}}{dt} + R_{2q} i_{2q} \tag{2.9}$$

The stator flux linkage equations:

$$\Psi_d = -L_d i_d + L_{ad} i_{fd} + L_{ad} i_{1d} \tag{2.10}$$

$$\Psi_q = -L_q i_q + L_{aq} i_{1q} + L_{aq} i_{2q} \tag{2.11}$$

The rotor flux linkage equations:

$$\Psi_{fd} = L_{ffd} i_{fd} + L_{ad} i_{1d} - L_{ad} i_d \tag{2.12}$$

$$\Psi_{1d} = L_{ad} i_{fd} + L_{11d} i_{1d} - L_{ad} i_d \tag{2.13}$$

$$\Psi_{1q} = L_{11q} i_{1q} + L_{aq} i_{2q} - L_{aq} i_q \tag{2.14}$$

$$\Psi_{2q} = L_{aq} i_{1q} + L_{22q} i_{2q} - L_{aq} i_q \tag{2.15}$$

The electromagnetic torque equation:

$$T_e = \Psi_d i_q - \Psi_q i_d \tag{2.16}$$

The overall differential equations which describe the transient performance of the synchronous machine are given by the following matrix equation:

$$\left[\frac{dX_{syn}}{dt}\right] = [At_{syn}][X_{syn}] + [Bt_{syn}]\begin{bmatrix} V_{td} \\ V_{tq} \\ e_{fd} \end{bmatrix} \tag{2.17}$$

where

$$[X_{syn}] = [i_d \quad i_q \quad i_{fd} \quad i_{1q} \quad i_{1d} \quad i_{2q}]^T$$

$$[At_{syn}] = [L]^{-1}[Qt]$$

$$[Bt_{syn}] = [L]^{-1}[Rt]$$

$$[L] = \begin{bmatrix} -L_d & 0 & L_{ad} & 0 & L_{ad} & 0 \\ 0 & -L_q & 0 & L_{aq} & 0 & L_{aq} \\ -L_{ad} & 0 & L_{ffd} & 0 & L_{ad} & 0 \\ 0 & -L_{aq} & 0 & L_{11q} & 0 & L_{aq} \\ -L_{aq} & 0 & L_{ad} & 0 & L_{11d} & 0 \\ 0 & -L_{aq} & 0 & L_{aq} & 0 & L_{22q} \end{bmatrix} \tag{2.18}$$

$$[Qt] = \begin{bmatrix} \omega_0 R_a & -\omega L_q & 0 & \omega L_{aq} & 0 & \omega L_{aq} \\ \omega L_d & \omega_0 R_a & -\omega L_{ad} & 0 & -\omega L_{ad} & 0 \\ 0 & 0 & -\omega_0 R_{fd} & 0 & 0 & 0 \\ 0 & 0 & 0 & -\omega_0 R_{1q} & 0 & 0 \\ 0 & 0 & 0 & 0 & -\omega_0 R_{1d} & 0 \\ 0 & 0 & 0 & 0 & 0 & -\omega_0 R_{2q} \end{bmatrix}$$

$$[Rt] = \begin{bmatrix} \omega_0 & 0 & 0 \\ 0 & \omega_0 & 0 \\ 0 & 0 & \omega_0 \\ 0 & 0 & 0 \\ 0 & 0 & 0 \\ 0 & 0 & 0 \end{bmatrix}$$

Here, the superscript ^{T} means matrix transpose.

2.3.5 Modeling of the excitation system

The excitation system model is given in Figure 2.8 [40]. Data for the system is given in Appendix A.

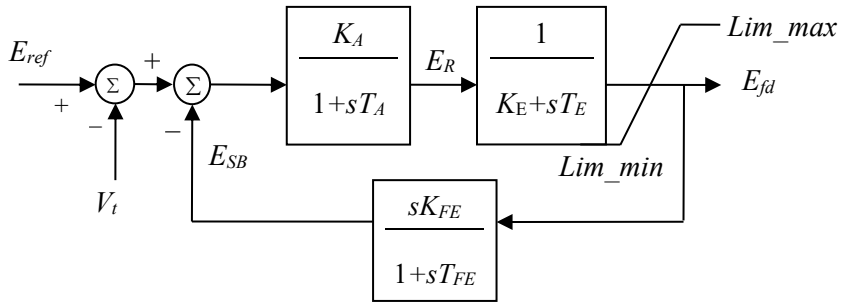

Figure 2.8: Excitation system block diagram.

The state-space equation of the excitation system is given by Equation 2.19

$$\left[\frac{dX_v}{dt}\right] = [At_v][X_v] + [Bt_v]\begin{bmatrix} V_t \\ E_{ref} \end{bmatrix} \tag{2.19}$$

where

$$[X_v] = \begin{bmatrix} e_{fd} & E_R & E_{SB} \end{bmatrix}^T$$

$$[At_v] = \begin{bmatrix} -\frac{K_E}{T_E} & \frac{1}{T_E}\frac{R_{fd}}{L_{ad}} & 0 \\ 0 & -\frac{1}{T_A} & -\frac{K_A}{T_A} \\ -\frac{K_E K_F}{T_E T_F}\frac{L_{ad}}{R_{fd}} & \frac{K_F}{T_F T_E} & -\frac{1}{T_F} \end{bmatrix}$$

$$[Bt_v] = \begin{bmatrix} 0 & 0 \\ -\frac{K_A}{T_A} & \frac{K_A}{T_A} \\ 0 & 0 \end{bmatrix}$$

2.3.6 Modeling of the DFIG wind turbine

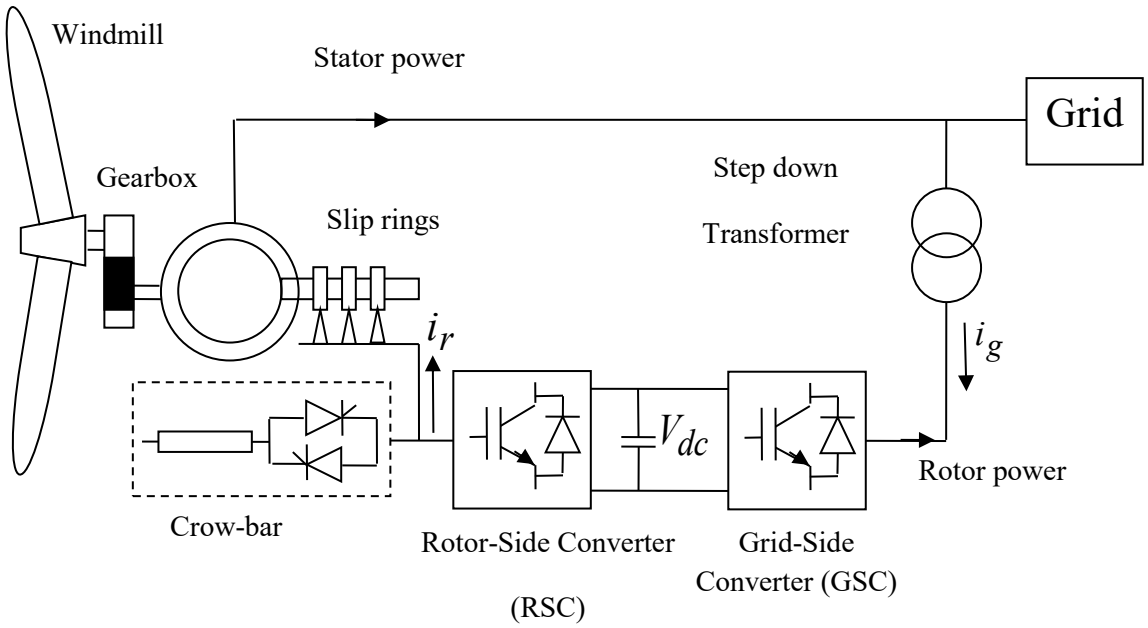

Figure 2.9: Schematic diagram of a DFIG wind turbine.

In the case of a doubly fed induction generator (DFIG) type wind turbine, the stator of the induction machine is connected directly to the grid. The wound rotor is then connected to the grid via a back-to-back (BTB) partial scale power converter. This BTB link consists of two, three

phase pulse width modulated (PWM) voltage source converters (VSCs) (a rotor side converter and a grid side converter) coupled to a DC bus. A crowbar is used as a backup to protect the power electronics converter against overvoltage or thermal breakdown. Details of the mathematical modeling and control of the DFIG wind turbine are given in reference [41].

The aggregated model of a 1.5 MW, 60 Hz DFIG type wind turbine given in reference [42] is utilized in this thesis. Within the model there is capability to control the pitch thereby limiting the maximum speed of the turbine. In addition a DC resistive chopper is used to limit the DC voltage, preventing the crowbar from operating during an AC fault. A two mass model is utilized to represent the low frequency oscillation in the turbine [43] - [44].

2.3.7 Modeling of the Photovoltaic array

A photovoltaic (PV) array consists of multiple PV modules linked in series and parallel for the purpose of obtaining the desired current and voltage output. The array feeds a DC/DC boost converter through a DC disconnect switch. The output of a PV array depends on the level of solar irradiance and surface temperature present in the atmosphere. This level varies over the course of the day. As a result, maximum power point trackers (MPPTs) are used to ensure the most efficient mode of operation of the PV array. The MPPT is responsible for adjusting the DC/DC converter switch in order to match the load impedance to the current and voltage output of the array at the maximum power point. This occurs when a DC voltage is fed into a 3-legged 6 switch voltage source inverter (VSI) to output the same voltage as a line-to line sinusoid. An LC filter is then used to smooth out harmonics before feeding an isolating transformer. The transformer connects to the grid via an AC disconnect switch. Details of the mathematical modelling and control are given in reference [45].

2.4 Summary

Chapter 2 has provided an introduction into typical distribution systems and microgrid networks utilized in the study of this thesis. In addition, details are offered with regards to the various models and components used in the EMTP-RV software environment. Models presented include distribution lines, loads, synchronous generators, transformers, DFIG wind turbines and PV arrays.

3. A NOVEL RECLOSING SCHEME FOR MITIGATION OF DISTRIBUTED GENERATION EFFECTS ON OVERCURRENT PROTECTION

3.1 Introduction

This chapter presents a novel scheme to mitigate distribution generation (DG) effects on existing fuse-recloser infrastructure in radial distribution networks. The proposed method employs the use of a control unit, a variable load bank and a dedicated recloser at the point of common coupling (PCC) between the DG unit and the distribution network. Investigations are conducted through several time-domain simulations to ascertain the suitability of the novel reclosing technique for the purpose of mitigating the effects of DG sources without the requirement to alter existing overcurrent protection infrastructure.

3.2 Mitigation of Distributed Generation Effects on Overcurrent Protection

Conceptually, inclusion of DER/DG sources has attracted growing attention, especially in the context of smart grid operation, since DG sources can be installed locally to individual loads. This practice introduces unique challenges. Traditional grid operations and short circuit characteristics can potentially be affected, yielding degradation in existing equipment adequacy [2]-[4]. The extent of influence is determined through DG size, location, type and interconnection methods [31], [46] - [47]. IEEE standard 1547 [46] was introduced to address possible disconnection of all DG units following a distribution system fault, resulting in zero short circuit current contribution from the DG unit to the fault in the distribution network, which allowed for restoration of the initial fuse-recloser coordination. Widespread use of the IEEE standard 1547 [48] suggests that it has become global in its application.

In addition to IEEE standard 1547, multiple methods have been proposed to mitigate the effects of DG units on existing overcurrent protection. Mitigation is the first step in understanding the effects of DG units on individual distribution networks, but it is also imperative that the level of penetration that yields degradation in existing protection infrastructure adequacy should be ascertained. In references [31], [47] methods for determination

of DG penetration levels that result in fuse-recloser coordination degradation are presented. In reference [31], it is further proposed that the DG penetration be limited to a specific level based on the unique feeder. Although effective, this method lacks long term feasibility. Another solution offered is the redesign of the existing infrastructure. This is a reliable method but may be economically infeasible depending on the size of the distribution network.

In addition to re-engineering and penetration limitation, many researchers offer solutions that allow for increased levels of DG integration. Reference [7] presents a method where individual relays are pre-programmed with every anticipated state that the network will encounter. Based on the state of the network, the protection settings will adapt. The key drawback is that the method may be ineffective when a state is encountered that was not expected. Generally, all previously proposed methods capable of mitigating the effects of DG units on existing protection infrastructure [5] have advantages and drawbacks. Some of these include voltage based methods [49], which monitor the DG source voltage and use these to discriminate fault types.

Another viable protection infrastructure option following DG integration is to install a current-limiting device that is self-triggering, rapidly activated within milliseconds, and failsafe. Fault Current Limiters (FCLs) are series devices with low impedance (considered zero) during steady state operation but change to a high impedance value, limiting short circuit current following a fault [26].

3.3 The Proposed Reclosing Scheme

In review of Section 3.2, it can be inferred that the majority of utilities and publications aim to mitigate the influence of DG units on existing protection infrastructure through two main concepts: the first is complete disconnection of the DG unit. This causes the unit to shut down following disconnection and reconnect following fault clearance by the existing network protection infrastructure. The second concept is to restrict the DG short circuit contribution to minimal levels such that the original coordination is not disturbed.

The proposed scheme works through disconnection of the DG source following fault detection and excessive current increase, but maintains operation of the unit at its pre-fault load sharing level with no need for immediate shut down. This allows for the DG source to maintain

its pre-fault speed and frequency, resulting in a fast reconnection of the unit following fault clearance. The key effect of this method is a significant reduction in the costs of shut down and restarting procedures [50] - [51].

The proposed scheme (designated as R_D) is applied at the PCC between the DG unit and the overall network. This can be expressed diagrammatically via Figure 3.1.

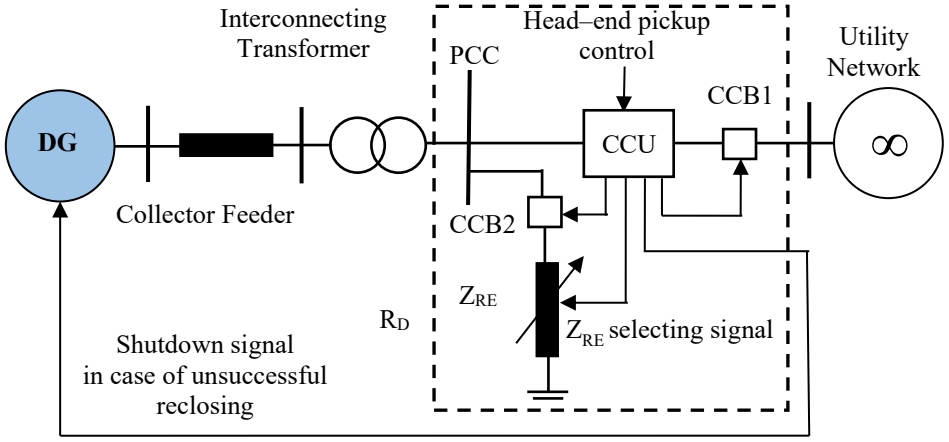

Figure 3.1: DG source interconnection with the R_D recloser.

The structure of this scheme can be expressed in three parts:

1. The communication and control unit (CCU).
2. The controlled transfer impedance.
3. The sequence of operation.

3.3.1 The Central Control Unit

The CCU contains two key components: the receiver/transmitter (R/T) unit and the control component of the DG recloser (DG-RC). The R/T unit is designed to allow for R_D to receive a fault detection signal from the head-end recloser. The DG-RC unit is designed to detect the rise in the DG terminal current and will produce a tripping signal if this current exceeds a preset pickup value. If both signals from the R/T and DG-RC unit are present then the CCU will transmit a control signal to the circuit breaker CCB1 (normally closed) in Figure 3.1 to disconnect the DG unit from the network.

The pickup settings of the DG-RC unit are directly related to the DG unit rating (I_{DGrat}). Through multiple short circuit studies conducted, it was observed that the DG current output will

not exceed three and two times the rated DG current following reconnection from a phase and ground fault respectively. As a result the DG-RC pickup settings can be expressed as:

$$I_{pickupP} = 3 \times I_{DGrat} \tag{3.1}$$

$$I_{pickupg} = 2 \times I_{DGrat} \tag{3.2}$$

where

$I_{pickupP} = \text{DG} - \text{RC phase pickup current (A)}$

$I_{pickupg} = DG - RC\ ground\ pickup\ current\ (A)$

$\text{I}_{\text{DGrat}} = \text{rated DG unit current (A)}$

When the CCU transmits to CCB1, it will send another two signals: one to controlled transfer impedance (Z_{RE}) and one to CCB2. The signal to Z_{RE} prompts selection of the value of the transfer impedance. The signal to CCB2 acts to close the normally- open circuit breaker, resulting in the transfer impedance being connected at the PCC between the DG unit and the distribution network.

Through observation of Figure 3.1, it is apparent that there is a requirement for a communication link between the head-end recloser and R_D. Although this particular component is outside the scope of this thesis, Ethernet Fiber Links technology should be adequate for this application with a delay time in the order of only a few milliseconds [52]. Although this technology should be adequate for this application, there are many others that would be potentially viable. In order to account for the communication, a delay time of 5 milliseconds is used in time-domain simulations.

Another important aspect of the scheme is the circuit breakers. CCB1 and CCB2 are thyristor-based circuit breakers (TBCBs) which have a fast clearing time (microsecond scale) [53]. As a result a 10 microsecond delay is utilized in the investigations of this thesis to account for the clearing time of the breaker.

3.3.2 The Controlled Transfer Impedance Z_{RE}

The purpose of the controlled transfer impedance is to allow for the DG unit to maintain its operation at the same pre-fault levels in terms of current, frequency and terminal voltage after

it is disconnected from the distribution network following a fault. This will allow for the DG unit to be easily reconnected to the system following fault clearing.

The value of the transfer impedance to be connected at the PCC can be determined through the use of Equation 3.3.

$$Z_{RE} = \frac{V_{ph}^2}{DG_{pre-fault\ output}} = \frac{V_{ph}^2}{(S_{sys} + S_{local})} = \frac{V_{ph}}{I_{ph}} \times \left(\frac{P_{ph}}{\left(\sqrt{P_{ph}^2 + Q_{ph}^2}\right)} + j \frac{Q_{ph}}{\left(\sqrt{P_{ph}^2 + Q_{ph}^2}\right)} \right) \tag{3.3}$$

where

$V_{ph} =$ phase voltage of the system (kV)

$S_{sys} =$ MVA supplied by the DG unit to the system

$S_{local} =$ local load MVA

$I_{ph} =$ phase current of the system (A)

$P_{ph} =$ pre − fault phase active power (MW)

$Q =$ pre − fault phase reactive power (MVAR)

Equation 3.3 reveals a relationship between the DG current contribution during the fault and Z_{RE}. This relationship can be exploited when determining the value of the transfer impedance. The CCU is responsible for the selection of the transfer impedance value based on the pre-fault measurements of real and reactive power delivered by the DG unit with the corresponding voltage and current. From these measurements, and using Equation 3.3, the value of Z_{RE} in the form $R_{RE}+jX_{RE}$ can be calculated using power equations [17]. The calculated values are stored in temporary memory after a half second delay.

Values are read half a second before the fault because a steady state short circuit can be considered by the CCU to be present after 30 cycles (half second in a 60 Hz system) following fault inception [54]. This means that the R_{RE} and X_{RE} transmitted to the load bank are from a steady state operating condition as R_D is expected to operate within a few cycles of fault inception. There is an advantage in selecting Z_{RE} based on pre-fault conditions, as factors such as

fault location, system topology and fault impedance will have no influence on the calculation procedure.

3.3.3 Sequence of Operation

The sequence of operation for the R_D recloser can be explained in the following steps:

1. The CCU will measure the steady-state outputs of the DG unit to determine the necessary value of Z_{RE}.
2. When a fault occurs, the head-end recloser will detect it when the short circuit current from the substation exceeds the pickup setting. Following detection, the head-end recloser will transmit via a communication channel to the CCU. Before this transmission has even occurred, the CCU will have been constantly measuring the outputs from the DG source.
3. When the CCU receives the head-end recloser trip signal and the DG current output is in excess of the DG-RC pickup setting (for a phase or ground fault) then the CCU will produce a trip signal instructing CCB1 to disconnect the DG unit from the network.
4. At the same time as step 3, the CCU will send a control signal to CCB2 and Z_{RE}. This signal will force CCB2 to close onto the value of Z_{RE} as determined by Equation 3.3. This allows for the DG unit to maintain its pre-fault speed and frequency which will facilitate a faster reconnection time following fault clearance.
5. Once the fault is clear, the head-end recloser will send a clear signal to the CCU. The CCU will then wait a minimum reclose time (0.5 seconds). The CCU will wait to receive a synch-signal from a synchronizer to indicate that the DG unit is synchronized with the distribution network.
6. When the minimum wait time is exceeded and a synch-signal is received then R_D will attempt to reconnect the DG source to the network by opening CCB2 and closing CCB1.
7. If the DG unit fails to reclose at least twice or the fault is unable to be cleared from the network within a preset time frame, R_D will send a shutdown signal to the DG source.

3.4 Application of the Proposed Scheme

This section aims to demonstrate the effectiveness of the proposed scheme R_D through four comparative studies. These studies can be expressed as:

1. The application of a conventional method whereby the loss of coordination (LOC) limit is determined for a network under study. Limiting the DG penetration to levels below the LOC limit will result in existing fuse-recloser coordination being maintained.
2. Time-domain simulations are presented to demonstrate the effectiveness of the proposed scheme for different fault types.
3. The proposed scheme is compared to one other method of mitigating DG short circuit contributions, namely superconducting fault current limiters (SFCLs).
4. The proposed scheme is investigated under various changes in fault impedance, fault duration and interconnecting transformer types.

The system that is utilized in the studies in the chapter is presented in Figure 2.1 in Chapter 2. The DG unit that is utilized in the studies of this chapter is a synchronous generator. Data for the generator is presented in Appendix A.

3.4.1 Application of a Conventional Method to Determine Loss of Coordination Limits

There are two distinct methods which are conventionally used when dealing with integration of DG units into a distribution network:

1. Restricting the level of DG penetration on the network to those that are below the LOC limit.
2. Limiting the points in a network where the DG unit is able to be connected.

Reference [47] presents a method for determination of LOC limits for candidate DG connection points in distribution networks that have DG penetration present. The method works by conducting simulations that determine the level of short circuit current that is output by a DG unit for various fault locations in the network. Once fuse-recloser coordination is lost, the LOC limit for the candidate connection point with DG type is found.

In Figure 2.1, the candidate DG connection points are selected to be buses at L2, L3 and L5. Utilizing the algorithm in reference [47], the following LOC limits are obtained:

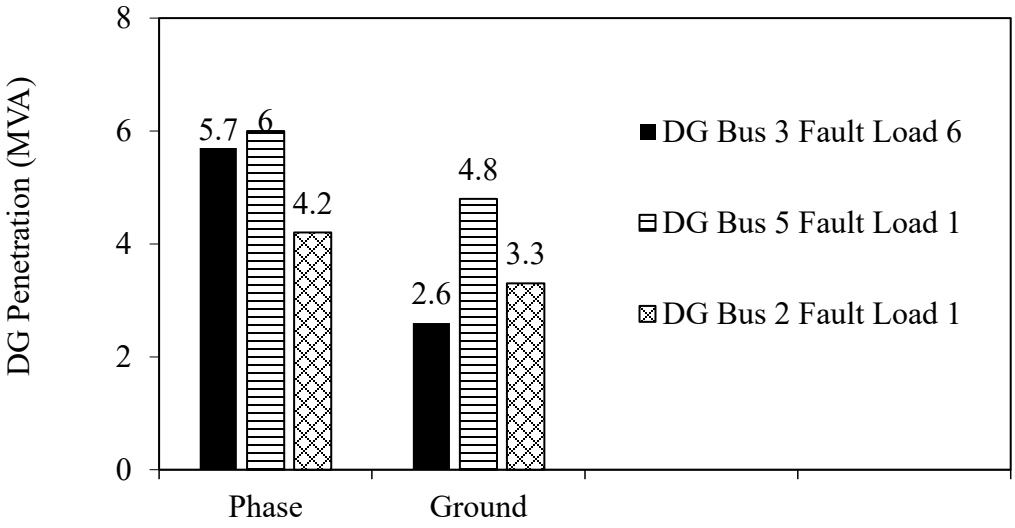

Figure 3.2: LOC limits for the candidate DG connection points - Yg/Yg interconnection transformer.

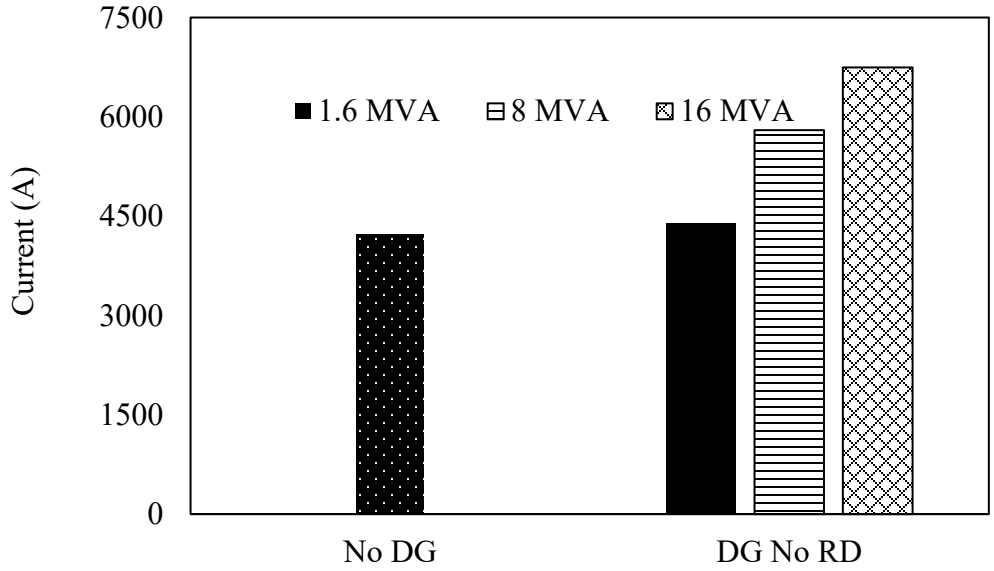

Figure 3.3: Short circuit levels experienced by F1 for a three-phase fault on load L1 with varying DG ratings connected at L2.

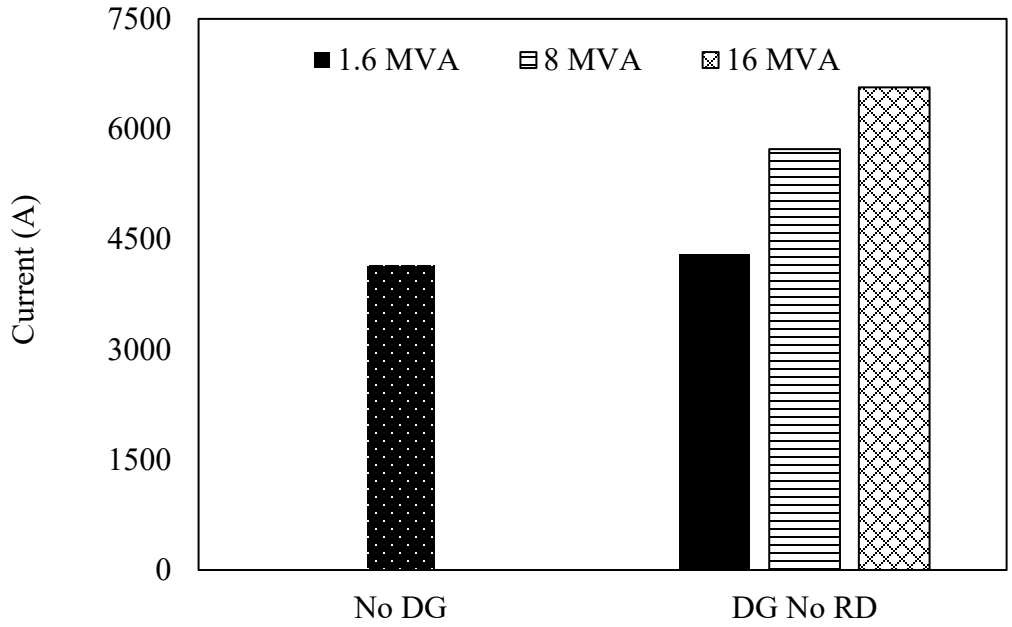

Figure 3.4: Short circuit levels experienced by F1 for a double line-to-ground fault on load L1 with varying DG ratings connected at L2.

Through observation of Figure 3.2, it is apparent that LOC will first occur when a DG source is connected at load busses 2 or 3 during a three-phase or line-to-line-to-ground fault near loads L1 or L6. In the case of a three-phase fault, the LOC limit will first occur for a DG unit connected to load bus 2 when the fault is at load L1. In the case of the line-to-line to ground fault, the LOC limit will first occur for a DG unit connected to load bus 3 for a fault at load L6. The LOC limit for the network is presented in Figure 2.1 is 4.2 MVA for phase faults and 2.6 MVA for ground faults.

In order to demonstrate the effects of the DG unit on the existing short circuit characteristics of the distribution network, a small case study was conducted for a DG unit of varying capacity connected to load bus 2 for a fault on load L1.

Figures 3.3 and 3.4 demonstrate the short circuit current experienced by fuse F1 when a fault occurs at load L1. Observation reveals that when there is DG penetration on the network, there is a simultaneous increase in short circuit current experienced by the fuse. As a result the fuse will operate faster than the capacity built into the design, potentially resulting in a loss of coordination between the fuse and upstream devices such as head-end reclosers. This captures one of the key challenges associated with integration of DG units into distribution networks.

3.4.2 Application of the Proposed Scheme to Mitigate DG Influences on Overcurrent Protection

Two case studies are presented to demonstrate the efficacy of the proposed scheme for mitigation of DG influences on fuse-recloser coordination. The case studies showcase the capability of the proposed scheme in managing DG penetrations beyond the LOC limit of individual feeders. The second investigates the efficacy of the proposed approach under varying fault types. The case studies are expressed in Table 3.1 with diagrammatic representation in Figure 3.5.

Table 3.1: Case studies.

	Case Study-1	Case Study-2
Fault type	Three-Phase	Line-to-Line-to-Ground
Fault location	Load L1	
Fault inception	1 second of simulation time	
Fault duration	Sustained fault	
DG connection point	at L2	
DG pre-fault load sharing condition & PF	0.8 of 8 MVA DG, 0.9 power factor	
DG transformer configuration	Yg/Yg	

Before conducting the studies in Table 3.1, it is prudent to determine the pickup settings of R_D in addition to determining the range of transfer impedances. As per Equations 3.1 and 3.2, the phase and ground settings for an 8 MVA synchronous machine based (SM-based) DG source are as such:

$$I_{DGrat} = \frac{8 \times 10^6}{\sqrt{3} \times 25000} = 184.75\ A$$

$$I_{pickupP} = 3 \times 184.75 = 554.26\ A$$

$$I_{pickupg} = 2 \times 184.75 = 369.5\ A$$

From these equations, the phase and ground pickup currents are selected to be 555 A and 370 A respectively.

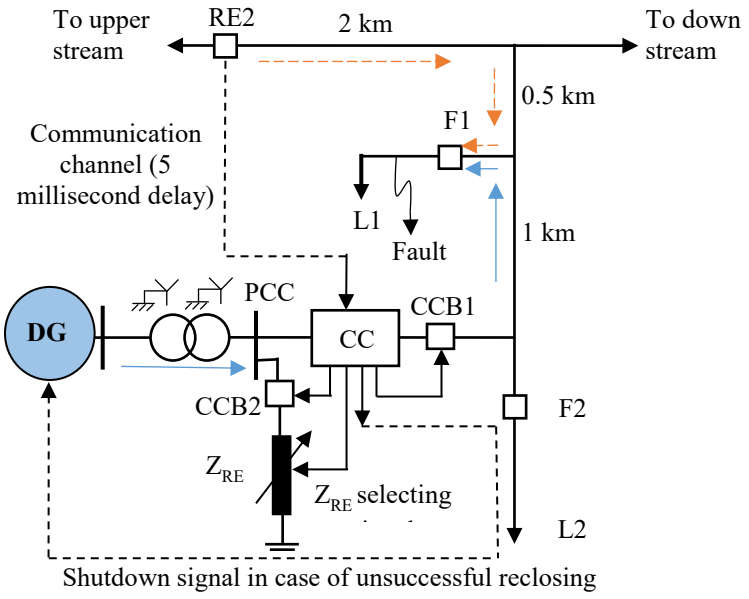

Figure 3.5: Fault applied on load L1 with the DG unit at load 2.

In these case studies, the local load connected to the DG unit terminals is assumed to be zero. For simplicity reasons, the range of load-sharing conditions compensated for in Z_{RE} for these case studies is restricted to three. It should be noted that there could be an infinite number of possible values for Z_{RE} in a given range of operating conditions. The number of conditions that Z_{RE} is capable of transferring is also related to the load bank itself. If the installation was to only have discrete values of impedance, then the values of Z_{RE} would have to be selected in a range. If the load bank was capable of dynamically changing its impedance based on inputs then discretizing the ranges would be unnecessary and only Equation 3.3 would be required. For the case studies presented in Chapter 3, a range for discrete impedance values is specified.

Utilizing Equation 3.3, Z_{RE} is determined for pre-fault load sharing conditions where the DG unit is loaded to 80%, 70% and 60% capacity respectively. For the case of the 80% loading factor, the 8 MVA DG unit is connected to a 25 kV network. As such the Z_{RE} values are determined as:

$$R_{RE} = \frac{(\frac{25}{\sqrt{3}})^2}{0.8 \times 8/3} \times 0.9 = 88\ \Omega$$

$$X_{RE} = \sqrt{\left(\frac{(\frac{25}{\sqrt{3}})^2}{0.8 \times 8/3}\right)^2 - \left(\frac{(\frac{25}{\sqrt{3}})^2}{0.8 \times 8/3} \times 0.9\right)^2} = 43\ \Omega$$

A similar approach is taken with the 70% and 60% case. The values for Z_{RE} with their corresponding ranges can be summarized in Table 3.2.

Table 3.2: Possible DG load sharing conditions and pickup settings.

Load sharing condition, p.u. of DG MVA	LS_3	LS_2	LS_1
	0.6	0.7	0.8
Corresponding R_{RE} , Ω	R_{RE3}	R_{RE2}	R_{RE1}
	118	101	88
Corresponding X_{RE} , Ω	X_{RE3}	X_{RE2}	X_{RE1}
	57	49	43
Pre-fault measured R range, Ω	P_3	P_2	P_1
	$110 \leq R$	$95 \leq R < 110$	$R < 95$
Pre-fault measured X range, Ω	G_3	G_2	G_1
	$53 \leq X$	$46 \leq X < 53$	$X < 46$
Phase pickup current, A	555		
Ground pickup current, A	370		

For the purpose of clear figure presentation, a duration time from 0.9 seconds to 1.6 seconds is only shown for the cases where the proposed scheme is not applied, while a longer duration from 0.8 seconds to 7.8 seconds is shown for the cases that include the proposed scheme. All values are stated in RMS unless otherwise indicated. It should also be noted that additional case study data is offered in Appendix B.

3.4.2.1 Case Study-1

Figures 3.6 to 3.9 present the time domain simulations results for Case Study-1.

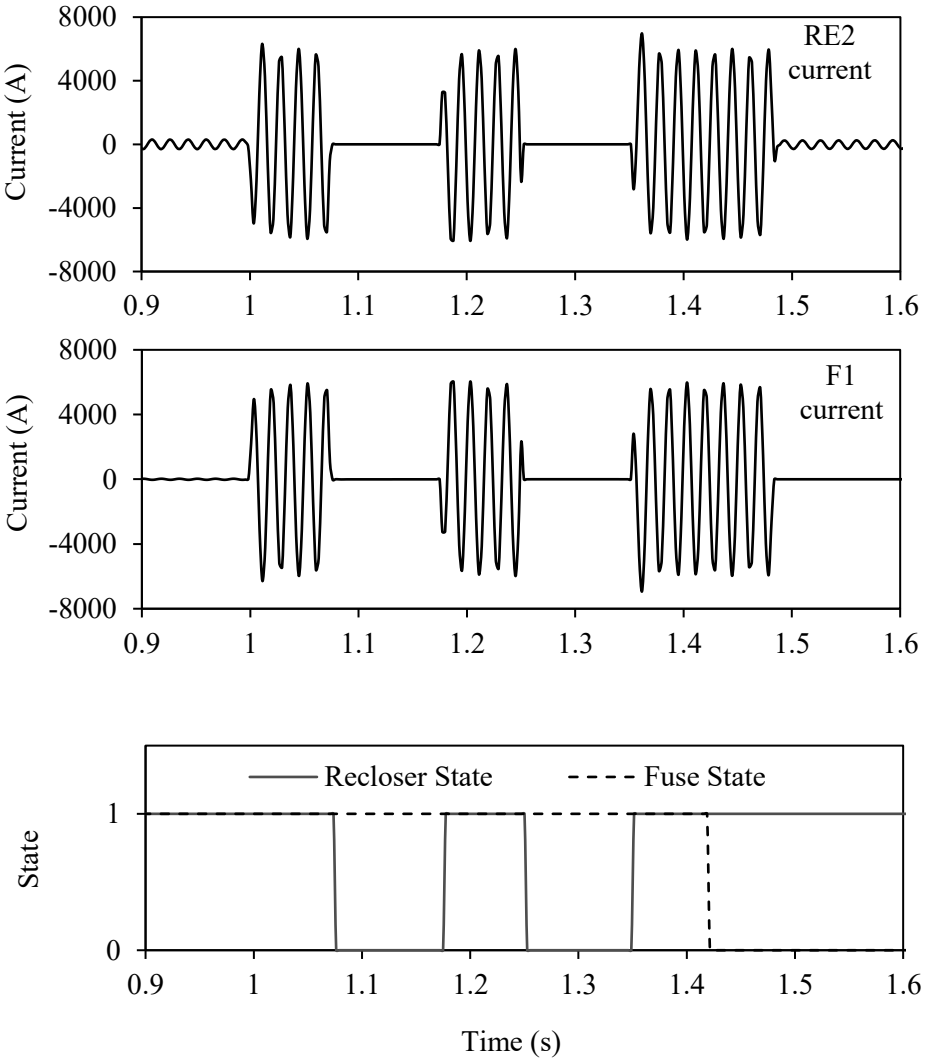

Figure 3.6: Case Study-1 without the DG source: RE2 current, F1 current, RE2 and F1 state signals.

Figure 3.6 presents Case Study-1 for the condition where there is no DG penetration on the network. Observation reveals coordination between the downstream fuse (F1) and the head-end recloser (RE2) for the system given in Figure 2.1. When there is no DG penetration, RE2 operates twice in its fast mode before the fuse F1 clears the fault. Further observation makes it apparent that the short circuit currents experienced by RE2 and F1 are 4244 A and 4229 A respectively. This corresponds to a clearing time of 1.0762 seconds and 1.424 seconds respectively. This case demonstrates coordination between the fuse and upstream recloser.

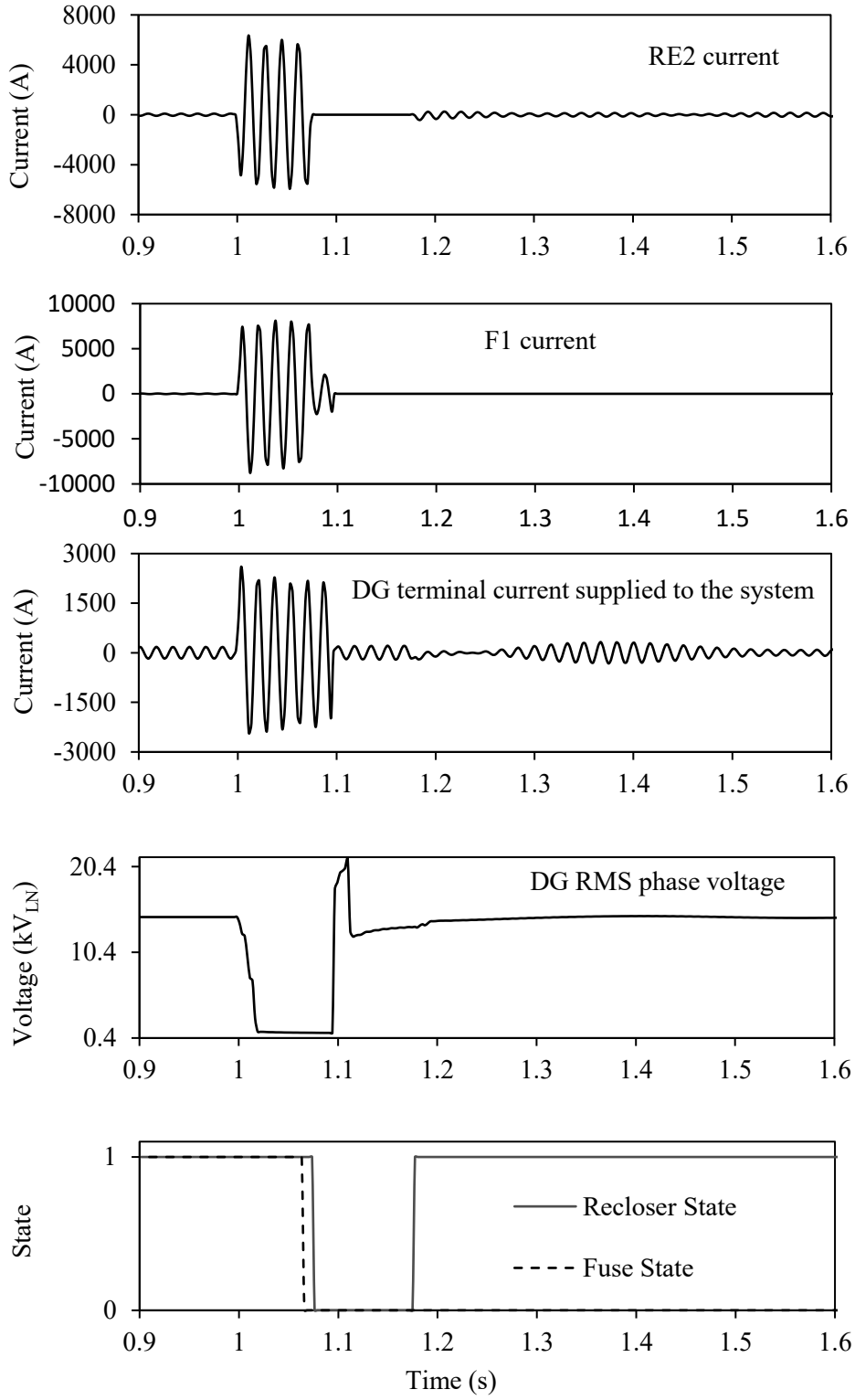

Figure 3.7: Case Study-1 with the DG source connected at L2 when RD is not applied: RE2 current, F1 current, DG terminal current, DG RMS phase voltage, RE2 and F1 state signals.

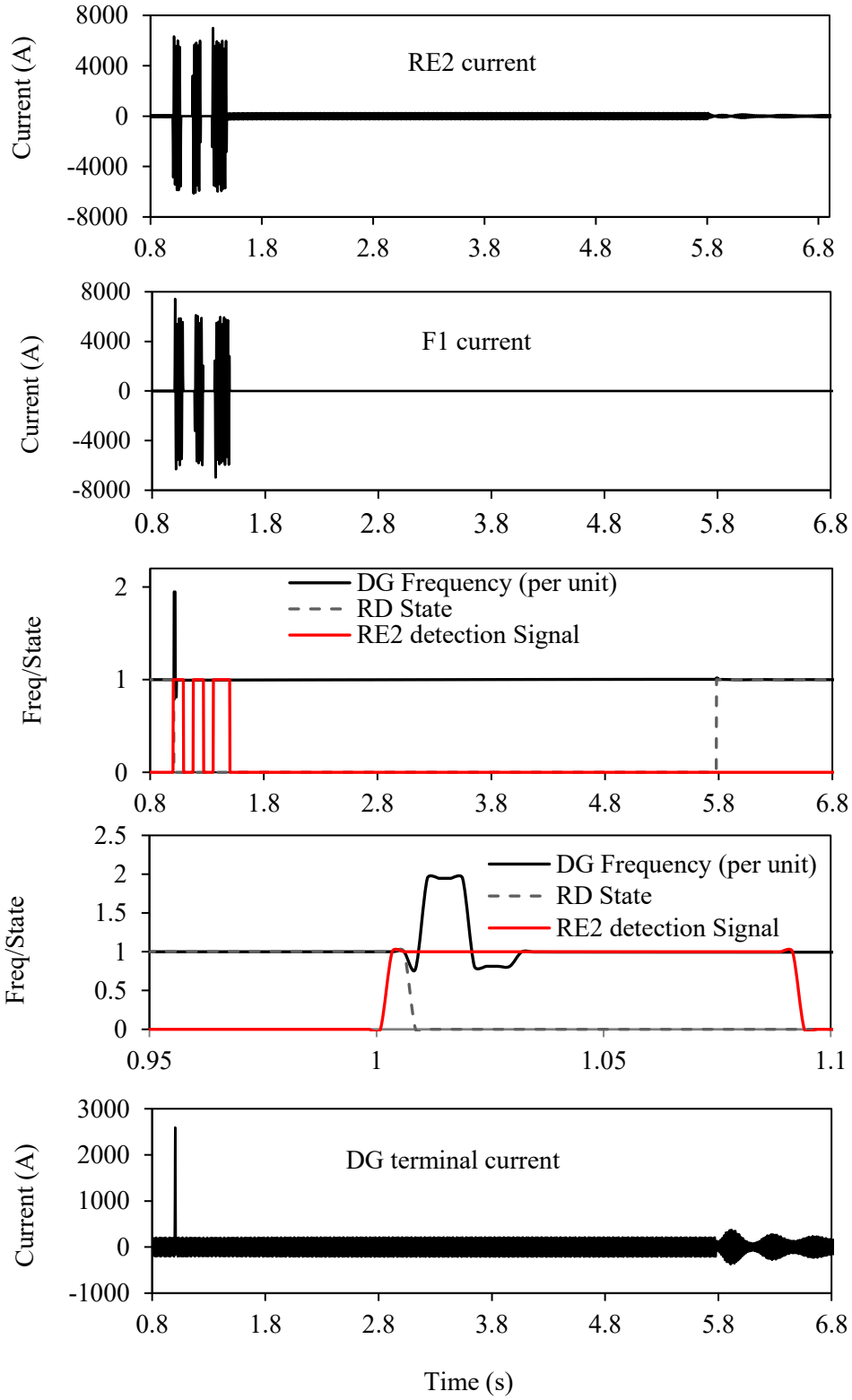

Figure 3.8: Case Study-1 with the DG source at L2 when RD is applied: RE2 current, F1 current, RE2, RD communication & DG frequency, Zoom on RE2, RD signals, DG terminal current.

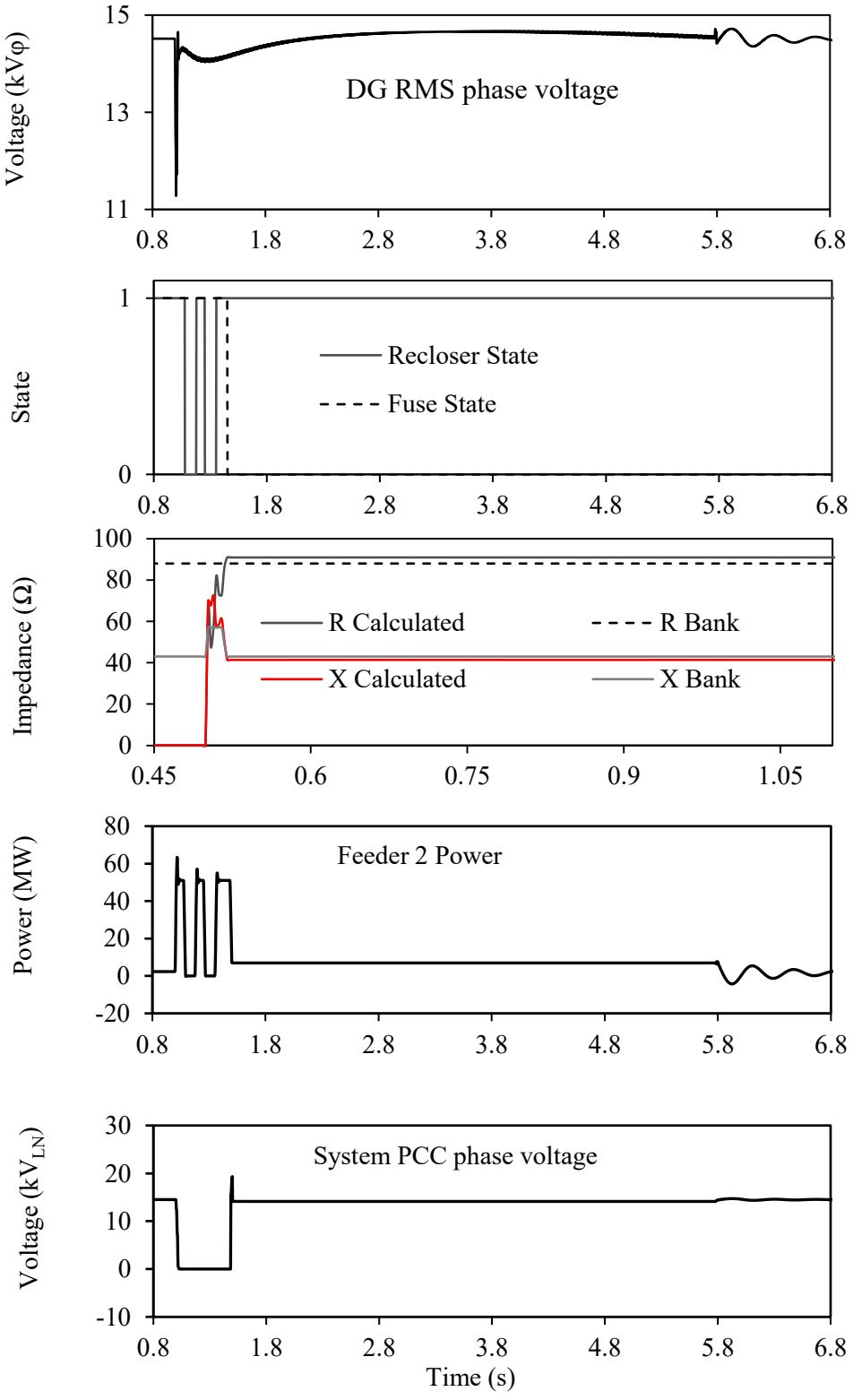

Figure 3.9: Case Study-1 with the DG source at L2 when RD is applied: DG voltage, State signals, load bank calculated and actual values, Feeder 2 active power and System PCC phase voltage.

Figure 3.7 presents Case Study-1 for conditions where an 8 MVA SM-based DG source is connected to the L2 lateral while R_D is not in service. Observation reveals that the short circuit current experienced by RE2 is 4241 A while the short circuit current experienced by fuse F1 increases to 5800 A. The resultant increase in the short circuit current in F1 is expected, attributed to the fault being fed by two independent sources (the utility and the DG source). The clearing times corresponding to the short circuit currents experienced by RE2 and F1 are 1.0762 seconds and 1.0659 seconds respectively. Furthermore, it can be seen in Figure 3.7 that the fuse F1 operates before RE2. This demonstrates the existence of the coordination problem as the original fuse-saving scheme is violated. It is worth noting that in this case RE2 was intentionally left to operate despite the fuse F1 operating. This was to allow for an easy comparison between the clearing times of the fuse and head-end recloser. Lastly, it can be observed that due to the fault, the DG terminal voltage dropped to 0.993 kV.

Figures 3.8 and 3.9 present Case Study-1 for the 8 MVA DG source connected to the L2 lateral while R_D is in service. Observation reveals that when the proposed scheme is implemented, the short circuit current experienced by RE2 remains relatively unchanged at 4242 A while the level experienced by the fuse F1 decreases to 4226 A. It can also be observed that RE2 detects the fault and notifies R_D via the communication channel at 1.004 seconds, resulting in the DG source disconnecting from the network and feeding Z_{RE} at 1.013 seconds (less than one cycle following fault occurrence).

Figures 3.8 and 3.9 also demonstrate the DG terminal current, voltage and the per unit frequency for the following progression: the DG source disconnects from the network then switches to Z_{RE} before reconnecting to the network following successful reclosing at 5.82 seconds. This demonstrates that the proposed scheme disconnects the DG source but keeps it operational until fault clearance before reconnecting to the network within a 4.82 second timeframe. This highlights that reconnection of the DG is faster under the proposed scheme than in current utility practices.

In the context of system performance it can be observed that the voltage drops to 11.274 kV in contrast to 0.994 kV when R_D is not in service. Furthermore, the overshoot frequency when reconnecting the DG source to the network is 1.018 per unit (61.08 Hz) before it decays to a nominal level. In addition it can be seen that RE2 returns to its regular operating time of 1.0761

seconds which allows for an attempted clearing of a temporary fault if the fuse F1 clears it at 1.453 seconds. Further observation of Figure 3.9 makes it apparent that the system regains its normal operating state post fault (following reconnection of the DG source). It should be noted that the Feeder 2 power is measured at RE2 and that the system voltage is measured at the PCC on the system side of the breaker. This demonstrates the capacity of the proposed scheme to restore coordination to the system without limiting the DG penetration.

3.4.2.1 Case Study-2

Figures 3.10 to 3.13 present the time domain simulations results for Case Study-2.

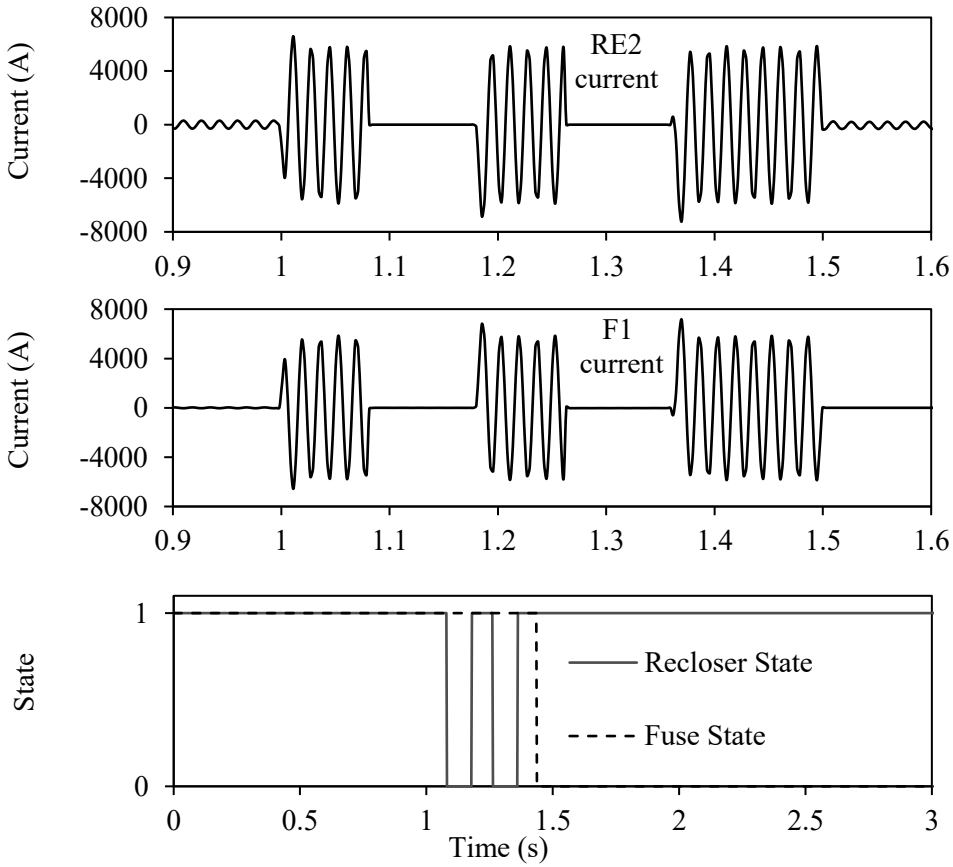

Figure 3.10: Case Study-2 without the DG source: RE2 current, F1 current, RE2 and F1 state signals.

Figure 3.10 presents Case Study-2 for the condition where there is no DG penetration on the network. Through observation it can be seen that there is coordination between the downstream fuse (F1) and the head-end recloser (RE2) for the system given in Figure 2.1. When there is no DG penetration, RE2 operates twice in its fast mode before the fuse F1 clears the fault.

Further observation makes it apparent that the short circuit currents experienced by RE2 and F1 are 4162 A and 4141 A respectively. This corresponds to a clearing time of 1.0814 seconds and 1.437 seconds respectively. This case demonstrates coordination between the fuse and upstream head-end recloser.

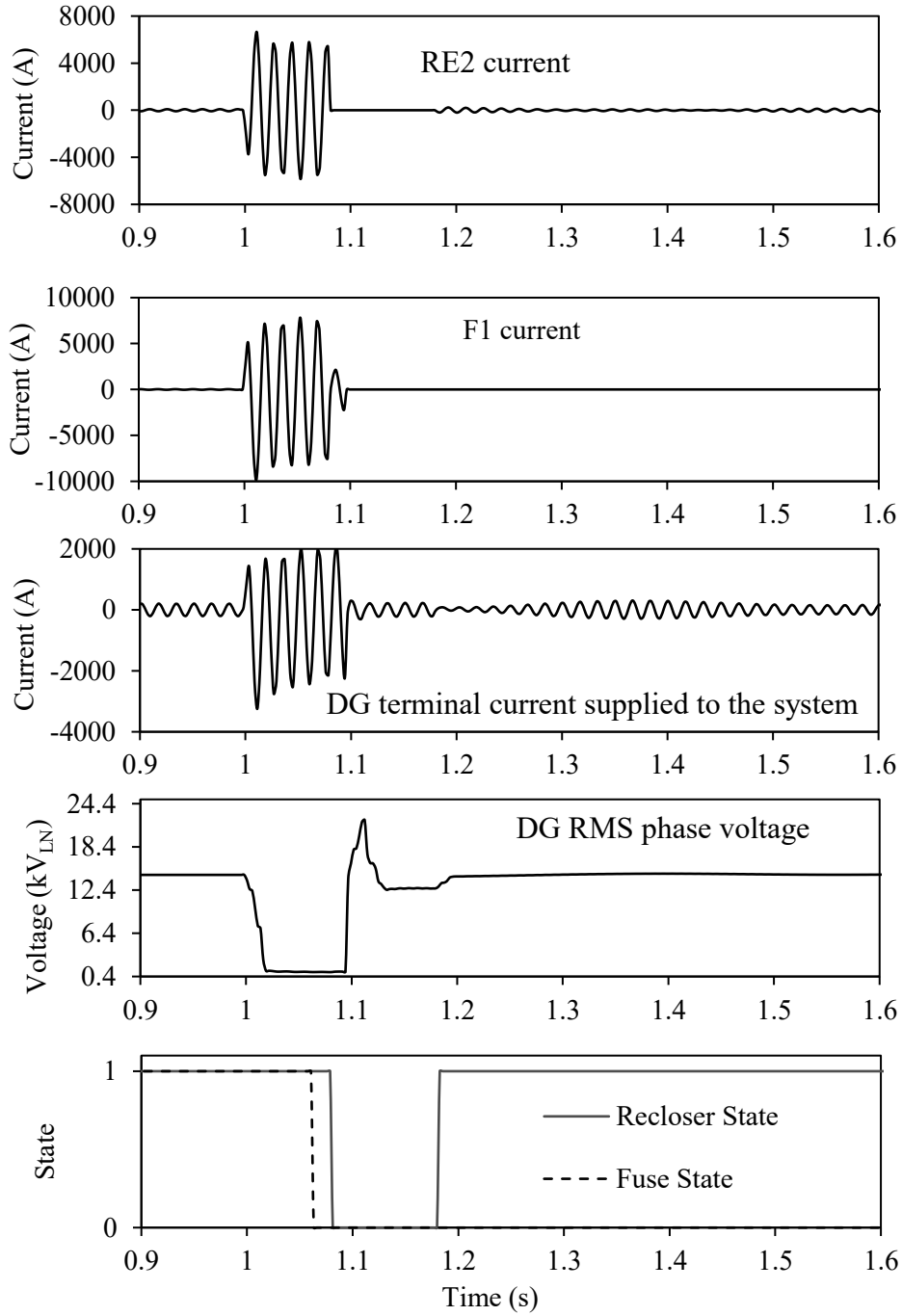

Figure 3.11: Case Study-2 with the DG source connected at L2 when RD is not applied: RE2 current, F1 current, DG terminal current, DG RMS phase voltage. RE2 and F1 state signals.

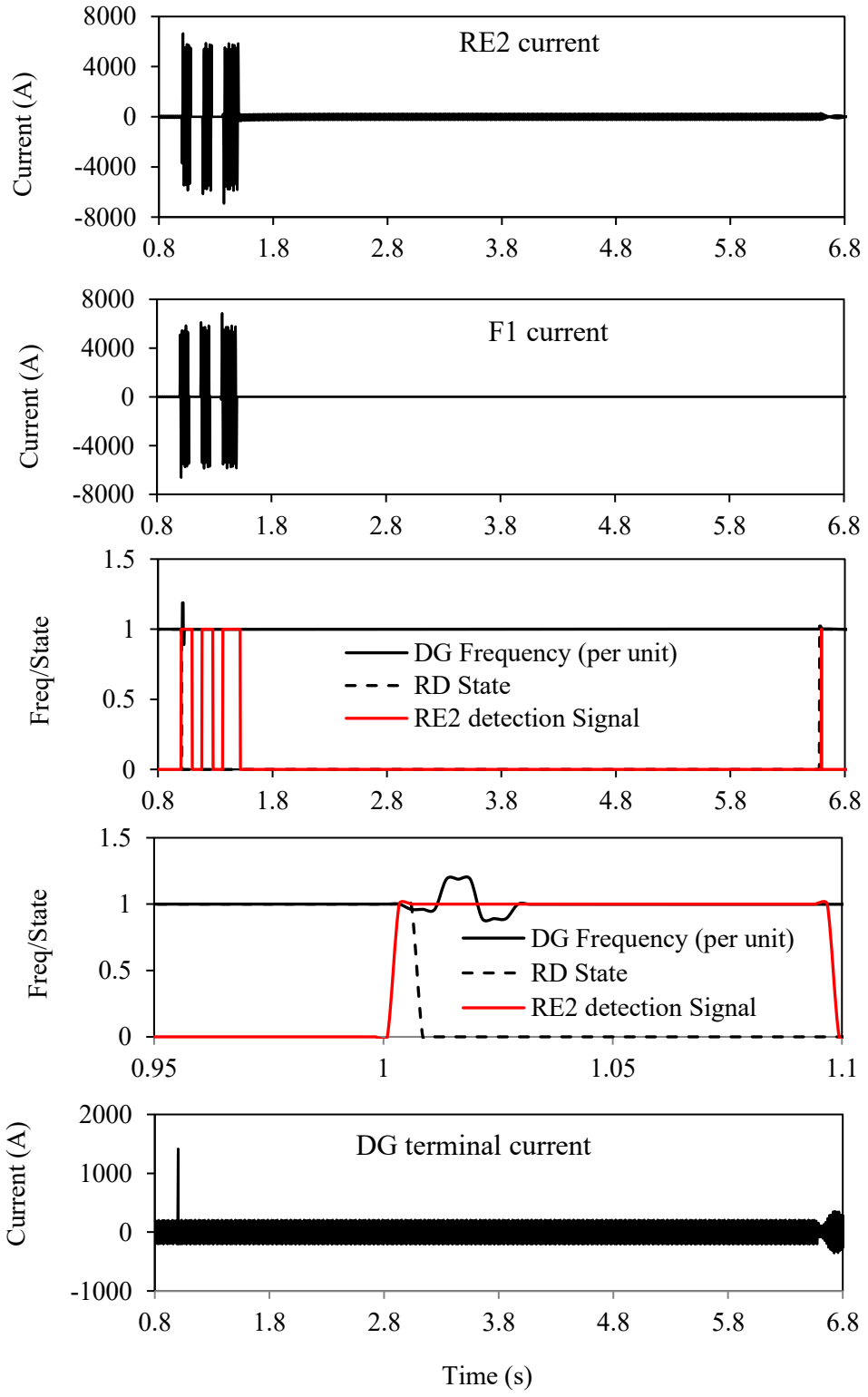

Figure 3.12: Case Study-2 with the DG source at L2 when RD is applied: RE2 current, F1 current, RE2, RD communication & DG frequency, Zoom on RE2, RD signals, DG terminal current.

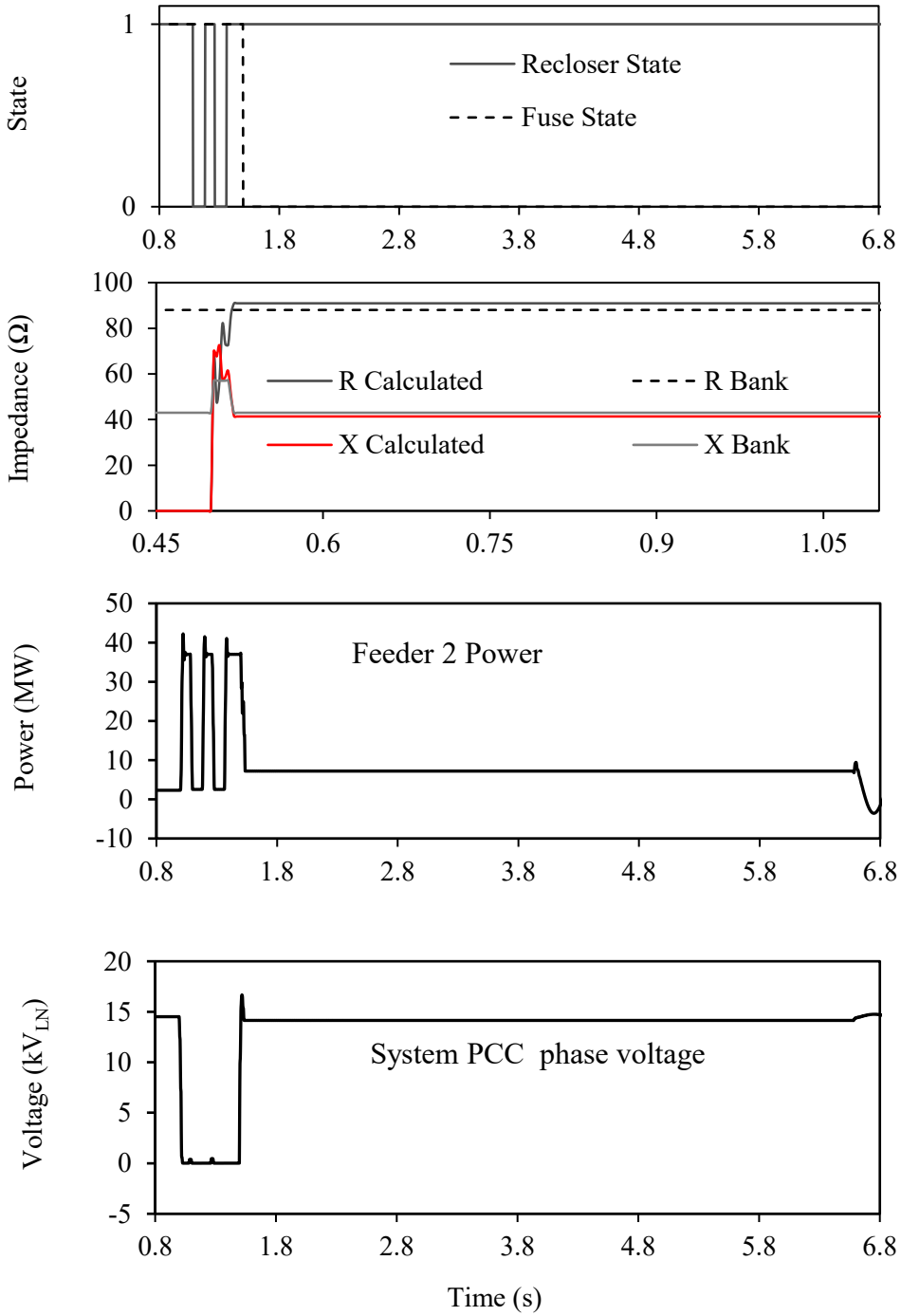

Figure 3.13: Case Study-2 with the DG source at L2 when RD is applied: DG voltage, State signals, load bank calculated and actual values, Feeder 2 active power and System PCC phase voltage.

Figure 3.11 presents Case Study-2 for the conditions where an 8 MVA SM-based DG source is connected to the L2 lateral while R_D is not in service. Through observation it can be seen that the short circuit current experienced by RE2 is 4160 A while the short circuit current experienced by fuse F1 increases to 5728 A. Again, the increase in the short circuit current in F1 is expected, attributed to the fault being fed by two independent sources (the utility and the DG source). The clearing times corresponding to the short circuit currents experienced by RE2 and F1 are 1.0812 seconds and 1.0632 seconds respectively. Furthermore, it can be seen that the fuse F1 operates before RE2. This again demonstrates the existence of the coordination problem as the original fuse-saving scheme is violated. Lastly, it can be seen that due to the fault, the DG terminal voltage dropped to 1.016 kV.

Figures 3.12 and 3.13 present Case Study-2 for the 8 MVA DG source connected to the L2 lateral while R_D is in service. Observation reveals that when the proposed scheme is implemented the short circuit current experienced by RE2 remains relatively unchanged at 4157 A while the level experienced by the fuse F1 decreases to 4137 A. It can also be observed that RE2 detects the fault and notifies R_D via the communication channel at 1.004 seconds resulting in the DG source disconnecting from the network and feeding Z_{RE} at 1.013 seconds (less than one cycle following fault occurrence).

Figures 3.12 and 3.13 also demonstrate the DG terminal current, voltage and the per unit frequency for the following progression: the DG source disconnects from the network and switches to Z_{RE} before reconnecting to the network following successful reclosing at 6.579 seconds. This demonstrates that the proposed scheme disconnects the DG source but keeps it operational until fault clearance before reconnecting to the network within a 5.579 second timeframe. This highlights that reconnection of the DG is faster under the proposed scheme than in current utility practices.

In the context of system performance it can be observed that the voltage dropped to 11.938 kV in contrast to 1.016 kV when R_D is not in service. Furthermore, the overshoot frequency when reconnecting the DG source to the network is 1.022 per unit (61.35 Hz) before it decays to a nominal level. In addition it can be seen that RE2 returns to its regular operating time of 1.0812 seconds which allows for an attempt at clearing a temporary fault before the fuse F1 clears it at 1.499 seconds. Further observation of Figure 3.13 makes it apparent that the system

regains its normal operating state post fault (following reconnection of the DG source). It should be noted that the Feeder 2 power is measured at RE2 and that the system voltage is measured at the PCC on the system side of the breaker. This demonstrates the capacity of the proposed scheme to restore coordination to the system without limiting the DG penetration.

3.4.3 Comparison with other Techniques to Mitigate DG Influences on Overcurrent Protection

In this section, another scheme presented in the literature, namely superconducting fault current limiters, is applied to Case Study-1 to demonstrate the efficacy of the proposed scheme. In this case, a 30 ohm resistive SFCL with the model presented in [26] is connected at the DG terminal in lieu of R_D. Time domain simulations are presented in Figures 3.14 and 3.15. In practice, an SFCL is required to limit the short circuit current to three and five times that of the line nominal current. This is to prevent protection system failure when there is an inability to differentiate between faults and overload currents (for example large load switching) for values lower than three times. If the short circuit current exceeds five times the line nominal then excessive heating can occur in the SFCL [26]. Observation of Figures 3.14 and 3.15 make it apparent that the peak steady state current experienced by the DG source is 206 A. Following fault inception, the SFCL limits the current to 659 A in the second cycle (3.68 times the steady state value), demonstrating the expected operation of the SFCL.

Furthermore, it can be seen that when the SFCL is in service the short circuit currents experienced by RE2 and F1 are 4242 A and 4555 A respectively. Although RE2 operates before F1, F1 continues to receive a current of 460 A even without the utility connection. This results in F1 melting at 1.2213 seconds before RE2 is able to conduct its second operation. In this case the SFCL does not maintain the original coordination of the system for a DG size of 8 MVA. In conclusion, a comparison of results between Sections 3.4.2 and 3.4.3 makes it apparent that the proposed scheme in Section 3.4.2 is more robust at restoring fuse-recloser coordination for DG penetrated feeders than the SCFL solution.

Another potential solution that has been presented previously is the utilization of discharge circuits within the DG [55]. When a discharge resistance is added to the field circuit at the fault instant it reduces the current contribution by the DG during the fault. More specific, it accelerates the decrease in the transient component (the transition to steady state is much faster).

However, the field discharge circuit has almost no impact on the sub-transient part of the AC component of the generator's current due to the fact that damper windings play the leading role during the sub-transient period. In addition, the capability of the field discharge in reducing the generator's RMS AC current is affected by the value of field discharge resistance. Thus, the capability of the field discharge is also affected by the operating condition of system protection (i.e. operating intervals of instantaneous, extremely inverse-time and short time-delay overcurrent devices). Finally, it can be concluded that applying the field discharge circuit may be sufficient to reduce the DG contribution to fault current. In other words, in some cases (according to the operating interval of certain overcurrent protective function) the field discharge might not be effective enough to prevent miscoordination.

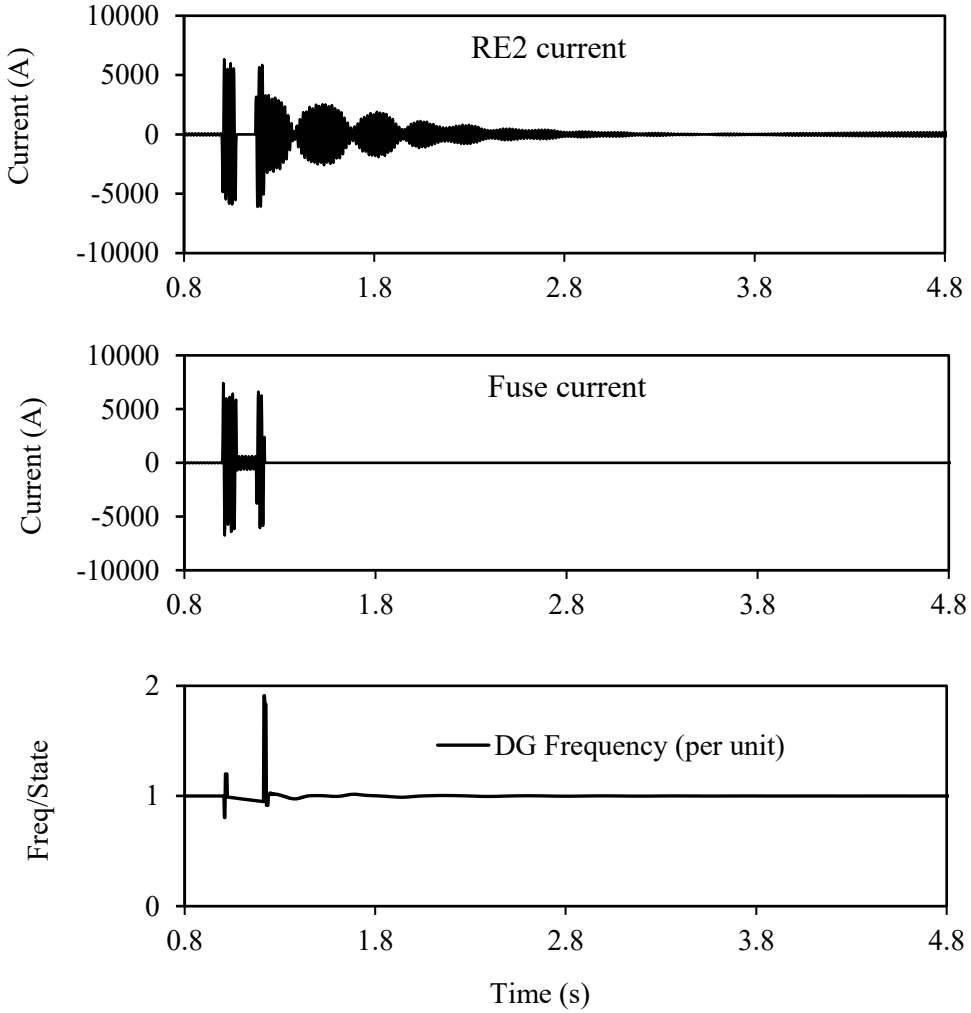

Figure 3.14: Case Study-1 with the DG source at L2 with a 30 Ω resistive SFCL applied at the PCC: RE2 current, F1 current, DG frequency.

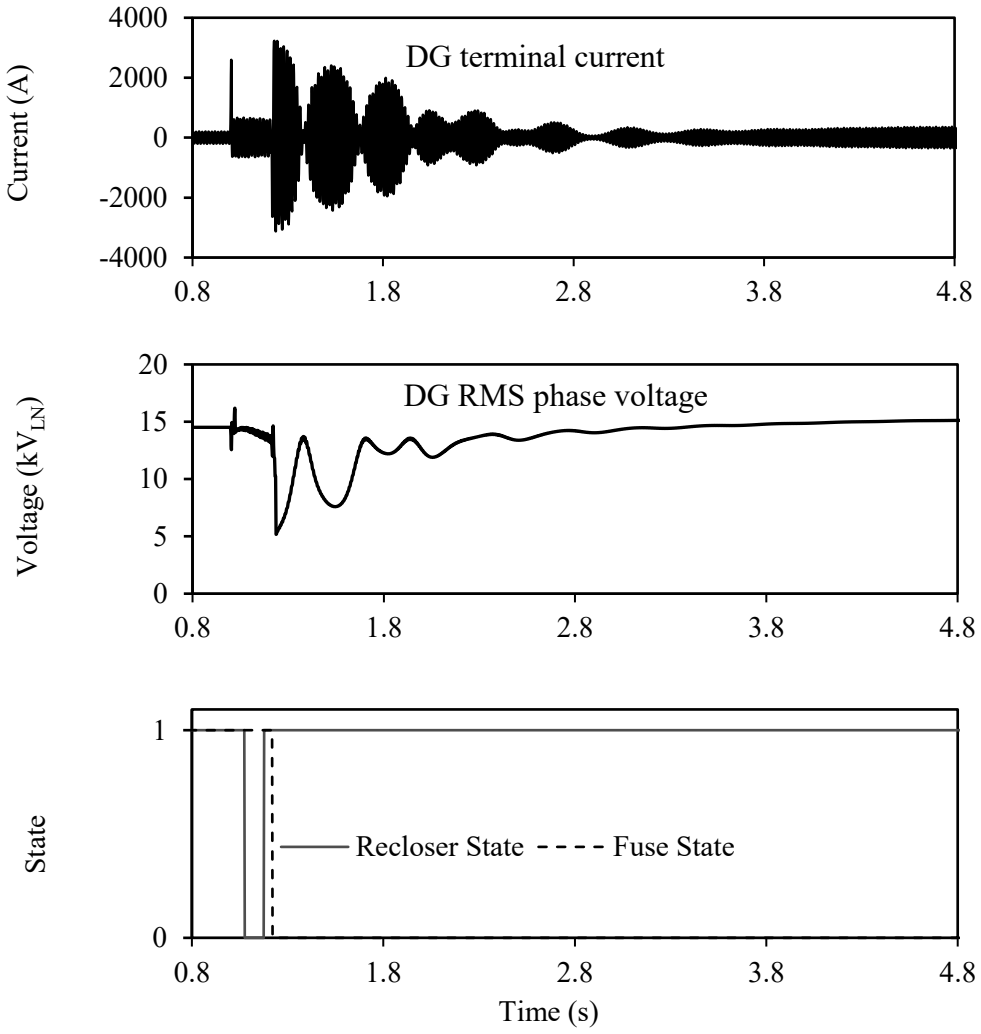

Figure 3.15: Case Study-1 with the DG source at L2 with a 30 **Ω** resistive SFCL applied at the PCC: DG terminal current, DG RMS phase voltage, State signals.

3.4.4 Generalization of the proposed scheme

3.4.4.1 Impact of changing the fault resistance

To aid in verification of the robustness of the proposed scheme, the impact of changing the fault resistance is investigated for Case Study-1. Figure 3.16 presents the zoom on the RE2 and R_D signals when the fault experiences an impedance of 3 ohms. As can be observed, when fault impedance is present, RE2 produces a fault signal 50 microseconds slower than the bolted fault case. In contrast, R_D produces a signal 2.6 milliseconds slower than the bolted fault case. Although the overall operation of the proposed scheme is slower, it is still able to maintain the original coordination of the distribution network. Further results are presented in Appendix B.

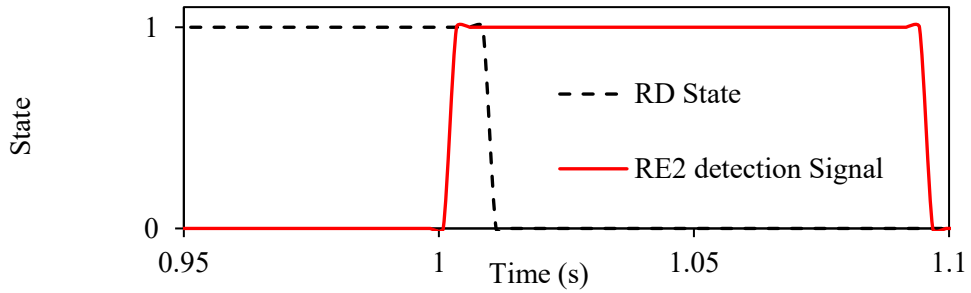

Figure 3.16: Case Study-1 with the DG source at L2 when RD is applied and the fault impedance is 3 Ω: Zoom on RE2, RD communication.

3.4.4.2 Impact of changing the fault duration

In this section, the fault duration is reduced to 0.12 seconds as opposed to a permanent fault. Comparison of the case presented in Section 3.4.2.1 with Figures 3.17 and 3.18 reveal that fault levels of RE2 and F1, with the tripping time of RE2, are similar to the case where a permanent fault is present. Additionally, it can be observed in Figures 3.17 and 3.18 that the DG unit reconnects with the network at the same time as that outlined in Section 3.4.2.1. Overall, this demonstrates the efficacy of the proposed scheme in restoring fuse-recloser coordination through an allowance of temporary fault clearing without premature fuse operation.

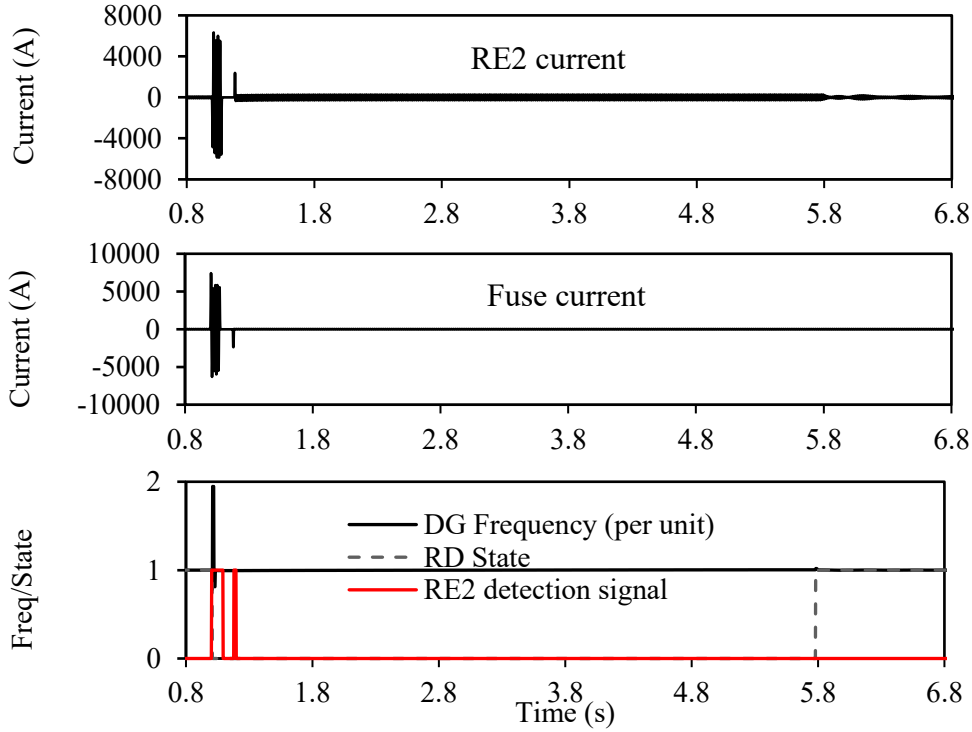

Figure 3.17: Case Study-1 with the DG source at L2 when RD is applied for a fault duration of 0.12 seconds: RE2 current, F1 current.

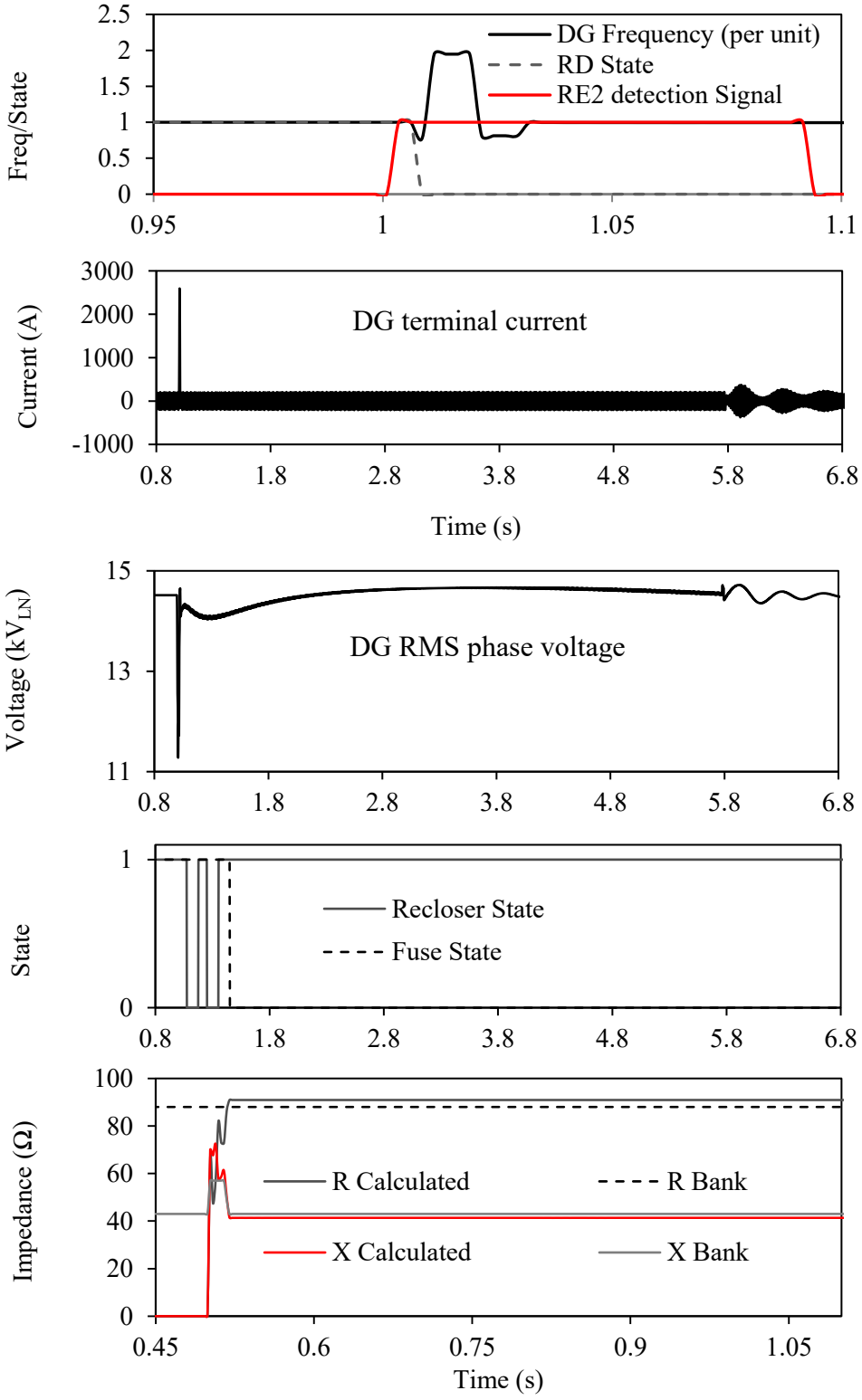

Figure 3.18: Case Study-1 with the DG source at L_2 when R_D is applied for a fault duration of 0.12 seconds: RD communication & DG frequency, zoom on DG frequency, RE2, RD signals, DG terminal current, DG RMS phase voltage, State signals, load bank calculated and actual values.

3.4.4.3 Impact of changing the interconnecting transformer

Figures 3.19 and 3.20 demonstrate the variation in short circuit current experienced by the fuse F1 for Case Study-1 and Case Study-2 when the interconnecting transformer type is changed. As can be observed in Figures 3.19 and 3.20, when the interconnecting transformer type changes, there is a change in the short circuit current experienced by the fuse. Furthermore, it can be seen that with the presence of R_D, when a fault occurs, the short circuit levels return to non-DG penetrated network levels. This highlights the efficacy of the proposed approach for multiple transformer types. Additional results are offered in Appendix B.

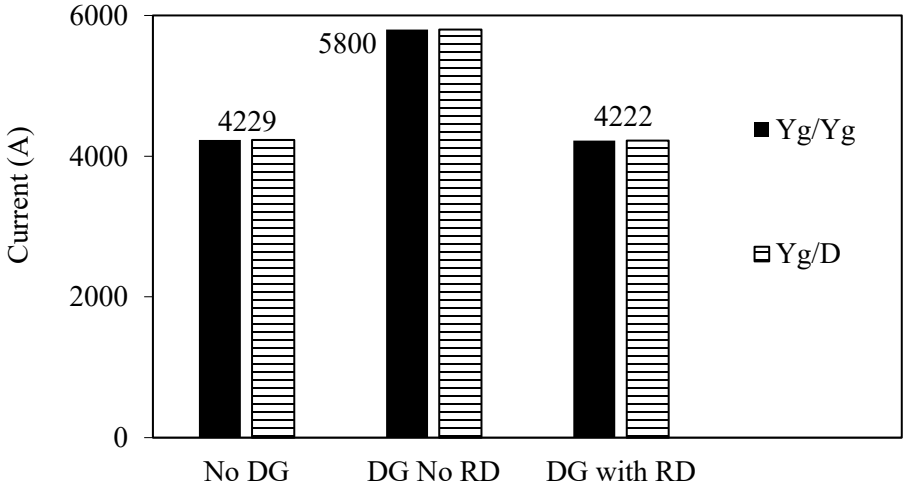

Figure 3.19: Short circuit levels experienced by F1 for a three-phase-G fault on load L1, 8 MVA DG connected at L2. Two different interconnecting transformer types: Yg/Yg and Yg/D.

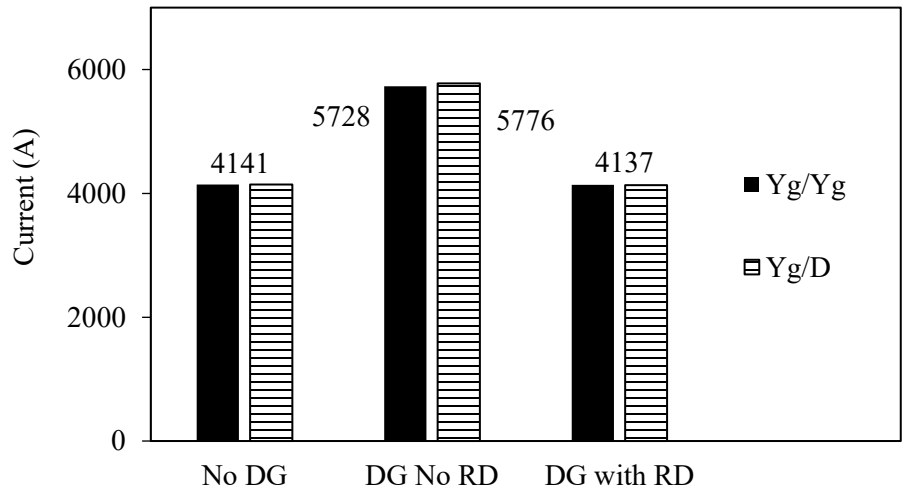

Figure 3.20: Short circuit levels experienced by F1 for a line-to-line-to-ground fault on the load L1, 8 MVA DG connected at L2. Two different interconnecting transformer types: Yg/Yg and Yg/D.

3.5 Summary and Conclusions

This chapter presents a novel reclosing scheme for mitigation of DG source effects on existing distribution network protection infrastructure without the need for alteration of settings. Results demonstrate the efficacy of the proposed scheme for multiple scenarios, including three-phase and line-to-line-to-ground faults, resulting in the removal of the need to limit DG penetration as proposed in traditional methods. As a result, this chapter offers significant value in the domain of network expansion planning, as there is no longer a requirement to re-engineer networks to accommodate increasing levels of DG penetration.

Case studies conducted also demonstrate that the proposed scheme provides disconnection from the DG unit effectively, whilst maintaining operation at pre-fault load sharing levels without the requirement of shutting down. This allows the DG to maintain its pre-fault operating speed and frequency, facilitating a faster reconnection to the distribution network following successful fault clearance. The outcome is a direct reduction in shut down and restart procedures required by the DG unit. From the context of system performance, results indicate that normal operating states are achieved once network faults are cleared and reconnection of the DG unit occurs.

A comparison with the application of SFCLs is also offered in the context of the case studies presented. This comparison highlights that the proposed scheme is more flexible and effective in the context of restoration of fuse-recloser coordination in distribution networks with DG penetration. Although outside the scope of this thesis, it is prudent to mention that should multiple DG sources be required to be connected; the reconnection of DG units would need to be coordinated in order to mitigate transients.

4. ALLEVIATION OF LOSS OF COMMUNICATION LINKS IN DISTRIBUTION NETWORKS THROUGH A FAULT DETECTION TECHNIQUE

4.1 Introduction

This chapter presents a current measurement-based fault detection technique to be used as a substitute for the currently used communication link between the utility head end recloser and distributed generation (DG) units in distribution networks. The technique utilizes a tripping signal when a change in current that exceeds a pre-specified minimum is detected over an adequate time window. This signal is designed as a substitute for the communication link from the head end recloser in Chapter 3. This new signal, in combination with the technique specified in Chapter 3, is investigated through several time-domain simulations to ascertain the suitability of substituting the communication link for the fault detection technique.

4.2 Fault Detection in Electrical Networks

As indicated in Chapter 3, integration of DG sources, for the purpose of meeting local power demands can result in observable changes in short circuit current characteristics. Methods proposed for the purpose of mitigating these changes utilize communication links to protect DG units and the overall network, since they allow for increased flexibility in operation [56]. References [57]-[59] utilize communication links to allow for adaptive overcurrent protection to be implemented in the network such that settings can be adjusted for various impacts caused by DG units. Additionally, in reference [56] a technique is provided that allows the utility to control and adjust operation modes and short circuit behavior of DG units through a communication interface. Reference [60] utilizes a communication link that connects fault detectors in order to identify line faults through synchrophasor data processing.

The key difficulty associated with communication-based techniques in the context of protection with DG penetration, is vulnerability in the event of communication failure. In the context of fault detection, one of many techniques that have been proposed is a travelling wave based protection scheme, presented in references [61] and [62]. This method is unreliable when

employed to discriminate between load variations and faults. In reference [63], an impedance based method is presented that is capable of utilizing data points to determine apparent impedances such that faults and their locations can be estimated through iterative algorithms. The main concern with this type of algorithm is the slow speed at which it operates when the network topology is complicated.

4.3 The Proposed Current Measurement-Based Fault Detection Technique

Section 4.2 is a review of a variety of methods for fault detection, each with their own advantages and inefficiencies. Against this background, the proposed fault detection technique measures the difference in the RMS current output by a DG source interconnected to the distribution network over a predefined time period (Δt). This can be formally defined as the rate of change of current (ROCOC) (ΔI) over the time period Δt. This method can be visually represented via Figure 4.1.

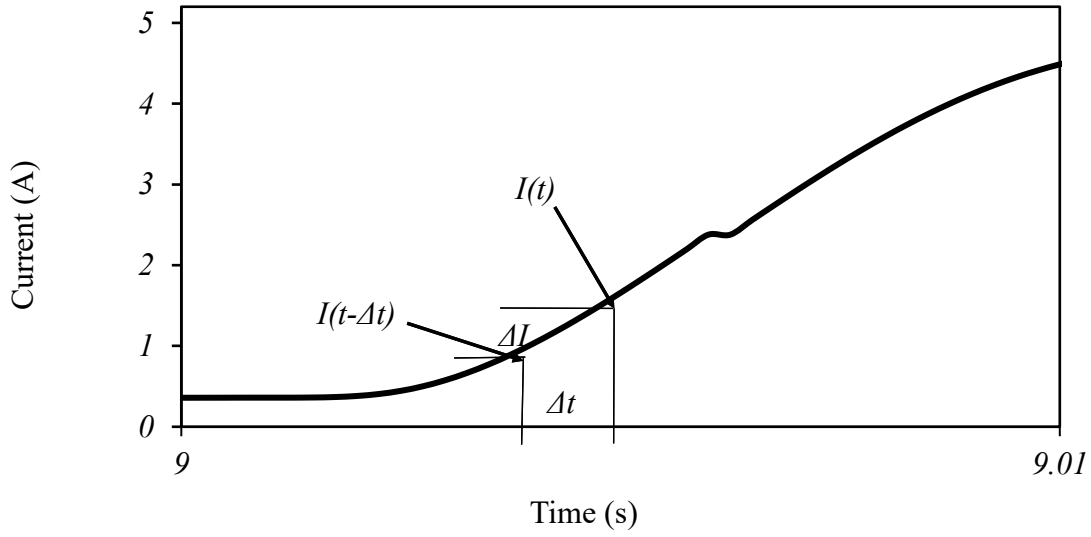

Figure 4.1: ROCOC measurement of a time period of Δt.

In accordance with reference [64], one twentieth of a cycle is an adequate time window for detection in changes in voltage and current. From this, the moveable time period Δt is defined by:

$$\Delta t = \frac{1}{20f} \tag{4.1}$$

where $\Delta t = time\ period\ (seconds)$

$$f = system\ frequency\ (Hz)$$

Furthermore, the ROCOC can be defined by:

$$\Delta I = I(t) - I(t - \Delta t) \tag{4.2}$$

where $\Delta I = current\ change\ over\ \Delta t\ (A/second)$

$I(t) = DG\ output\ current\ at\ time$ t

$I(t - \Delta t) = DG\ output\ current\ at\ time\ t - \Delta t$

Through the use of Equations 4.1 and 4.2, if ΔI exceeds a preset value over a time period of Δt then the DG source is deemed to be detecting a fault. From a practical standpoint, when ΔI exceeds the ROCOC pickup value, this value is held for one second in order to allow a brief window in which the short circuit currents can stabilize to a set value following their transient period.

4.4 Application of the Proposed Fault Detection Technique

This section aims to demonstrate the effectiveness of the proposed technique when integrated into the scheme proposed in Chapter 3. As discussed in Chapter 3, the R_D scheme detects a fault through the communication link between the head end recloser and DG unit central control unit (CCU). For the studies conducted in this chapter, the receiver/transmitter (R/T) within the CCU is blocked and replaced with the signal from the fault detection technique. In order to aid in clarity, this adjusted scheme is designated as RD-mod. It should also be noted that the transfer impedance in this chapter is taken as exact.

Four case studies are presented to demonstrate the efficacy of the proposed technique. Case studies showcase the ability of the technique to detect faults, and substitute for the utility-DG communication link for varying fault locations, fault types, fault impedance and for a large sudden load change. The case studies are expressed in Table 4.1 and Figure 4.2.

Table 4.1: Case studies.

	Case Study-1	Case Study-2	Case Study-3	Case Study-4
Fault type/Disturbance	Solid Line-to-Line-to-Ground	Solid Line-to-Ground	Line-to-Ground, R_f = 3 Ω	Sudden 10MVA
Fault/Disturbance location	Load L1	Load L5	Load L5	Load L2
Fault/Disturbance inception time and duration	1 second of simulation time, Sustained fault			
PCC	at L2			
DG pre-fault load sharing condition & PF	0.8 of 8 MVA SM-based DG, 0.9 pf			

Case studies presented in Table 4.1 can be expressed diagrammatically in Figure 4.2. It should be noted that the system utilized in these studies is presented in full in Figure 2.1.

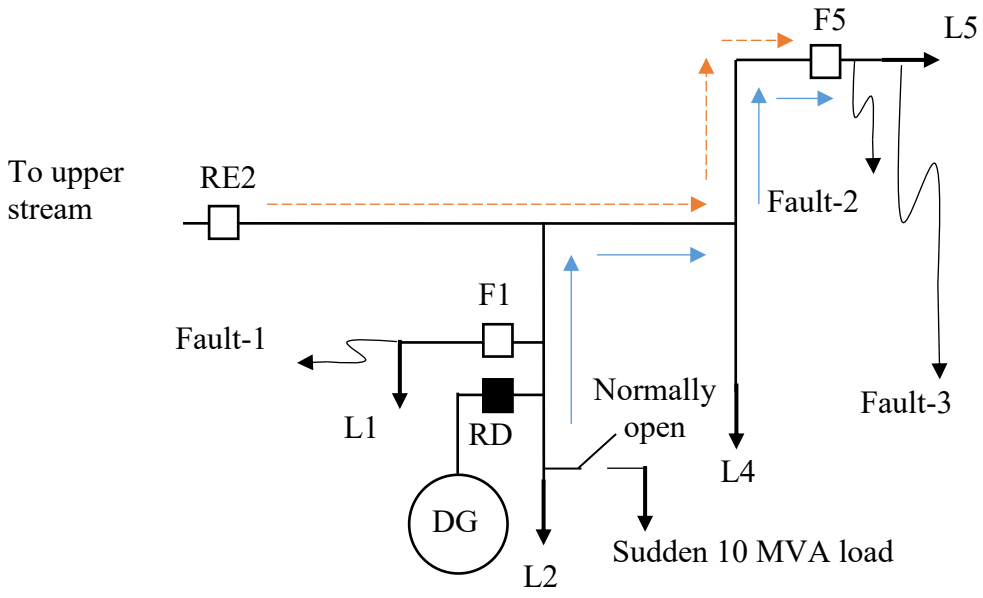

Figure 4.2: Diagrammatic version of the case studies.

The case studies presented in this chapter have many similar conditions to that in Chapter 3. As a result the phase and ground pickup currents are selected to be 555 A and 370 A respectively as per Equations 3.1 and 3.2. Through preliminary simulations, it was found that the pre-fault outputs from the DG unit are as such:

- I_{ph} = 146 A
- V_{ph} = 14.515 kV
- P_{ph} = 1.91984 MW
- Q_{ph} = 0.873122 MVAR

Through the use of Equation 3.3, the transfer impedance is determined to be 90.5+j41.16 ohms. Again it should be noted that values specified curing case studies are in RMS unless otherwise stated. It should also be noted that additional case study data is offered in Appendix C.

The system frequency utilized in this Chapter is 60 Hz. According to Equation 4.1 the time period can be determined by:

$$\Delta t = \frac{1}{20 \times 60} = 0.8333\ milliseconds$$

Multiple case studies were conducted other than the ones specified. These studies were conducted with results given in Appendix C. As a result of those case studies, it can be determined that the ROCOC for an 8 MVA DG source did not go below 20 A/second for any fault. As a result the ROCOC pickup value utilized is 20 A/second.

4.4.1 Case Study-1: Bolted double line-to-ground fault

Figure 4.3 presents the time domain simulation results for Case Study-1 where an 8 MVA DG source is connected to the L2 lateral while RD-Mod is in service and a line-to-line-to-ground fault occurs on load L1 one second into the simulation time as per Figure 4.2. Figure 4.3 makes it apparent that the DG and subsequent fuse (F1) current begins to ramp up following the inception of Fault-1. At this point, RD-mod measures the change in the current over the time period Δt (0.8333 milliseconds) where it reaches a peak ROCOC (ΔI) of 131 A/second which is greater than the pickup value of 20 A/second. As a result, RD-mod signals a fault has occurred and the DG source switches from the network to the transfer impedance at 1.01045 seconds. Comparatively, in Case Study-2 in Chapter 3 (the case where the communication link is present

and the fault detection technique is not) a switch to the DG source from the network to the transfer impedance is at 1.013 seconds. Significantly, the RD-mod is faster at detecting the fault than the communication link reported in Chapter 3. Due to the rapid detection of the fault by the RD-mod, the DG source switched to the transfer impedance, resulting in restoration of existing fuse recloser coordination. The network returned to normal operation following fault clearance.

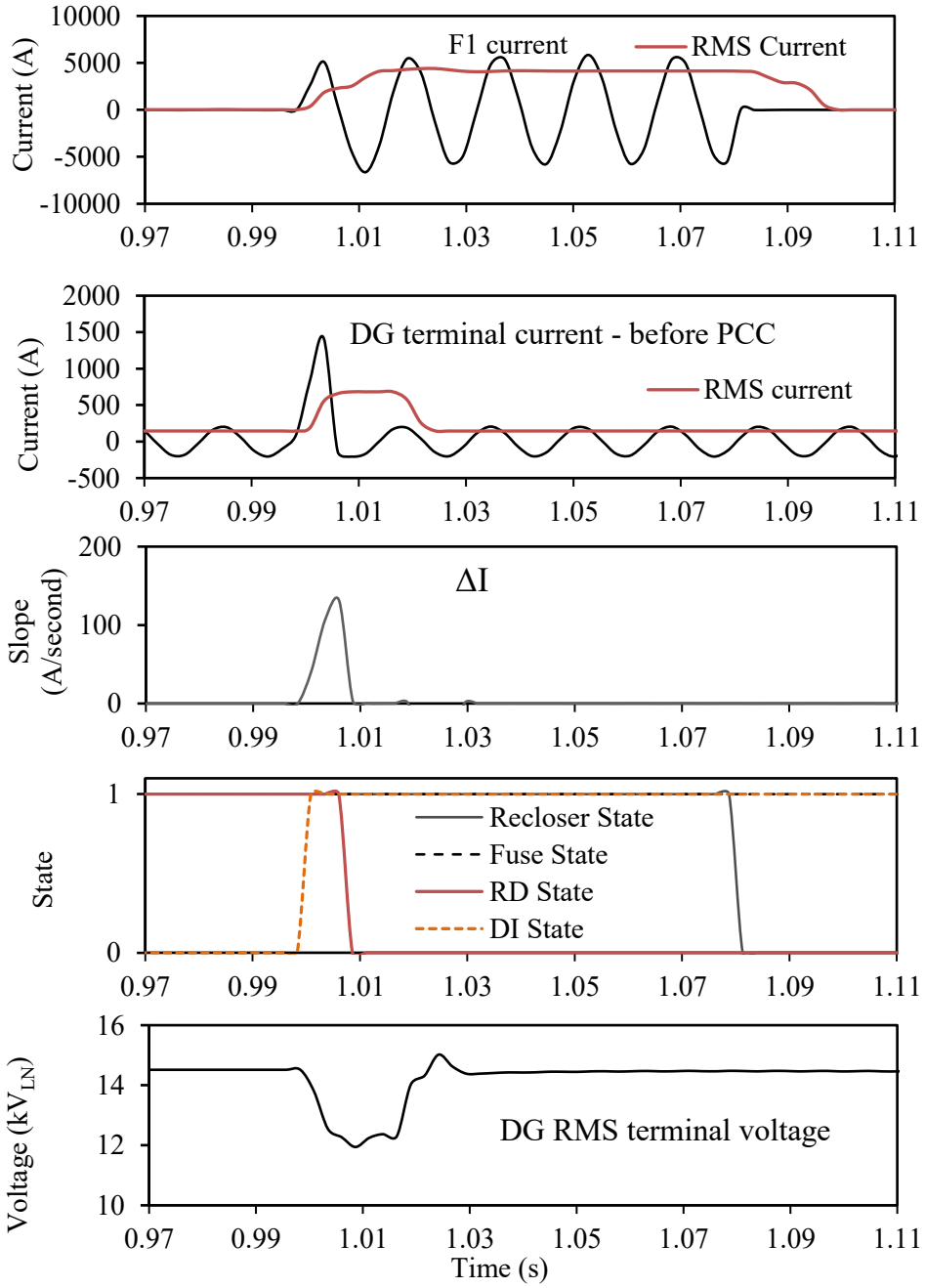

Figure 4.3: Case Study-1: F1 current, DG terminal current before PCC, *ΔI*, DG voltage, State signals.

4.4.2 Case Study-2: Bolted single line-to-ground fault

Figure 4.4 presents the time domain simulation results for Case Study-2 where an 8 MVA DG source is connected to the L2 lateral while RD-Mod is in service. A single line-to-ground fault occurs on load L5 one second into the simulation time as per Figure 4.2.

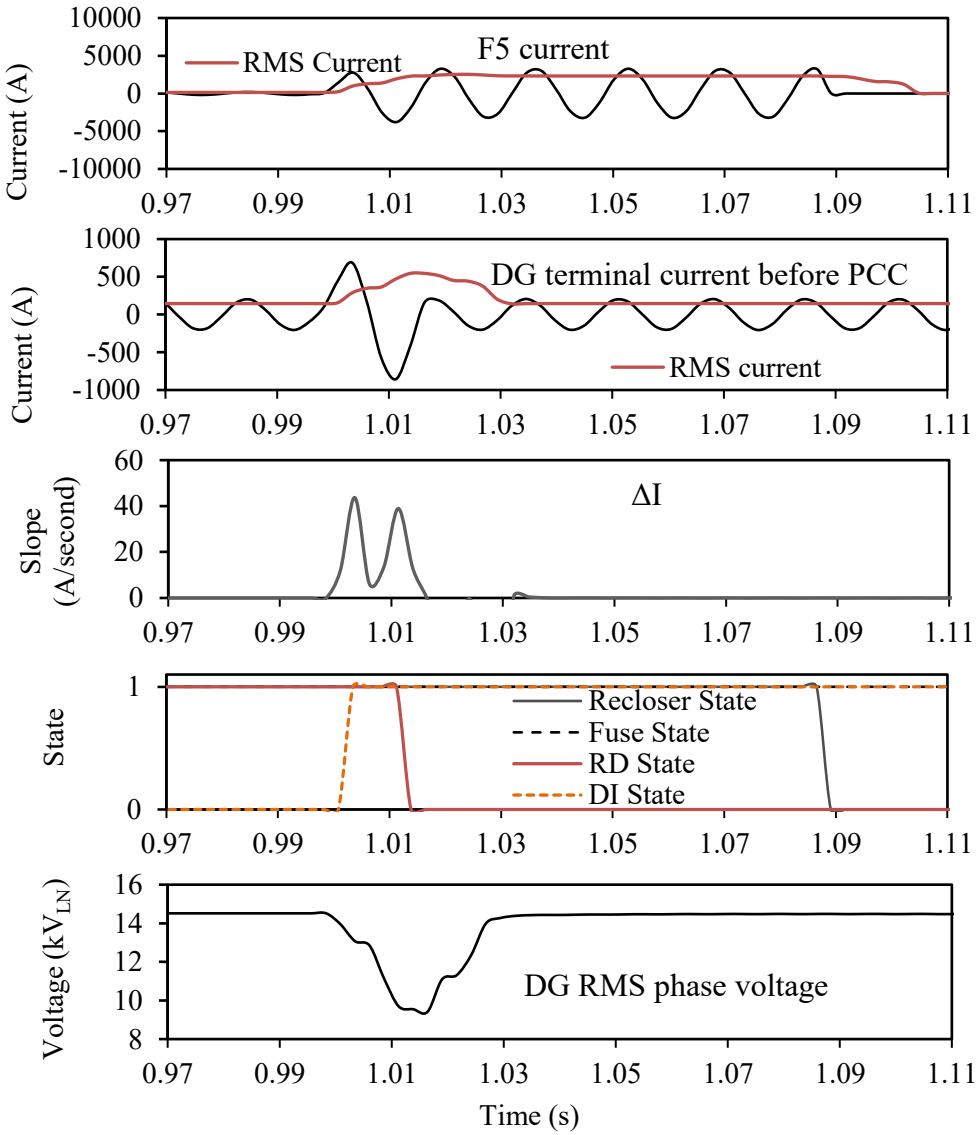

Figure 4.4: Case Study-2: F1 current, DG terminal current before PCC, *ΔI*, DG RMS phase voltage, State signals.

Observation of Figure 4.4 makes its apparent that following the inception of Fault-2, the DG and subsequent fuse (F5) current begins to ramp up. At this point, RD-mod measures the change in the current over the time period *Δt* (0.8333 milliseconds) where it reaches a peak ROCOC (*ΔI*) of 44 A/second which is greater than the pickup value of 20 A/second. As a result,

RD-mod signals the occurrence of a fault; subsequently switching the DG source from the network to the transfer impedance at 1.0139 seconds. Due to the rapid detection of the fault by the RD-mod, the DG source switched to the transfer impedance, resulting in restoration of existing fuse recloser coordination. The network returned to normal operation following fault clearance.

4.4.3 Case Study-3: 3 ohm single line-to-ground fault

Figure 4.5 presents the time domain simulation results for Case Study-3 where an 8 MVA DG source is connected to the L2 lateral with RD-Mod. A single line-to-ground fault with an impedance of three ohms occurs on load L5 one second into the simulation time as per Figure 4.2.

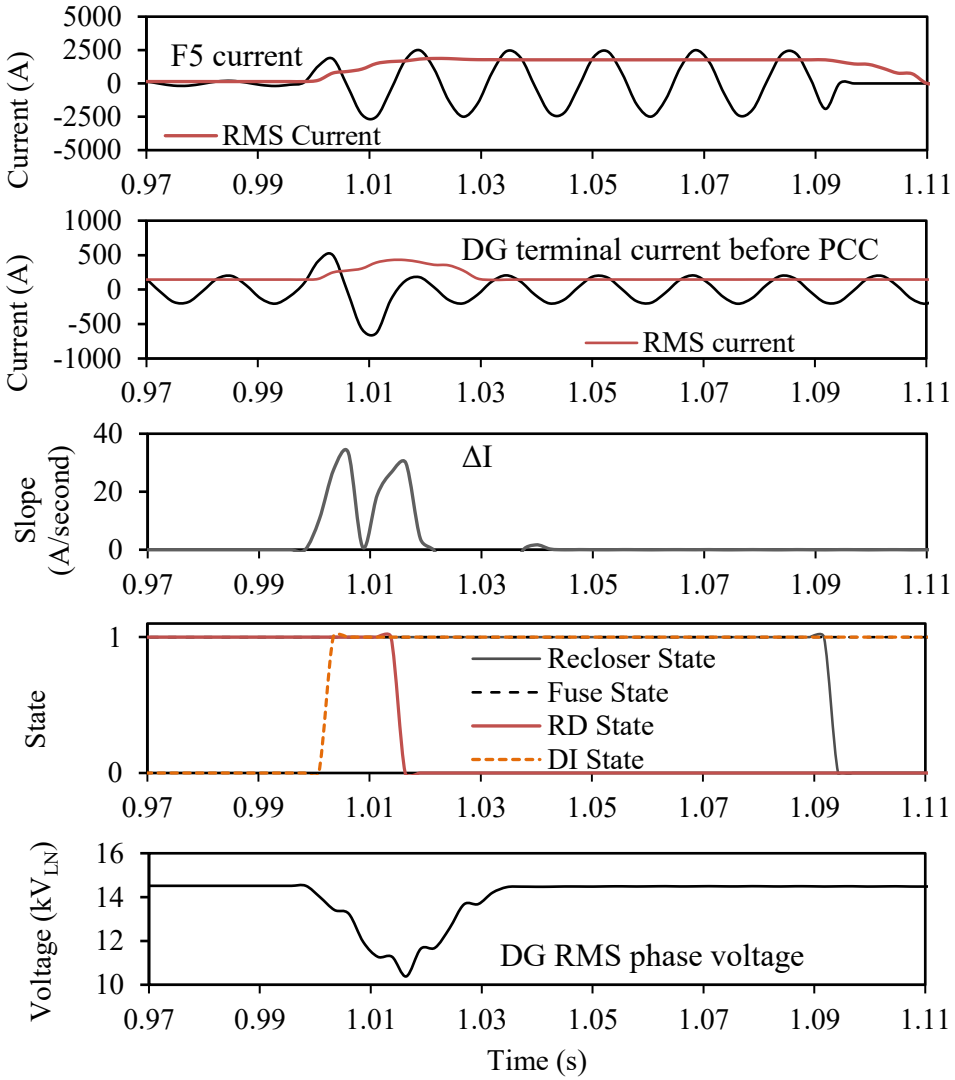

Figure 4.5: Case Study-3: F1 current, DG terminal current before PCC, *ΔI*, DG RMS phase voltage, State signals.

Observation of Figure 4.5 makes its apparent that following the inception of Fault-3, the DG and subsequent fuse (F5) current begins to ramp up. At this point, RD-mod measures the change in the current over the time period Δt (0.8333 milliseconds). It reaches a peak ROCOC (ΔI) of 33 A/second which is greater than the pickup value of 20 A/second. As a result, RD-mod signals a fault, subsequently switching the DG source from the network to the transfer impedance at 1.0164 seconds. In comparison, in Case Study-2, where the fault is bolted without an impedance value, the transfer occurs at 1.0139 seconds. It is apparent that RD-mod is slower in Case Study-3 than it is in Case Study-2. This is expected as the three ohm fault impedance will reduce the short circuit current output from the DG source and the utility. Although the fault impedance increases the transfer time, RD-mod was still able to detect the fault and the DG source was able to be switched to the transfer impedance, resulting in restoration of existing fuse recloser coordination with the network returning to normal operation following fault clearance.

4.4.4 Case Study-4: Sudden load change

Figure 4.6 presents the time domain simulation results for Case Study-4 where an 8 MVA DG source is connected to the L2 lateral while RD-Mod is in service and a 10 MVA load is suddenly applied on load L2 one second into the simulation time as per Figure 4.2.

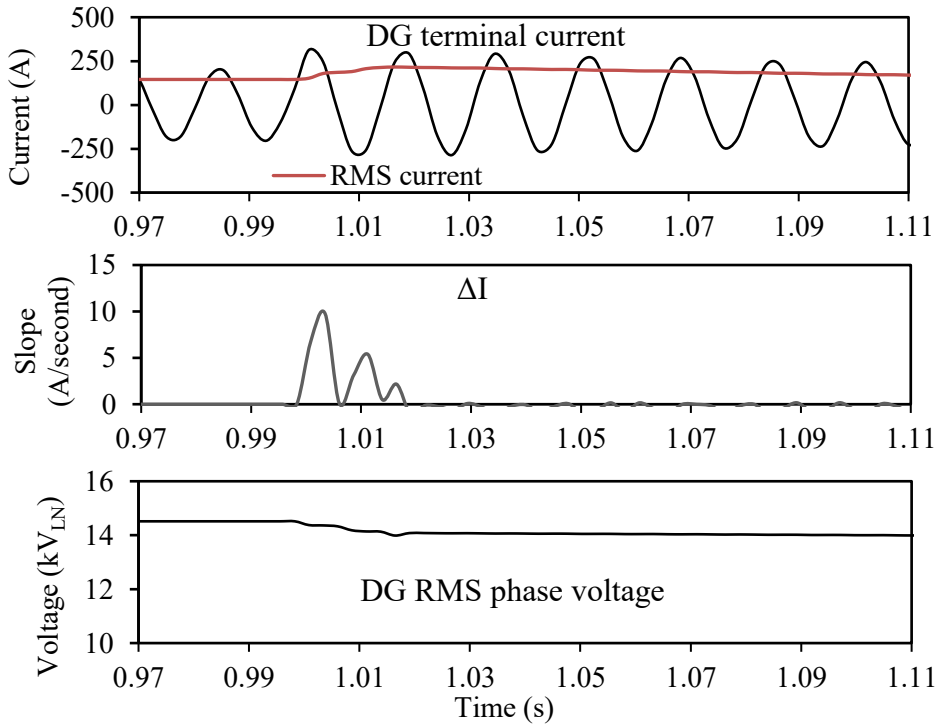

Figure 4.6: Case Study-4: DG terminal current before PCC, ΔI, DG RMS phase voltage.

Observation of Figure 4.6 makes it apparent that following the connection of the 10 MVA load, the DG current begins to ramp up. At this point, RD-mod measures the change in the current over the time period Δt (0.8333 milliseconds) where it reaches a peak ROCOC (ΔI) of 9.77 A/second which is less than the pickup value of 20 A/second. As a result, RD-mod indicates that no fault has occurred so the DG source will ride through the transient event. This means that the proposed technique does not measure a change in current in excess of the ROCOC pickup setting which resulted in a continuous connection between the DG source and the network. As such RD-mod was successfully able to discriminate between a switching load and network fault.

4.5 Summary and Conclusions

This chapter presents a current measurement-based fault detection technique to be used as a substitute for the communication link between the utility head end recloser and DG sources in distribution networks. Results demonstrate the efficacy of the proposed technique through multiple case studies that investigate scenarios such as varying fault types, fault locations, fault impedance and sudden large switching loads. These case studies are implemented within the structure of the DG recloser proposed in Chapter 3 with the communication link between the head end recloser and DG unit disabled.

Case studies conducted demonstrate that the proposed system successfully detects fault occurrences, allowing for the RD-mod recloser to disconnect the DG unit from the network and onto the transfer impedance while maintaining the original fuse recloser coordination. Following fault clearance the DG unit is able to be reconnected and operate as per pre-fault conditions. Furthermore RD-mod was able to successfully discriminate between a large switching load and a fault. Consequently the fault detection technique is able to add robustness to the approach specified in Chapter 3 as it no longer relies on a communication link to discriminate between switching transients and faults.

5. A PROTECTION SCHEME FOR MICROGRIDS UTILIZING DIFFERENTIAL AND ADAPTIVE OVERCURRENT RELAYS

5.1 Introduction

This chapter presents a hybrid adaptive overcurrent and differential protection scheme that has the capability of compensating for significant changes in short circuit current characteristics of microgrids when transitioning between islanded and grid connected modes. It is proposed that adaptive overcurrent relays be used for the protection of individual load points whilst differential relays are utilized to protect load buses and feeder backbones. This segmentation reduces the need for equipment upgrades and minimizes setting computation complexity. The scheme is tested using multiple time-domain simulations, to determine its efficacy in protecting the microgrid in both grid and islanded modes.

5.2 Protection Schemes for Microgrids

As indicated in Chapters 3 and 4, the inclusion of DER/DG sources has been attracting growing attention; with particular focus on the microgrid, since it can operate under multiple configurations. A microgrid can be defined as a low or medium voltage network that contains a cluster of local loads and DG sources that are capable of operating in both islanded and grid connected modes [8]. The modes of operation are dependent on the presence of a utility connection. Microgrids offer distinct advantages, particularly in remote areas where power delivery is not reliable, since they reduce line losses, prevent network congestion and reduce the probability of supply interruption due to their islanding capability [51]. This can be attributed to the ability of microgrids to adjust topology whilst utilizing DG sources close to the load points.

As with DG integration, microgrids also introduce unique operational and protection challenges. Many of these challenges are similar to those encountered in DG integration, however microgrids offer additional difficulties due to topological changes when switching between grid and islanded modes. One of these challenges is associated with drastic short circuit behavioral changes when transitioning between modes. When the microgrid is in islanded mode,

the utility supply is disconnected (typically due to a disturbance or planned disconnection). The DG sources continue to supply the load locally [8]. Following islanding, there is a significant reduction in the magnitude of the short circuit currents in the network. This is attributed to the lack of utility connection, which would traditionally serve as the main source of short circuit currents during a fault. Another challenge is attributed to potential bi-directional power flow within the microgrid, which contradicts the traditional unidirectional power flow characteristic of distribution networks. In this context, existing traditional overcurrent protection devices may be rendered inadequate due to their reliance on high short circuit currents within the network. This is of particular concern in microgrids with a predominance of inverter based DG sources such as solar PV, which limit short circuit current to prevent overloads on individual components [65].

Research into microgrid protection schemes with the capacity to navigate changes in magnitudes of short circuit currents in grid and islanded modes is emerging. A number of potential solutions have been offered.

Reference [4] contains an observation that integration of adaptive overcurrent relays can be difficult, due to the advanced technology required for practical implementation, and to the ability of the relay to self-monitor and compute multiple settings for distinctly different microgrid topologies. These relays require complex hardware and software units to accommodate a variety of topological configurations. An additional complication lies in the demand for fast relaying communication capacities. This means that significant upgrades are required to existing infrastructure to make it “smart ready” and to facilitate interfacing between adaptive overcurrent relays and the network.

In reference [5], an off-line analysis methodology is presented that allows for the determination of suitable tripping characteristics in individual relays for every possible state the network and microgrid might encounter. This methodology is efficient only when there is substantial knowledge of the network and microgrid, ensuring that every possible state can be programmed into the relay. Should a state occur that was not pre-programmed, the relay could operate incorrectly or fail completely.

In reference [49], a voltage based differential protection scheme is introduced to address high impedance faults in radial and meshed networks. Communicative overlays are integrated into the relays to make this scheme operate correctly. These relays require synchronized

measurements that can be rendered inadequate when imbalances in the system phases are present.

Another viable protection infrastructure option for microgrids is the use of a differential current protection scheme in conjunction with a communication channel, as outlined in reference [66]. This differential protection scheme is shown to be effective in both grid and islanded modes under a variety of fault types and impedances. A key requirement for this scheme is the need for relays on each end of the line to be replaced, in addition to extensive adaption to communication requirements. As a result, differential current protection schemes may not be feasible due to infrastructure upgrade costs.

5.3 The Proposed Microgrid Protection Scheme

In summary, Section 5.2 outlined the technical difficulties posed in the field of microgrid protection due to the inherent short circuit changes experienced when transitioning between grid and islanded modes. In addition, there is often a need for significant infrastructure upgrades. In mitigation of these factors, a hybrid microgrid protection scheme that utilizes both differential and adaptive overcurrent relays is presented in this chapter. The proposed scheme utilizes differential relays for the protection of microgrid interconnecting buses and feeders in conjunction with adaptive overcurrent relays for load points. This approach allows for multiple microgrid protection methods to be utilized in conjunction with one another, providing additional options for utilities and private owners. The scheme also would allow for segmented installation of equipment where budget constraints are an issue.

5.3.1 Adaptive Overcurrent Protection

In traditional distribution networks, devices such as relays, reclosers and fuses are utilized to protect feeders and their lateral taps. In these traditional networks, reclosers are set to operate within fractional timeframes in order to allow for self-clearing, preventing unnecessary de-energization when a fault is temporary. Following a set number of operations by the recloser, the switching time reverts to a slow characteristic to allow for fuses to operate and clear the fault. This is the general principle operating in traditional fuse-saving schemes [17]. The scheme relies on high levels of short circuit current to allow for fuse-saving coordination. This is an inherent problem in microgrids, since they operate in both grid and islanded modes, yielding drastic changes in their short circuit current characteristics. As a consequence, the traditional

overcurrent schemes utilized in traditional networks may become unsuitable. One method that is able to address this phenomenon is adaptive overcurrent protection.

In adaptive overcurrent protection, relays capable of sensing grid conditions are utilized to facilitate modification of TCC characteristics and settings [65]. This is typically accomplished when an external communication device interfaces with the relay and inputs the grid condition as islanded or grid-connected. Although effective, the inherent inefficiency associated with this practice is the requirement for every topology of the microgrid to be known and programmed into the relay. For highly complex networks, this may not be feasible, which creates malfunction vulnerabilities within the relay when un-programmed states are encountered.

5.3.2 Differential Current Protection

Differential protection is based on the concept of measurements of current entering and leaving a protective zone. This can be conceptually visualized as such:

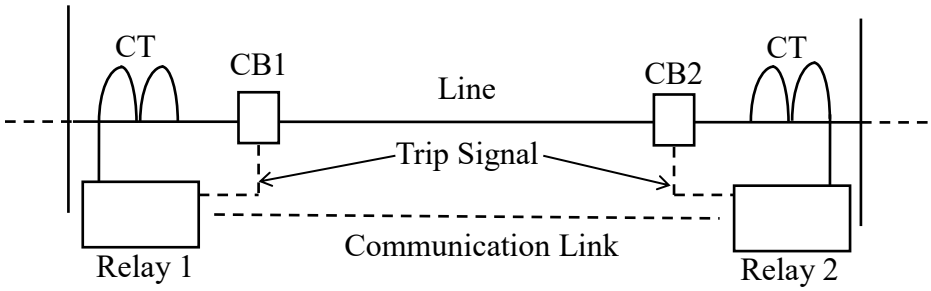

Figure 5.1: A line protected by a differential scheme.

As indicated in Figure 5.1, each line end is equipped with a local current transformer (CT) with a corresponding circuit breaker. The CT's secondary output is connected to the corresponding relay (for example relay 1) which communicates details about the current magnitude and phase angle to the opposing line relay (for example relay 2). The relays will measure the difference between these communicated current values from the CTs and will instruct the circuit breakers to open if they exceed a predetermined threshold [67]. Considering that differential protection schemes rely on comparisons between current levels only, rather than magnitudes, they are effective at overcoming challenges associated with topological changes in microgrids. The key drawback associated with differential current schemes is the requirement to

have relays placed at either end of the protective zone, creating significant financial burden when network upgrades are required [65].

5.3.3 The Hybrid Scheme

The effectiveness of both adaptive overcurrent and differential current protection schemes have been demonstrated in the context of microgrids, however their practical implementation is typically limited by factors such as technical and cost-related challenges. As a consequence, a hybrid approach is proposed, utilizing both adaptive overcurrent and differential current protection schemes in a bid to overcome individual inefficiencies. In this approach, the requirement for detection and isolation of all abnormal conditions within the microgrid is addressed, to allow for the un-faulted sections to remain connected to power supplies.

In the proposed scheme, differential relays are utilized to protect both the feeders and the interconnecting load buses. This can be represented visually via Figures 5.1 and 5.2 [67].

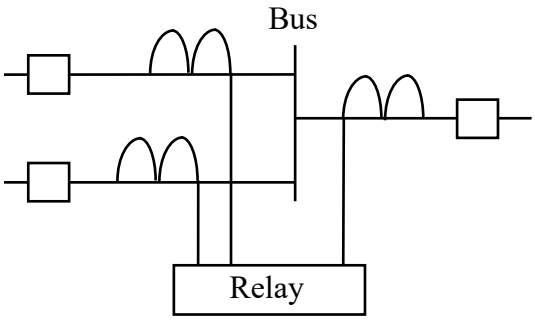

Figure 5.2: A load bus protected by a differential scheme.

The adaptive overcurrent relays are placed at the point of common coupling (PCC) between the load and the feeder where their settings are adjusted according to whether the microgrid is in grid or islanded mode. The adaptive overcurrent relays are notified of the microgrid topology through signals transmitted through a communication link between the relays and interconnecting relay (the relay coupling the utility connection to the microgrid).

The main advantage of this approach lies in its scalability. If either adaptive overcurrent or differential schemes were to be solely utilized then significant relay upgrades would be required within the microgrid. This is due to the fact that these schemes can be prone to failure if not implemented entirely. In this approach, the differential protection can be implemented on a

large or small scale depending on the application in question. With reference to the adaptive overcurrent protection, it can be adjusted to coordinate with existing downstream load point (downstream of the load taps adaptive overcurrent relay) reclosers and fuses or can be utilized as an instantaneous relay. As a consequence excessive infrastructure upgrades may be mitigated. Furthermore, the adaptive overcurrent and differential protection do not require coordination as both methods utilize different tripping algorithms.

5.3.3.1 Sequence of Operation

For the sequence of operation, CTs measure the current at each end of the feeder lines and load buses. These CTs connect to a relay (as indicated in Figure 5.1) which transmit and receive measured current values to and from neighboring relays. If the difference between the relay currents exceeds a predetermined threshold, the relays indicate that a short circuit has occurred on the line or bus and instructs the circuit breakers to open the faulted segment. When the difference between the relay currents is below the predetermined threshold then the short circuit is deemed to be outside of the protective zone of the relay, and it will not operate.

For the load lateral taps, the adaptive overcurrent relays analyze the input signals communicated from the interconnecting circuit breaker to determine if the microgrid is in grid or islanded mode. CTs are responsible for allowing the adaptive overcurrent relays to measure the magnitude of the current. In the event of a downstream fault within the load (this could be near the relay or deeper into the subnetwork fed by the lateral tap) the current magnitude rises rapidly such that it exceeds a predetermined pickup setting. At this point the adaptive relay will instruct the corresponding circuit breaker to open to clear the fault. When there is no fault or the fault occurs upstream of the adaptive relay, the measured current will be below the preset pickup setting and as such will not instruct the circuit breaker to open.

5.3.3.2 Protection Settings

A similar methodology, reference [67], is utilized for the differential current relays settings, with a typical tripping characteristic illustrated in Figure 5.3. As can be observed in Figure 5.3, the two key parameters that dictate the operational characteristics of the differential relay are the restraint and the differential pickup current. These values will determine where operating and restraining regions exist for the differential relay. The pickup current can be defined by Equation 5.1 [67].

$$I_{DIFFPKP} = |I_1| - |I_2| \tag{5.1}$$

Where $I_{DIFFPKP}$ is the differential pickup current in amperes and I_1 and I_2 are the secondary CT phasor currents from each relay in amperes.

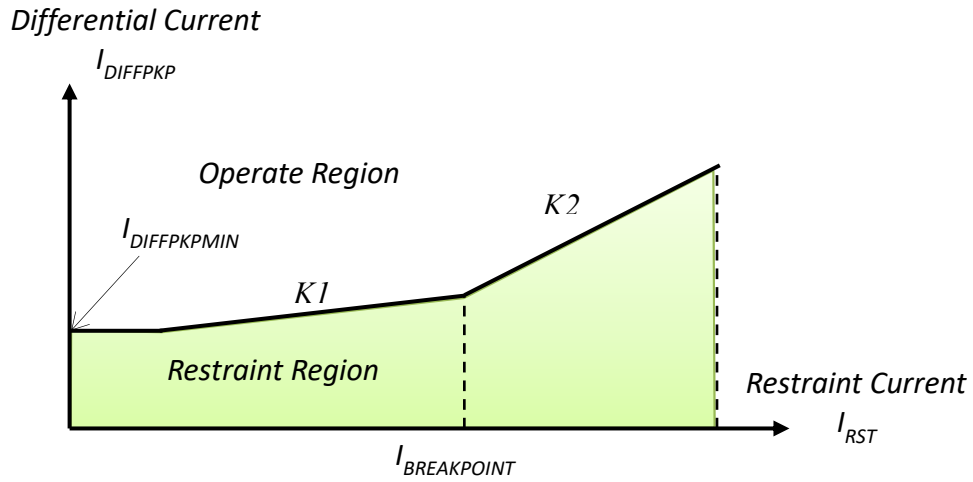

Figure 5.3: A typical differential current relay characteristic.

The restraint current can be defined by Equation 5.2 [67].

$$I_{RST} = |I_1 + I_2| \times \frac{1}{2} \tag{5.2}$$

During a normal steady state operation, the differential current reading for the relays is theoretically zero however, due to factors such as line charging, CT saturation and inaccuracies in the CT mismatch; this is rarely the case in practice [66]. To accommodate the mismatches between practical and theoretical results, the typical minimum pickup setting utilized in differential current relays is 0.25 A on the secondary [67].

Another important factor indicated in Figure 5.3 is the *K1* and *K2* values. These values are defined as the slope of the percentage differential characteristic [67] and they are generally expressed in percentage values. These values cause an increase in the pickup setting proportionate to the fault level increase as defined by Equation 5.3.

$$I_{DIFFPKP} = K \times I_{RST} \tag{5.3}$$

Typical values of *K1* and *K2* are 20% and 98% respectively [68].

The final setting for the differential protection is the breakpoint. This is the setting responsible for indicating which *K* value is to be used in Equation 5.3. A typical setting for the breakpoint is 5 A on the secondary [67].

The adaptive overcurrent relays at the lateral load taps are set such that their pickup settings are greater than double the normal load current but less than one third of the minimum fault current [69]. In a microgrid, the settings are required for both phase and ground type faults in both grid and islanded topologies. The pickup settings are determined by taking the greater of Equations 5.4 and 5.5.

$$I_{PKPx} = \frac{1}{3} \times I_{fmintx} \tag{5.4}$$

$$I_{PKPx} = 2 \times I_{Load} \tag{5.5}$$

where I_{PKPx} is the pickup current in amperes for mode *x* of the microgrid (grid or islanded mode), I_{Load} is the lateral taps expected load current in amperes and I_{fmintx} is the minimum short circuit current experienced by the relay for a fault type *t* in mode *x* in amperes.

5.4 Application of the Proposed Microgrid Protection Scheme

Two case studies are presented in this section to demonstrate the efficacy of the proposed scheme for protection of microgrids operating in either grid or islanded mode. These case studies showcase the capacity of the proposed scheme in managing the variations in short circuit current based on microgrid topology. These case studies are conducted utilizing the network indicated in Figure 2.5 with the details expressed in Table 5.1.

Table 5.1: Microgrid Case studies.

	Case Study-1	Case Study-2
Fault type	Three-Phase	Three-Phase
Fault location	Line 1	Load 1
Fault inception	1 second of simulation time	
Fault duration	Sustained fault	

Case studies presented in Table 5.1 can be expressed diagrammatically in Figure 5.4.

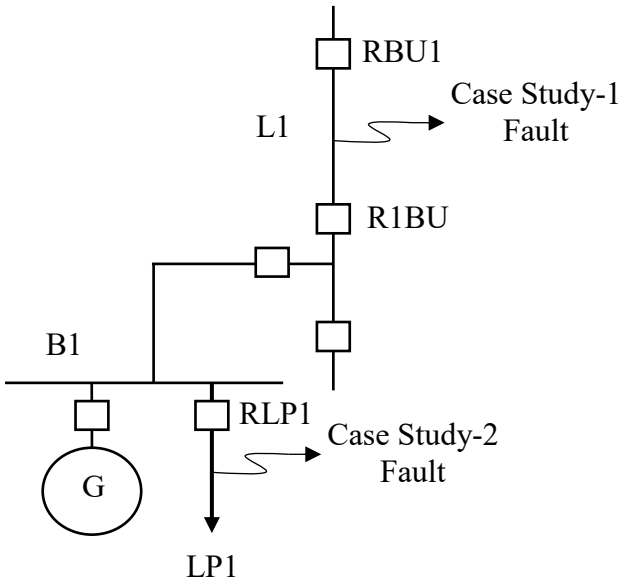

Figure 5.4: Fault applied at line1/load1 for Case Study-1/2.

The first case study is used to demonstrate the efficacy of the differential current relays in separating a feeder line when a fault occurs within its zone of protection. The second case study is utilized to demonstrate the efficacy of the adaptive overcurrent protection in removing a fault that occurs on the load point. The second case study highlights the ability of the differential current relay in discriminating against faults that lie outside of its protection zone.

For the case studies outlined in Table 5.1, all DG sources are solar PV, connected at each load point as indicated in Figure 5.4. The PV DG's are sized such that they are operating at 0.2 MW at a power factor of 0.9 during steady state. Note: all values in the case studies are expressed in RMS unless otherwise specified and each case study is conducted in both grid and islanded mode.

Before conducting the studies in Table 5.1, it is prudent to determine the protection settings of each relay. Short circuit data associated to the microgrid with PV and synchronous machine based (SM-based) DG sources is given in Appendix D.

It should be noted that all relays had a 5 millisecond delay incorporating into them to account for detection and breaker operation.

5.4.1 Differential Relay Settings

When determining the differential relay settings, it is prudent to factor in a CT ratio that is suitable for the application. As indicated in Figure 2.5, the total load expected to be supplied through line 1 is 1 MVA which gives a current as:

$$I_{Load1} = \frac{1 \times 10^6}{\sqrt{3} \times 13800} = 41.84\ A$$

This calculation indicates that a CT ratio of 50:5 would be adequate. Low turns ratio CTs can be prone to saturation under high short circuit current conditions [70]. In accordance with IEEE standard C37.110, CTs are required to operate accurately up to 20 times their rated current during short circuit conditions. As per Appendix D, the maximum short circuit currents experienced by the relays is 2691 A. This would mean that the minimum CT ratio required would be:

$$I_{CT\ min} = \frac{2691}{20} = 134.55\ A$$

The closest standard CT rating that exceeds the minimum value is 150:5. As such the CT ratio selected is 150:5.

As indicated in discussions in Section 5.3.3.2, the ratings that can be utilized for the differential relays are (note per unit values are on a 5 A base):

$$I_{DIFFPKPMIN} = 0.25\ A = 0.05\ per\ unit$$

$$I_{BREAKPOINT} = 5\ A = 1\ per\ unit$$

$$K1 = 20\%$$

$$K2 = 98\%$$

5.4.2 Adaptive Overcurrent Relay Settings

As indicated in Section 5.3.3.2, in order to determine the adaptive overcurrent relay settings it is imperative to know the expected load and short circuit current during both grid and island mode conditions. For load 1 in Figure 5.4 the load current can be determined by:

$$I_{Load1} = \frac{0.2 \times 10^6}{\sqrt{3} \times 13800} = 8.37\ A$$

As per Appendix D, the minimum short circuit currents experienced by the load points is 1431 A and 2206 A for phase and ground faults respectively during grid connected mode. In contrast, the minimum short circuit currents experienced by the load points is 54 A and 89 A for phase and ground faults respectively during islanded mode. Utilizing Equation 5.4, the phase and ground settings for the adaptive overcurrent relay can be determined by:

$$I_{PKPphasegrid} = \frac{1}{3} \times 1431 = 477\ A$$

$$I_{PKPgroundgrid} = \frac{1}{3} \times 2206 = 735\ A$$

$$I_{PKPphaseisland} = \frac{1}{3} \times 54 = 18\ A$$

$$I_{PKPgroundisland} = \frac{1}{3} \times 89 = 29\ A$$

As per Equation 5.5, the pickup setting associated to the load current can be found by:

$$I_{PKPx} = 2 \times I_{Load} = 2 \times 8.37 = 16.74\ A$$

As a result of the discussions in Section 5.3.3.2, the pickup settings of the adaptive overcurrent relay are:

$$I_{PKPphasegrid} = 477\ A$$

$$I_{PKPgroundgrid} = 735\ A$$

$$I_{PKPphaseisland} = 18\ A$$

$$I_{PKPgroundisland} = 29\ A$$

For consistency purposes, the CT ratios are the same as those determined for the differential current relay.

It should be noted that the adaptive overcurrent relays in this chapter are set to operate instantaneously when pickup settings are exceeded.

5.4.3 Case Study-1

Figure 5.5 presents Case Study-1 for the condition where the microgrid is operating in the topology of grid connected mode. Through observation it can be seen that following the fault inception 1 second into the simulation, the short circuit current flowing through relay RBU1 rises rapidly until it peaks at a value of 2075 A. The differential current begins to rise rapidly following fault inception until it peaks at 12.5 per unit with a corresponding restraint current of 12.98 per unit. As a consequence of these conditions, the differential relay protecting line 1 detects a short circuit condition and causes the circuit breakers RBU1 and R1BU to trip 0.00745 seconds after fault inception. This demonstrates the capability of the relay to detect the fault within its protection zone, disconnecting the faulted segment from the microgrid.

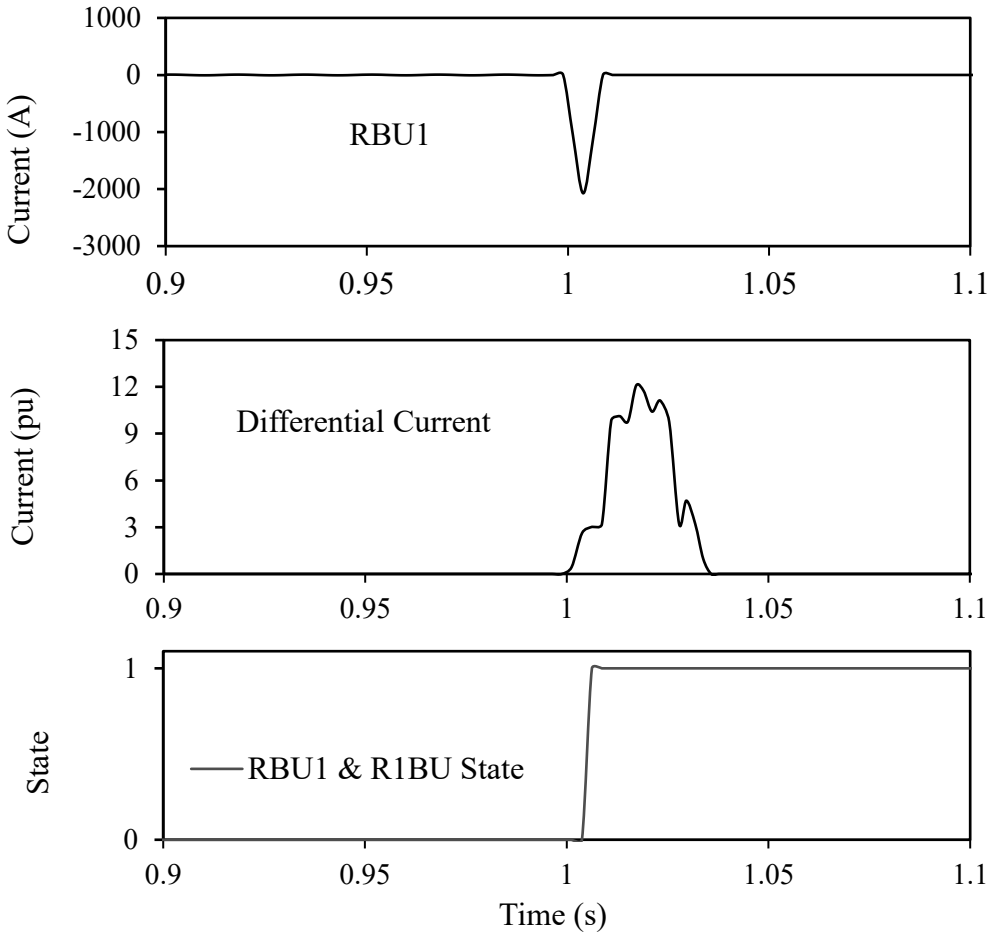

Figure 5.5: Case Study-1 during grid connected mode: RBU1 current, RBU1 & B1BU differential current, RBU1 & R1BU state signals.

Figure 5.6 presents Case Study-1 for the condition where the microgrid is operating in the topology of islanded mode. Through observation it can be seen that following the fault inception 1 second into the simulation, the short circuit current flowing through relay RBU1 rises until it peaks at a value of 40 A. The differential current begins to rise rapidly following fault inception until it peaks at 0.18 per unit with a corresponding restraint current of 0.05 per unit. As a consequence of these conditions it can be observed that the differential relay protecting line 1 can detect a short circuit condition and cause the circuit breakers RBU1 and R1BU to trip 0.00735 seconds after fault inception. This demonstrates the capability of the relay to detect faults within the protection zone, disconnecting the faulted segment from the microgrid.

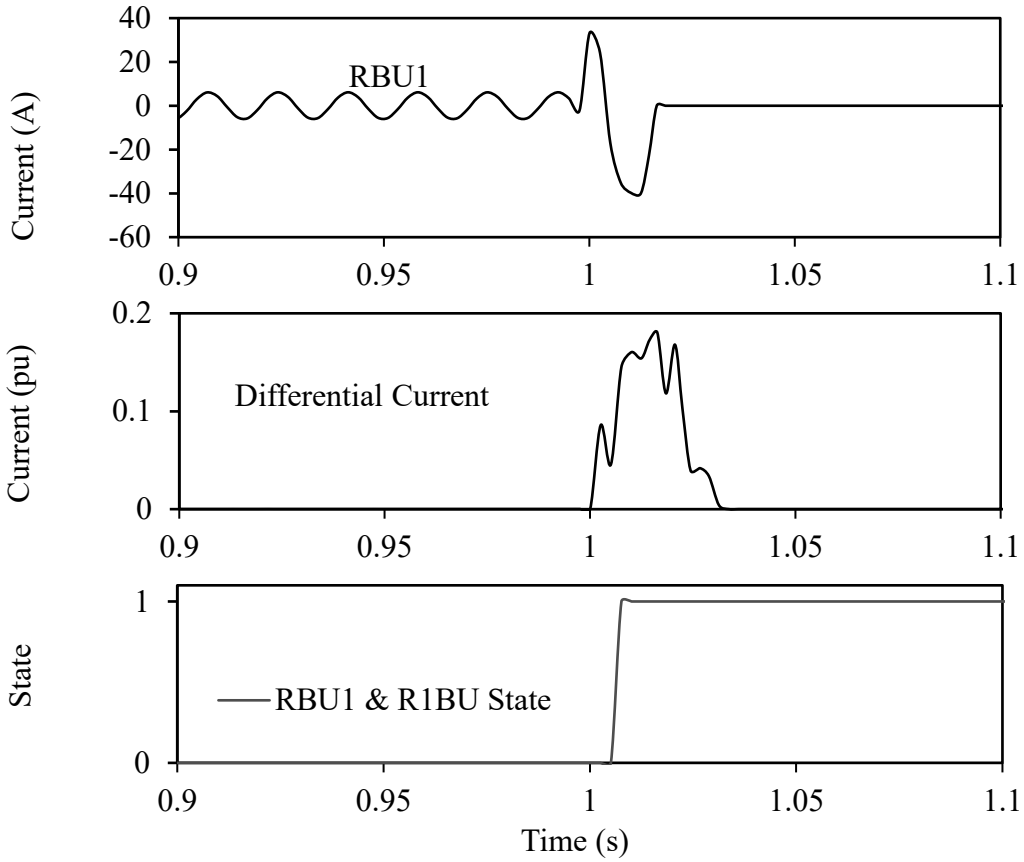

Figure 5.6: Case Study-1 during islanded mode: RBU1 current, RBU1 & B1BU differential current, RBU1 & R1BU state signals.

Comparing results obtained in Figures 5.5 and 5.6 makes it apparent that the short circuit current experienced by the differential relay protecting line 1 drops significantly during the microgrid islanded condition as opposed to the grid connected mode. The short circuit current in islanded mode is 19.27% of the current experienced in grid connected mode. Despite this

significant decrease in current, the differential relay could still clear the faulted segment of the microgrid successfully, demonstrating the efficacy of the proposed approach.

5.4.4 Case Study-2

Figure 5.7 presents Case Study-2 for the microgrid operating in the topology of grid connected mode. Observation reveals that following the fault inception 1 second into the simulation, the short circuit current flowing through relay LP1 rises rapidly until it peaks at a value of 1660 A. The differential current begins rising marginally following fault inception until it peaks at 0.000576 per unit with a corresponding restraint current of 11.3 per unit. Consequentially, the differential relay protecting line 1 discriminates against the fault experienced on load 1 as it falls outside of its protection zone and thus circuit breakers RBU1 and R1BU are signaled to remain closed. In addition, it is observed that the phase grid connected pickup current of the LP1 adaptive overcurrent relay is exceeded, yielding a breaker tripping time of 0.051 seconds. This demonstrates that adaptive overcurrent and differential relays operate correctly, given the fault location, indicating compatibility of use in conjunction with one another. Furthermore, the adaptive overcurrent relay is demonstrated to be capable of detecting the fault within the protection zone, disconnecting the faulted lateral load tap from the microgrid.

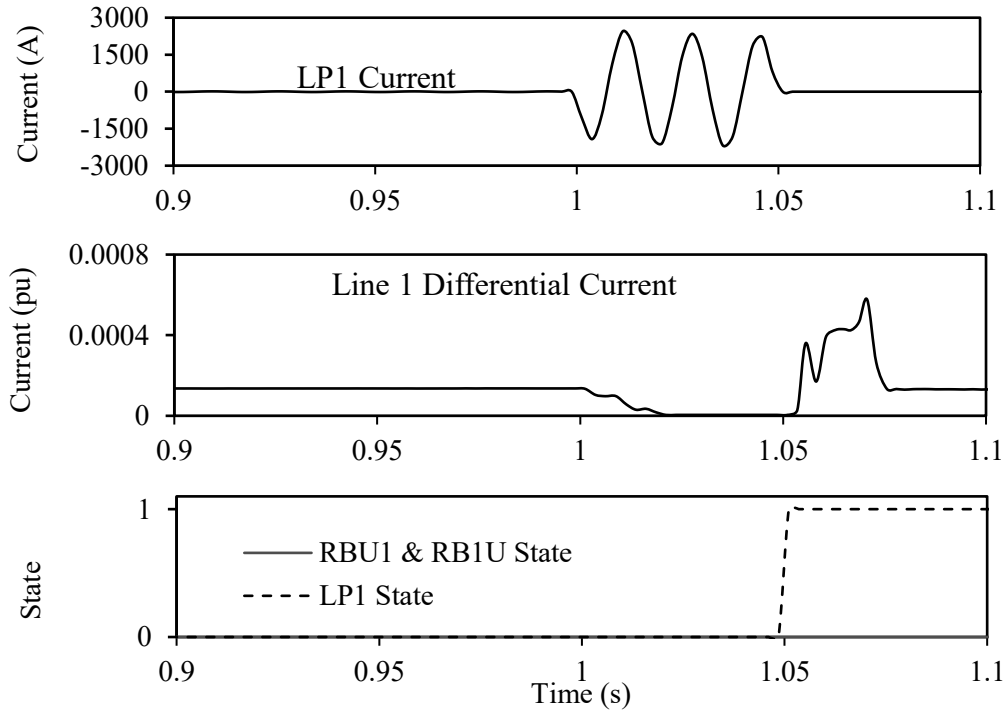

Figure 5.7: Case Study-2 during grid connected mode: LP1 current, RBU1 & B1BU differential current, RBU1 & R1BU state signals.

Figure 5.8 presents Case Study-2 for the condition where the microgrid is operating in the topology of islanded mode. Following the fault inception 1 second into the simulation, the short circuit current flowing through relay LP1 rises until it peaks at a value of 55 A. Again, it can be seen that the differential current peaks at 0.000576 per unit with a corresponding restraint current of 1.77 per unit. Consequentially, the differential relay protecting line 1 discriminates against the fault experienced on load 1 as it falls outside of the protection zone and thus instructs circuit breakers RBU1 and R1BU to remain closed. In addition, the phase islanded pickup current of the LP1 adaptive overcurrent relay is exceeded, yielding a breaker tripping time of 0.0457 seconds. Again, this demonstrates that both the adaptive overcurrent and differential relays operate correctly, considering the fault location, which indicates that they are compatible for use in conjunction with one another. Furthermore, the adaptive overcurrent relay is demonstrated to be capable of detecting and clearing within the protection zone, disconnecting the faulted lateral load tap from the microgrid.

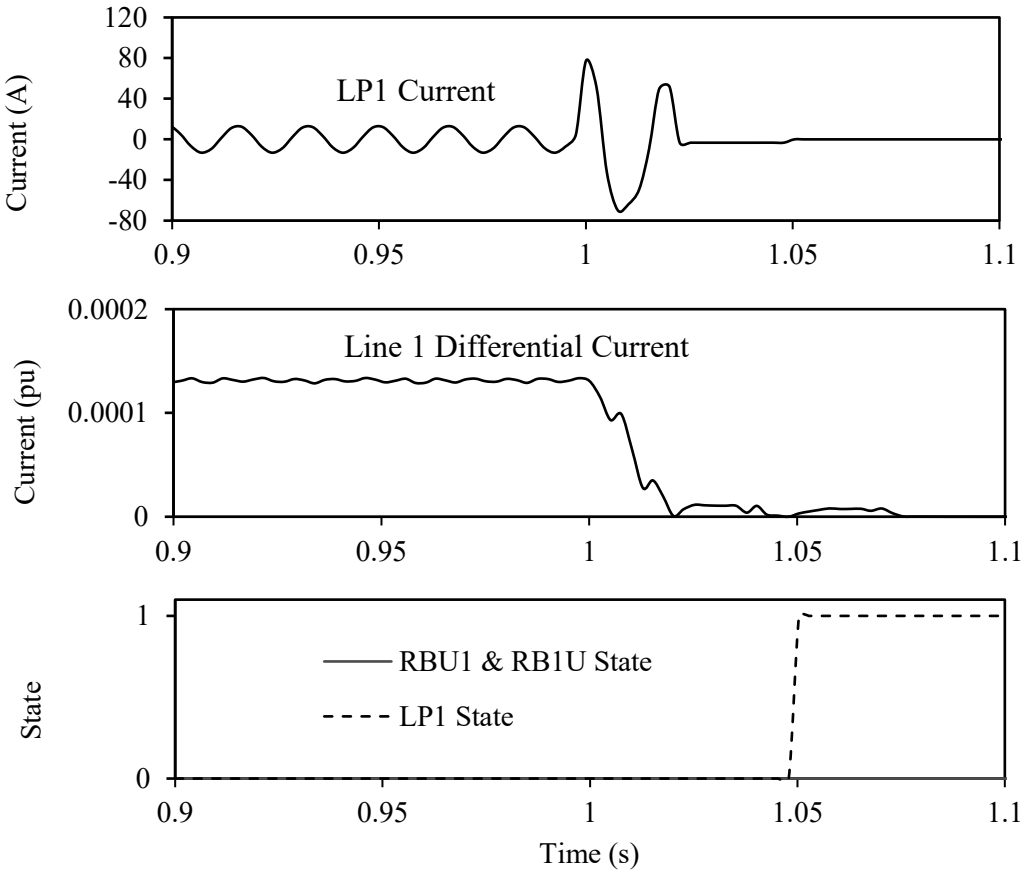

Figure 5.8: Case Study-2 during islanded mode: LP1 current, RBU1 & B1BU differential current, RBU1 & R1BU state signals.

Comparison of results obtained in Figures 5.7 and 5.8 makes it apparent that the adaptive overcurrent relay is effective at removing lateral load tap faults despite topological changes with the microgrid. It is apparent that the short circuit current experienced by the adaptive overcurrent relay protecting line 1 drops significantly during the microgrid islanded condition as opposed to the grid connected mode. The short circuit current in islanded mode is 33.13% of the current experienced in grid connected mode. Despite this significant decrease in current, the adaptive overcurrent relay was still able to clear the faulted segment of the microgrid. Lastly, it can be observed that in both cases the differential relay was able to discriminate against the fault, preventing the circuit breaker operation along the feeder backbone, successfully demonstrating the efficacy of the proposed approach.

In a traditional distribution protection scheme a fuse would typically be used to protect the load. In Case Study-2 a Kearney 20T fuse would be adequate for a steady state load current of 9 A. This fuse has a minimum melting current of 40 A. In the islanded mode case indicated in Figure 5.8 this fuse would only experience a short circuit current of 55 A. This current would correspond to a minimum melting time of approximately 15 seconds [71]. Typically, utilities require that a fault be removed from any system within 3 seconds [14]. Calculations indicate that a typical fuse used in the distribution network would fail to meet specified fault clearing requirements during an islanded mode. This highlights the suitability of the proposed approach in lieu of traditional protection methods.

Multiple case studies were conducted other than the ones specified in this chapter. In the additional case studies using multiple fault types and locations in conjunction with multiple DG types (PV and SM-based) were utilized. All results demonstrated similar characteristics to the ones highlighted in this Chapter. In every case the differential relays were able to discriminate between faults that were inside the protection zone and those that were outside of it, tripping only when required. Additionally, all adaptive overcurrent relays were able to remove faults that occurred in both microgrid topologies.

5.5 Summary and Conclusions

This chapter presents a hybrid adaptive overcurrent and differential current protection scheme to compensate for drastic changes in short circuit currents experienced in microgrids following transitions between grid and islanded modes. Results make it apparent that the proposed approach is effective at clearing faults within the microgrid regardless of operational mode. Furthermore, results demonstrate the efficacy of the proposed approach in discriminating against faults that fall outside of the protection zone for any given relay with no false tripping instances occurring. The proposed scheme is likely to require fewer infrastructure upgrades in existing utility networks, since it can be installed in segments rather in its entirety. This is particularly useful when budget constraints are a concern.

Results obtained demonstrate inefficiencies associated with traditional fuse protection for loads when microgrid conversion is required. This is attributed to the inability of fuses to adjust TCC settings when the microgrid transitions between grid and islanded modes resulting in significant differences between short circuit currents in grid and islanded modes. The inefficiency associated with traditional fuse protection is not present for the adaptive overcurrent relays proposed as replacements for the fuses.

In summary, results indicate that adaptive overcurrent and differential current relays do not require coordination, since upstream differential relays do not operate for faults that are outside of the zone of protection.

6. A REGRESSION ANALYSIS AND PARTICLE SWARM TECHNIQUE TO ALLOW FOR CONTINUOUS CONNECTION OF MICROGRIDS DURING DISTRIBUTION NETWORK FAULTS

6.1 Introduction

This chapter presents a smart protection scheme using polynomial regression analysis (PRA), in conjunction with particle swarm optimization (PSO), with a directional element to prevent excessive short circuit current contribution from microgrids during a grid fault. Through the application of this scheme at the point of common coupling (PCC), partial continual operation of the microgrid is permissible during grid faults without the need for complete disconnection. Investigations are conducted through several time-domain simulations, designed to ascertain the suitability of the proposed scheme for the purpose of mitigating the effects of the microgrid on existing grid short circuit protection infrastructure.

6.2 Microgrid Effects on Distribution Networks

Due to a consumer-driven increase in demand for energy and increasingly complex grids, supplemental generation is being explored by utilities as a means of reducing strain on existing sources. As mentioned in previous chapters, one such solution, which delivers power on a local level, circumventing the need for increases in generation capacity, is distributed generation (DG)/distributed energy resources (DERs) [1]. Sources such as photovoltaic (PV), wind and biogas within individual or clustered load centers, converted to microgrids, are being explored to service local energy needs. Chapter 5 explores the advantages of microgrids in the context of system loss and interruption reduction, however microgrids introduce unique challenges, especially in the context of operational and protection constraints. When applied to a traditional distribution network designed on the basis of large short circuit currents with a unidirectional power flow characteristic, the inclusion of microgrids like DERs can result in the degradation of these common characteristics observed in classical networks [3].

The literature suggests that, when determining the effects on existing distribution feeder

protection infrastructure, investigations are often carried out by treating microgrids as a lumped DG source [31]. As a result, mitigation of excessive short circuit current contribution from DG sources onto the distribution network is achieved through techniques which reduce fault current from the DG source itself [55]. In the context of DG short circuit current contributions, Kalman filter techniques are also offered as a means of predicting fault level contributions in distribution networks [72] - [73].

With increasing penetration of DERs on networks, another solution is PSO, whereby operational issues are solved through optimization of specified constraints [23], [74] - [75]. Multiple applications utilize PSO in the context of power systems [74], [76].

6.3 The Proposed Scheme

Section 6.2 investigates microgrid integration and prediction/optimization algorithms in the context of power systems, viable for use by utilities. The use of PSO in a power systems context is becoming popular due to its simplicity in calculation. Although interesting, there is very little research that reports on the prediction and mitigation of short circuit contributions from microgrids during utility faults for the purposes of maintaining existing protection infrastructure adequacy. In this context, Chapter 6 offers a potential solution.

In order to maintain the existing protection infrastructure adequacy the fault level contributions from generation plants within microgrids are required to be determined. This will identify what the contribution from the generation plants are and will highlight the level of short circuit current mitigation required. For simple networks where every possible combination of the generation plants (i.e. which plants are operating or not), wind speed, irradiance and system loading condition is plausible, a simple current source model could be utilized. However, practically, the number of generation combinations could be excessive (for example if there were 24 plants there would be 24 factorial different combinations) and knowing every wind speed and irradiance combination is practically infeasible. As such a combination of a statistical and optimization algorithm should be used to predict short circuit contributions.

The proposed scheme in this chapter utilizes a relay at the PCC between the microgrid and the distribution network. Within the relay, a direction sensing unit is used to determine the direction of flow of current (during a short circuit) which permits the scheme to operate only if

the current flow is from the microgrid to the distribution network. Failing this, the scheme is blocked and the internal microgrid protection is left to operate and clear the internal fault. When the scheme is permitted to operate, the polynomial regression analysis (PRA) uses the wind speed, irradiance and availability data to determine individual generation plant contributions from the microgrid to the distribution network. The PSO algorithm determines the minimum number of generation units within the plants that need to be disconnected such that the overall short circuit contribution of the microgrid to the utility during a grid fault does not yield loss of protection coordination. This allows for the connection between the microgrid and utility to be maintained, mitigating operational disturbances.

6.3.1 Overall Sequence of Operation

The proposed scheme's interconnecting block is applied at the PCC between the microgrid and the utility network as demonstrated in Figure 6.1.

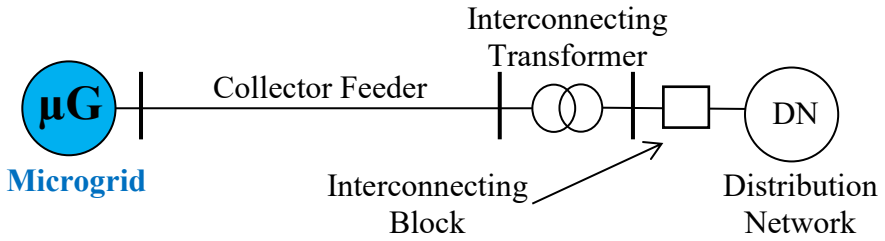

Figure 6.1: Location of the interconnecting block.

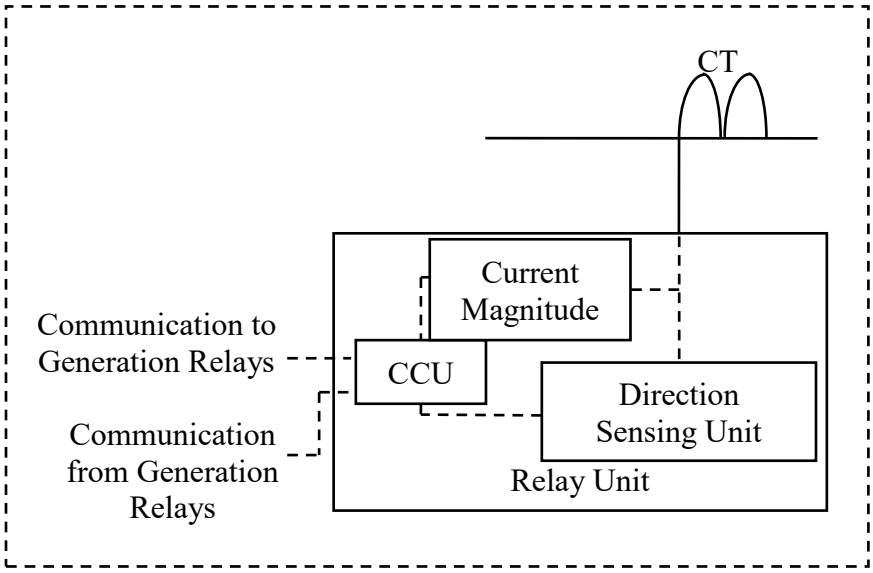

Figure 6.2: Components of the interconnecting block in the proposed scheme.

As can be seen in Figure 6.2, a directional sensing unit is integrated into the relay of the proposed scheme, facilitating communication between the DG sources in the microgrid and corresponding generation unit breakers. The proposed scheme is responsible for detecting the short circuit contribution from the microgrid to the utility during a fault. The method can be explained using the following steps:

1. Before the proposed scheme can work properly, the loss of coordination (LOC) limit for the given distribution utility network is required. In practice this limit would be provided by the utility however in this thesis it is determined using the method specified in reference [47]. The LOC limit is the maximum level of short circuit current that is permitted to flow from the microgrid to the utility for a fault before loss of coordination occurs between the reclosers and fuses. In this thesis a safety multiplication factor of 0.9 is used i.e. if the current flowing from the microgrid to the utility is greater than 0.9 times the LOC limit current, then the pickup value of the proposed scheme is exceeded. This is also known as the corrected LOC limit. The location of the fault that yields the LOC in the network is taken as the point for all short circuit measurements for the PRA conducted in Section 6.3.2.
2. The current is fed into the relay unit via a CT. Then the current magnitude and direction is determined and communicated to the central control unit (CCU). If the current flow is from the utility to the microgrid then the CCU blocks communication between the relay and the generation unit interconnecting relays within the microgrid generation plants. This is to allow for the protection infrastructure specified in Chapter 5 to clear the internal microgrid fault without interference from the proposed scheme. In order to accomplish this, the proposed scheme is required to have a directional sensing unit integrated into the architecture as demonstrated in Figure 6.2.
3. If the current is flowing from the microgrid to the utility and the short circuit contribution exceeds the pre-specified corrected LOC limit, then the CCU determines the short circuit current outputs from the microgrid generation plants through the use of regression analysis. The regression analysis takes training data from a multitude of cases for a specific microgrid to determine the short circuit contribution to utility faults from generation plants under varying conditions. This forms the basis for short

circuit current contribution predictions to aid in identification of individual units within generation plants that require their contributions to be curtailed.

4. The relay within each generation plant communicates the current status to the CCU within the interconnecting block. This communication includes wind speeds (for wind turbines), solar irradiance level (for PV sources), the output power (for SM based plants, e.g. operating at 80% of capabilities) and also the status of each generator (i.e. if it is online or not).
5. Utilizing the data from the generation relays in addition to the information from the current magnitude and direction sensing units within the proposed scheme, the PRA equations are used within the PSO algorithm to determine the minimum number of units to be disconnected within the plants to maintain utility protection coordination.

Through observation of Figure 6.2, it is apparent that there is a requirement for a communication link between the proposed schemes' CCU and the generation plant's relays. Although this particular component is outside the scope of this thesis, Ethernet Fiber Links technology should be adequate for this application with a delay time in the order of only a few milliseconds [52]. Although this technology should be adequate for this application, there are many others that would be potentially viable. In order to account for the communication, a delay time of five milliseconds is used in time-domain simulations.

6.3.2 Regression Analysis for the Prediction of Fault Current Contributions

The key inputs that are required to be determined for the regression analysis is the percentage penetration from each generation plant in conjunction with the wind speed, solar irradiance and output of synchronous machine based (SM-based) (biogas) generators. The topology of the microgrid feeders plus pre-fault loading and post-fault measurements are required to determine percentage penetration for each feeder. This can be described as such:

In order to determine the percentage penetration of each generation plant, the feeder pre-fault current levels are required to be utilized in conjunction with:

$$PEN_{P1} = \frac{I_{P1}}{I_{P1}+I_{P2}+I_{P3}} \times 100 \tag{6.1}$$

$$PEN_{P2} = \frac{I_{P2}}{I_{P1}+I_{P2}+I_{P3}} \times 100 \tag{6.2}$$

$$PEN_{P3} = \frac{I_{P3}}{I_{P1}+I_{P2}+I_{P3}} \times 100 \quad (6.3)$$

$$PEN_{P4} = \frac{I_{P4}}{I_{P4}+I_{P5}+I_{P6}} \times 100 \quad (6.4)$$

$$PEN_{P5} = \frac{I_{P5}}{I_{P4}+I_{P5}+I_{P6}} \times 100 \quad (6.5)$$

$$PEN_{P6} = \frac{I_{P6}}{I_{P4}+I_{P5}+I_{P6}} \times 100 \quad (6.6)$$

where PEN_{Px} is the percentage penetration of generation plant x in percent. The plant currents can be expressed diagrammatically as per Figure 6.3. As can be seen in Equations 6.1 to 6.6, only generation plants that are connected to the same feeder are considered in the percentage penetration calculations.

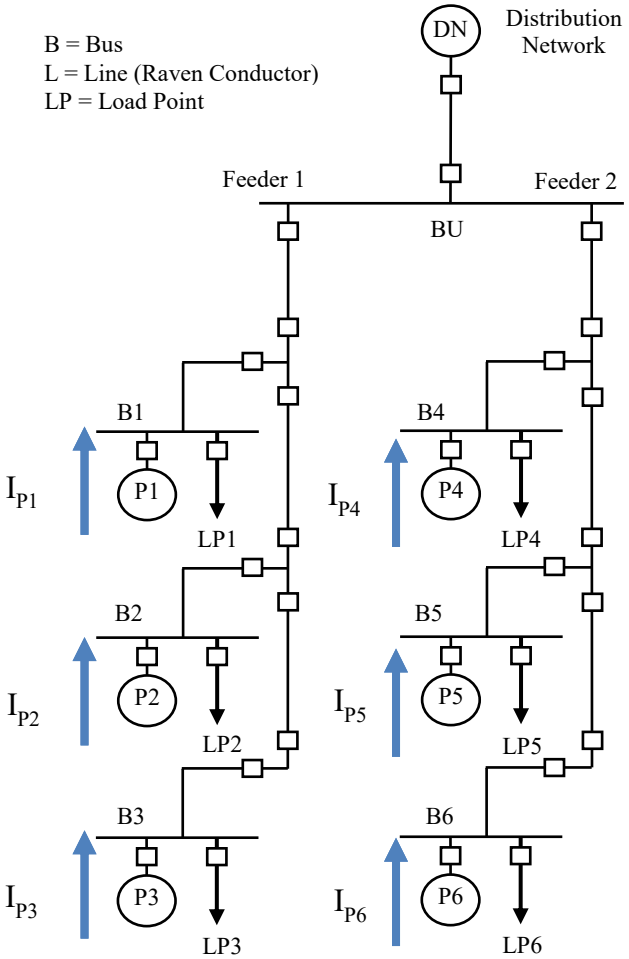

Figure 6.3: Example diagram of current measurements.

To determine the percentage rating of a generation plant, the type of generators present in the plant is required to be known in addition to the pre-fault loading conditions. For a SM-based generation plant the following can be used to express the percentage rating:

$$r_{PSM} = \frac{S_{output}}{S_{rated}} \times 100 \tag{6.7}$$

where r_{PSM} is the percentage rating of a SM-based generation plant, S_{output} is the pre-fault output of the SM-based generation plant in MVA and S_{rated} is the rated MVA output of the SM-based generation plant.

Similarly for the wind based generation plants, the following is used to express the percentage rating:

$$r_{PW} = \frac{CWS}{RWS} \times 100 \tag{6.8}$$

where r_{PW} is the percentage rating of a wind based generation plant, CWS and RWS are the current and rated wind speeds respectively in meters per second. It should be noted that Equation 6.8 assumes that the wind turbine diameters and air density are constant. As such the power output of the turbine is only related to the velocity of the wind. In the event that the wind speed is greater than the rated wind speed, r_{PW} will be forced to be one. The reason for this is wind turbines will not generate above their rated power output (which first occurs at the rated wind speed) even when exceeding the rated wind speed. When the rated wind speed is exceeded the wind power curve of any turbine becomes flat until it reaches its cutout speed [11].

For a PV based generation plant the following is used to express the percentage rating:

$$r_{PPV} = \frac{CI}{RI} \times 100 \tag{6.9}$$

where r_{PPV} is the percentage rating of a PV based generation plant, CI is the current irradiance and RI is the rated irradiance in Watts per square meter. It should be noted that CI is measured as the irradiance level that actually strikes the solar array; as such the power converted is related to the number of modules, the area of the panels and the irradiance level. In Equation 6.9 it is assumed that the area of the panels and the number of panels are constant hence the output of the PV plant is only related to the irradiance striking the panels.

With the inputs defined, the PRA is able to account for variations in solar irradiance, wind speed and availability of generation plant resources to predict the short circuit contribution that will occur for a grid fault from the microgrid.

To allow for accurate predictions by the PRA, training data is required. This data is accumulated through numerous short circuit analysis studies that are required to be conducted on a given system. The percentage rating of the generation plants in addition to the penetration percentile are required to be recorded with the corresponding short circuit contribution for a variety of fault types. The more data points accumulated, the more accurate the PRA will be.

The first set of data points required correspond to the maximum short circuit contribution from a generation plant. A generation plant will deliver its maximum short circuit contribution when no other generation plants are in operation. This set of data must be accumulated for many percentage ratings of the generation plant (in these cases the percentage penetration is 100%).

The second set of data points required correspond to the minimum short circuit current contribution from a generation plant. This occurs when all the other generation plants are operating at their rated capacity (in these cases the percentage penetration will gradually decrease as the percentage rating decreases).

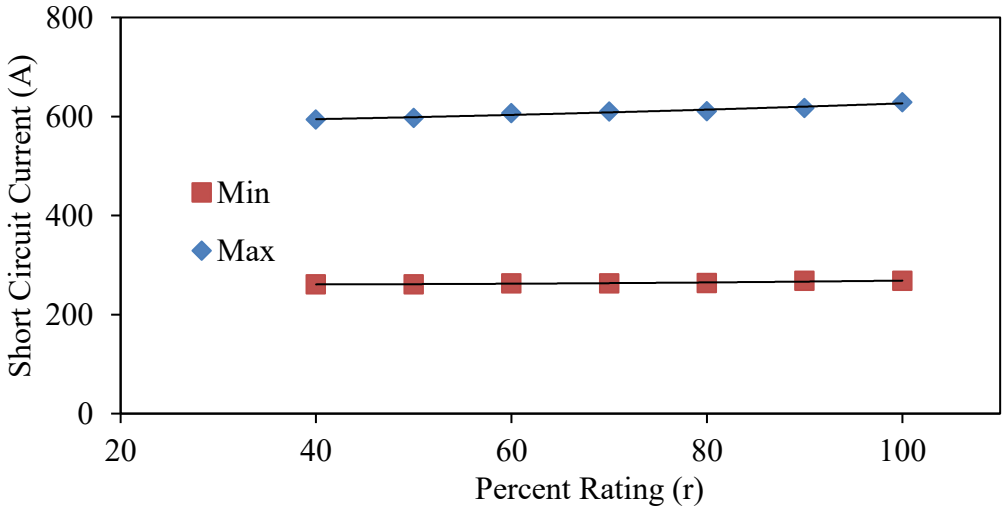

Figure 6.4: Example of short circuit current versus percentage generation plant rating for maximum and minimum cases.

The maximum and minimum cases are plotted with the short circuit current on the vertical axis with the percentage rating on the horizontal axis. As illustrated in Figure 6.4.

In this thesis, all the predictions are scaled according to the maximum penetration case. As such a line of best fit is required for the maximum penetration case. Utilizing regression techniques discussed in Section 1.4, a quadratic equation of best fit can be expressed generically:

$$I_{frtPi} = \delta_{tPi}(r_{Pi})^2 + \alpha_{tPi}(r_{Pi}) + \beta_{tPi} \tag{6.10}$$

where I_{fitPi} is the predicted short circuit level for generation plant i with a percentage rating r (r_{Pi}) and fault type t. It should be noted that δ, α and β are coefficients of the prediction polynomial that correspond to the specific generation plant, rating and fault type. It should be noted that for fitted polynomial equations of orders higher than two (upper exponents), the coefficients associated to the upper exponents of were of negligible magnitude hence polynomials of degree 2 (quadratic) were selected for equations of best fit. This is the same justification for all subsequent equations in this chapter (Equations 6.12 to 6.16).

Once the maximum and minimum short circuit contribution cases are plotted, additional data is required to be obtained and plotted at individual rating states of the generation plant as defined by Equations 6.7 to 6.9. This additional data is used to scale the maximum short circuit case expressed in Equation 6.10 for predictions. The short circuit data must be scaled according to Equation 6.11:

$$RA_{pt} = I_{fprt}/I_{f100t} \tag{6.11}$$

where RA_{pt} is the ratio of the actual short circuit current level output by the generation plant at rating r for a fault type of t and penetration p. the denominator of Equation 6.11 represents the fault level during the maximum output case (When only a single generation plant is operating). This allows for all other short circuit levels to be expressed in per unit quantities using the maximum case as the base.

Consider an example case of a SM-based generation plant; the output can be run for a percentage rating of 100%, 90%, 80%, 70% and 60% to capture a wide cross-section of results for scaling. These cases are then fit with a quadratic polynomial. Consider the following sample data for the 100% and 90% rated case for a single line-to-ground fault:

Table 6.1: Sample fault data for a SM generation plant at an output rating of 100% and 90%.

r = 100%			r = 90%		
Fault level (A)	PEN (%) (p)	$I_{fprLG}/I_{f100rLG}$	Fault level (A)	PEN (%) (p)	$I_{fprLG}/I_{f100rLG}$
629	100	1	617	100	1
277	47.727	0.440	276	45.882	0.447
272	31.579	0.432	271	30	0.439
268	23.823	0.426	268	22.504	0.434

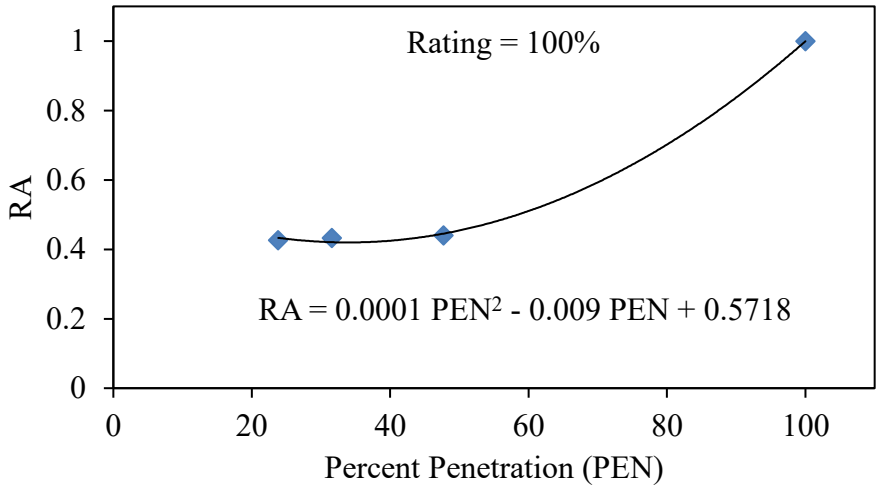

Figure 6.5: Example of single line-to-ground short circuit ratios versus percentage penetration for a SM-based Plant operating at rated output.

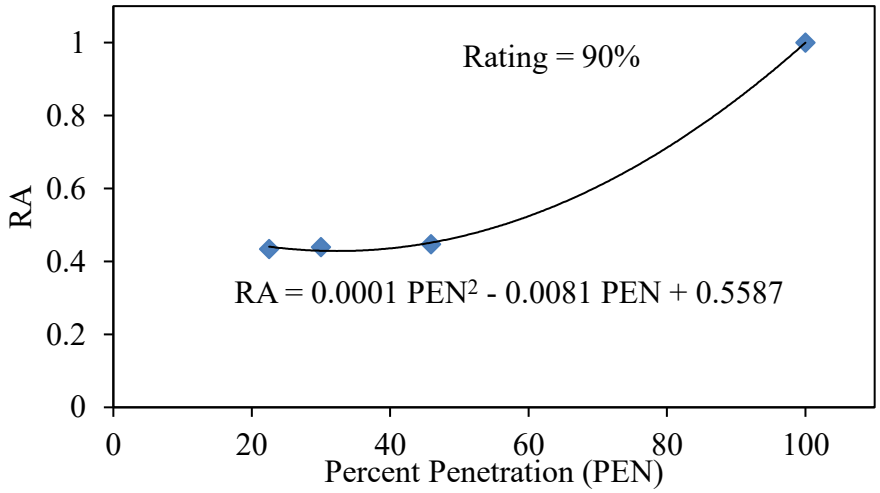

Figure 6.6: Example of single line-to-ground short circuit ratios versus percentage penetration for a SM-based Plant operating at 90% rated output.

As can be seen in Table 6.1, the short circuit levels are scaled according to the maximum penetration case. For example, the rated output of the SM-based plant at 90% with a penetration of 30% gives a fault level of 271 A. The corresponding maximum case fault level is 617 A. With scaling as per Equation 6.11, this yields:

$$RA_{30LG} = \frac{271}{617} = 0.439$$

Plotting these cases with the fault ratio on the vertical axis and the penetration percentage on the horizontal axis allows for a prediction of the short circuit ratio at a specific rating and percentage penetration. An example for a 100% and 90% case can be seen in Figures 6.5 and 6.6 respectively.

Similar to Equation 6.10, a quadratic polynomial is fit to the data for individual operating outputs. These equations can be expressed generically in the form:

$$RA_{prtPi} = \tau_{rtPi}(PEN_{rPi})^2 + \gamma_{rtPi}(PEN_{rPi}) + \varepsilon_{rtPi} \tag{6.12}$$

As observed in Figures 6.5 and 6.6, the corresponding quadratic polynomials for the example cases with ratings 100% and 90% are as such;

$$RA_{p100LGPi} = 0.0001(PEN_{rPi})^2 - 0.009(PEN_{rPi}) + 0.5718$$

$$RA_{p90LGPi} = 0.0001(PEN_{rPi})^2 - 0.0081(PEN_{rPi}) + 0.5587$$

Equation 6.12 is used for discrete percentage ratings of the generation plant (i.e. 100%, 90% etc.). In order to predict the correct short circuit ratio, the generation plant would need to be operating at discrete percentage ratings previously accounted for in the data. It is not feasible to account for every scenario, hence the individual coefficients in Equation 6.12 need to be adjusted according to the percentage rating. To do this, each coefficient must be plotted on a graph with values serving as the vertical axis while the percentage rating serves as the horizontal axis. Note the following sample data from the case of a SM-based generation plant with a single line-to-ground fault type, with the output ratings of the machine varying from 100% to 60% in 10% increments.

Table 6.2: Ratio scaling coefficients for a SM-based generation plant for a single line-to-ground fault.

Percentage Rating (r)	τ	γ	ε
100	0.00013	-0.00897	0.57180
90	0.00012	-0.00806	0.55868
80	0.00011	-0.00647	0.52376
70	0.00010	-0.00553	0.50345
60	0.00009	-0.00429	0.48137

The coefficients in Table 6.2 are plotted as such:

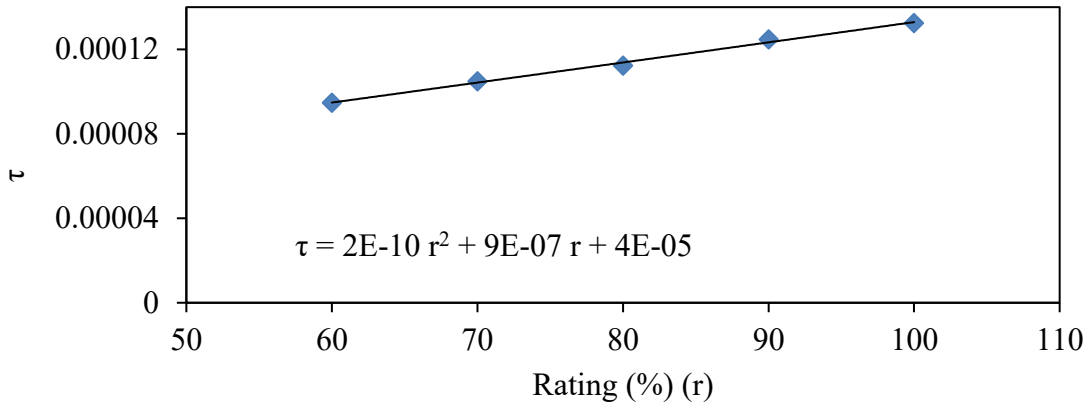

Figure 6.7: Example of single line-to-ground τ coefficients versus percentage rating for a SM-based generation plant.

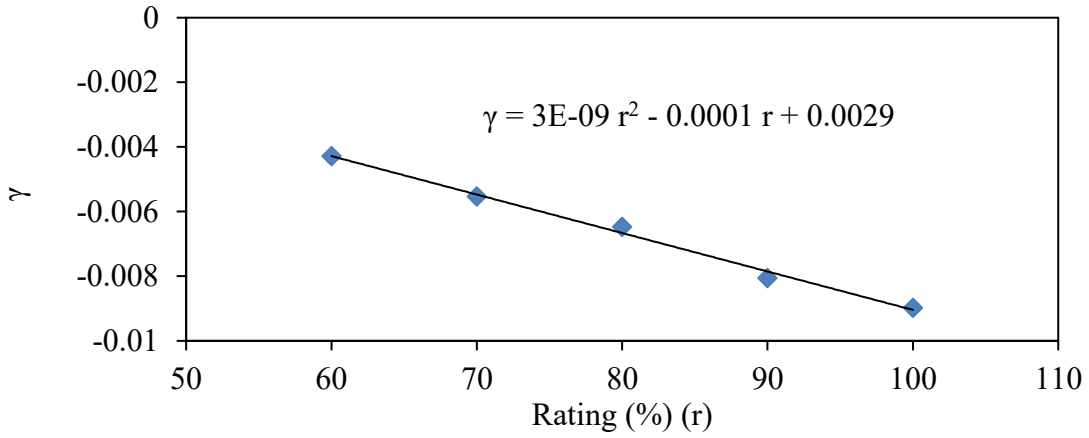

Figure 6.8: Example of single line-to-ground γ coefficients versus percentage rating for a SM-based generation plant.

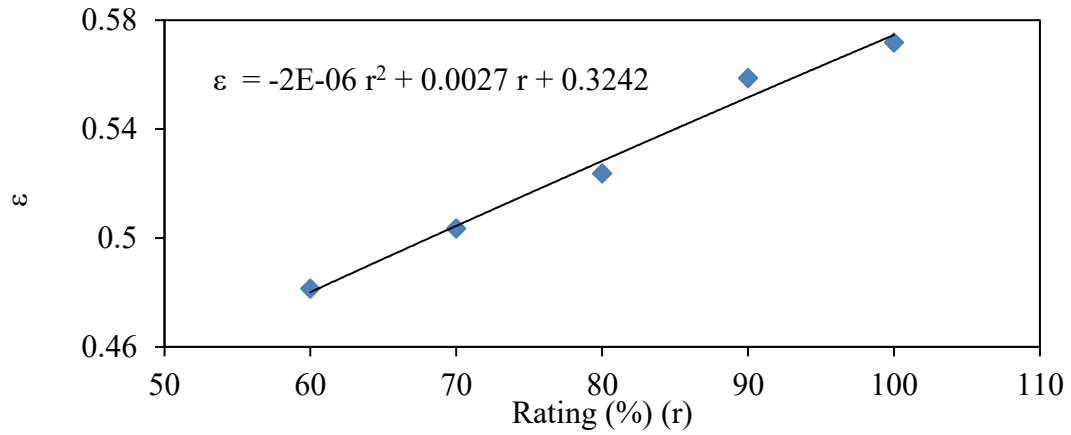

Figure 6.9: Example of single line-to-ground ε coefficients versus percentage rating for a SM-based generation plant.

Similar to Equation 6.12, a quadratic polynomial is fit to the data to determine the coefficients. These equations can be expressed generically in the form:

$$\tau_{crtPi} = a_{rtPi}(r_{Pi})^2 + b_{rtPi}(r_{Pi}) + c_{rtPi} \tag{6.13}$$

$$\gamma_{crtPi} = d_{rtPi}(r_{Pi})^2 + f_{rtPi}(r_{Pi}) + g_{rtPi} \tag{6.14}$$

$$\varepsilon_{crtPi} = h_{rtPi}(r_{Pi})^2 + k_{rtPi}(r_{Pi}) + m_{rtPi} \tag{6.15}$$

These are known as the corrected coefficients (denoted *c*)

As a result, Equation 6.12 can now be expressed using the corrected coefficients:

$$RA_{cprtPi} = \tau_{crtPi}(PEN_{rPi})^2 + \gamma_{crtPi}(PEN_{rPi}) + \varepsilon_{crtPi} \tag{6.16}$$

where Equation 6.16 gives the predicted short circuit ratio relative to the maximum penetration case. As such, in order to predict the short circuit current that will be output by a generation plant, Equation 6.16 is multiplied by Equation 6.10 to give:

$$I_{fprtPi} = I_{frtPi} \times RA_{cprtPi} \tag{6.17}$$

Equation 6.17 gives the predicted fault current for generation plant *i* at a penetration percentage *p* with an operating output of *r* percent of the plant rating for a fault type *t* in Amperes.

This procedure is conducted for every generation plant and fault type to be able to predict the short circuit contribution from the microgrid to the utility during short circuit conditions.

6.3.3 Particle Swarm Optimization for Selection of Generation Plant Contribution Mitigation

As specified in Section 6.3.1, PSO is utilized to determine which units within the generation plants are required to be disconnected to prevent LOC on the utility network. The PSO utilizes the prediction method specified by the regression analysis in Section 6.3.2 in conjunction with traditional PSO methods to make this determination.

The traditional PSO algorithm is specified in Section 1.5 of this thesis. Although the traditional PSO is effective, it has been demonstrated to potentially converge prematurely [77]. In reference [77], a solution has been offered to mitigate premature convergence, accomplished through the addition of a new term in the velocity update equation specified in Equation 1.7 for the global best particle. Using an index of τ, the following position update equation is utilized for the global best particle only (all other particles continue to use Equation 1.7).

$$x_{n+1}^{\tau} = g_{best} + \omega_n v_n^{\tau} + p_n(1 - 2r_2) \tag{6.18}$$

Where the factor p_n is adapted after each iteration. This is updated according to the rules specified in Equations 6.19 to 6.21 [77]:

$$p_{n+1} = 2p_n, if\ number\ of\ successes > 15 \tag{6.19}$$

$$p_{n+1} = 0.5p_n, if\ number\ of\ failures > 5 \tag{6.20}$$

$$p_{n+1} = p_n, otherwise \tag{6.21}$$

where p_0 is equal to one. A failure occurs if the current global best particle is in the same position as the previous global best particle. A success occurs when the current global best particle is in a different position to the previous global best particle. It is important to note that when a failure occurs the number of successes is reset to zero and when a success occurs the number of failures is reset to zero.

PSO works on the premise of optimizing a specific objective function with specified constraints. In the case of the problem presented, the objective is to make the short circuit

contribution from the microgrid to a utility fault less than the LOC limit (we represent this as u_1 in the PSO algorithm). The first constraint in this problem is related to the number of generation units that are mitigated (this is designated the *SourceCount*). The second constraint is related to the difference between the numbers of sources mitigated in each plant (this is designated u_2). This is to remove bias from the optimization spreads the effects of the mitigation (e.g. it is desirable rather trip one generator from two different plants than two generators from the same plant). As indicated in Section 6.3.2, the predictions equations are non-linear and the constraints associated to the PSO are integer values. As such this is a mixed integer, non-linear optimization problem. The function proposed for use in the PSO scheme is as such:

$$Minimize\ (u_1 + u_2 - SourceCount) \tag{6.22}$$

where

$$SourceCount = \sum_{i=1}^{n}(PR_{Pi} \times N_{Pi}) \tag{6.23}$$

where PR_{Pi} is the percentage reduction determined by the PSO algorithm (e.g. 80% would mean that the number of generation sources within generation plant *i* would need be reduced to 80% of what it was when the fault occurred. If there were 5 sources at generation plant *i* then an output of 80% would mean that one source would be disconnected). N_{Pi} is the number of generation sources within generation plant *i* and *n* is the number of generation plants.

The function in Equation 6.22 is based on reducing penalty factors u_1 and u_2. The penalty factor u_1 is related to the LOC limit of the network. If the predicted short circuit contribution from the regression analysis is above the corrected LOC limit then u_1 equates to 1000 or else it is zero. This ensures that the optimal solution will always be below the LOC limit.

The penalty factor u_2 is introduced to try and mitigate bias within the PSO algorithm in the context of choosing which generation plant's sources will be disconnected. This is accomplished by taking the absolute of the difference for each $PR_{Pi} \times N_{Pi}$ value. Consider an example where there are 6 generation plants with 5 generation sources within each plant. The penalty factor u_2 is calculated through:

$$u_2 = \sum_{j=1}^{15} z_j \tag{6.24}$$

$$z_j = ABS([5 - PR_{Pk} \times N_{Pk}] - [5 - PR_{Pl} \times N_{Pl}]) \times \frac{1}{5} \tag{6.25}$$

where k and l are plant numbers that cannot be equal to each other. Equation 6.25 is repeated for every combination of the plants (e.g. if there are 6 plants with 5 sources then there are 15 combinations).

In order for the PSO algorithm to work correctly the inputs that are required are the current percentage output of SM-based generation plants, the wind speed and the irradiance level. These are then used to calculate the percentage penetrations as per Equations 6.1 to 6.6 and the percentage rating as per Equations 6.7 to 6.9. These values are determined through real time monitoring of the generation plants.

PSO operates on the basis of trialing a set number of candidate solutions before there is an adjustment to these initial candidate solutions using the algorithm procedure set out in Section 1.5. This means that a number of initial trials are required to be programmed into the PSO algorithm. In order to accomplish this, a random continuous uniform distribution function is programmed into the PSO algorithm that gives 1000 random candidate initial solutions. It should be noted that one solution that is also programmed into the PSO algorithm is the net zero case where every generation plant and source is removed from the network.

The PSO algorithm is set to take the greatest current value as the predicted short circuit current. This means that for a phase fault when the PSO algorithm runs a case, if the three-phase fault is predicted to be greater than the line-to-line fault, then the predicted phase short circuit current is taken as the three-phase fault. This same decision process is utilized for the ground faults.

The population of random candidate solutions is run through the PSO algorithm, integrated with the PRA tool, to determine the optimal solution. Once the optimal solution is determined, it is stored in the CCU and transmitted via a communication channel to the relays of each generation plant in the scenario where the current exceeds the corrected LOC limit and is flowing from the microgrid to the utility.

6.4 Application of the Proposed Scheme

This section aims to demonstrate the effectiveness of the proposed scheme through multiple comparative studies. As specified in Figure 3.2, LOC first occurs for a microgrid connected at distribution bus 2 when a fault occurs at load L1: that is, the microgrid is integrated

into the network at distribution bus 2 in this chapter. The system utilized in the studies in this chapter is similar to that of Figure 2.1 in Chapter 2, in conjunction with Figure 2.5. These adjusted networks are presented in Figures 6.10 and 6.11.

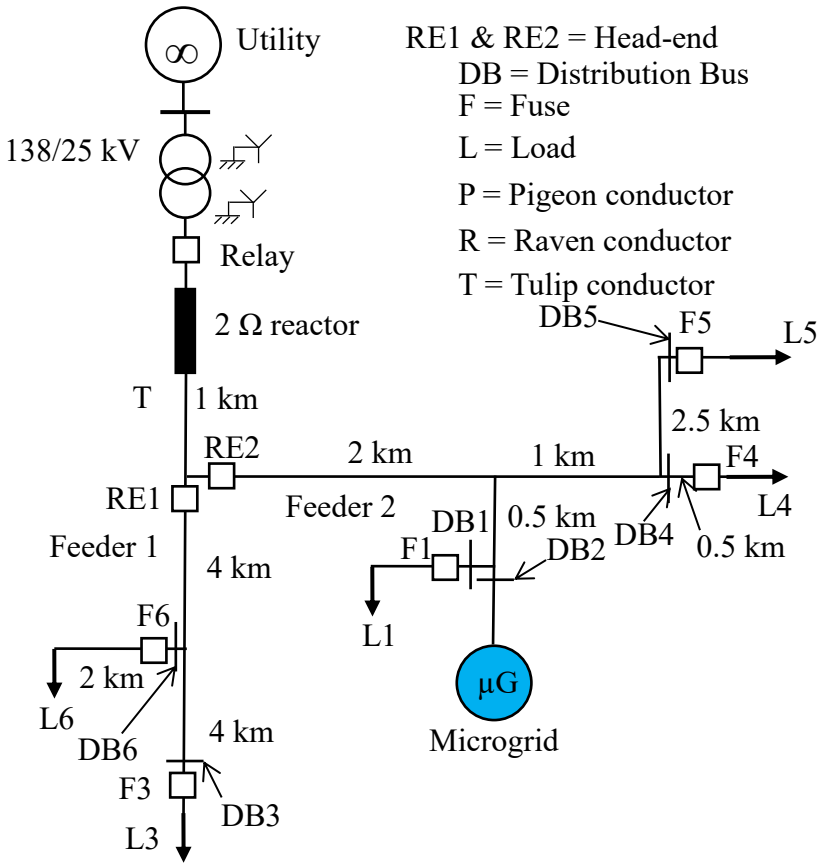

Figure 6.10: The system under study with a microgrid connected at distribution bus 2.

The system presented in Figure 6.10 consists of a substation serving two 25 kV feeders. As mentioned in Chapter 2, there are three types of loads present in the network, namely: constant impedance (L1 and L4), constant power (L3) and composite loads (L5 and L6). The microgrid is integrated into the network where load point 2 was previously located. Fuse protection is employed to protect all load points except the microgrid, and each feeder is protected by its own designated recloser (RE1 and RE2). The microgrid is connected through the interconnecting block and a 25/13.8 kV transformer. As per Section 2.2.3, the fuse sizes and load sizes of each load are specified in Table 6.3.

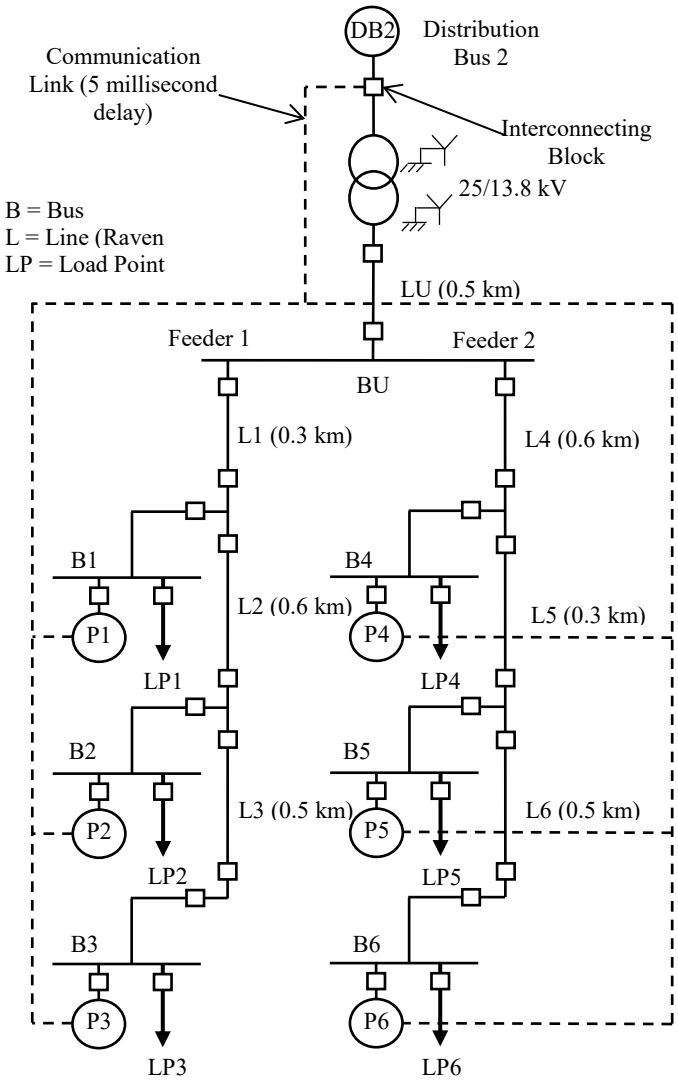

Figure 6.11: Single line diagram of the microgrid under study.

Table 6.3: Load demand and fuse sizes for the system under study.

Load number/demand (MVA)	1/1MVA	2/6 MVA	3/2 MVA	4/1 MVA	5/6 MVA	6/5 MVA
S&C SM4, 5 Fuse size	175E	N/A	125E	150E	150E	125E

It should be noted that the settings of the head end reclosers are the same as that specified in previous chapters. The microgrid integrated into the network is detailed in Figure 6.11.

The microgrid consists of six main buses. All loads are operating at a demand of 1 MW with a 0.9 power factor. The generation sources within each plant are summarized in Table 6.4. Furthermore, through observation of Figure 6.11 it can be seen that there is a communication link between the interconnecting block and the decision relays within the generation plants. As illustrated in Figures 6.12 to 6.14, within the generation plants there is a decision relay that reads the information communicated from the interconnecting block stating which generating units are required to be tripped (decided by the regression and PSO algorithm). The decision relay then transmits a trip signal to the circuit breakers for the relevant generating units. The generation sources within the plants couple at a common bus before being converted through a transformer to the voltage of the microgrid.

Table 6.4: Microgrid plant information.

Plant	1	2	3	4	5	6
Type	SM	DFIG	PV	DFIG	PV	SM
Number of units	5	2	5	2	5	5
Unit size (MVA)	0.2	1.5	0.1	1.5	0.5	0.4
Plant Size (MVA)	1	3	0.5	3	2.5	2

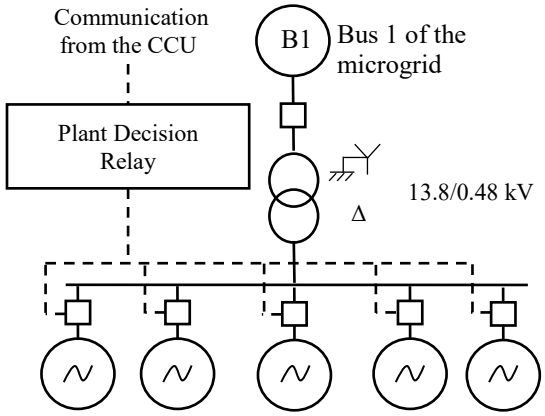

Figure 6.12: Internal connections of a SM-based generation plant connected to bus B1 in the microgrid.

Plant 1 has five 0.2 MVA synchronous generators (SM) operating at a power factor of 0.9. Plant 2 has two 1.5 MVA doubly fed induction generator (DFIG) type wind turbines with a rated wind speed of 11.24 meters per second. Plant 3 has five 0.1 MVA photovoltaic (PV) plants with

a rated irradiance of 1000 W/m^2. Plant 4 has two 1.5 MVA DFIG type wind turbines with the same rating as bus 2. Plant 5 has five 0.5 MVA PV plants with the same rating as bus 2. Plant 6 has five 0.4 MVA synchronous generators with the same operating conditions as bus 1.

The placement of breakers and relays within the microgrid is the same as that specified in Chapter 5. Protection settings will be discussed in subsequent sections of this chapter.

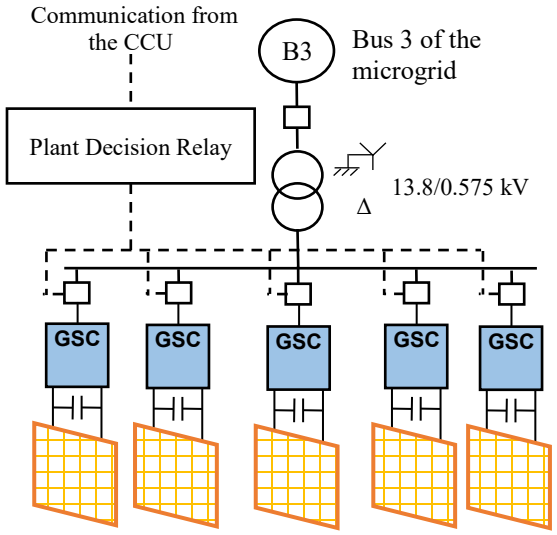

Figure 6.13: Internal connections of a PV based generation plant connected to bus B3 in the microgrid.

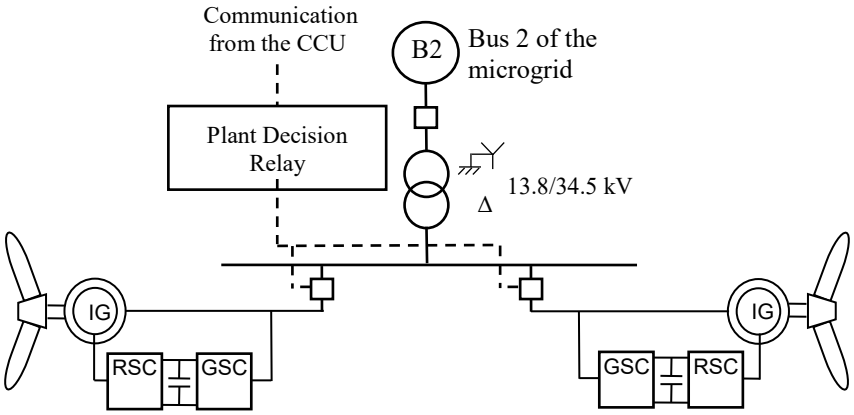

Figure 6.14: Internal connections of a wind based generation plant connected to bus B2 in the microgrid.

6.4.1 Determination of Loss of Coordination Limits

As discussed in Section 3.4.1, reference [47] presents a method for determination of LOC limits for candidate microgrid connection points in distribution networks. The method presented

in reference [47] gives the LOC limit in terms of MVA of the DG unit. In the case of the method specified in Section 6.3, it is necessary for the LOC limit to be determined in terms of fault current as opposed to MVA rating. As such in this chapter, the method discussed in Section 3.4.1 is utilized with a minor change, whereby the LOC limit is expressed in terms of fault current.

For a microgrid integrated into DB2 of the network specified in Figure 6.10, the LOC limit was found to be 438 A and 395 A for phase (three-phase and line-to-line) and ground (line-to-line-to-ground and line-to-ground) faults respectively. This occurs when the fault is located on load L1. It should also be noted that the LOC limit is for an operating voltage of 25 kV.

6.4.2 Microgrid Protection Settings

As discussed, the microgrid protection scheme that is deployed in the system under study is the same as that indicated in Chapter 5. As indicated in Sections 5.4.1 and 5.4.2, buses and lines are protected with differential current relays while load taps are protected using adaptive overcurrent relays. The procedure for determining the settings is as outlined in Chapter 5. It should be noted that the adaptive overcurrent protection relays were not utilized in the studies of this chapter.

As indicated in Table 6.3, the maximum total load expected to be supplied through a line is 3 MVA which gives a current as:

$$I_{Load1} = \frac{3 \times 10^6}{\sqrt{3} \times 13800} = 125.51\ A$$

This would indicate that a CT ratio of 150:5 would be adequate. Low turns ratio CTs can be prone to saturation under high short circuit current conditions [70]. In accordance with IEEE standard C37.110, CTs are required to operate accurately up to 20 times their rated current during short circuit conditions. The maximum short circuit currents experienced by the relays never exceed 2800 A. This would mean that the minimum CT ratio required would be:

$$I_{CT\ min} = \frac{2800}{20} = 140\ A$$

The closest standard CT rating that exceeds the minimum value is 150:5. As such the CT ratio selected is 150:5.

As indicated in discussions in Section 5.3.3.2, the ratings that can be utilized for the differential relays are (note per unit values are on a 5 A base):

$$I_{DIFFPKPMIN} = 0.25\ A = 0.05\ per\ unit$$

$$I_{BREAKPOINT} = 5\ A = 1\ per\ unit$$

$$K1 = 20\%$$

$$K2 = 98\%$$

6.4.3 Training of the Regression Analysis and Particle Swarm Optimization

As discussed, in order for the PRA and PSO algorithm to make accurate predictions, a series of fault data is required. In order to accumulate the necessary data, multiple case studies were conducted for each generation plant.

6.4.3.1 Photovoltaic Plants Fault Analysis Cases

In the case of PV based generation plants, the short circuit current of the DG units are limited by the inverters used in the modules [78] - [79]. As a consequence the fault level output by the PV plants does not exceed a common value for each fault type. As a result, the short circuit output of the PV plant was taken as constant when in operation, or taken as zero when not in operation. For the PV plants, the following short circuit data was obtained through fault analysis simulations and are thus utilized as the fault levels expected from the PV plants:

Table 6.5: PV generation plant fault current information.

Plant	Three-Phase fault current (A)	Line-to-line fault current (A)	Line-to-line-to-ground fault current (A)	Single line-to-ground fault current (A)
3	20	23	45	50
5	83	60	155	165

It should be noted that the PV plants are at their maximum output when the irradiance is 1000 W/m^2.

6.4.3.2 Wind Based Plant Fault Analysis Cases

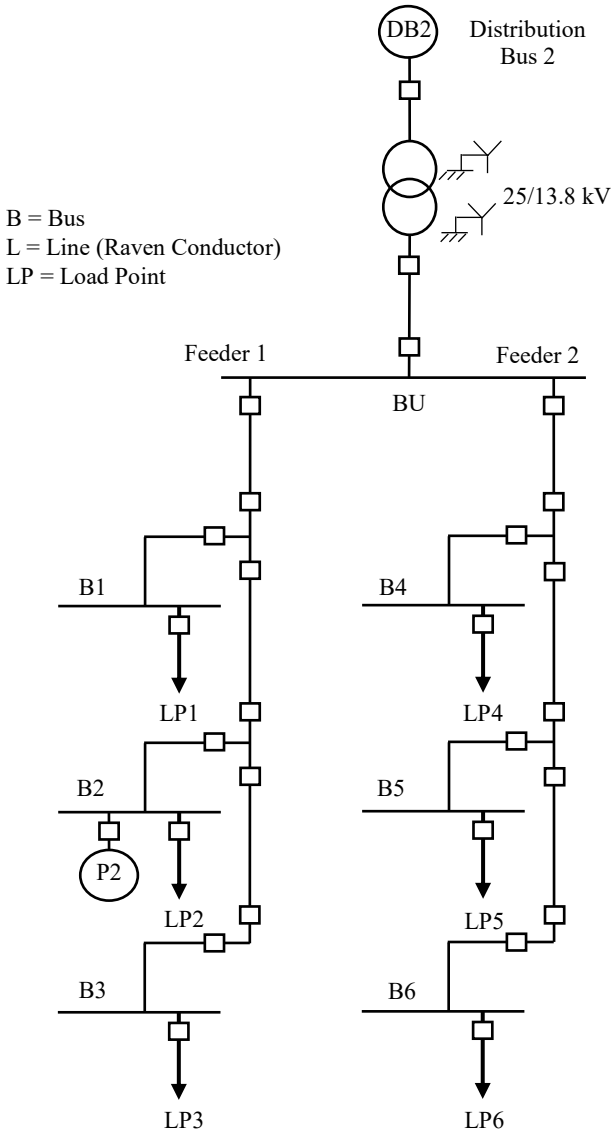

Figure 6.15: Microgrid setup for the maximum short circuit current contribution case for Plant 2.

As indicated in Table 6.4, there are two wind based generation plants in the system under study located at Plant 2 and Plant 4. In order to accumulate the necessary training data, multiple sample short circuit case studies were conducted. The first set of studies conducted were when all generation plants are disconnected except for Plant 2 or 4 depending on which plant is being observed. This is done for all fault types and, as discussed previously, is the maximum short circuit case. The microgrid setup for these cases is shown in Figures 6.15 and 6.16.

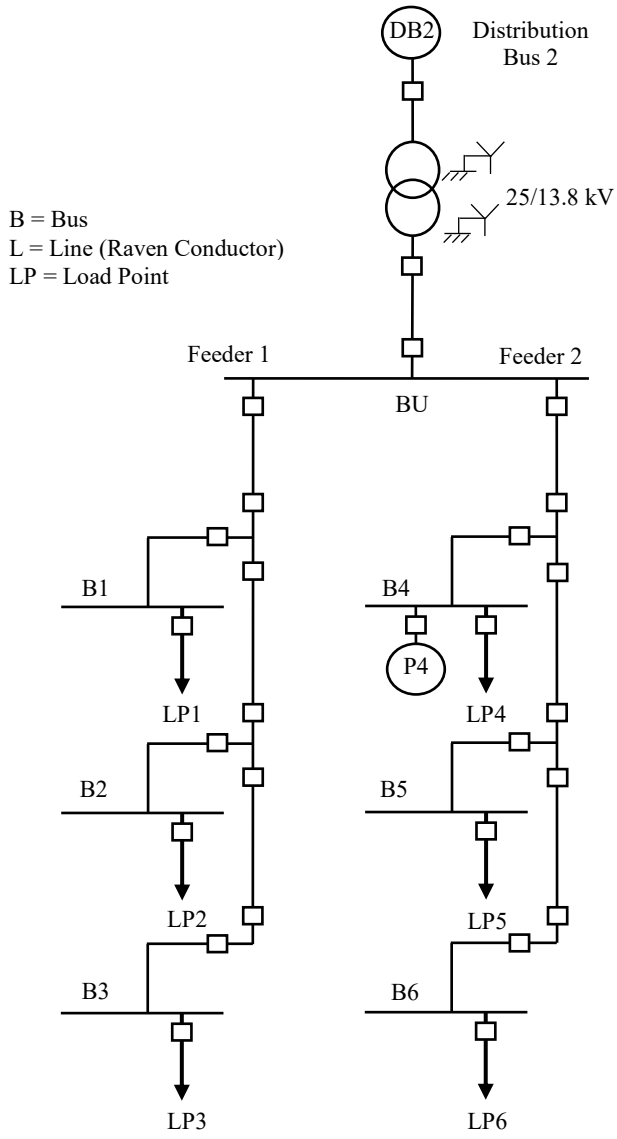

Figure 6.16: Microgrid setup for the maximum short circuit current contribution case for Plant 4.

The short circuit studies are conducted by applying faults of various types at the load L1 in Figure 6.10. The outputs of the generation plants were varied by adjusting the wind speed. Each plant is made up of two 1.5 MVA DFIG wind turbines connected in parallel with one another, as indicated in Figure 6.14, with a rated wind speed of 11.24 meters per second. The wind speeds used in the simulation were 11.24, 11, 10, 9 and 8 meters per second, which vary r_{PW} as defined in Equation 6.8. From each study the percentage penetration was recorded (100% in the maximum penetration case) in conjunction with the short circuit output of the generation plants. The results for the training cases are outlined in Appendix E.1 and E.2.

The second sample case considered is when all the other generation plants are operating at maximum rated output. The only variable that is adjusted is the wind speed. The wind is adjusted again for speeds of 11.24, 11, 10, 9 and 8 meters per second. Results for the training cases are outlined in Appendix E.1 and E.2.

The third sample case study involved inactive PV plants (3 and 5) (i.e. the irradiance is 0 W/m^2) and the SM-based plants (Plants 1 and 6) which are operating at 80% of their rated output. Results for the training cases are outlined in Appendix E.1 and E.2.

The final sample case study considered is when the PV plants (3 and 5) are not operating (i.e. the irradiance is 0 W/m^2) and the SM-based plants (1 and 6) are operating at 60% of their rated output. Results for the training cases are outlined in Appendix E.1 and E.2.

Utilizing the results given in Appendix E.1 and E.2 in conjunction with the procedure outlined in Section 6.3.2, the following maximum short circuit prediction equations are obtained:

$$I_{fr3PP2} = 0.0128(r_{P2})^2 - 1.469(r_{P2}) + 318.16$$

$$I_{frLLP2} = 0.0251(r_{P2})^2 - 2.243(r_{P2}) + 296.17$$

$$I_{frLLGP2} = 0.0171(r_{P2})^2 - 3.278(r_{P2}) + 988.50$$

$$I_{frLGP2} = -0.0011(r_{P2})^2 + 1.011(r_{P2}) + 973.59$$

$$I_{fr3PP4} = 0.0130(r_{P4})^2 - 1.440(r_{P4}) + 318.43$$

$$I_{frLLP4} = 0.0253(r_{P4})^2 - 2.244(r_{P4}) + 298.26$$

$$I_{frLLGP4} = 0.0114(r_{P4})^2 - 2.566(r_{P4}) + 1086.95$$

$$I_{frLGP4} = -0.0003(r_{P4})^2 + 0.827(r_{P4}) + 1111.56$$

The correction coefficient equations are given in the form:

$$\tau_{crtPi} = a_{rtPi}(r_{Pi})^2 + b_{rtPi}(r_{Pi}) + c_{rtPi}$$

$$\gamma_{crtPi} = d_{rtPi}(r_{Pi})^2 + f_{rtPi}(r_{DGi}) + g_{rtPi}$$

$$\varepsilon_{crtPi} = h_{rtPi}(r_{Pi})^2 + k_{rtPi}(r_{Pi}) + m_{rtPi}$$

The corresponding coefficients for the correction coefficient equations are:

Table 6.6: Coefficients for correction coefficient equations for generation plant 2.

Fault Type	Three-Phase	Line-to-Line	Line-to-Line-to-Ground	Line-to-Ground
a	1.5756E-07	-1.5021E-07	4.8098E-07	3.8523E-07
b	-2.1432E-05	2.3834E-05	-6.3758E-05	-5.0521E-05
c	6.7719E-04	-9.4261E-04	2.2646E-03	1.8419E-03
d	-2.9774E-05	2.9067E-05	-8.6526E-05	-6.8977E-05
f	4.2680E-03	-4.6184E-03	1.1717E-02	9.2214E-03
g	-1.3867E-01	1.8673E-01	-4.1090E-01	-3.2841E-01
h	1.4022E-03	-1.4051E-03	3.8428E-03	3.0451E-03
k	-2.1253E-01	2.2358E-01	3.8428E-03	-4.1691E-01
m	8.0967E+00	-8.2509E+00	3.8428E-03	1.5421E+01

Table 6.7: Coefficients for correction coefficient equations for generation plant 4.

Fault Type	Three-Phase	Line-to-Line	Line-to-Line-to-Ground	Line-to-Ground
a	1.0254E-07	-1.5021E-07	4.8098E-07	3.8523E-07
b	-1.3039E-05	2.3834E-05	-6.3758E-05	-5.0521E-05
c	4.3112E-04	-9.4261E-04	2.2646E-03	1.8419E-03
d	-1.7795E-05	2.9067E-05	-8.6526E-05	-6.8977E-05
f	2.3828E-03	-4.6184E-03	1.1717E-02	9.2214E-03
g	-7.7390E-02	1.8673E-01	-4.1090E-01	-3.2841E-01
h	7.5369E-04	-1.4051E-03	3.8428E-03	3.0451E-03
k	-1.0788E-01	2.2358E-01	3.8428E-03	-4.1691E-01
m	4.4271E+00	-8.2509E+00	3.8428E-03	1.5421E+01

These corrected coefficient equations are utilized in Equation 6.16 which is expressed as:

$$RA_{cprtPi} = \tau_{crtPi}(PEN_{rPi})^2 + \gamma_{crtPi}(PEN_{rPi}) + \varepsilon_{crtPi}$$

This gives a predicted short circuit current equation in the form:

$$I_{fprtPi} = I_{frtPi} \times RA_{cprtPi}$$

Note that all graphs and derivation of equations is outlined in Appendix E.5 and E.6.

6.4.3.3 Biogas Synchronous Machine Based Plant Fault Analysis Cases

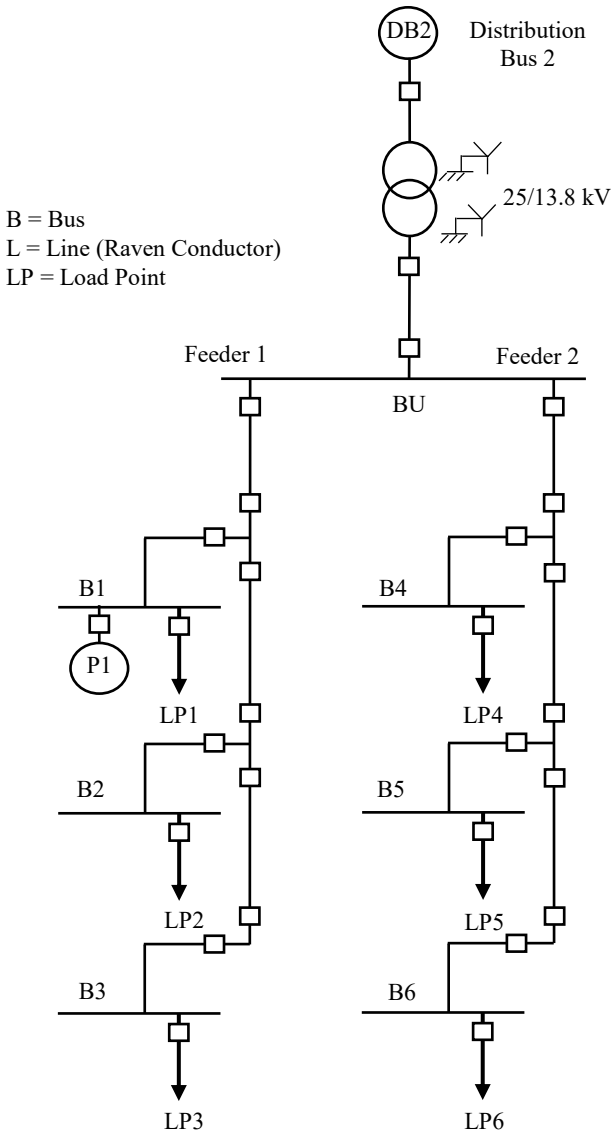

Figure 6.17: Microgrid setup for the maximum short circuit current contribution case for Plant 1.

As indicated in Table 6.4, there are two generation plants in the system under study, located at Plant 1 and Plant 6. In order to accumulate the necessary training data, multiple sample short circuit case studies were conducted. In the first set of studies conducted, all generation plants are disconnected except for Plant 1 or 6, depending on which plant is being observed. This is done for all fault types and, as discussed previously, is the maximum short circuit case. The microgrid setup for these cases is expressed in Figures 6.17 and 6.18.

The short circuit studies are conducted by applying faults of various types at load L1 in Figure 6.10. In addition, the output of the generation plants are varied. Each plant is made up of five synchronous generators (rated at 0.2 MVA and 0.4 MVA for Plant 1 and 6 respectively) connected in parallel with one another as indicated in Figure 6.12. The percentage ratings used (r_{PSM}) in simulation are 100%, 90%, 80%, 70% and 60%. From each study the percentage penetration was recorded (100% in the maximum penetration case) in conjunction with the short circuit output of the generation plants. The results for the training cases are outlined in Appendix E.3 and E.4.

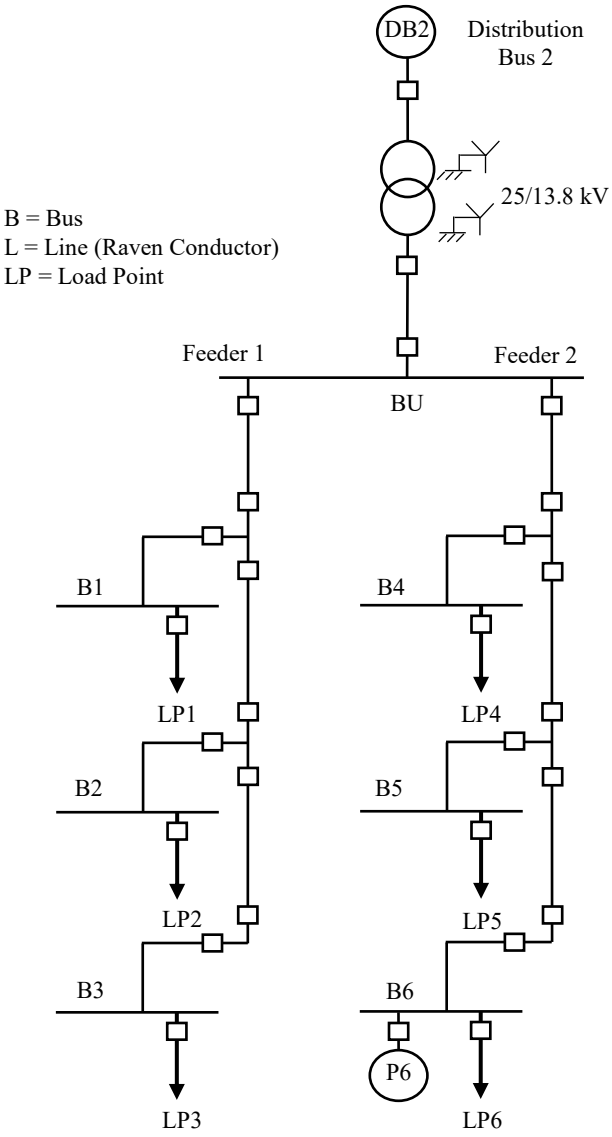

Figure 6.18: Microgrid setup for the maximum short circuit current contribution case for Plant 6.

The second sample case considered is when all the other generation plants are operating at maximum rated output. The only variable that is adjusted is the percentage output. The percentage ratings used (r_{PSM}) in simulation are 100%, 90%, 80%, 70% and 60%. Again, results for the training cases are outlined in Appendix E.3 and E.4.

The third sample case study considered is when the PV plants (Plants 3 and 5) are not operating (i.e. the irradiance is 0 W/m^2) and the wind based plants (Plants 2 and 4) are operating at a wind speed of 10 meters per second. Results for the training cases are outlined in Appendix E.3 and E.4.

The final sample case study considered is when the PV plants (Plants 3 and 5) are not operating (i.e. the irradiance is 0 W/m^2) and the wind based plants (Plants 2 and 4) are operating at a wind speed of 10 meters per second, but have one turbine disconnected (i.e. operating at 50% capacity of the plant but 100% capacity of a single turbine). Results for the training cases are outlined in Appendix E.3 and E.4.

Utilizing the results given in Appendix E.3 and E.4 in conjunction with the procedure outlined in Section 6.3.2, the following maximum short circuit prediction equations are obtained:

$$I_{fr3PP1} = -0.00012(r_{P1})^2 + 0.199(r_{P1}) + 188.29$$

$$I_{frLLP1} = -0.0006(r_{P1})^2 + 0.394(r_{P1}) + 178.43$$

$$I_{frLLGP1} = 0.0083(r_{P1})^2 - 0.874(r_{P1}) + 608.43$$

$$I_{frLGP1} = 0.0025(r_{P1})^2 + 0.182(r_{P1}) + 583.29$$

$$I_{fr3PP6} = 0.0057(r_{P6})^2 - 0.179(r_{P6}) + 329.50$$

$$I_{frLLP6} = 0.0077(r_{P6})^2 - 0.302(r_{P6}) + 309.64$$

$$I_{frLLGP6} = -0.0026(r_{P6})^2 + 1.017(r_{P6}) + 532.14$$

$$I_{frLGP6} = 0.0058(r_{P6})^2 + 0.001(r_{P6}) + 587.29$$

The correction coefficient equations are given in the form:

$$\tau_{crtPi} = a_{rtPi}(r_{Pi})^2 + b_{rtPi}(r_{Pi}) + c_{rtPi}$$

$$\gamma_{crtPi} = d_{rtPi}(r_{Pi})^2 + f_{rtPi}(r_{DGi}) + g_{rtPi}$$

$$\varepsilon_{crtPi} = h_{rtPi}(r_{Pi})^2 + k_{rtPi}(r_{Pi}) + m_{rtPi}$$

The corresponding coefficients for the correction coefficient equations are:

Table 6.8: Coefficients for correction coefficient equations for generation plant 1.

Fault Type	Three-Phase	Line-to-Line	Line-to-Line-to-Ground	Line-to-Ground
a	-1.6939E-10	-1.5021E-07	4.8098E-07	3.8523E-07
b	-7.4012E-07	2.3834E-05	-6.3758E-05	-5.0521E-05
c	2.0748E-05	-9.4261E-04	2.2646E-03	1.8419E-03
d	-7.1212E-08	2.9067E-05	-8.6526E-05	-6.8977E-05
f	1.0996E-04	-4.6184E-03	1.1717E-02	9.2214E-03
g	-1.6388E-03	1.8673E-01	-4.1090E-01	-3.2841E-01
h	8.6804E-06	-1.4051E-03	3.8428E-03	3.0451E-03
k	-3.5758E-03	2.2358E-01	3.8428E-03	-4.1691E-01
m	9.5567E-01	-8.2509E+00	3.8428E-03	1.5421E+01

Table 6.9: Coefficients for correction coefficient equations for generation plant 6.

Fault Type	Three-Phase	Line-to-Line	Line-to-Line-to-Ground	Line-to-Ground
a	7.3274E-09	-1.5021E-07	4.8098E-07	3.8523E-07
b	-8.7461E-07	2.3834E-05	-6.3758E-05	-5.0521E-05
c	1.9336E-05	-9.4261E-04	2.2646E-03	1.8419E-03
d	-1.1175E-06	2.9067E-05	-8.6526E-05	-6.8977E-05
f	1.4564E-04	-4.6184E-03	1.1717E-02	9.2214E-03
g	-3.0666E-03	1.8673E-01	-4.1090E-01	-3.2841E-01
h	3.8104E-05	-1.4051E-03	3.8428E-03	3.0451E-03
k	-5.7563E-03	2.2358E-01	3.8428E-03	-4.1691E-01
m	7.3274E-09	-1.5021E-07	4.8098E-07	3.8523E-07

These corrected coefficient equations are utilized in Equation 6.16 which is expressed as:

$$RA_{cprtPi} = \tau_{crtPi}(PEN_{rPi})^2 + \gamma_{crtPi}(PEN_{rPi}) + \varepsilon_{crtPi}$$

This gives a predicted short circuit current equation in the form:

$$I_{fprtPi} = I_{frtPi} \times RA_{cprtPi}$$

Note that all graphs and derivation of equations is outlined in Appendix E.7 and E.8.

6.4.4 PSO and Protection Settings

A critical component within the proposed scheme is the integration of a direction sensing unit. The directional components of the relay are discussed in Section 1.2.2. Considering that the interconnecting transformer between the microgrid and the utility is a double grounded wye (i.e. has a zero sequence source) and is considered to be a main feeder, the directional protection settings are selected to be:

- Relay connection angle: 90 degrees.
- Relay characteristic angle: 30 degrees.

The next characteristic setting required is the penalty factor associated with the LOC limit within the PSO algorithm. As per discussions in Section 6.3.3, the penalty factor u_1 is 1000 when the corrected LOC limit is exceeded; otherwise it is zero. The corrected LOC limit is 90% of the actual LOC limit. Given that the LOC limits determined in Section 6.4.1 are 438 A and 395 A, the corrected LOC limits are 394 A and 356 A for phase and ground faults respectively. As indicated in Figure 6.10, the interconnecting transformer has a voltage of 25 kV on the utility side and 13.8 kV on the microgrid side. This means that the LOC limit would be 794 A and 716 A for the phase and ground faults respectively when referred to the microgrid side. The corresponding corrected LOC limits are 714 A and 644 A for phase and ground faults respectively. As indicated in Figure 6.11, the interconnecting block is located on the utility side of the interconnecting transformer. This means that the corrected LOC limit input into the interconnecting block is required to be referred to the utility side of the transformer. As such, the following setting for the penalty factor is used:

- u_1 = 1000 when $I_{SCphase} \geq$ 394 A or $I_{SCground} \geq$ 356A.
- u_1 = 0 otherwise.

For the penalty factor u_2, the generation plants are assigned a disconnection value. For plants 1, 3, 5 and 6, when a generating unit is disconnected $PR_{Pi} \times N_{Pi}$ increases by one. For example for Plant 1 (five units within the plant) when the PSO algorithm requires two units to be disconnected, $PR_{P1} \times N_{P1}$ would be equal to two.

In the case of Plants 2 and 4, there are two large wind turbines that are in service. In order to account for the wind farms greater effect, the disconnection value is higher. When one turbine is disconnected $PR_{PW} \times N_{PW}$ is equal to two (where W in this context represents wind plants 2 or 4). When two turbines are disconnected $PR_{PW} \times N_{PW}$ is equal to minus one (i.e. $5\text{-}PR_{PW} \times N_{PW} = 6$).

As discussed in Section 1.5, some variables within the PSO algorithm require initial settings. In the case of this thesis the PSO algorithm utilizes the following standard settings:

- $c_1 = c_2 = 2$, also $c_1 + c_2 = 4$
- $\omega_0 = 1$
- $\alpha = 0.98$
- r_1 and r_2 are uniformly distributed random numbers in the range from 0 to 1.
- The function is the same as those specified in Equations 6.22 and 6.23.

6.4.5 Application of the Proposed Scheme to Mitigate Microgrid Influences on Existing Overcurrent Protection

One full case study is presented in this section to demonstrate the efficacy of the proposed scheme for mitigation of microgrid short circuit influences on existing network fuse-recloser coordination. The full case study includes simulation of multiple fault types, including a case where the fault occurs within the microgrid. The case studies showcase the capability of the proposed scheme to manage microgrid penetrations beyond the LOC limit of individual feeders. The details of the case studies are expressed in Table 6.10.

It should be noted that the bus voltages within the microgrid are all above 0.95 per unit when no generation sources are connected and the load is supplied purely by the utility connection. The per unit voltages are given in Table 6.11.

Table 6.10: Case studies.

	Case Study-1	Case Study-2	Case Study-3	Case Study-4	Case Study-5
Fault type	Three-phase	Line-to-Line	Line-to-Line-to-Ground	Line-to-Ground	Line-to-Line-to-Ground
Fault location	Load L1				Line 1 in the microgrid
Fault inception	1 second of simulation time				
Fault duration	Sustained fault				
microgrid connection point	At distribution bus 2 (DB2)				
SM-based plant operating point (% of rated)	100				
Wind speed (m/s)	11.24				
Irradiance (W/m^2)	1000				

Table 6.11: Per unit microgrid bus voltages without any generation sources.

Bus	1	2	3	4	5	6	Interconnection
Voltage (per unit)	0.97	0.955	0.95	0.966	0.955	0.95	0.971

Through use of Equations 6.8 to 6.13, the PRA algorithm programmed into the interconnecting block's CCU can determine the percentage penetrations of each generation plant. Through observation of Figure 6.19 the percentage penetrations can be determined as such:

$$PEN_{P1} = \frac{42}{42+126+8.3} \times 100 = 23.82\%$$

$$PEN_{P2} = \frac{126}{42+126+8.3} \times 100 = 71.47\%$$

$$PEN_{P3} = \frac{8.3}{42+126+8.3} \times 100 = 4.71\%$$

$$PEN_{P4} = \frac{126}{126+43+82} \times 100 = 50.20\%$$

$$PEN_{P5} = \frac{43}{126+43+82} \times 100 = 17.13\%$$

$$PEN_{P6} = \frac{82}{126+43+82} \times 100 = 32.67\%$$

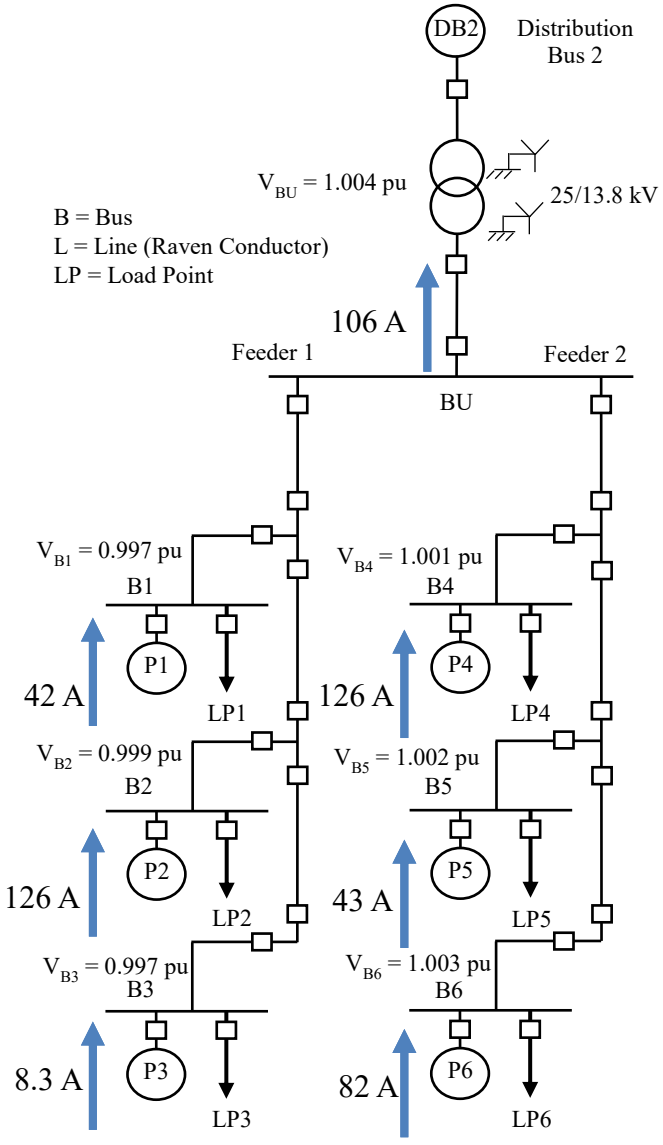

Figure 6.19: Pre-fault plant and microgrid current flows with per unit bus voltages for case studies 1 to 5.

Furthermore, observation of Figure 6.19 makes it apparent that the bus voltages increased when generation sources are integrated into the microgrid.

Through the utilization of Equations 6.14 to 6.16, it is apparent that the percentage ratings of each generation plant for the case studies presented in Table 6.10 are 100%. This means that the inputs given to the PSO algorithm are as such:

Table 6.12: Inputs for the proposed scheme for case studies 1 to 5.

Generation Plant	1	2	3	4	5	6
PEN_{Pi} (%)	23.82	71.47	4.71	50.20	17.13	32.67
R_{Pi} (%)	100	100	100	100	100	100

These initial conditions are input into the PRA and PSO algorithm programmed into the interconnecting block's CCU, resulting in the following predicted short circuit contribution generations:

Table 6.13: Predicted generation plant short circuit contributions for case studies 1 to 5.

Generation Plant	1	2	3	4	5	6
Three-phase fault current (A)	178	221	20	214	83	344
Line-to-Line fault current (A)	194	276	23	288	60	356
Line-to-Line-to-ground fault current (A)	195	467	45	538	155	362
Line-to-Ground fault current (A)	272	635	50	861	165	318

Table 6.14: Predicted overall microgrid short circuit contributions for case studies 1 to 5.

Fault type	Three-Phase	Line-to-Line	Line-to-Line-to-Ground	Line-to-Ground
Fault current (A)	1060	1197	1762	2301

Utilizing the analysis discussed in this chapter, the PSO algorithm determines the generating sources within the plants that are required to trip, such that mitigation of their short circuit effects on the utility occur following fault inception. The following results are obtained:

Table 6.15: Outputs from the proposed scheme's PSO for case studies 1 to 5.

Generating Plant	1	2	3	4	5	6
Number of generators to trip (phase)	0	2	0	2	0	0
Number of generators to trip (ground)	2	2	0	2	0	2

As a result of the DG sources being tripped, as indicated in Table 6.13, the short circuit contributions from the microgrid to the main utility are expected to decrease to the levels indicated in Table 6.16.

Table 6.16: Predicted overall microgrid short circuit contributions for case studies 1 to 5 following source tripping.

Fault type	Three-Phase	Line-to-Line	Line-to-Line-to-Ground	Line-to-Ground
Fault current (A)	669	652	623	638

It should be noted that the values expressed in Table 6.13 to Table 6.16 are measured on the 13.8 kV side of the interconnecting transformer. It should also be noted that the case studies presented are not the only results accumulated. Further studies are presented in Appendix F. Note that all values are stated in RMS unless otherwise specified.

6.4.5.1 Case Study-1

In Case Study-1, all the generating plants are operating at their maximum condition when a three-phase fault is applied to Load L1 within the utility network. As such this is a phase fault and as indicated in Table 6.15, two generating units are required to be tripped in plants 2 and 4. The short circuit contributions measured for the generating sources during the three-phase fault but before source tripping is given in Figure 6.20.

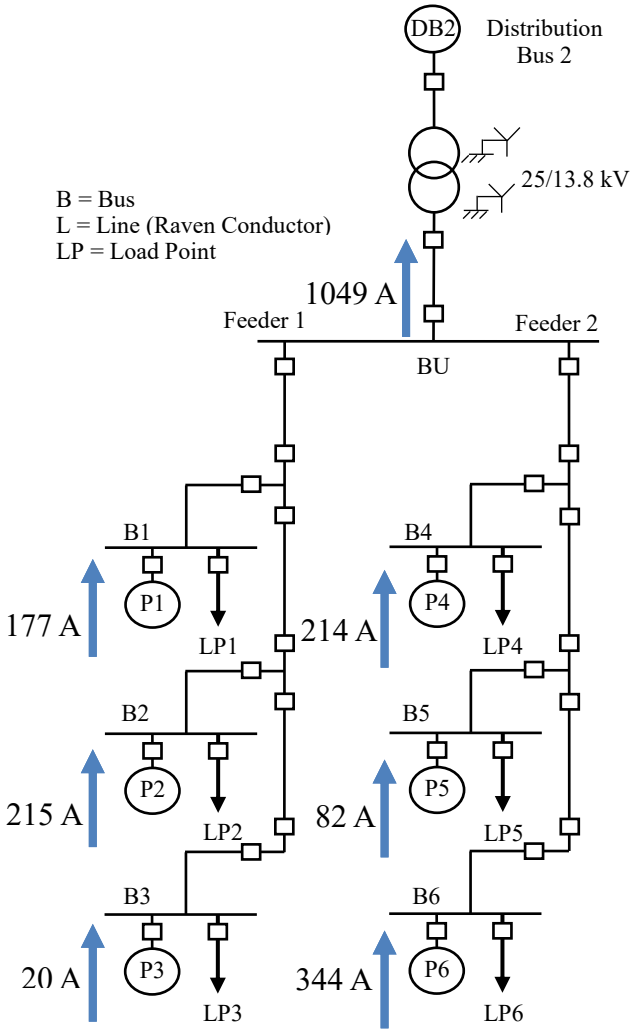

Figure 6.20: Plant and microgrid current flows for Case Study-1 during a three-phase fault before source tripping.

Comparison of short circuit contributions measured in Figure 6.20 with predicted contributions in Tables 6.13 and 6.14 result in the following percentage discrepancies between predicted and measured values:

Table 6.17: Percentage difference between measured and actual fault currents for Case Study-1.

Generating Plant	1	2	3	4	5	6	Overall Microgrid
Percentage difference (%)	0.56	2.71	0	0	1.20	0	1.03

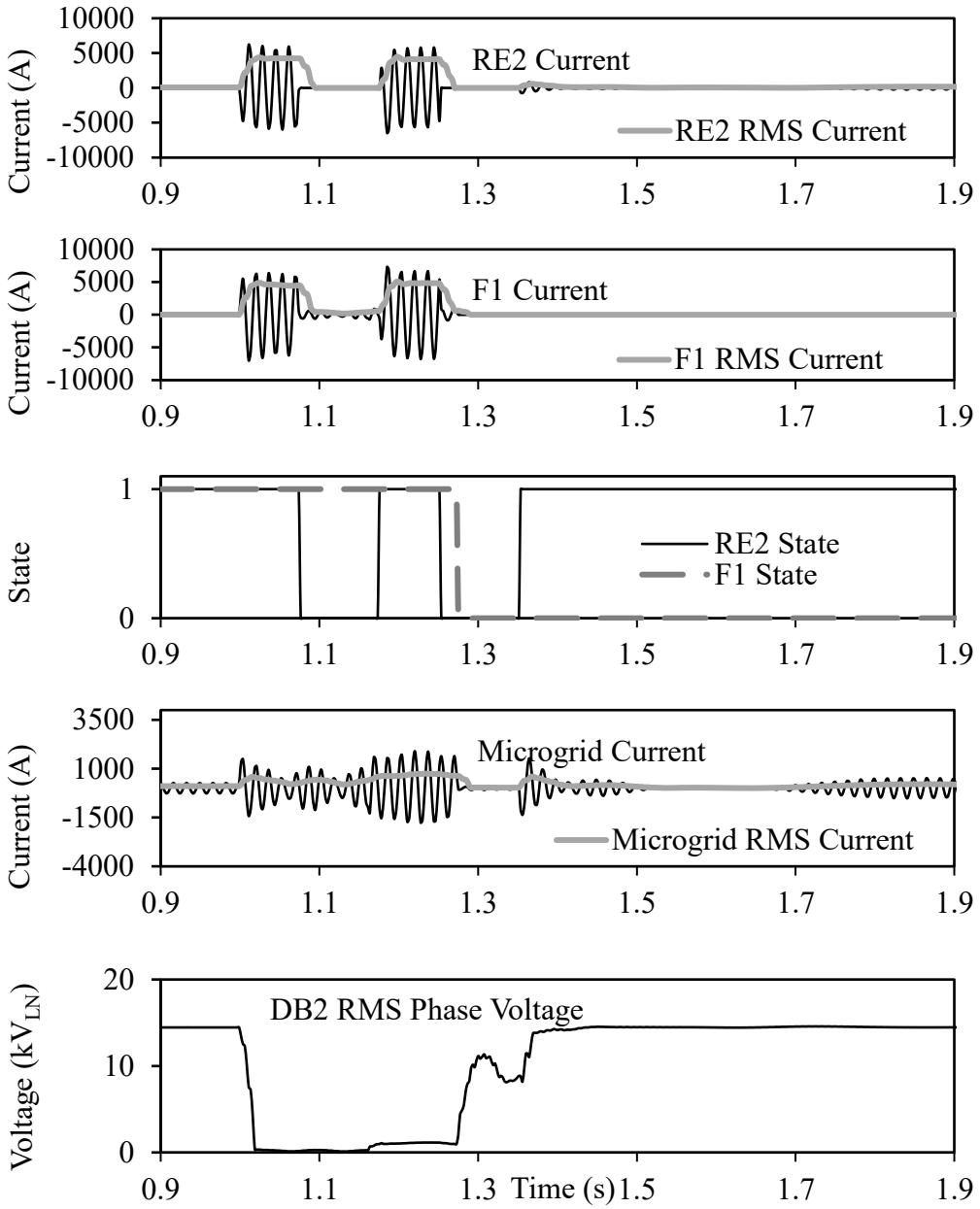

Figure 6.21: Case Study-1 without the proposed scheme: RE2 current, F1 current, RE2 and F1 state signals, microgrid grid current and DB2 RMS phase voltage.

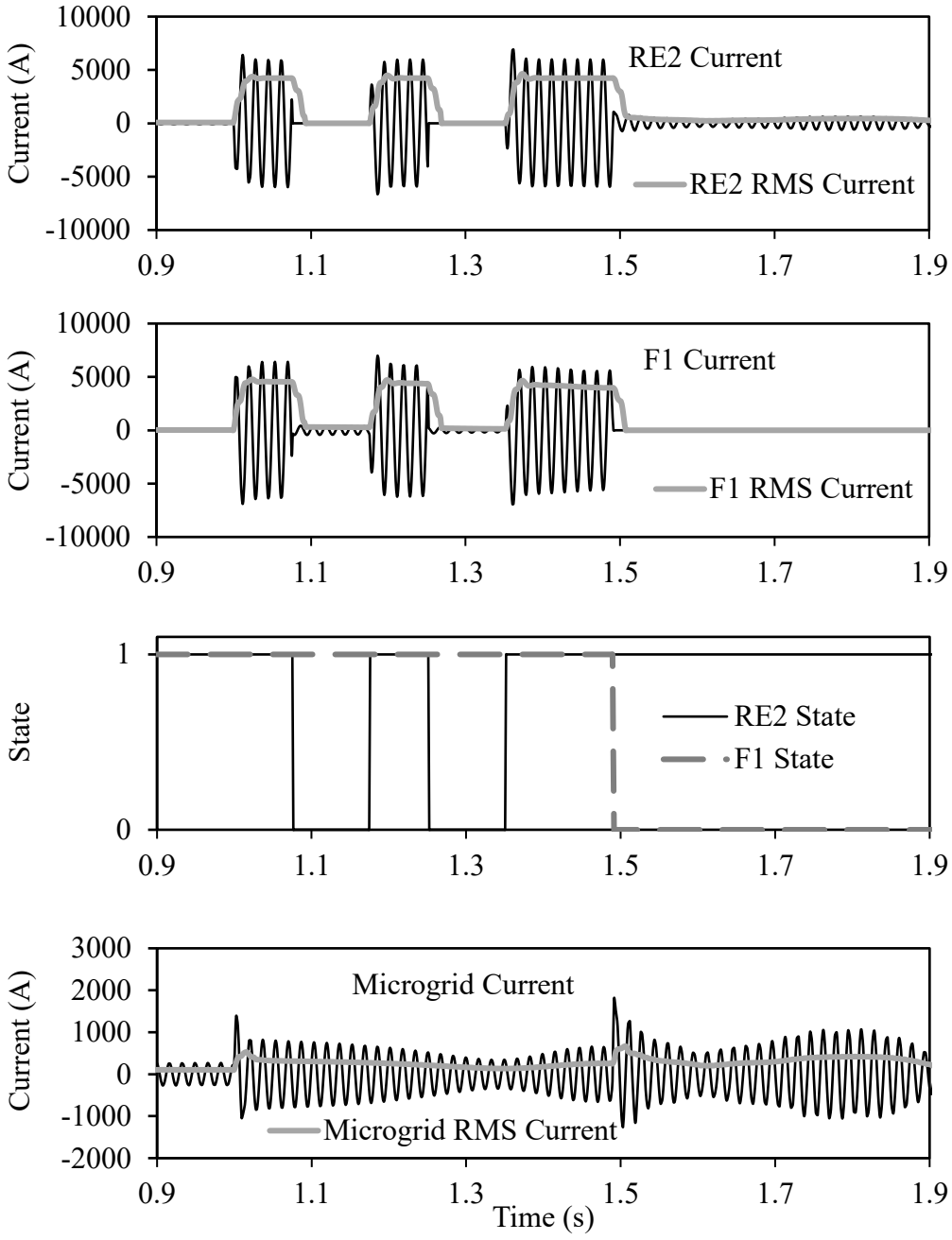

Figure 6.22: Case Study-1 with the proposed scheme: RE2 current, F1 current, RE2 and F1 state signals, microgrid grid current.

Figure 6.21 presents Case Study-1 for the condition where there is a microgrid connected at DB2 without the proposed scheme implemented. The short circuit contribution from the microgrid is 1049 A, exceeding the phase LOC limit of 793 A referred to the 13.8 kV side of the interconnecting transformer. Consequentially, the utility head end recloser (RE2) operates twice,

with the fuse (F1) melting before the second reclose occurs. As such, it is apparent that the coordination between RE2 and F1 is lost. Furthermore, it can be seen that the current contribution from the microgrid peaks at 1491 A_{peak} before dissipating to 1144 A_{peak} after one cycle. Figures 6.22 and 6.23 present Case Study-1 for the condition where there is a microgrid connected at DB2 with the proposed scheme implemented. As indicated in Table 6.15, two generating units require tripping in plants 1, 2, 4 and 6 in order to restore coordination.

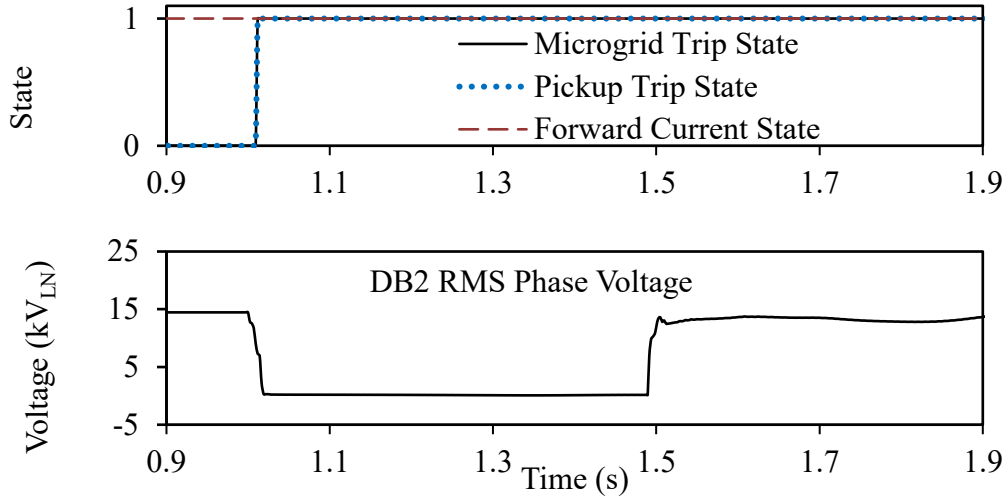

Figure 6.23: Case Study-1 with the proposed scheme: interconnecting relay states, DB2 RMS phase voltage.

As can be observed in Figures 6.22 and 6.23, during the steady-state condition the microgrid has a net current flow towards the utility grid that is maintained once the fault occurs. This means that the proposed scheme is allowed to continue if pickup levels are exceeded. Following the inception of a fault, the contribution of current from the microgrid to the utility increases until it exceeds the pickup current. At a simulation time of 1.0117 seconds (0.0117 seconds after fault inception), the proposed scheme notifies generating plants 2 and 4 to disconnect two sources each. At this point the microgrid short circuit current reduces to 672 A. As per Table 6.16, the PSO algorithm predicted a short circuit current of 669 A to be present following source disconnection. This means that the actual short circuit current was only 0.45% different than the predicted value, highlighting the efficacy of the prediction algorithm. It can also be seen that the current contribution from the microgrid peaks at 1375 A_{peak} before dissipating to 795 A_{peak} after one cycle when the proposed scheme is implemented. Further observation of Figure 6.22 makes it apparent that the system regains coordination between RE2

and F1, demonstrating the capacity of the proposed scheme to restore coordination to the system without limiting the microgrid penetration.

6.4.5.2 Case Study-2

In Case Study-2, all generating plants are operating in their maximum condition when a line-to-line fault is applied to DB1 within the utility network. This is a phase fault and, as indicated in Table 6.15, two generating units are required to be tripped in plants 2 and 4.

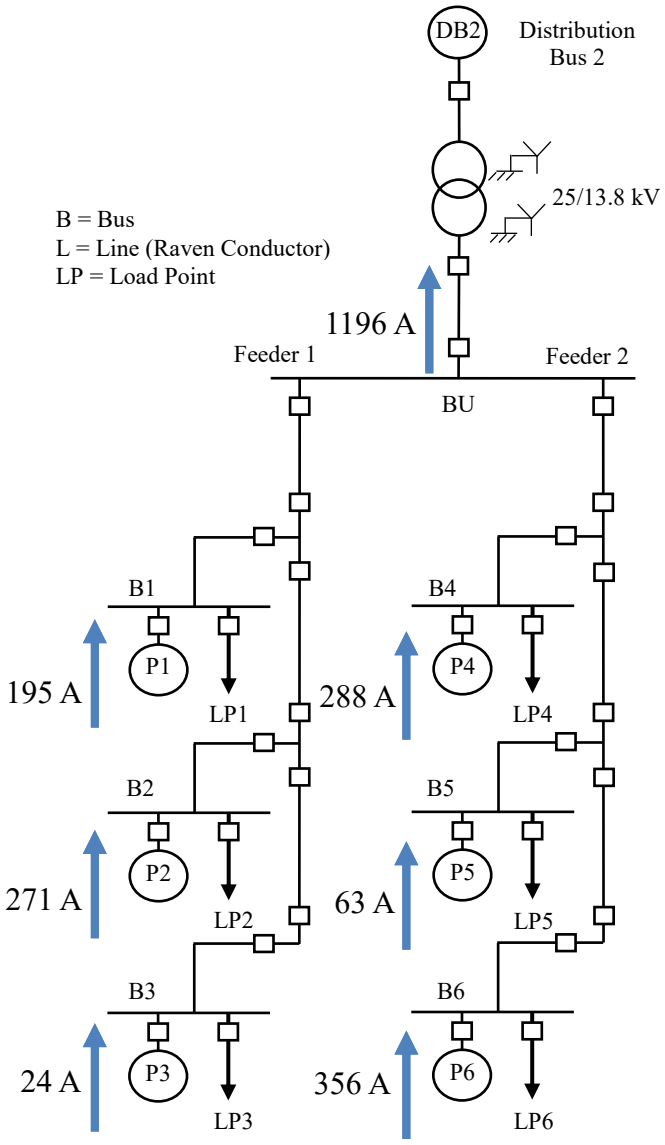

Figure 6.24: Plant and microgrid current flows for Case Study-2 during a line-to-line fault before source tripping.

The short circuit contributions measured for the generating sources during the line-to-line fault before source tripping is given in Figure 6.24. Comparison of short circuit contributions measured in Figure 6.24 with predicted contributions in Tables 6.13 and 6.14 result in the following percentage discrepancies between predicted and measured values:

Table 6.18: Percentage difference between measured and actual fault currents for Case Study-2.

Generating Plant	1	2	3	4	5	6	Overall Microgrid
Percentage difference (%)	0.51	1.81	4.34	0	5.00	0	0.08

As can be seen in Table 6.18, predicted short circuit levels are accurate when compared to actual measured values. Figures 6.25 and 6.26 presents Case Study-2 for the condition where there is a microgrid connected at DB2 without the proposed scheme implemented.

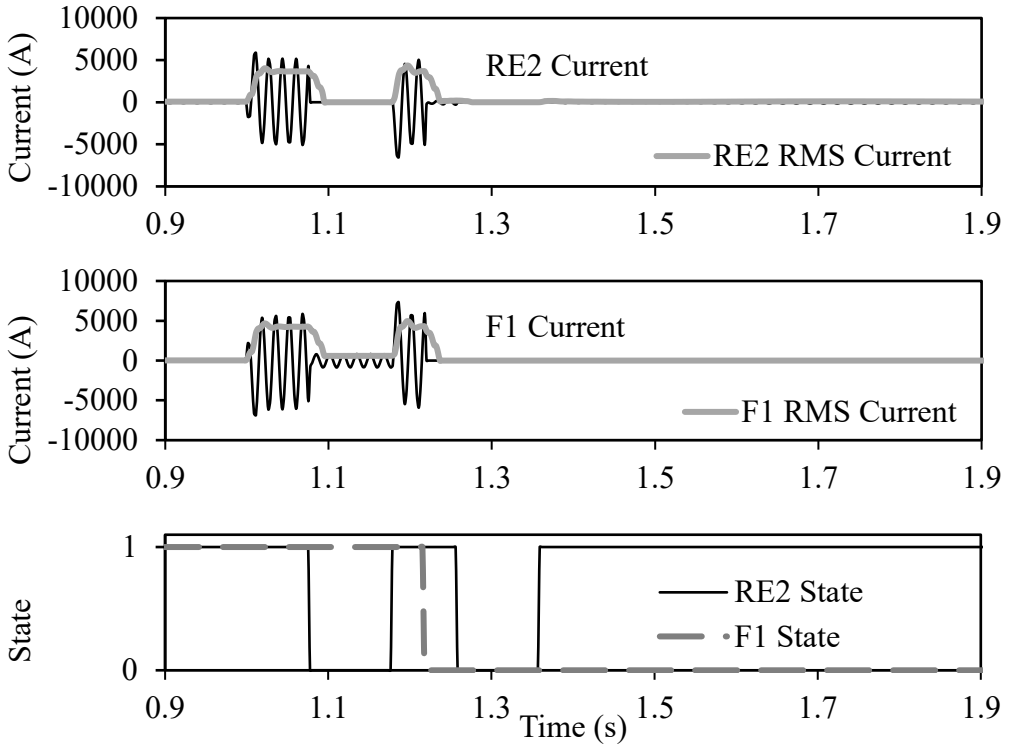

Figure 6.25: Case Study-2 without the proposed scheme: RE2 current, F1 current, RE2 and F1 state signals.

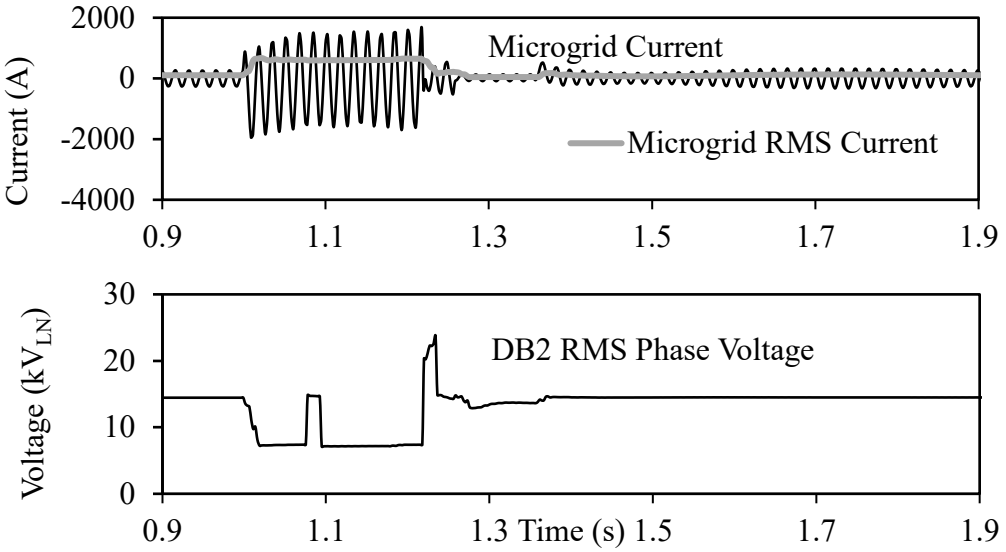

Figure 6.26: Case Study-2 without the proposed scheme: microgrid grid current and DB2 RMS phase voltage.

The short circuit contribution from the microgrid is 1196 A, exceeding the phase LOC limit of 793 A referred to the 13.8 kV side of the interconnecting transformer. Consequentially, the utility head end recloser (RE2) operates once with the fuse (F1) melting before the second trip from the recloser occurs. It is apparent that the coordination between RE2 and F1 is lost. It can also be seen that the current contribution from the microgrid peaks at 1945 A_{peak} before dissipating to1842 A_{peak} after one cycle.

Figures 6.27 and 6.28 present Case Study-2 for the condition where there is a microgrid connected at DB2 with the proposed scheme implemented. As per Table 6.15, two generating units must be tripped in plants 2 and 4 in order to restore coordination between RE2 and F1.

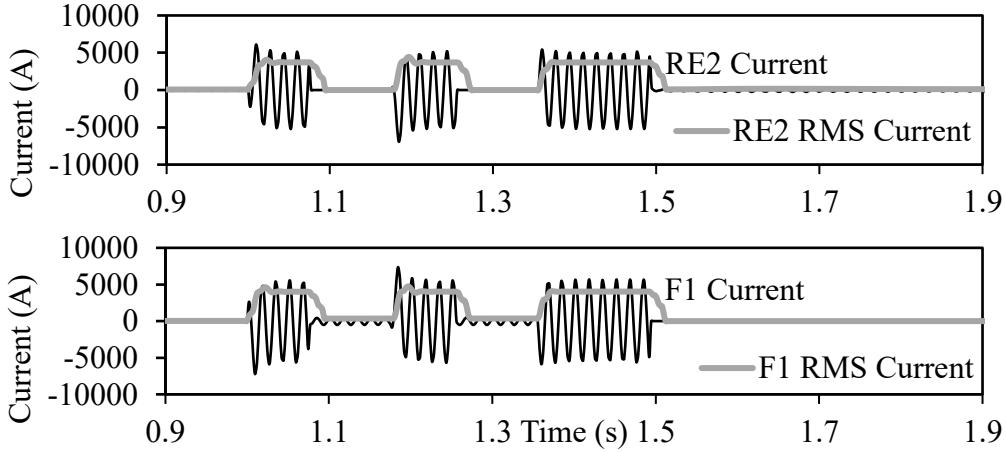

Figure 6.27: Case Study-2 with the proposed scheme: RE2 current, F1 current.

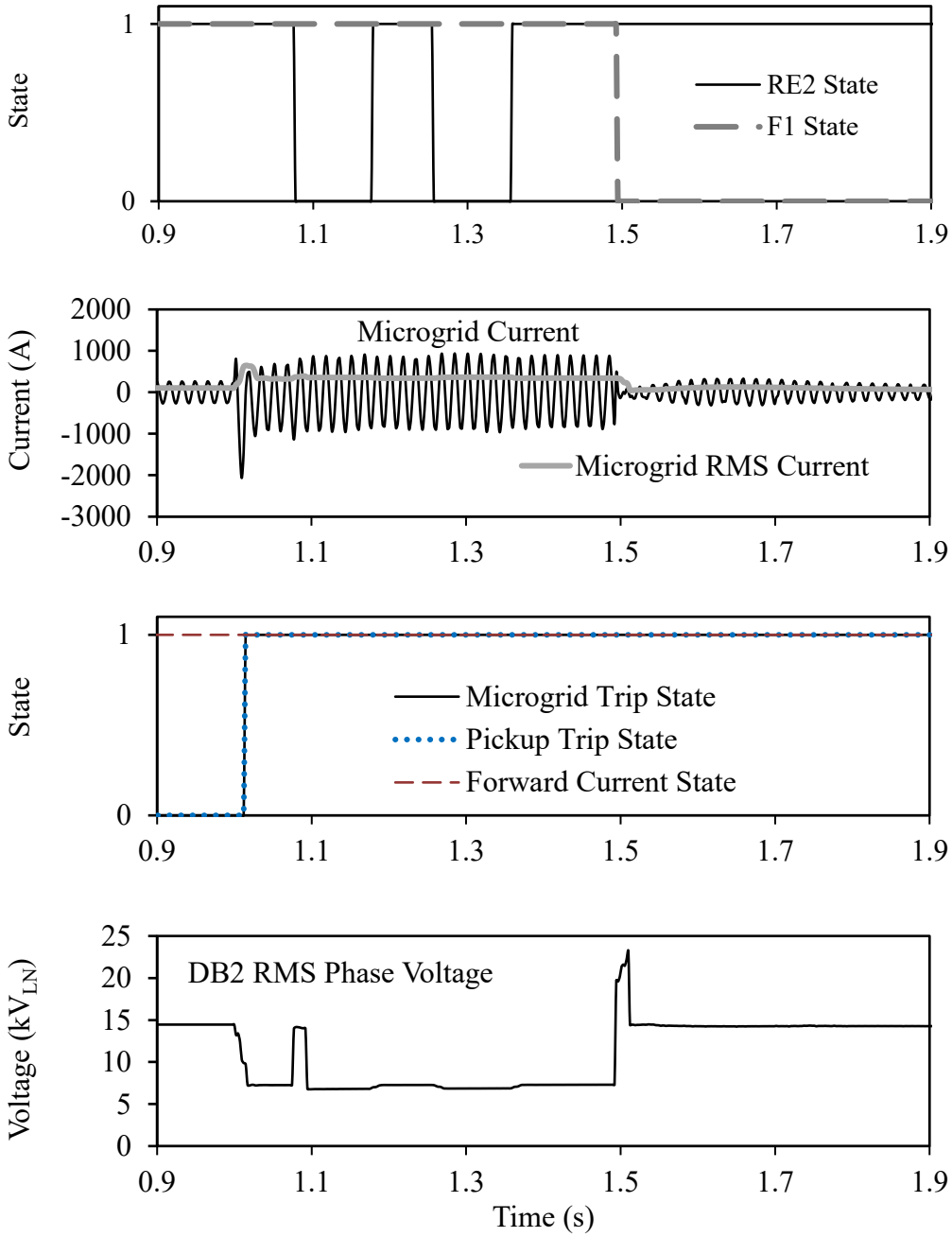

Figure 6.28: Case Study-2 with the proposed scheme: RE2 and F1 state signals and microgrid grid current, interconnecting relay states, DB2 RMS phase voltage.

As can be observed in Figures 6.27 and 6.28, during the steady-state condition the microgrid has a net current flow towards the utility grid that is maintained once the fault occurs. The result is that the proposed scheme can continue if pickup levels are exceeded. Following the inception of a fault, the contribution of current from the microgrid to the utility increases until it

exceeds the pickup current. At a simulation time of 1.0146 seconds (0.0146 seconds after fault inception), the proposed scheme notifies plants 2 and 4 to disconnect two sources each. At this point the microgrid short circuit current reduces to 651 A. As per Table 6.16, the PSO algorithm predicted a short circuit current of 652 A to be present following source disconnection. This means that there was only a 0.15% differential between the actual short circuit current and the predicted value, highlighting the efficacy of the prediction algorithm. It can also be seen that the current contribution from the microgrid peaks at 1866 A_{peak} before dissipating to 1055 A_{peak} after one cycle when the proposed scheme is implemented. Further observation of Figures 6.27 and 6.28 makes it apparent that the system regains coordination between RE2 and F1, demonstrating the capacity of the proposed scheme to restore coordination to the system without limiting the microgrid penetration.

6.4.5.3 Case Study-3

In Case Study-3, all generating plants are operating in their maximum condition when a line-to-line-to-ground fault is applied to load L1 within the utility network. This is a ground fault and, as indicated in Table 6.15, two generating units are to be tripped in plants 1, 2, 4 and 6.

The short circuit contributions measured for the generating sources during the double line-to-ground fault before source tripping are given in Figure 6.29. Comparison of short circuit contributions measured in Figure 6.29 with predicted contributions in Tables 6.13 and 6.14; result in the following percentage discrepancies between predicted and measured values:

Table 6.19: Percentage difference between measured and actual fault currents for Case Study-3.

Generating Plant	1	2	3	4	5	6	Overall Microgrid
Percent difference (%)	2.05	1.07	2.22	1.11	3.22	0.82	2.15

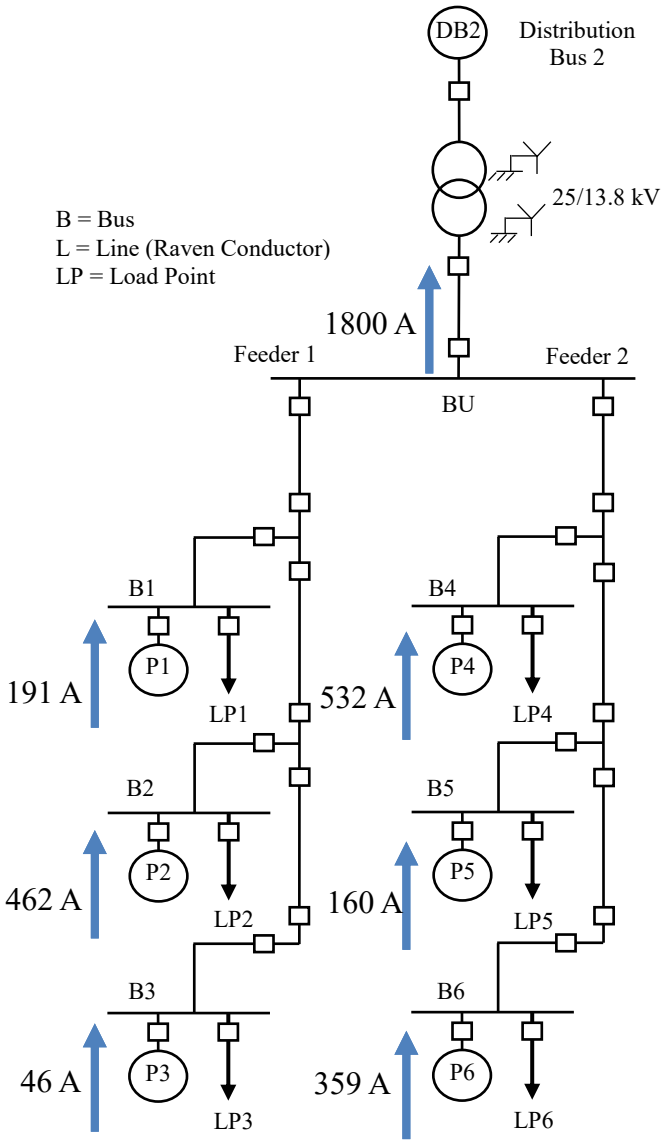

Figure 6.29: Plant and microgrid current flows for Case Study-3 during a line-to-line-to-ground fault before source tripping.

Figure 6.30 presents Case Study-3 for the condition where there is a microgrid connected at DB2 without the proposed scheme implemented. The short circuit contribution from the microgrid is 1800 A, exceeding the ground LOC limit of 716 A referred to the 13.8 kV side of the interconnecting transformer. Consequentially, it can be seen that the utility head end recloser (RE2) operates once with the fuse (F1) melting before the first reclose occurs. It is apparent that the coordination between RE2 and F1 is lost. It can also be seen that the current contribution from the microgrid peaks at 2545 A_{peak} before dissipating to 2052 A_{peak} after one cycle.

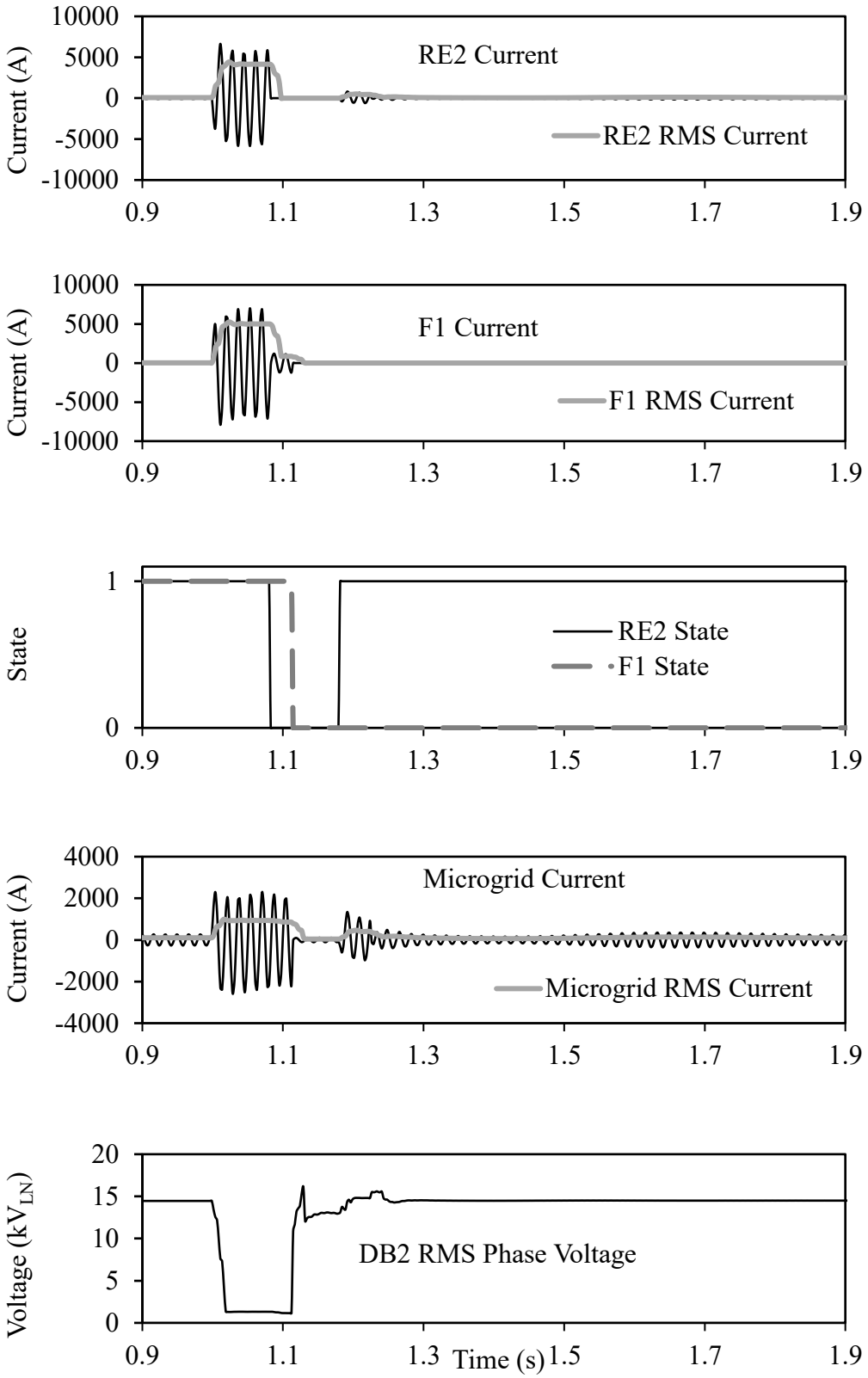

Figure 6.30: Case Study-3 without the proposed scheme: RE2 current, F1 current, RE2 and F1 state signals, microgrid grid current and DB2 RMS phase voltage.

Figures 6.31 and 6.32 present Case Study-3 for the condition where there is a microgrid connected at DB2 with the proposed scheme implemented. As indicated in Table 6.15, two generating units are required to be tripped in plants 1, 2, 4 and 6 in order to restore coordination between RE2 and F1.

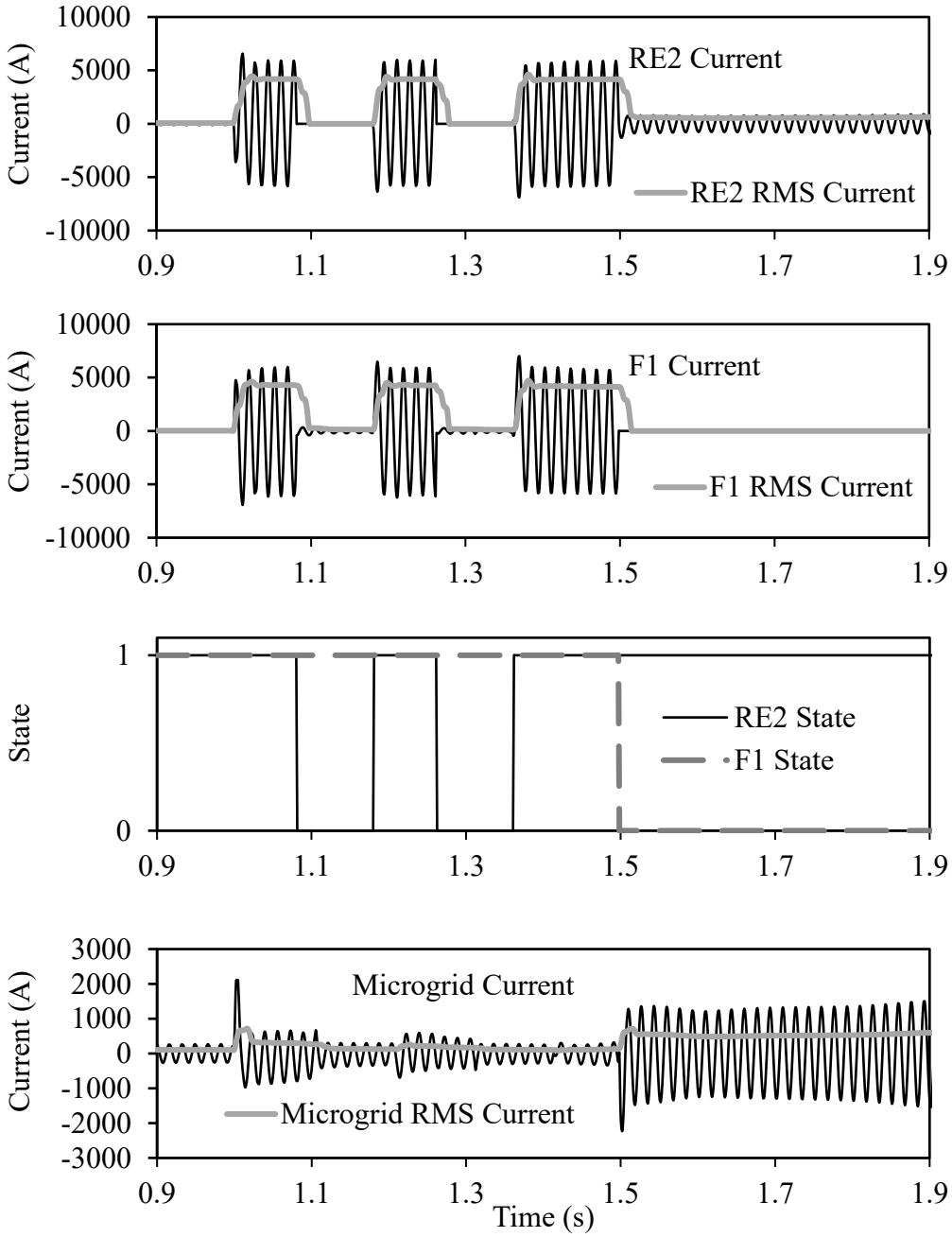

Figure 6.31: Case Study-3 with the proposed scheme: RE2 current, F1 current, RE2 and F1 state signals, microgrid grid current.

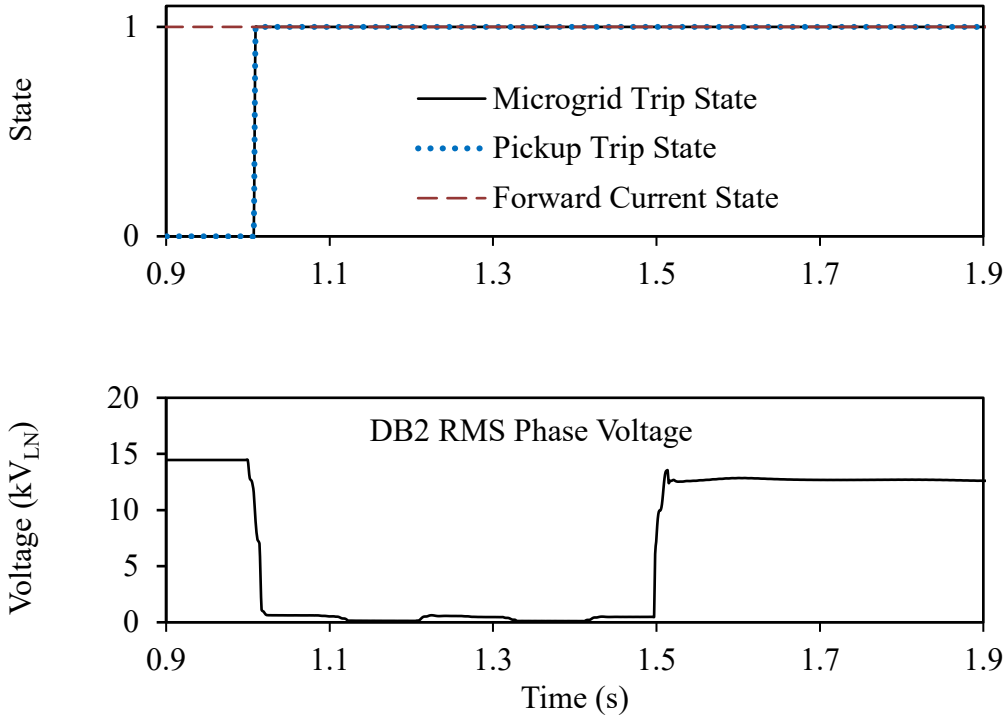

Figure 6.32: Case Study-3 with the proposed scheme: interconnecting relay states, DB2 RMS phase voltage.

As can be observed in Figures 6.31 and 6.32, during the steady-state condition the microgrid has a net current flow towards the utility grid that is maintained once the fault occurs. This means that the proposed scheme can continue if pickup levels are exceeded. Following the inception of a fault, the contribution of current from the microgrid to the utility increases until it exceeds the pickup current. At a simulation time of 1.0094 seconds (0.0094 seconds after fault inception), the proposed scheme notifies plants 1, 2, 4 and 6 to disconnect two sources each. At this point the microgrid short circuit current reduces to 605 A. As per Table 6.16, the PSO algorithm predicted a short circuit current of 623 A following source disconnection. This means that the differential between the actual short circuit current and the predicted value was only 2.89%, highlighting the efficacy of the prediction algorithm. It can also be seen that the current contribution from the microgrid peaks at 2100 A_{peak} before dissipating to 588 A_{peak} after one cycle when the proposed scheme is implemented. Further observation of Figure 6.31 makes it apparent that the system regains coordination between RE2 and F1, demonstrating the capacity of the proposed scheme to restore coordination to the system without limiting the microgrid penetration.

6.4.5.4 Case Study-4

In Case Study-4, all generating plants are operating in maximum condition when a line-to-ground fault is applied to load L1 within the utility network. This is a ground fault and, as indicated in Table 6.15, two generating units are required to be tripped in plants 1, 2, 4 and 6.

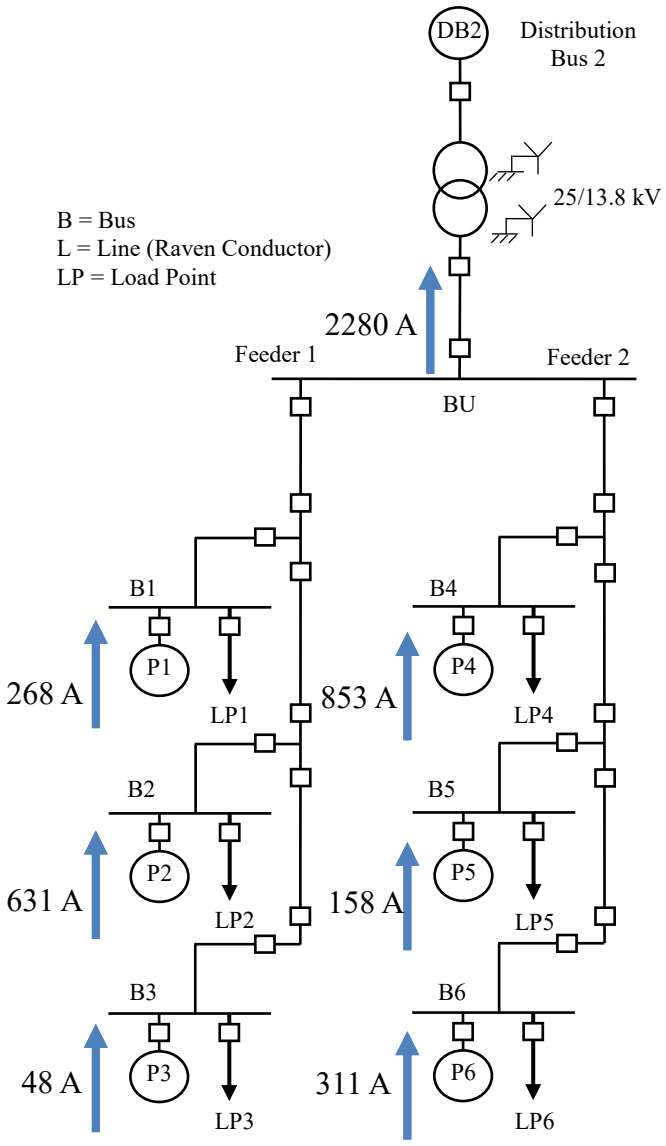

Figure 6.33: Plant and microgrid current flows for Case Study-4 during a single line-to-ground fault before source tripping.

The short circuit contributions measured for the generating sources during the single line-to-ground fault before source tripping are given in Figure 6.33. Comparison of short circuit contributions measured in Figure 6.33 with predicted contributions in Tables 6.13 and 6.14 result in the following percentage discrepancies between predicted and measured values:

Table 6.20: Percentage difference between measured and actual fault currents for Case Study-4.

Generating Plant	1	2	3	4	5	6	Overall Microgrid
Percentage difference (%)	1.47	0.62	4.00	0.92	4.24	2.2	0.91

As can be seen in Table 6.20, predicted short circuit levels are accurate when compared to actual measured values.

Figures 6.34 and 6.35 presents Case Study-4 for the condition where there is a microgrid connected at the DB2 without the proposed scheme implemented.

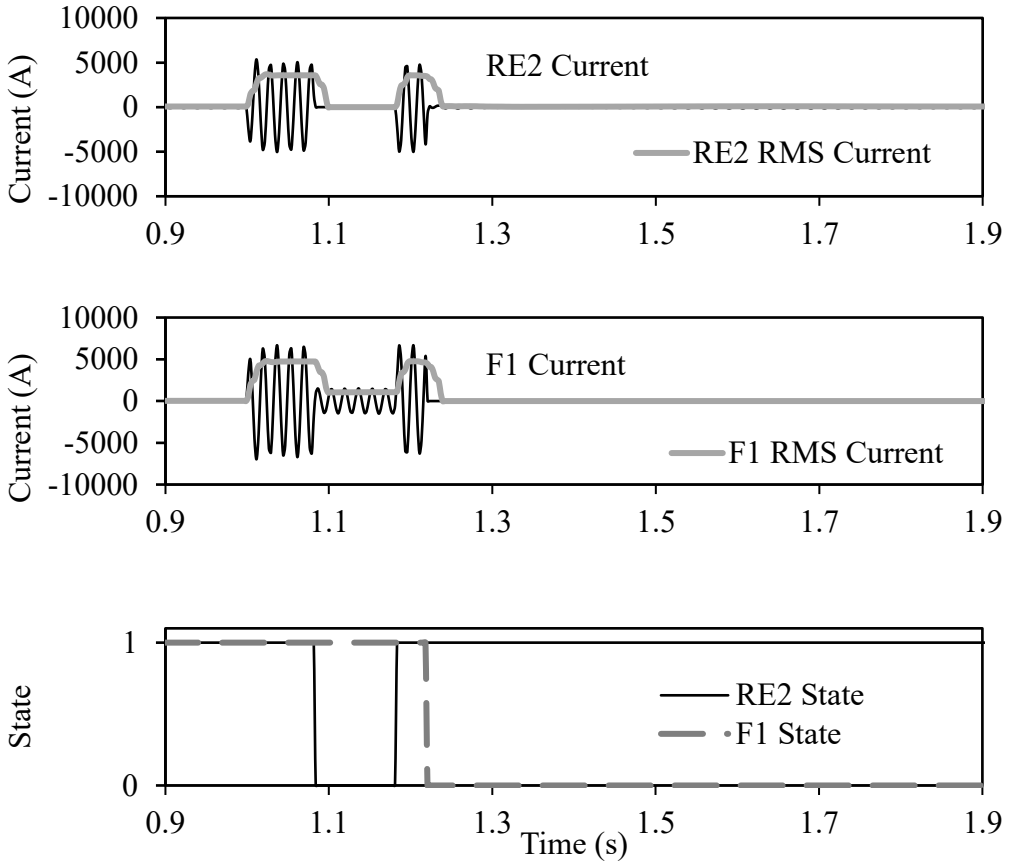

Figure 6.34: Case Study-4 without the proposed scheme: RE2 current, F1 current, RE2 and F1 state signals.

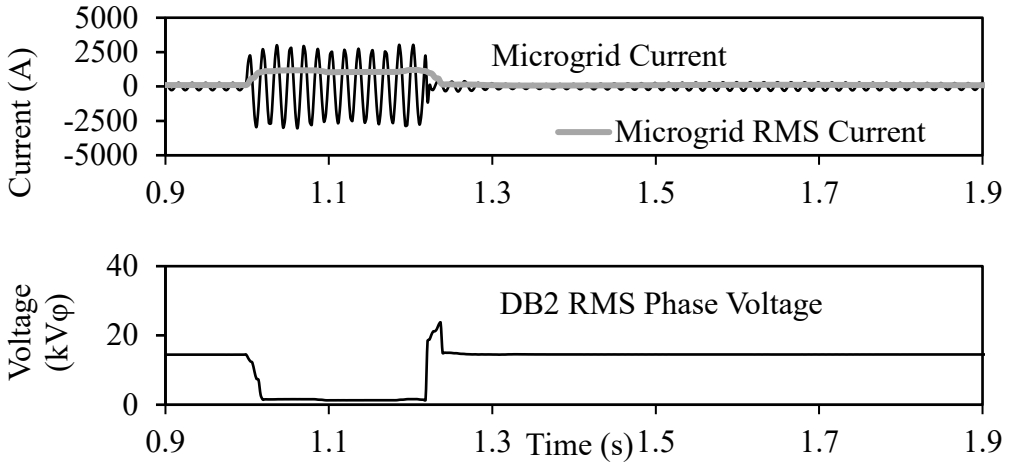

Figure 6.35: Case Study-4 without the proposed scheme: microgrid grid current and DB2 RMS phase voltage.

As can be seen, the short circuit contribution from the microgrid is 2280 A, exceeding the ground LOC limit of 716 A referred to the 13.8 kV side of the interconnecting transformer. Consequentially, it can be seen that the utility head end recloser (RE2) operates twice with the fuse (F1) melting before the second reclose occurs. As such, it is apparent that the coordination between RE2 and F1 is lost. It can also be seen that the current contribution from the microgrid peaks at 2221 A_{peak} before dissipating to 3200 A_{peak} after one cycle.

Figures 6.36 and 6.37 present Case Study-4 for the condition where there is a microgrid connected at DB2 with the proposed scheme implemented. As indicated in Table 6.15, two generating units are required to be tripped in plants 1, 2, 4 and 6 in order to restore coordination.

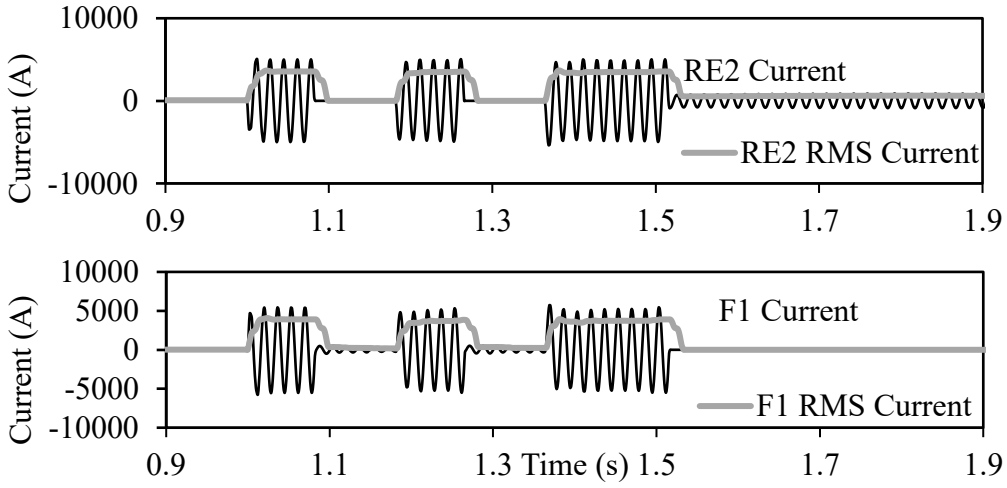

Figure 6.36: Case Study-4 with the proposed scheme: RE2 current, F1 current.

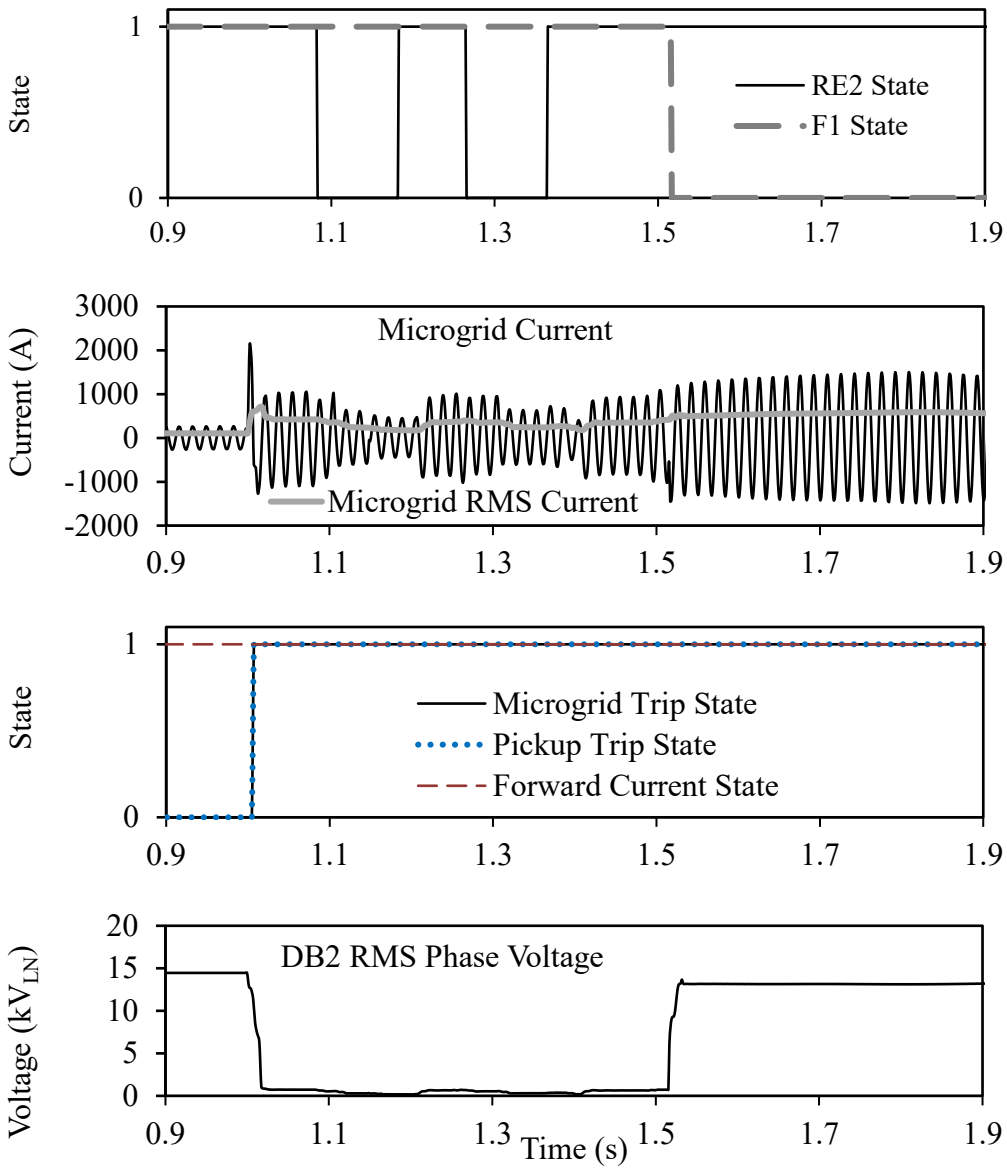

Figure 6.37: Case Study-4 with the proposed scheme: RE2 and F1 state signals and microgrid grid current, interconnecting relay states, DB2 RMS phase voltage.

6.4.5.5 Case Study-5

In Case Study-5, all generating plants are operating in their maximum condition when a line-to-line fault is applied to line L1 within the microgrid. In this case the directional sensing unit within the proposed scheme should give a blocking signal to prevent operation, allowing for the microgrid internal protection to clear the fault. Case Study-5 can be graphically depicted in Figure 6.38.

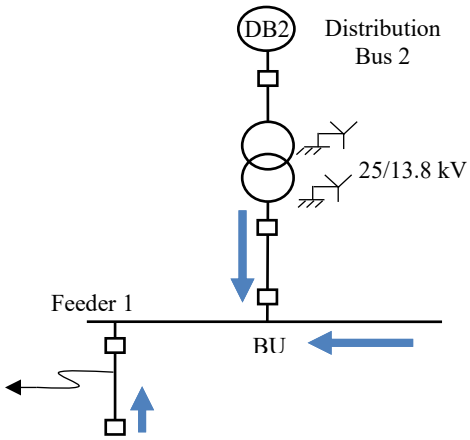

Figure 6.38: Current flows for Case Study-5 during a fault.

Figures 6.39 and 6.40 present Case Study-5 for the condition where there is a microgrid connected at DB2 with the proposed scheme implemented.

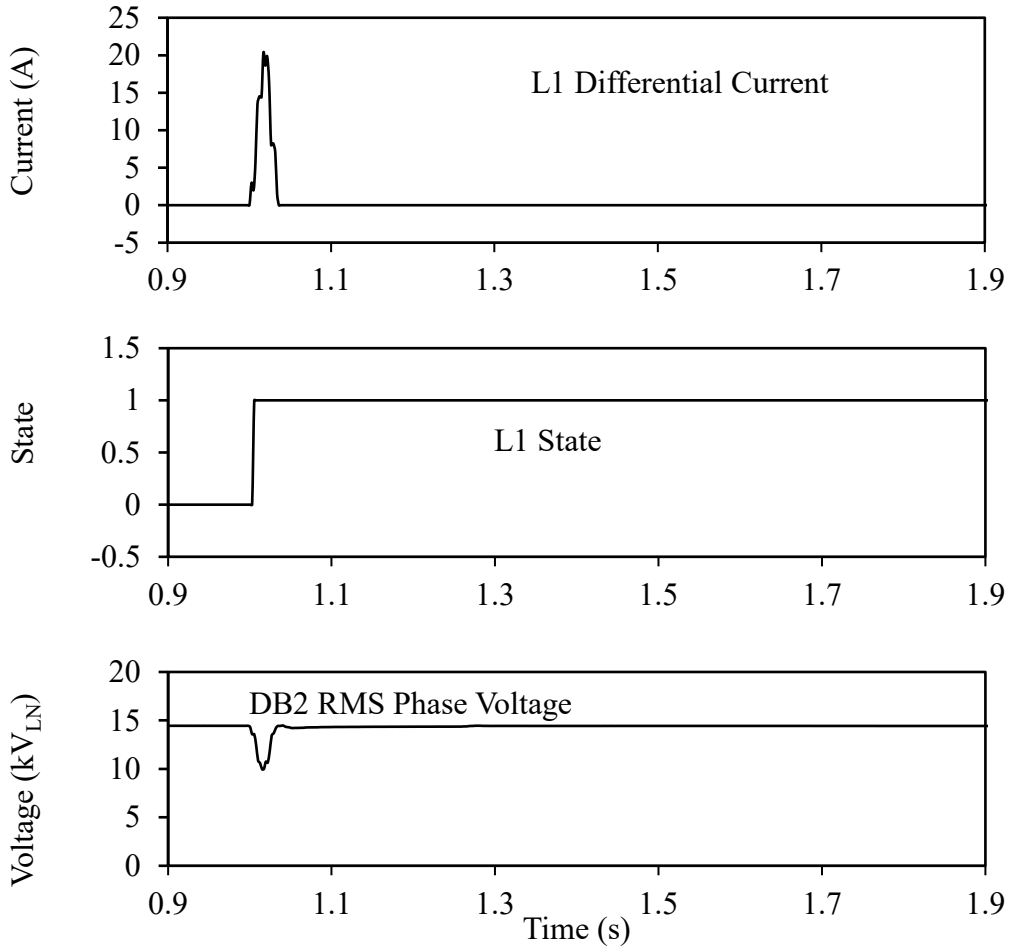

Figure 6.39: Case Study-5 with the proposed scheme: L1 differential current, L1 state, DB2 RMS phase voltage.

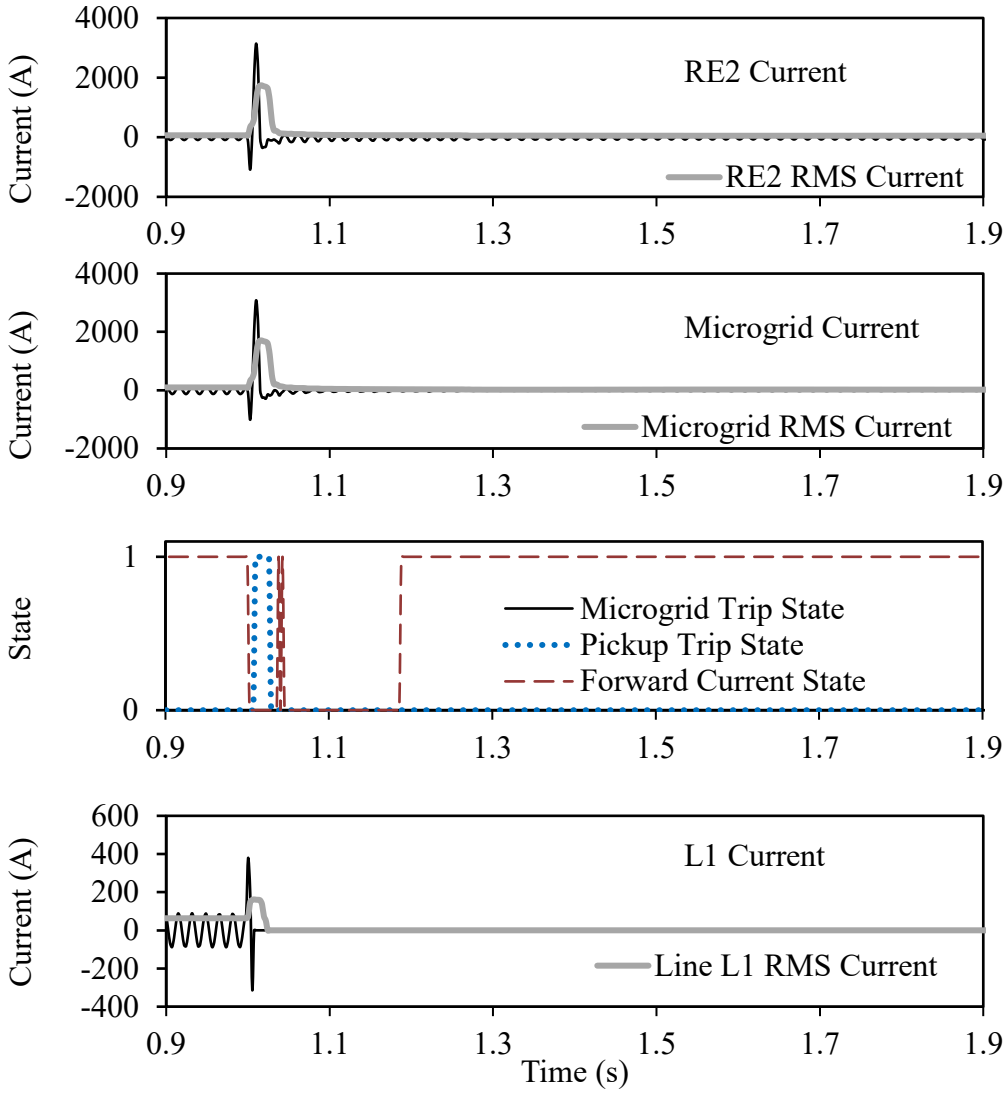

Figure 6.40: Case Study-5 with the proposed scheme: RE2 current, microgrid grid current, interconnecting relay states, line L1 current.

As can be observed in Figures 6.39 and 6.40, during the steady-state condition the microgrid has a net current flow towards the utility grid. When the fault occurs on line L1 within the microgrid, the directional element within the proposed scheme senses the current flowing from the utility to the microgrid. The proposed scheme is then blocked from operation. As such, through observation of Figure 6.39, it can be seen that the line L1 differential current begins to rapidly rise following fault inception before peaking at 20 A. The differential relay protecting line L1 operates at 1.00535 (0.00535 seconds after the fault occurs) seconds, clearing the fault from the microgrid. This highlights the efficacy of the scheme (particularly the directional element) with its compatibility with the microgrid protection scheme given in Chapter 5.

6.4.6 Application of the Proposed Scheme in Conjunction with the Reclosing and Fault Detection Method

As indicated in Section 6.4.5, the proposed scheme effectively identifies the generating plants that require mitigation with the purpose of preventing loss of distribution network protection coordination. The scheme works by tripping relevant generating sources within the plant, in order to return the network to pre-fault operation as quickly as possible. The operation of the scheme is demonstrated in a case study in Chapters 3 and 4, the same as that expressed in Appendix F.2 (grid condition 2); conditions with inputs and outputs of the PRA and PSO scheme given in Tables 6.21 to 6.23. Short circuit predictions and measurements are given in Appendix F.2.

Table 6.21: Complete integration study condition details.

Fault type	Fault location	Fault inception time	Fault duration	microgrid connection point	SM-based plants operating point (% of rated)	Wind speed (m/s)	Irradiance (W/m^2)
Line-to-Ground	Load L1	1 second	sustained	At DB2	100	0	0

Table 6.22: Inputs for the PRA and PSO scheme for the integration study.

Generation Plant	1	2	3	4	5	6
PEN_{DGi} (%)	100	0	0	0	0	100
r_{DGi} (%)	100	0	0	0	0	100

Table 6.23: Outputs from the proposed scheme's PSO for the integration study.

Generating Plant	1	2	3	4	5	6
Number of generators to trip (ground)	3	0	0	0	0	2

As can be seen in Table 6.23, during a ground fault Plants 1 and 6 are required to trip 3 and 2 units respectively. To allow for fast reclosure of these units (preventing a complete shutdown) the reclosing scheme (R_D) given in Chapter 3 is integrated in conjunction with the fault detection technique given in Chapter 4. Note that R_D is integrated into the low voltage side of the generating plant transformer indicated in Figure 6.12 with a voltage of 480 V. As per Equation 3.2, ground settings for 0.2 MVA and 0.4 MVA SM-based generating sources are:

$$I_{pickupgP1} = \frac{0.2 \times 10^6}{\sqrt{3} \times 480} \times 2 = 481.13\ A$$

$$I_{pickupgP6} = \frac{0.4 \times 10^6}{\sqrt{3} \times 480} \times 2 = 962.25\ A$$

From these equations, ground pickup currents for generating plants 1 and 6 are selected to be 481 A and 962 A respectively.

Utilizing Equation 3.3, Z_{RE} is determined for pre-fault load sharing conditions where the generating unit is loaded to 100%, (pre-fault values used in the following equations were obtained through simulation.) The Z_{RE} values for the generating sources in their respective plants are:

$$R_{REP1} = \frac{(\frac{0.46}{\sqrt{3}})^2}{0.2/3} \times 0.91 = 0.97\ \Omega$$

$$X_{REP1} = \sqrt{\left(\frac{(\frac{0.46}{\sqrt{3}})^2}{0.2/3}\right)^2 - \left(\frac{(\frac{0.46}{\sqrt{3}})^2}{0.2/3} \times 0.91\right)^2} = 0.44\ \Omega$$

$$R_{REDG6} = \frac{(\frac{0.464}{\sqrt{3}})^2}{0.4/3} \times 0.92 = 0.50\ \Omega$$

$$X_{REP6} = \sqrt{\left(\frac{(\frac{0.464}{\sqrt{3}})^2}{0.4/3}\right)^2 - \left(\frac{(\frac{0.464}{\sqrt{3}})^2}{0.4/3} \times 0.92\right)^2} = 0.21\ \Omega$$

The ROCOC pickup value is selected as 40 A/second. A similar approach is taken with the 70% and 60% case. The values for $Z_{RE,}$ with corresponding ranges, can be summarized in Table 3.2. The short circuit contributions measured for the generation sources during the single line-to-ground fault but before source tripping is given in Figure 6.41.

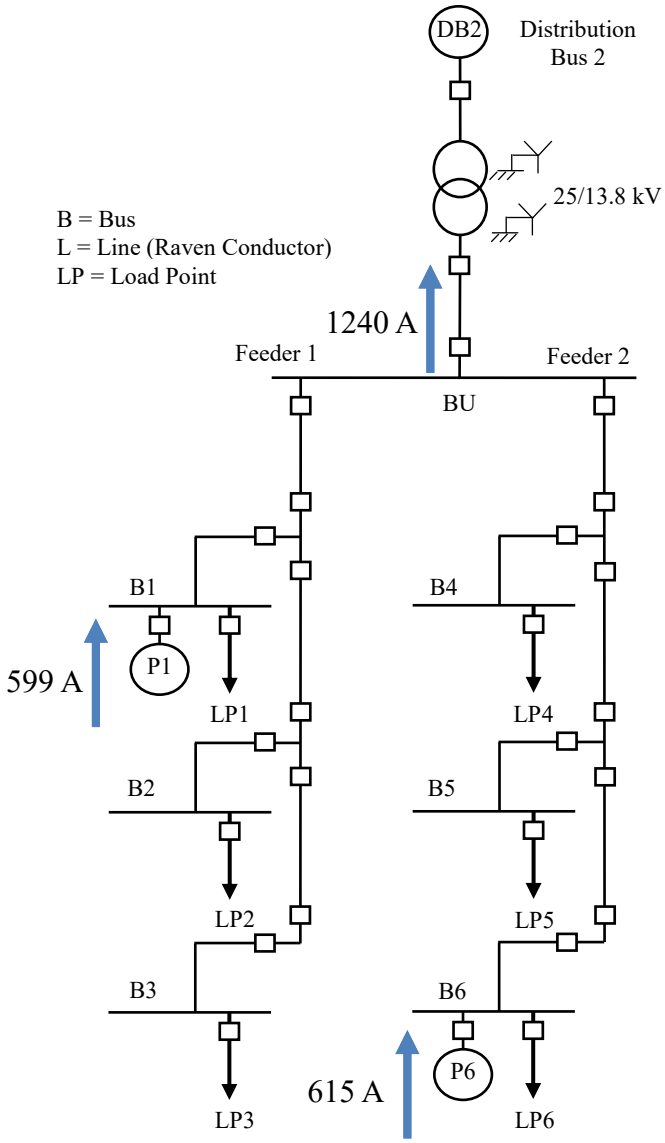

Figure 6.41: Plant and microgrid current flows for the complete integration study during a single line-to-ground fault before source tripping.

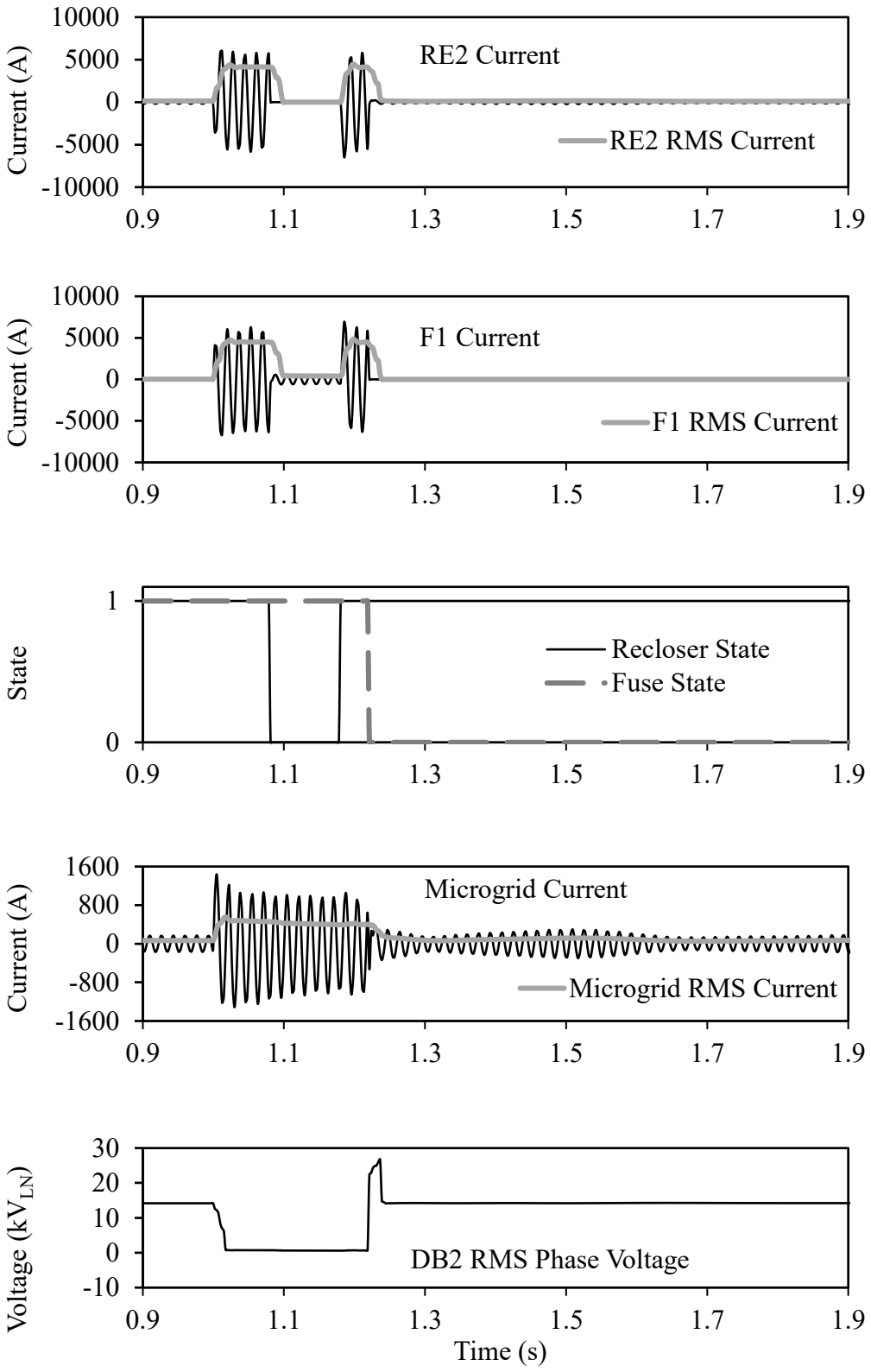

Figure 6.42: Integration study without the proposed scheme: RE2 current, F1 current, RE2 and F1 state signals, microgrid grid current and DB2 RMS phase voltage.

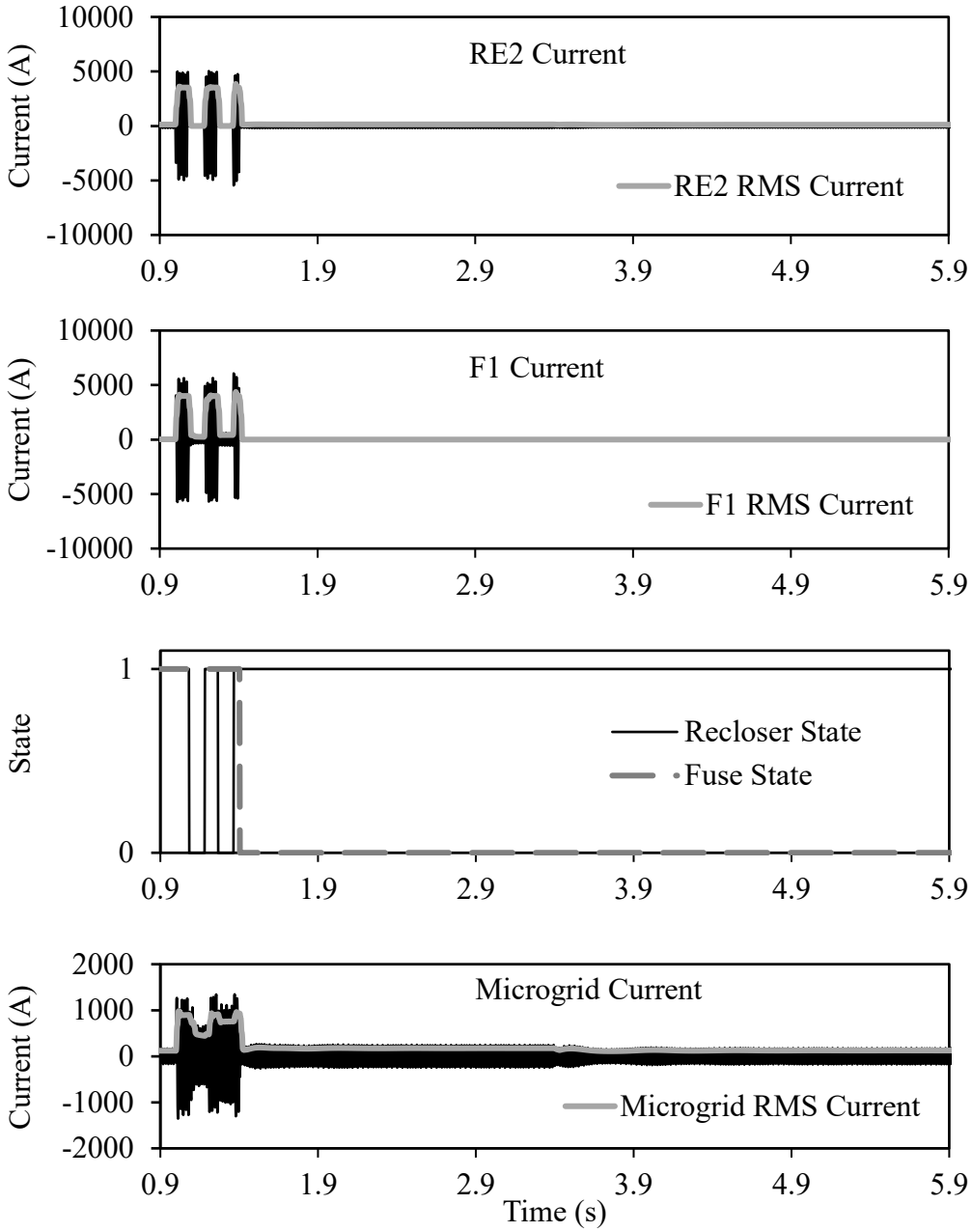

Figure 6.43: Integration study with the proposed schemes: RE2 current, F1 current, RE2 and F1 state signals, microgrid grid current.

Figure 6.42 presents the integration study without the proposed scheme implemented. As demonstrated, the short circuit contribution from the microgrid is 1240 A, exceeding the phase LOC limit of 716 A referred to the 13.8 kV side of the interconnecting transformer. Consequentially, the utility head end recloser (RE2) operates once, with the fuse (F1) melting before the second trip occurs. It is apparent that the coordination between RE2 and F1 is lost. It

can also be seen that the current contribution from the microgrid peaks at 1550 A_{peak} before dissipating to 1203 A_{peak} after one cycle.

Figures 6.44 and 6.45 present the integration study for the condition where there is a microgrid connected at DB2 with all the proposed schemes in Chapters 3 to 6 implemented in the proposed scheme. As indicated in Table 6.23, three generating units are required to be tripped in Plant 1and two in Plant 6 in order to restore coordination between RE2 and F1.

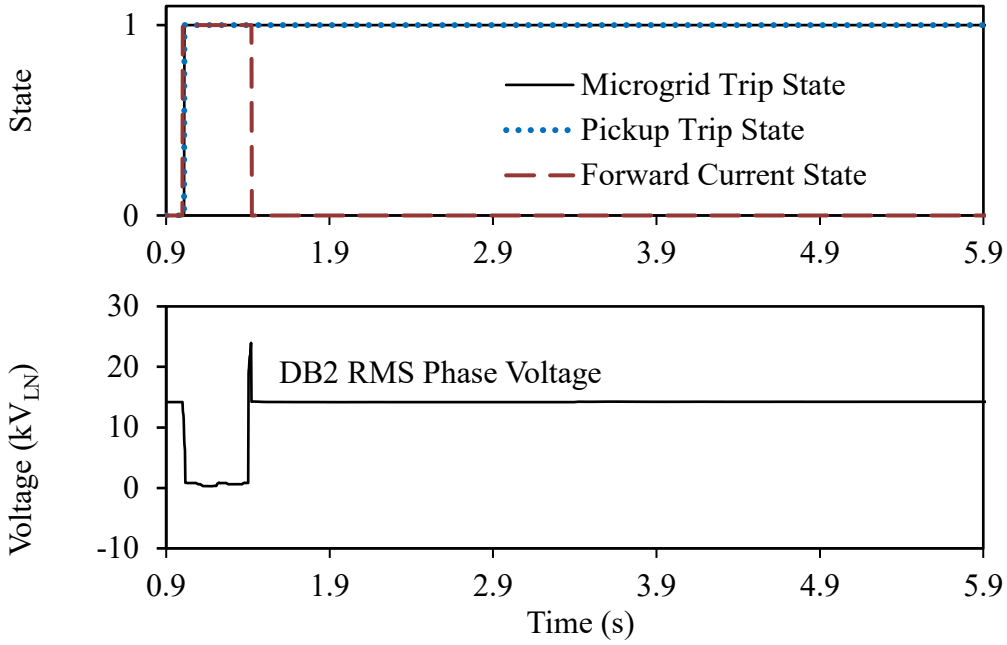

Figure 6.44: Integration study with the proposed schemes: interconnecting relay states, DB2 RMS phase voltage.

As can be observed in Figures 6.44 and 6.45, during the steady-state condition the microgrid has a net current flow from the utility grid in which directional flow from the microgrid changes once the fault occurs. This means that the proposed scheme continues to operate if pickup levels are exceeded. Following the inception of a fault, the contribution of current from the microgrid to the utility increases until it exceeds the pickup current. At a simulation time of 1.0122 seconds (0.0122 seconds after fault inception), the proposed scheme prompts plants 1 and 6 to disconnect three and two sources respectively, as per the results from the PRA and PSO scheme. At this point the microgrid short circuit current reduces to 645 A. As per Appendix F.2, the PSO algorithm predicted a short circuit current of 638 A to be present following source disconnection. This means that the actual differential between short circuit

current and the predicted value was only 1.03%, highlighting the prediction efficacy of the algorithm. It can also be seen that the current contribution from the microgrid peaks at 1267 A_{peak} before dissipating to 1023 A_{peak} after one cycle when the proposed scheme is implemented. Further observation of Figure 6.43 makes it apparent that the system regains coordination between RE2 and F1, demonstrating the capacity of the proposed scheme to restore coordination to the system without limiting the microgrid penetration.

It should be noted that for the integration study, the communication link from the head end recloser in the scheme (demonstrated in Figure 3.5) is substituted with the fault detection scheme in Chapter 4, in addition to a signal from the interconnecting relay from the microgrid. This means that for R_D to trip, the fault detection scheme has to indicate a fault, the microgrid interconnecting block has to indicate to the generating source that it is required to trip (through the PRA and PSO scheme) and the pickup current is required to be exceeded. Additionally, the microgrid protection scheme indicated in Chapter 5 is utilized to protect the internal microgrid. Figures 6.45 to 6.47 demonstrate the R_D, fault detection and microgrid protection scheme working in conjunction with the PRA and PSO scheme.

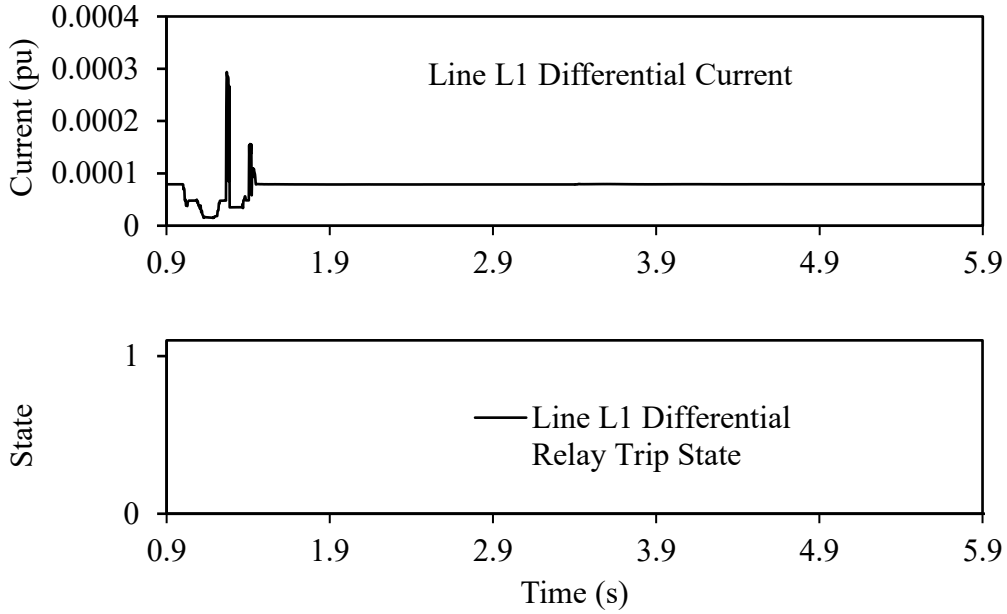

Figure 6.45: Integration study with the proposed schemes: Line L1 differential current, Line L1 differential trip state.

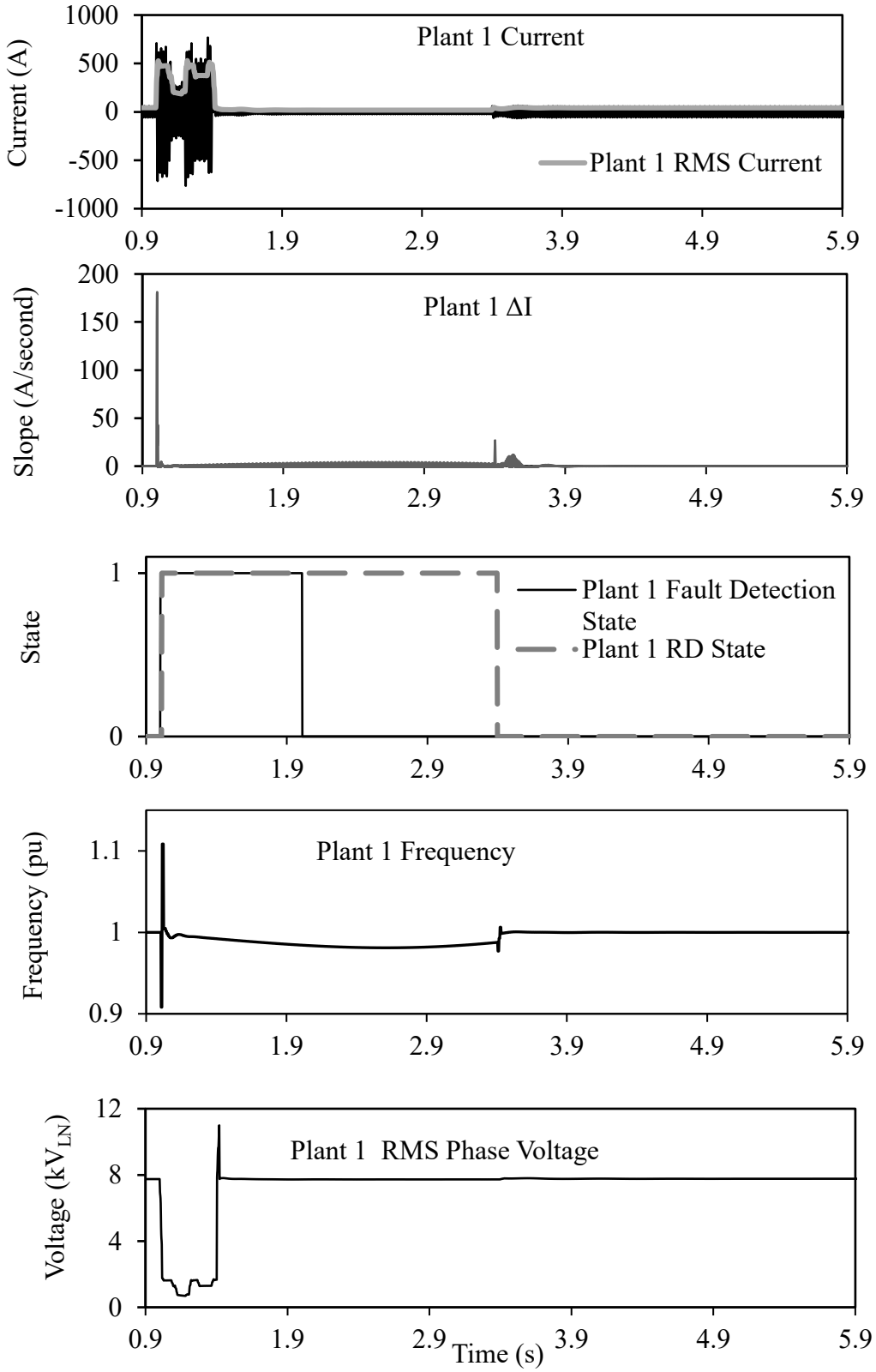

Figure 6.46: Integration study with the proposed schemes for plant 1: Plant current, Plant ΔI, Plant fault detection and RD state, Plant frequency, Plant phase voltage.

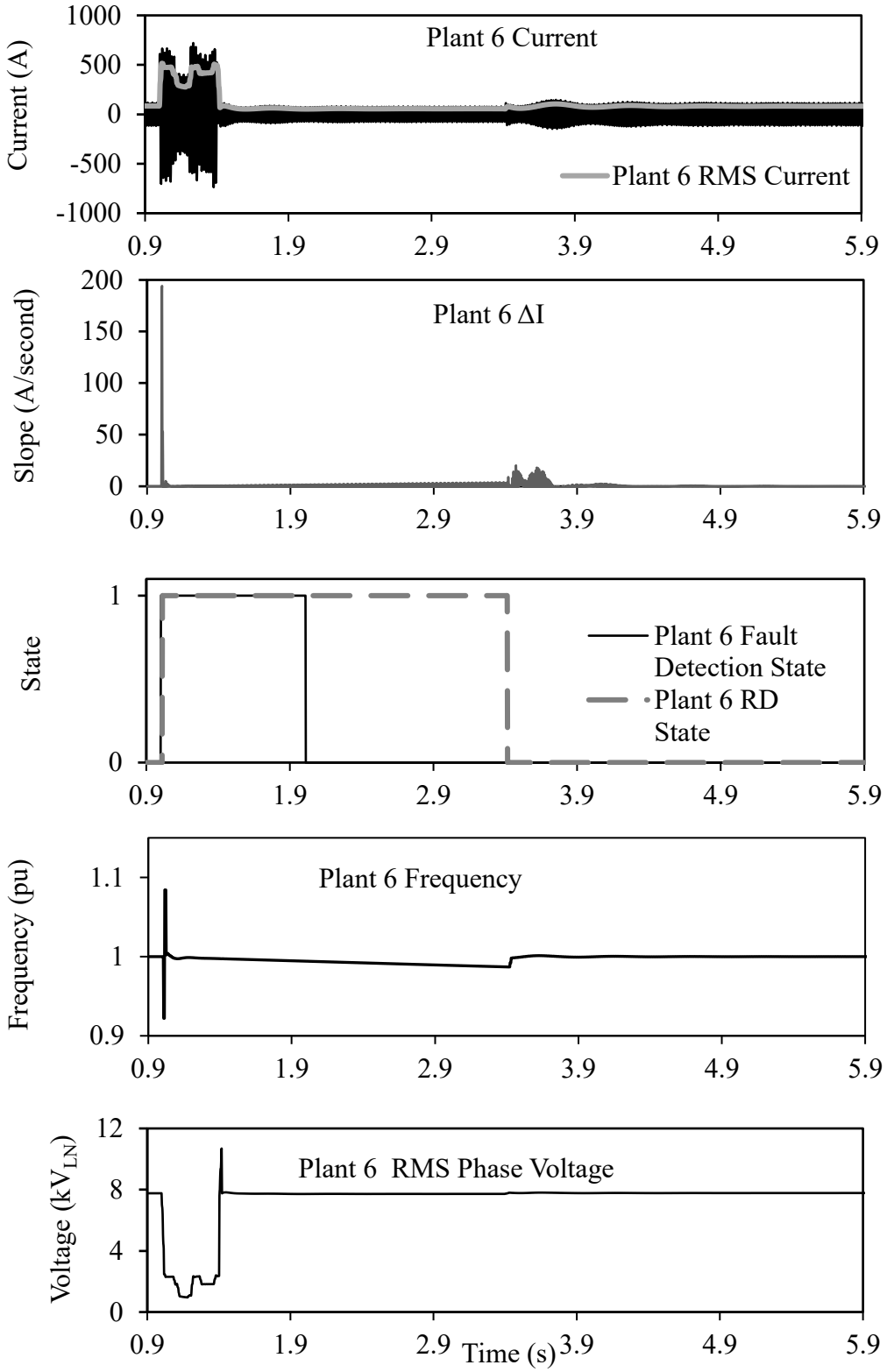

Figure 6.47: Integration study with the proposed schemes for plant 6: Plant current, Plant ΔI, Plant fault detection and RD state, Plant frequency, Plant phase voltage.

Figure 6.45 presents the time domain simulations for the differential relay protecting line L1 within the microgrid during the integration study. The differential current rises marginally following fault inception until it peaks at 0.000294 per unit. Consequentially, the differential relay protecting line L1 discriminates against the fault experienced on load L1 in the distribution network as it falls outside of its protection zone, and thus instructs circuit breakers RBU1 and R1BU to remain closed.

Figure 6.46 presents time domain simulations for Plant 1 for the integration study with R_D and the fault detection scheme (i.e. RD-mod) which facilitates fast reclosure of the DG sources required to trip as per instructions from the PRA and PSO scheme. Following fault inception, the plant current begins to ramp up. RD-mod measures the change in the current for the time period Δt (0.8333 milliseconds) where it reaches a peak ROCOC (ΔI) of 181 A/second, which is greater than the pickup value of 40 A/second. As a result, RD-mod signals the occurrence of a fault, which in conjunction with the signal from the microgrid interconnecting relay, causes three sources within Plant 1 to switch to a transfer impedance at 1.0122 seconds. Following fault clearance, the generating sources successfully reclose into the microgrid at 3.398 seconds (2.398 seconds after the fault occurs). The overshoot frequency upon reconnection is 1.00624 per unit (60.37 Hz) before it decays to a nominal level.

Figure 6.47 presents the time domain simulations for Plant 6 for the integration study with RD-mod, which facilitates fast reclosure of the sources required to trip as per instructions from the PRA and PSO scheme. Following fault inception, the plant current begins to ramp up. RD-mod measures the change in the current of the time period Δt where it reaches a peak ROCOC of 194 A/second, which is greater than the pickup value of 40 A/second. As a result, RD-mod signals the occurrence of a fault which, in conjunction with the signal from the microgrid interconnecting relay, causes two sources within Plant 6 to switch to their transfer impedance at 1.0122 seconds. Following fault clearance the sources successfully reclose into the microgrid at 3.4158 seconds (2.4158 seconds after the fault occurs). The overshoot frequency upon reconnection is 1.001247 per unit (60.07 Hz) before it decays to a nominal level.

Observation of Figures 6.43 to 6.47 makes it apparent that the integration of RD-mod in conjunction with the microgrid protection and PRA with PSO scheme, allows for efficient isolation of sources during utility faults to prevent LOC. This is particularly evident in Figure

6.43 which demonstrates that F1 melts after two recloses from RE2 during a fault, hence coordinating the devices. In addition, it can be seen that RD-mod aids in disconnecting generating sources but also allows for fast reclosure, returning the network to pre-fault operating conditions without the need to shut non-faulted components down.

6.5 Discussions and Comparison with Kalman Filters

As indicated previously, another method that can be utilized for prediction of short circuit contributions is Kalman Filters. Kalman filters work by using a series of measurements to produce an estimate on unknown variables. It firstly estimates the state variables in conjunction with uncertainties. When a second measurement is observed the estimates are updated using a weighted average [73]. In the context of this chapter, the Kalman filter would be unsuitable for estimation of short circuit currents mainly due to the nonlinear nature that the fault levels change. In cases where the short circuit level changes linearly, a Kalman filter may be used.

Additionally, Kalman filters create their predictions through an iterative process. This can take significant time when generating predictions from large data sets. Considering that PSO is also an iterative process, utilization of a Kalman filter for prediction of short circuit currents may create significant delays in generating optimized tripping results.

PRA utilizes data to generate lines of best fit to predict outputs for any given inputs. As such it is not generating results through an iterative process. This makes it more suitable for use in the application discussed in this chapter as it does not incur additional delays when making predictions. Additionally, the PRA can become more accurate when previously unknown data points are added to the data set utilized to create the predictive equations.

6.6 Summary and Conclusions

This chapter presents a protection scheme through the utilization of polynomial regression analysis in conjunction with particle swarm optimization with a directional element to prevent excessive short circuit current contribution from microgrids during a grid fault. Results presented demonstrate the efficacy of the proposed approach in mitigating microgrid short circuit current influences during utility faults in the context of loss of coordination.

Case studies conducted demonstrate that the proposed scheme is able to accurately predict the expected short circuit contributions from generating plants within a microgrid. This is

achieved through the use of polynomial regression analysis. This PRA consistently predicted short circuit values with less than 5 percent error, highlighting the robustness of the prediction approach. Results also demonstrate the efficacy of the prediction method for operating conditions that are not pre-determined. The PRA is then able to be used within a particle swarm optimization algorithm to determine which generating units within a given plant are required to be removed from the network during a fault to prevent LOC. In every case, no constraints were violated. This scheme removes the need for plant owners within microgrids to install a large number of mitigation devices.

The application of a fault within the microgrid demonstrated the efficacy of the directional element within the proposed scheme in the context of discriminating against internal microgrid and utility network faults.

A case study utilizes the concepts discussed in Chapters 3 to 6. During this integration study, the PRA and PSO algorithm is established to be effective in determining which generation sources are required to trip. RD-mod is then confirmed as being responsible for detecting the fault condition and the transfer of the relevant generation sources identified by the PSO algorithm to their respective transfer impedances. The outcome is coordination between the head end recloser and downstream fuse within the utility network. Following fault clearance, RD-mod is established as successful in reclosing the tripped generation sources back into the microgrid, allowing for the pre-fault operating conditions to continue. Ultimately, the study demonstrates that the microgrid protection scheme successfully discriminates against the utility network fault. This demonstrates that the concepts presented in this thesis are compatible.

7. SUMMARY AND CONCLUSIONS

7.1 Summary

The main objective of this research is to allow for integration of microgrids and DG units into distribution networks, in a manner which minimizes effects on the existing distribution network protection infrastructure.

Results presented in Chapters 3 to 6 make it apparent that intelligent schemes can be effectively utilized to prevent degradation of existing distribution network overcurrent protection adequacy. It was initially demonstrated that integration of a DG source or microgrid into a distribution network produced adverse effects on short circuit current characteristics, yielding degradation in existing protection infrastructure adequacy. It was ascertained that the level of impact that DG and microgrid sources can have on the network is dependent on source types (i.e. SM-based, PV or wind) and rated outputs. When large changes in short circuit currents occur due to source penetration, existing protection infrastructure settings may become inadequate, requiring changes in settings. In complex systems, changes can be difficult and the effects of changes can involve mitigation of sources.

As demonstrated in Chapter 3, when a SM-based DG source is integrated into a distribution network, the existing fuse-recloser protection coordination can be violated for low levels of penetration. Existing methods for mitigation are to limit the penetration level, trip and shut down the DG source, or to mitigate the short circuit level output from the DG source. Results from Chapter 3 indicate that another possible short circuit current mitigation method is to switch the DG source from the network to a transfer impedance. This makes it possible to maintain the pre-fault frequency and speed, allowing a fast reconnection time back into the network once the fault is cleared. The requirement to limit the penetration level of the DG source is removed, and there is no need for significant investment in protection devices capable of sustaining long term, high magnitude fault levels. Additionally the scheme is shown to be effective when the fault impedance is increased. In Chapter 3, it is also demonstrated that the reclosing scheme is effective when compared to an existing potential DG mitigation solution in FCLs.

Chapter 4 presents a fault detection scheme based on measurements of the rate of change of current output by DG sources. This scheme was designed to mimic the possibility of a failure within the communication system, a requirement for the reclosing scheme in Chapter 3 to work. Results in Chapter 4 make it apparent that there is a significant difference in the ROCOC when the changes are attributed to switching transients or load changes as opposed to an actual fault. Results demonstrate that by having an understanding of the short circuit behavior of the DG sources in addition to their dynamics, it is possible to determine a ROCOC level that faults will exceed but other transients will not. This allows for discrimination between transients and short circuits, and can be integrated for this purpose into protective devices that rely on alternate mechanisms such as communication links. By integrating the ROCOC scheme into the reclosing scheme outlined in Chapter 3, the ROCOC scheme was proven to be effective in its purpose, successfully substituting the communication link used by the reclosing scheme.

In Chapter 5, results make it apparent that a significant challenge is the inherent changes in short circuit current magnitudes in microgrids when transferring between grid and islanded modes of operation. What makes this particularly difficult is that traditional protection mechanisms in distribution networks typically rely on unidirectional power flows in conjunction with large magnitude short circuit currents. Results obtained and reported in Chapter 5 point to differential relays as a feasible solution to clear faults within a microgrid, regardless of short circuit current magnitudes. In addition, differential relays have the capacity to discriminate between in-zone and out-of-zone faults, using a comparison of current measurements and removing the reliance on large magnitude short circuit levels. This removes the tendency towards failure when switching between grid and islanded operations. The differential relays can also be integrated in parallel with adaptive overcurrent protection that can be set to coordinate with existing load point downstream overcurrent protection devices. The outcome is to allow for the scheme to be integrated segmentally when constraints such as budgetary considerations are present.

To understand how microgrids can affect utility network overcurrent protection, a regression and particle swarm optimization technique is presented in Chapter 6. This PRA and PSO scheme is utilized to effectively predict short circuit current contributions from the microgrid to the utility network, and indicate which generating units should be subject to

mitigation techniques or be disconnected. Equations presented demonstrate that short circuit current contributions from generation plants are dependent on factors such as generator type, in addition to percentage rated output and percentage penetrations relative to other plants on the same feeder. Short circuit current contribution dynamically changes as a factor of these variables. Results obtained demonstrate that the PRA and PSO method is able to accurately predict (within 5% in all cases) the short circuit contributions from the microgrid during the fault, and after generating sources are tripped off by the PSO scheme.

Furthermore, results in Chapter 6 indicate that the integration of the proposed schemes presented in Chapters 3 to 6 together make the protection of microgrids and mitigation of their potentially undesirable short circuit current contributions plausible. The PRA and PSO algorithm is used to indicate which generating sources are required to be mitigated through predictive methods. This, in conjunction with the fault detection technique in Chapter 4, can be utilized to instruct the reclosing scheme given in Chapter 3 to trip the relevant generation sources from the microgrid, thereby preventing excessive short circuit contributions which could potentially result in the coordination limit being surpassed. The reclosing scheme is then able to allow for a fast reconnection of generating units following fault clearance by the utility network, preventing a shutdown of those units and potentially saving the unit owner from undesirable downtime and restart costs. In addition, results indicate that the differential protection scheme proposed in Chapter 5 can be integrated into the microgrid without interfering with schemes associated with interconnecting blocks and generating units. This means that the schemes can be used in parallel or integrated into one another, to allow for a complete protection scheme of microgrids that are integrated into distribution networks without the need for the utility to redesign existing protection infrastructure.

Economic concerns are key factors affecting the practicality of integrating the proposed approaches. Engineers should consider the comparative cost of adjusting the existing protection settings or the cost of purchasing, maintaining, and installing the schemes presented, factoring in costs of shut downs and failures. Practical applications are in regions that have an expanding population size, and remote settlements requiring network upgrades to meet increases in power demand. The proposed techniques offer significant value in the domain of network expansion

planning, as they allow for microgrid and DG source penetration into distribution networks without significant re-engineering work or limiting capacity.

7.2 Conclusions

Studies in this thesis lead to the following conclusions:

1. DG sources and microgrids have the capacity to adversely affect existing distribution network short circuit characteristics based on both size and source type.
2. Increased short circuit currents associated to integration of DG sources and microgrids can yield degradation of existing fuse-recloser coordination thus causing a loss of coordination.
3. Mitigation of DG short circuit contributions is plausible through the use of reclosing schemes in conjunction to switching impedances. These switching schemes have the capacity to mitigate but also allow for fast reconnection due to the maintenance of pre-fault speed and frequencies of individual sources thus prevent unnecessary shut downs.
4. Measurements of the rate of change of current output by DG sources are an effective method for discriminating between system transients and faults. These techniques can be effectively substituted into schemes (such as the reclosing technique presented) that rely on communication links for fault detection thus making them more robust and independent.
5. Microgrid protection is an inherently difficult field due to drastic changes in short circuit currents when transitioning between grid and islanded operations.
6. Hybrid differential and adaptive overcurrent protection is an effective means of protecting microgrids as they can contend with the drastic short circuit current changes without failure.
7. Differential and adaptive overcurrent protection do not require to be coordinated with one another hence are compatible for parallel use.
8. Polynomial regression analysis can be an effective method for predicting short circuit contributions from microgrids to utility networks regardless of source type and size. The efficacy of such methods is dependent on accurate training data.

9. Short circuit contributions from generating sources within microgrids to utility networks are dependent on the source rating, operating point and associated penetration percentage when compared to other sources on the same feeder.
10. Particle swarm optimization can be utilized in conjunction with polynomial regression to determine which units within a generating plant are required to be mitigated such that the loss of coordination limit of the utility network is not exceeded.
11. The use of reclosing schemes, fault detection techniques, hybrid microgrid protection schemes and prediction and optimization algorithms is an effective means of allowing complete integration of microgrids into utility networks without compromising the existing protection infrastructure adequacy.
12. The proposed schemes presented in this thesis offers significant practical value in the domain of network expansion planning and reinforcement options in power distribution networks, as well as demonstrating and predicting the effect of generation sources and microgrid penetration on existing protection infrastructure in distribution networks.

This thesis is a stepping-stone in the direction of more research on DG and microgrid influence mitigation on existing distribution system short circuit characteristics and fuse-recloser protection infrastructure. It is hoped that the research work documented in this thesis will provide useful guidance for conducting more studies and analyzing other technical issues that might be impacted by DG source and microgrid integration.

REFERENCES

[1] G. Pepermans, J. Driesen, D. Haeseldonckx, R. Belmans and W. D'Haeseleer, "Distributed Generation: Definition, benefits and issues," *Energy Policy - Elsevier,* vol. 33, no. 6, pp. 787-798, Apr 2005.

[2] N. Rajaei, M. H. Ahmed, M. M. A. Salama and R. K. Varma, "Fault Current Management Using Inverter-Based Distributed Generators in Smart Grids," *IEEE Transactions on Smart Grid,* vol. 5, no. 5, pp. 2183-2193, September 2014.

[3] K. Deng, X. He, D. Bi and C. Feng, "An adaptive protection method for the inverter dominated microgrid," in *International Conference on Electrical Machines and Systems*, Beijing, 2014.

[4] P. Gupta, R. S. Bhatia and D. K. Jain, "Adaptive protection schemes for the microgrid in a smart grid scenario," in *Innovative Smart Grid Technologies - Asia*, Bangalore, 2013.

[5] Oudalov, A. Fidigatti, T. Degner, B. Valov, C. Hardt, J. M. Yarza, R. Li, N. Jenkins, B. Awad, F. V. Ovebeeke, N. Hatziargyriou and M. Lorentzou, "Novel protection systems for microgrids," 2009.

[6] M. R. Islam and H. A. Gabbar, "Study of Micro Grid Safety & Protection Strategies with Control System Infrastructures," *Smart Grid and Renewable Energy,* vol. 3, pp. 1-9, 2012.

[7] G. Buigues, A. Dysko, V. Valverde, I. Zamora and E. Fernandez, "Microgrid Protection: Technical challenges and existing techniques," in *International Conference on Renewable Energies and Power Quality*, Bilbao, 2013.

[8] M. R. Islam and H. A. Gabbar, "Analysis of Microgrid Protection Strategies," in *IEEE International Conference on Smart Grid Engineering*, Oshawa, 2012.

[9] C. Yuan, M. A. Haj-Ahmed and M. S. llindala, "An MVDC Microgrid for a Remote Area Mine Site: Protection, Operation and Control," in *IEEE Industrial Applications Society General Meeting*, Vancouver, 2014.

[10] M. P. Nthontho, S. P. Chowdhury, S. Winberg and S. Chowdhury, "Protection of Domestic Solar Photovoltaic Based Microgrid," in *11th International Conference on Developments in Power Systems Protection*, Birmingham, 2012.

[11] G. M. Masters, Renewable and Efficient Electric Power Systems, Hoboken: John Wiley & Sons, 2004.

[12] "Renewable Energy," United Nations High-Level Group on Sustainable Energy for all, 2012. [Online]. Available: http://www.se4all.org/our-vision/our-objectives/renewable-energy/. [Accessed 4 November 2014].

[13] C. J. Mozina, "Impact of Green Power Generation on Distribution Systems in a Smart Grid," in *Power Systems Conference and Exposition (PSCE)*, Phoenix, 2011.

[14] SaskPower, "Generation interconnection requirements at voltages 34.5 kV and below," March 2005. [Online]. Available: www.saskpower.com/poweringyourfuture/pdfs/NUG345kV.pdf. [Accessed September 2015].

[15] D. J. Glover, M. S. Sarma and T. J. Overbye, Power System Analysis and Design, 4th ed., Stamford: Cengage Learning, 2008.

[16] J. L. Blackburn and T. J. Domin, Protective Relaying: Principles and Applications, 4th ed., Boca Raton: CRC Press, 2014.

[17] P. M. Anderson, Power System Protection, Hoboken: John Wiley & Sons, 1999.

[18] T. Gonen, Electric Power Distribution System Engineering, 2nd ed., Boca Raton: Taylor & Francis Group, 2008.

[19] B. Ram and D. N. Vishwakarma, Power System Protection and Switchgear, New Delhi: Tata McGraw-Hill, 1995.

[20] J. J. Justo, F. Mwasilu, J. Lee and J. Jung, "AC-Microgrids versus DC-Microgrids with distributed energy resources," *Renewable and Sustainable Energy Reviews,* vol. 24, pp. 387-485, 2013.

[21] N. I. Sapankevych and R. Sankar, "Constrained Motion Particle Swarm Optimization and Support Vector Regression for Non-linear Time Series Regression and Prediction Applications," in *IEEE Conference on Machine Learning and Applications*, Miami, 2013.

[22] J. Kennedy and R. Eberhart, "Particle Swarm Optimization," in *IEEE International Conference on Neural Networks*, Perth, 1995.

[23] M. A. Hassan and M. A. Abido, "Optimal Design of Microgrids in Autonomous and Grid-Connected Modes Using Particle Swarm Optimization," *IEEE Transactions on Power Electronics,* vol. 26, no. 3, pp. 755-769, 2011.

[24] B. Panigrahi, A. Abraham and S. Das Eds, Computational Intelligence in power Engineering, Berlin: Springer-Verlag, 2010.

[25] U.S. Department of Energy, "Fault Current Limiters," 6 November 2009. [Online]. Available: http://energy.gov/sites/prod/files/oeprod/DocumentsandMedia/hts_fcl_110609.pdf. [Accessed 29 May 2014].

[26] M. Elsamahy, S. O. Faried and T. S. Sidhu, "Impact of Superconducting Fault Current Limiters on the Coordination Between Generator Distance Phase Backup Protection and Generator Capability Curves," *IEEE Transactions on Power Delivery,* vol. 26, no. 3, pp. 1854-1863, July 2011.

[27] L. Wang, P. Jiang and D. Wang, "Summary of Superconducting Fault Current Limiter Technology," in *Frontiers in Computer Education*, Berlin, Springer, 2012, pp. 819-825.

[28] H. Arai, M. Inaba, T. Ishigohka, H. Tanaka, K. Arai, M. Furuse and M. Umeda, "Fundamental Characteristics of Superconducting Fault Current Limiter Using LC Resonance Circuit," *IEEE Transactions on Applied Superconductivity,* vol. 16, no. 2, pp. 642-645, June 2006.

[29] S. O. Faried and M. Elsamahy, "Incorporating superconducting fault current limiters in the probabilistic evaluation of transient recovery voltage," *IET Generation, Transmission & Distribution,* vol. 5, no. 1, pp. 101-107, 2011.

[30] T. A. Short, Electric Power Distribution Handbook, Boca Raton: CRC Press, 2004.

[31] T. K. Abdel-Galil, A. E. B. Abu-Elanin, E. F. El-Saadany, A. Girgis, A. R. I. Mohamed, M. M. A. Salama and H. H. M. Zeineldin, "Protection Coordination Planning with Distributed Generation," Qualsys Engco Inc, 2007.

[32] S&C Electric Company, "SM Power Fuses," S&C Electric Company, 2018. [Online]. Available: http://www.sandc.com/en/products--services/products/sm-power-fuses/. [Accessed 15 January 2016].

[33] Asea Brown Boveri (ABB), "ABB PCD Control Protection Curves," September 2002. [Online]. Available: http://www05.abb.com/global/scot/scot235.nsf/veritydisplay/1bc69ae25de85ac585256c44005e98c4/$file/pcd%20protection%20curves.pdf. [Accessed 15 July 2014].

[34] M. R. Islam and H. M. Gabbar, "Analysis of Microgrid Protection Strategies," in *IEEE International Conference on Smart Grid Engineering*, Oshawa, 2012.

[35] EMTP-RV, EMTP Help Center, Montreal: EMTP-RV, 2016.

[36] J. M. Gers and E. J. Holmes, Protection of Electricity Distribution Networks, 2nd ed., London: The Institution of Engineering and Technology, 2004.

[37] H. Joshi, Residential, Commercial and Industrial Electrical Systems, vol. 3, New Delhi: Tata McGraw-Hill, 2008.

[38] P. Kundur, Power System Stability and Control, New York: McGraw-Hill, 1994.

[39] H. Dommel, EMTP Theory Book, Microtran Power System Analysis Corporation, 1996.

[40] Y. Yu, Electrica Power System Dynamics, New York: Academic Press, 1983.

[41] A. D. Hansen, G. Michalke, P. Sorensen, T. Lund and F. Iov, "Co-ordinated Voltage Control of DFIG Wind Turbines in Uninterrupted Operation during Grid Faults," *Wind Energy,* vol. 10, no. 1, pp. 51-68, 2007.

[42] O. Anaya-Lara, N. Jenkins, J. Ekanayake, P. Cartwright and M. Hughes, Wind Energy Generation: Modelling and Control, John Wiley & Sons, 2009.

[43] J. Morren, S. W. H. de Haan, P. Bauer, J. Pierik and J. Bozelie, "Comparison of Complete and Reduced Models of a Wind Turbine with Doubly-fed Induction Generator," in *10th European Conference on Power Electronics and Applications*, Toulouse, 2003.

[44] J. G. Slootweg, H. Polinder and W. L. Kling, "Representing Wind Turbine Electrical Generating Systems in Fundamental Frequency Simulations," *IEEE Transactions on Energy Conversion,* vol. 18, no. 4, pp. 516-524, 2003.

[45] V. K. Sood and P. Bhalla, "EMTP Model of Grid Connected PV System," in *International Conference on Power Systems Transients*, 2013, 2013.

[46] "IEEE Standard for Interconnecting Distributed Resources with Electric Power Systems," 2003.

[47] K. A. Wheeler, M. Elsamahy and S. O. Faried, "Assessment of Distributed Generation Influences on Fuse-Recloser Protection Systems in Radial Distribution Networks," in *IEEE PES Transmission and Distribution Conference and Exposition*, Dallas, 2016.

[48] "Generation interconnection requirements at voltages 34.5 kV and below," SaskPower, 2005.

[49] H. Al-Nasseri, "A new voltage based relay scheme to protect micro-grids dominated by embedded generation using solid state converters," in *19th International Conference on Electricity Distribution*, Vienna, 2007.

[50] X. Lou, D. K. Y. Yau, H. H. Nguyen and B. Chen, "Profit-Optimal and Stability-Aware Load Curtailment in Smart Grids," *IEEE Transactions on Smart Grid,* vol. 4, no. 3, pp. 1411-1420, 2013.

[51] I. Waseem, M. Pipattanasomporn and S. Rahman, "Reliability Benefits of Distributed Generation as a Backup Source," in *IEEE PES General Meeting*, Calgary, 2009.

[52] S. Pagadrai, M. Yilmaz and P. Valluri, "Smart-Grid Backbone Network Real-Time Delay Reduction via Integer Programming," *IEEE Transactions on Neural Networks and Learning Systems,* vol. 27, no. 8, pp. 1787-1792, 2016.

[53] J. Prigmore, G. Tcheslavski and C. Bahrim, "An ICGT-based Electronic Circuit Breaker Design for a 12.47 kV Distribution System," in *IEEE PES General Meeting*, Minneapolis, 2010.

[54] "IEEE Recommended Practice for Protection and Coordination of Industrial and Commercial Power Systems (IEEE Buff Book)," IEEE Std. 242-2001.

[55] H. Yazdanpanahi, W. Xu and Y. W. Li, "A Novel Fault Current Control Scheme to Reduce Synchronous DG's Impact on Protection Coordination," *IEEE Transactions on Neural Networks,* vol. 27, no. 14, pp. 542-551, 2014.

[56] A. Cataliotti, V. Cosentino, S. Guaiana, D. Di Cara, N. Panzavecchia and G. Tine, "An Interface Protectiono System with Power Line Communication for Distributed Generators Remote Control," in *IEEE International Workshop on Applied Measurements for Power Systems*, Aachen, 2014.

[57] H. M. Zeineldin, H. H. Sharaf and E. El-Saadany, "Protection Coordination for Microgrids with Grid-Connected and Islanded Capabilities using Dual Setting Directional Overcurrent Relays," *IEEE Transactions on Smart Grid,* p. DOI: 10.1109/TSG.2016.2546961, 2016.

[58] S. T. Srinivas and H. Swarup, "Optimal relay coordination and communication based protection for microgrids," in *IEEE Region 10 Symposium*, Cochin, 2017.

[59] F. Coffele, C. Booth and A. Dysko, "An Adaptive Overcurrent Protection Scheme for Distribution Networks," *IEEE Transactions on Power Delivery,* vol. 30, no. 2, pp. 561-568, 2015.

[60] Y. Seyedi and H. Karimi, "Coordinated Protection and Control Based on Synchrophasor Data Processing in Smart Distribution Networks," *IEEE Transactions on Power Systems,* p. DOI: 10.1109/TPWRS.2017.2708662, 2017.

[61] N. Davydova and G. Hug, "Travelling Wave Based Protection for Medium Voltage Grids with Distributed Generation," in *IEEE PowerTech Conference*, Manchester, 2017.

[62] M. Michalic, W. Rebizant, M. Lokuwicz, S. J. Lee and S. H. Kang, "High Impedance Fault Detection in Distribution Networks with the use of Wave-let Based Algorithm," *IEEE Transactions on Power Delivery,* vol. 21, no. 4, pp. 1793-1802, 2006.

[63] Y. S. Ko, T. K. Kang, H. Y. Park, H. Y. Kim and H. S. Nam, "The FRTU-Based Fault-Zone Isolation Method in the Distribution Systems," *IEEE Transactions on Power Delivery,* vol. 25, no. 2, pp. 1001-1009, 2010.

[64] X. Jin, R. Gokaraju, R. Wierckx and O. Nayak, "High Speed Digital Distance Relaying Scheme using FPGA and IEC 61850," *IEEE Transactions on Smart Grid,* p. DOI: 10.1109/TSG.2017.2655499, 2017.

[65] N. A. Mohamed and M. M. Salama, "A review on the Proposed Solutions to Microgrid Protection Problems," in *IEEE Conference on Electrical and Computer Engineering*, Vancouver, 2016.

[66] M. Dewadasa, A. Ghosh and G. Ledwich, "Protection of Microgrids Using Differential Relays," in *IEEE AUPEC*, Brisbane, 2011.

[67] S. T. Horowitz and A. G. Phadke, Power System Relaying, 4th ed., Wiley and Sons Ltd., 2014.

[68] General Electric Power Management, *T60 Percent Differential Calculations,* 2002.

[69] L. L. Grigsby, Power System Stability and Control, 2nd ed., CRC Press, 2007.

[70] *IEEE Guide for the Application of Current Transformers Used for Protective Relaying Purposes,* 2007.

[71] Cooper Power Systems, "Kearney Type T TCC," 2013. [Online]. Available: http://www.cooperindustries.com/content/dam/public/powersystems/resources/library/Kearney/K51000AB.pdf. [Accessed January 2017].

[72] D. H. Trinh and H. Chafouk, "Fault Detection and Isolation using Kalman Filter Bank for a Wind Turbine Generator," in *IEEE Mediterranean Conference on Control and Automation*, Corfu, 2011.

[73] E. Mukherjee, S. Sengupta and S. P. Duttagupta, "A Heuristic Approach of Estimation and Prediction of Short-Circuit Current of a Photovoltaic Cell by Kalman Filter," in *IEEE India Conference*, Pune, 2014.

[74] M. M. Mansour, S. F. Mekhamer and N. E. El-Kharbawe, "A Modified Particle Swarm Optimizer for the Coordination of Directional Overcurrent Relays," *IEEE Transactions on Power Delivery,* vol. 22, no. 3, pp. 1400-1410, 2007.

[75] M. A. Abido, "Optimal Design of Power-System Stabilizers Using Particle Swarm Optimization," *IEEE Transactions on Energy Conversion,* vol. 17, no. 3, pp. 406-413, 2002.

[76] N. I. Sapankevych and R. Sankar, "Constrained Motion Particle Swarm Optimization and Support Vector Regression for Non-Linear Time Series Regression and Predication Applications," in *IEEE Conference on Machine Learning and Applications*, Miami, 2013.

[77] F. van den Bergh and A. P. Engelbrecht, "A New Locally Convergent Particle Swarm Optimizer," in *IEEE International Conference on Systems, Man and Cybernetics*, Tunisia, 2002.

[78] F. Katiraei, J. Holbach and T. Chang, "Investigation of Solar PV Inverters Current Contributions during Faults on Distribution and Transmission Systems Interruption Capacity," in *Western Protective Relay Conference*, Spokane, 2012.

[79] D. Turcotte and F. Katiraei, "Fault Contribution of Grid-Connected Inverters," in *IEEE Electric Power and Energy Conference*, Montreal, 2009.

APPENDIX A

DATA FOR THE MODELS AND SYSTEMS UNDER STUDY

A.1 Synchronous Generators

Table A.1: Synchronous generator data.

Armature resistance, r_a , p.u.	0.002
Direct-axis synchronous reactance, x_d , p.u.	2.9
Quadrature-axis synchronous reactance, x_q , p.u.	1.4
Direct-axis transient reactance, x'_d , p.u.	0.254
Direct-axis subtransient reactance, x''_d , p.u.	0.14
Quadrature-axis subtransient reactance, x''_q , p.u.	0.154
T'_d , s	0.09
T''_d , s	0.011
T'_q ,s	0.09
T''_q ,s	0.011
Moment of inertia	1.4

A.2 DFIG Wind Farms

Table A.2: DFIG wind farm data.

Generator capacity (MVA)	1.5
Generator voltage (kV)	0.575
DC nominal voltage (V)	1150
Number of poles	6
Average wind speed (m/s)	11.24

A.3 PV Farms

Table A.3: PV plant data.

Generator voltage (kV)	Rated irradiance (W/m^2)	Temperature reference (degrees Celsius)
0.575	1000	25

A.4 Line and Cable Data

Table A.4: Line data.

Conductor Type	Raven	Pigeon	Tulip
Positive Sequence Resistance (Ω/km)	0.536	0.339	0.173
Positive Sequence Reactance (Ω/km)	0.342	0.323	0.291
Positive Sequence Capacitive Reactance (µS/km)	5.102	5.405	5.848
Zero Sequence Resistance (Ω/km)	1.548	0.979	0.4996
Zero Sequence Reactance (Ω/km)	0.988	0.933	0.84
Zero Sequence Capacitive Reactance (µS/km)	1.99	2.109	2.398

A.5 Transformers

Table A.5: Transformer data.

	Substation	Interconnecting Transformer	SM Plants	Wind Plants
Rating, MVA	100	100	5	200
Rated voltage	138/25 kV	13.8/25 kV	0.48/13.8 kV	34.5/13.8 kV
Winding X (per unit)	0.001	0.625	0.11	0.011
Winding impedance on winding 1	0.1	0.1	0.9	0.9
Configuration	Wye-Gnd/ Wye-Gnd	Wye-Gnd/ Wye-Gnd	Delta/Wye-Gnd	Delta/Wye-Gnd

A.6 Exciter Data

Table A.6: SEXS Exciter and PSS1A Stabilizer data.

$T_A = 0$	$T_E = 0$
$T_B = 0$	$E_{max} = 10$
$K = 100$	$E_{min} = -10$
$A_1 = 0$	$A_2 = 0$
$T_1 = 0$	$T_2 = 0.7$
$T_3 = 0.1$	$T_4 = 0.7$
$V_{STMAX} = 0.15$	$V_{STMIN} = -0.15$
$T_5 = 0.016$	$T_6 = 0$
$K_S = 5$	

A.7 Governor Data

Table A.7: IEEEG3 Governor data.

$T_G = 0.5$	$T_P = 0.04$
$T_R = 4$	$P_{max} = 1$
$SIGMA = 0.05$	$P_{min} = 0.01$
$DELTA = 0.3$	$U_0 = 0.25$
$U_C = -0.1$	

APPENDIX B

CASE STUDY DATA AND RESULTS FOR THE DG RECLOSING SCHEME

Table B.1: Results for a DG unit at bus 2 and a fault at bus 1 for a Wye grounded Delta transformer connection.

	Rating (MVA)	16	16	8	8	1.6	1.6
		100%	100%	50%	50%	10%	10%
	Fault Type	Three-Phase	Double-Line-to-Ground	Three-Phase	Double-Line-to-Ground	Three-Phase	Double-Line-to-Ground
RE2 FAST	Current (A)	4244	4162	4244	4162	4244	4162
	Trip Time (s)	0.0755	0.0798	0.0755	0.0798	0.0755	0.0798
	Current (A) with RD	4239	4152	4242	4154	4244	4157
	Trip Time (s) with RD	0.0759	0.0806	0.0757	0.0805	0.0756	0.0802
DG	Current (A)	1564	1689	873	933	196	206
	Reconnect time (s)	5.1857	5.3307	3.1520	3.2210	4.8072	2.3152
	Trip Time (s)	0.0112	0.0130	0.0080	0.0101	0.0088	0.0085
Fuse 1	Current (A)	4229	4141	4229	4141	4229	4141
	Trip Time (s)	0.0990	0.1035	0.0990	0.1035	0.0990	0.1035
	Current (A) with RD	4222	4134	4222	4134	4230	4137
	Trip Time (s) with RD	0.0991	0.1044	0.0991	0.1014	0.0990	0.1045

Table B.2: Results for a DG unit at bus 2 and a fault at bus 1 for a Wye grounded Wye grounded transformer connection.

	Rating (MVA)	16	16	8	8	1.6	1.6
		100%	100%	50%	50%	10%	10%
	Fault Type	Three-Phase	Double-Line-to-Ground	Three-Phase	Double-Line-to-Ground	Three-Phase	Double-Line-to-Ground
RE2 FAST	Current (A)	4244	4162	4244	4162	4244	4162
	Trip Time (s)	0.0755	0.0798	0.0755	0.0798	0.0755	0.0798
	Current (A) with RD	4239	4152	4242	4154	4244	4157
	Trip Time (s) with RD	0.0759	0.0806	0.0757	0.0800	0.0756	0.0802
DG	Current (A)	2760	2918	1848	1893	516	531
	Reconnect time (s)	6.7173	7.9034	4.3300	5.2200	5.8096	7.6100
	Trip Time (s)	0.0060	0.0080	0.0068	0.0072	0.0070	0.0066
Fuse 1	Current (A)	4229	4141	4229	4141	4229	4141
	Trip Time (s)	0.0990	0.1035	0.0990	0.1035	0.0990	0.1035
	Current (A) with RD	4222	4132	4222	4134	4230	4137
	Trip Time (s) with RD	0.0991	0.1042	0.0988	0.1040	0.0990	0.1017

Table B.3: Results for a DG unit at bus 5 and a fault at bus 1 for a Wye grounded Delta transformer connection.

	Rating (MVA)	16	16	8	8	1.6	1.6
		100%	100%	50%	50%	10%	10%
	Fault Type	Three-Phase	Double-Line-to-Ground	Three-Phase	Double-Line-to-Ground	Three-Phase	Double-Line-to-Ground
RE2 FAST	Current (A)	4244	4162	4244	4162	4244	4162
	Trip Time (s)	0.0755	0.0798	0.0755	0.0798	0.0755	0.0798
	Current (A) with RD	4236	4139	4240	4141	4244	4160
	Trip Time (s) with RD	0.0758	0.0806	0.0757	0.0806	0.0756	0.0802
DG	Current (A)	1288	1381	742	778	163	168
	Reconnect time (s)	3.9368	4.0135	3.2387	3.3345	2.5126	7.3214
	Trip Time (s)	0.0154	0.0140	0.0152	0.0135	0.0092	0.0085
Fuse 1	Current (A)	4229	4141	4229	4141	4229	4141
	Trip Time (s)	0.0990	0.1035	0.0990	0.1035	0.0990	0.1035
	Current (A) with RD	4238	4136	4238	4139	4229	4140
	Trip Time (s) with RD	0.0990	0.0962	0.0990	0.1045	0.0986	0.1039

Table B.4: Results for a DG unit at bus 5 and a fault at bus 1 for a Wye grounded Wye grounded transformer connection.

	Rating (MVA)	16	16	8	8	1.6	1.6
		100%	100%	50%	50%	10%	10%
	Fault Type	Three-Phase	Double-Line-to-Ground	Three-Phase	Double-Line-to-Ground	Three-Phase	Double-Line-to-Ground
RE2 FAST	Current (A)	4244	4162	4244	4162	4244	4162
	Trip Time (s)	0.0755	0.0798	0.0755	0.0798	0.0755	0.0798
	Current (A) with RD	4238	4138	4242	4140	4244	4161
	Trip Time (s) with RD	0.0758	0.0806	0.0757	0.0806	0.0756	0.0803
DG	Current (A)	2157	2167	1459	1499	430	430
	Reconnect time (s)	6.3780	6.4368	3.5198	3.6965	1.7769	3.8841
	Trip Time (s)	0.0098	0.0122	0.0081	0.0080	0.0070	0.0066
Fuse 1	Current (A)	4229	4141	4229	4141	4229	4141
	Trip Time (s)	0.0990	0.1035	0.0990	0.1035	0.0990	0.1035
	Current (A) with RD	4236	4135	4240	4137	4229	4140
	Trip Time (s) with RD	0.0987	0.1039	0.0965	0.1045	0.0981	0.1045

Table B.5: Results for a DG unit at bus 6 and a fault at bus 1 for a Wye grounded Delta transformer connection.

	Rating (MVA)	16	16	8	8	1.6	1.6
		100%	100%	50%	50%	10%	10%
	Fault Type	Three-Phase	Double-Line-to-Ground	Three-Phase	Double-Line-to-Ground	Three-Phase	Double-Line-to-Ground
RE2 FAST	Current (A)	4244	4162	4244	4162	4244	4162
	Trip Time (s)	0.0755	0.0798	0.0755	0.0798	0.0755	0.0798
	Current (A) with RD	4266	4185	4244	4188	4245	4161
	Trip Time (s) with RD	0.0754	0.0798	0.0755	0.0797	0.0755	0.0798
DG	Current (A)	1009	1022	591	606	140	150
	Reconnect time (s)	1.7481	1.7462	1.9520	2.0145	3.9692	2.7812
	Trip Time (s)	0.0164	0.0165	0.0156	0.0153	0.0150	0.0131
Fuse 1	Current (A)	4229	4141	4229	4141	4229	4141
	Trip Time (s)	0.0990	0.1035	0.0990	0.1035	0.0990	0.1035
	Current (A) with RD	4251	4165	4228	4168	4230	4140
	Trip Time (s) with RD	0.0993	0.1017	0.0990	0.1030	0.0992	0.1035

Table B.6: Results for a DG unit at bus 6 and a fault at bus 1 for a Wye grounded Wye grounded transformer connection.

	Rating (MVA)	16	16	8	8	1.6	1.6
		100%	100%	50%	50%	10%	10%
	Fault Type	Three-Phase	Double-Line-to-Ground	Three-Phase	Double-Line-to-Ground	Three-Phase	Double-Line-to-Ground
RE2 FAST	Current (A)	4244	4162	4244	4162	4244	4162
	Trip Time (s)	0.0755	0.0798	0.0755	0.0798	0.0755	0.0798
	Current (A) with RD	4266	4186	4268	4188	4244	4163
	Trip Time (s) with RD	0.0754	0.0797	0.0754	0.0797	0.0755	0.0798
DG	Current (A)	1491	1428	1063	1025	333	330
	Reconnect time (s)	4.0190	1.3838	3.4707	3.6357	1.6469	5.9997
	Trip Time (s)	0.0168	0.0141	0.0141	0.0128	0.0076	0.0071
Fuse 1	Current (A)	4229	4141	4229	4141	4229	4141
	Trip Time (s)	0.0990	0.1035	0.0990	0.1035	0.0990	0.1035
	Current (A) with RD	4251	4166	4253	4168	4228	4142
	Trip Time (s) with RD	0.0997	0.1032	0.0992	0.1030	0.1003	0.1042

Table B.7: Results for a DG unit at bus 3 and a fault at bus 6 for a Wye grounded Delta transformer connection.

	Rating (MVA)	16	16	8	8	1.6	1.6
		100%	100%	50%	50%	10%	10%
	Fault Type	Three-Phase	Double-Line-to-Ground	Three-Phase	Double-Line-to-Ground	Three-Phase	Double-Line-to-Ground
RE2 FAST	Current (A)	3090	2953	3090	2953	3090	2953
	Trip Time (s)	0.0750	0.0874	0.0750	0.0874	0.0750	0.0874
	Current (A) with RD	3084	2941	3085	2943	3090	2953
	Trip Time (s) with RD	0.0754	0.0879	0.0753	0.0879	0.0751	0.0876
DG	Current (A)	1138	1183	647	686	153	153
	Reconnect time (s)	5.0480	5.1491	3.1375	3.2168	2.9630	1.7664
	Trip Time (s)	0.0156	0.0146	0.0154	0.0140	0.0110	0.0122
Fuse 1	Current (A)	3077	2939	3077	2939	3077	2939
	Trip Time (s)	0.0994	0.1093	0.0994	0.1093	0.0994	0.1093
	Current (A) with RD	3084	2941	3086	2943	3077	2938
	Trip Time (s) with RD	0.0990	0.1098	0.0990	0.1097	0.0992	0.1097

Table B.8: Results for a DG unit at bus 3 and a fault at bus 6 for a Wye grounded Wye grounded transformer connection.

	Rating (MVA)	16	16	8	8	1.6	1.6
		100%	100%	50%	50%	10%	10%
	Fault Type	Three-Phase	Double-Line-to-Ground	Three-Phase	Double-Line-to-Ground	Three-Phase	Double-Line-to-Ground
RE2 FAST	Current (A)	3090	2953	3090	2953	3090	2953
	Trip Time (s)	0.0750	0.0874	0.0750	0.0874	0.0750	0.0874
	Current (A) with RD	3084	2941	3085	2943	3090	2953
	Trip Time (s) with RD	0.0754	0.0879	0.0753	0.0879	0.0751	0.0876
DG	Current (A)	1797	1759	1241	1231	374	388
	Reconnect time (s)	5.8148	5.8793	3.3322	3.4640	1.8006	1.6162
	Trip Time (s)	0.0146	0.0129	0.0087	0.0087	0.0072	0.0069
Fuse 1	Current (A)	3077	2939	3077	2939	3077	2939
	Trip Time (s)	0.0994	0.1093	0.0994	0.1093	0.0994	0.1093
	Current (A) with RD	3084	2941	3085	2943	3077	2938
	Trip Time (s) with RD	0.0993	0.1095	0.0987	0.1107	0.1010	0.1095

Table B.9: Recloser RE2 results for a DG unit at bus 2 and a fault at bus 1 for a Wye grounded Wye grounded transformer connection with varying fault impedances.

Fault Impedance (ohm)	Fault Type	Current (A) NO DG	Model (s) NO DG	Current (A) WITH DG	Model (s) WITH DG
0	Three-Phase	4244	0.0755	4239	0.0758
1	Three-Phase	3748	0.076	3632	0.07695
6.25	Three-Phase	1890	0.08155	1630	0.0868
8.125	Three-Phase	1590	0.08395	1320	0.09135
0	Line-to-Line-to-Ground	4162	0.0798	4120	0.0807
1	Line-to-Line-to-Ground	4294	0.0797	4233	0.0805
6.25	Line-to-Line-to-Ground	4086	0.07995	3976	0.08125
8.125	Line-to-Line-to-Ground	4031	0.0802	3916	0.0814
0	Three-Phase	4244	0.0755	4241	0.0757
1	Three-Phase	3748	0.076	3686	0.07655
6.25	Three-Phase	1890	0.08155	1789	0.08295
8.125	Three-Phase	1590	0.08395	1509	0.08735
0	Line-to-Line-to-Ground	4162	0.0798	4141	0.0806
1	Line-to-Line-to-Ground	4294	0.0797	4262	0.08045
6.25	Line-to-Line-to-Ground	4086	0.07995	4015	0.081
8.125	Line-to-Line-to-Ground	4031	0.0802	3960	0.08115

Table B.10: Fuse 1 and DG current results for a DG unit at bus 2 and a fault at bus 1 for a Wye grounded Wye grounded transformer connection with varying fault impedances.

Impedance (ohm)	Fault Type	Current (A) NO DG	Model (s) NO DG	Current (A) WITH DG	Model (s) WITH DG	DG Current (A)
0	Three-Phase	4229	0.1323	6745	0.08675	2543
1	Three-Phase	3689	0.15635	5474	0.10035	2050
6.25	Three-Phase	1750	0.5192	2017	0.2448	687
8.125	Three-Phase	1442	0.74865	1632	0.26625	592
0	Line-to-Line-to-Ground	4141	0.1368	6567	0.08895	2478
1	Line-to-Line-to-Ground	4266	0.13515	6714	0.0871	2511
6.25	Line-to-Line-to-Ground	4030	0.1425	6407	0.09055	2451
8.125	Line-to-Line-to-Ground	3971	0.14455	6305	0.09075	2466
0	Three-Phase	4229	0.1323	5800	0.0973	1603
1	Three-Phase	3689	0.15635	4849	0.1212	1348
6.25	Three-Phase	1750	0.5192	2017	0.2448	436
8.125	Three-Phase	1442	0.74865	1553	0.26975	336
0	Line-to-Line-to-Ground	4141	0.1368	5728	0.09625	1617
1	Line-to-Line-to-Ground	4266	0.13515	5828	0.0972	1620
6.25	Line-to-Line-to-Ground	4030	0.1425	5528	0.1008	1600
8.125	Line-to-Line-to-Ground	3971	0.14455	5518	0.1007	1599

Table B.11: Recloser RE2 results for a DG unit at bus 5 and a fault at bus 1 for a Wye grounded Wye grounded transformer connection with varying fault impedances.

Fault Impedance (ohm)	Fault Type	Current (A) NO DG	Model (s) NO DG	Current (A) WITH DG	Model (s) WITH DG
0	Three-Phase	4244	0.0755	4104	0.0759
1	Three-Phase	3748	0.076	3531	0.07725
6.25	Three-Phase	1890	0.08155	1580	0.08675
8.125	Three-Phase	1590	0.08395	1286	0.0907
0	Line-to-Line-to-Ground	4162	0.0798	4105	0.0807
1	Line-to-Line-to-Ground	4294	0.0797	3535	0.08235
6.25	Line-to-Line-to-Ground	4086	0.07995	1651	0.09795
8.125	Line-to-Line-to-Ground	4031	0.0802	1378	0.10325
0	Three-Phase	4244	0.0755	4160	0.0758
1	Three-Phase	3748	0.076	3650	0.07515
6.25	Three-Phase	1890	0.08155	1749	0.08435
8.125	Three-Phase	1590	0.08395	1441	0.0873
0	Line-to-Line-to-Ground	4162	0.0798	4161	0.08045
1	Line-to-Line-to-Ground	4294	0.0797	3662	0.0814
6.25	Line-to-Line-to-Ground	4086	0.07995	1754	0.0944
8.125	Line-to-Line-to-Ground	4031	0.0802	1478	0.09885

Table B.12: Fuse 1 and DG current results for a DG unit at bus 5 and a fault at bus 1 for a Wye grounded Wye grounded transformer connection with varying fault impedances.

Impedance (ohm)	Fault Type	Current (A) NO DG	Model (s) NO DG	Current (A) WITH DG	Model (s) WITH DG	DG Current (A)
0	Three-Phase	4229	0.1323	6068	0.0939	2021
1	Three-Phase	3689	0.15635	4786	0.11365	1605
6.25	Three-Phase	1750	0.5192	1965	0.14535	615
8.125	Three-Phase	1442	0.74865	1431	0.4914	533
0	Line-to-Line-to-Ground	4141	0.1368	6060	0.0939	2026
1	Line-to-Line-to-Ground	4266	0.13515	4903	0.1135	1596
6.25	Line-to-Line-to-Ground	4030	0.1425	1925	0.1377	626
8.125	Line-to-Line-to-Ground	3971	0.14455	1570	0.4611	677
0	Three-Phase	4229	0.1323	5452	0.10285	1354
1	Three-Phase	3689	0.15635	4542	0.12795	1090
6.25	Three-Phase	1750	0.5192	1893	0.31515	380
8.125	Three-Phase	1442	0.74865	1540	0.41325	321
0	Line-to-Line-to-Ground	4141	0.1368	5444	0.1017	1347
1	Line-to-Line-to-Ground	4266	0.13515	4517	0.12665	1066
6.25	Line-to-Line-to-Ground	4030	0.1425	1888	0.135	384
8.125	Line-to-Line-to-Ground	3971	0.14455	1534	0.4158	297

APPENDIX C

CASE STUDY DATA AND RESULTS FOR THE DG RECLOSING AND FAULT DETECTION SCHEME

Table C.1: Results for ROCOC for the bolted fault cases.

Fault at	DG at	Rating (MVA)	Fault Type	RD Trip Time (s)	ΔI (A/s)
1	2	8	Three-Phase	0.01245	218
1	2	8	Line-to-Line-to-Ground	0.01045	131
5	2	8	Three-Phase	0.00905	114
5	2	8	Line-to-Line-to-Ground	0.01245	92
1	5	8	Three-Phase	0.01425	163
1	5	8	Line-to-Line-to-Ground	0.01315	99
2	5	8	Three-Phase	0.01465	130
2	5	8	Line-to-Line-to-Ground	0.00915	83

Table C.2: Results for ROCOC for faults with a 3 Ω fault impedance.

Fault at	DG at	Rating (MVA)	Fault Type	RD Trip Time (s)	ΔI (A/s)
1	2	8	Three-Phase	0.01117	119
1	2	8	Line-to-Line-to-Ground	0.0117	125
5	2	8	Three-Phase	0.0164	74
5	2	8	Line-to-Line-to-Ground	0.0136	108
1	5	8	Three-Phase	0.01475	93
1	5	8	Line-to-Line-to-Ground	0.00975	94
2	5	8	Three-Phase	0.01785	80
2	5	8	Line-to-Line-to-Ground	0.01755	103

Table C.3: Results for ROCOC for a sudden load change.

DG size	DG location	Fault bus	Load Change (MVA)	ΔI (A/s)
8	2	2	10	8.11
8	2	5	10	7

Table C.4: Results for ROCOC for varying DG locations, sizes and fault impedances.

DG size	DG location	Fault bus	Fault type	Fault Impedance (Ω)	ΔI (A/s)
8	2	1	Three-Phase	0	218
8	2	1	Line-to-Ground	0	90
8	2	1	Line-to-Ground	10	28
8	2	1	Line-to-Line	0	210
8	2	1	Line-to-Line-to-Ground	0	131
8	2	5	Three-Phase	0	114
8	2	5	Three-Phase	10	38
8	2	5	Line-to-Ground	0	48
8	2	5	Line-to-Ground	10	20
8	2	5	Line-to-Line	0	60
8	2	5	Line-to-Line-to-Ground	0	92
4	2	1	Line-to-Ground	0	62
4	2	1	Line-to-Ground	10	20
4	2	5	Line-to-Ground	0	33
4	2	5	Line-to-Ground	10	18

APPENDIX D

CASE STUDY DATA FOR THE HYBRID MICROGRID PROTECTION SCHEME

Table D.1: Short circuit data for PV based DG sources with a microgrid in grid connected mode.

Fault Type	Three-Phase		Line-to-Line		Line-to-Ground		Line-to-Line-to-Ground	
Relay	I_{fmax}	I_{load}	I_{fmax}	I_{load}	I_{fmax}	I_{load}	I_{fmax}	I_{load}
RUM	1774	20	1774	20	1824	20	1775	20
RP1	1719	10	1685	10	2124	10	2195	10
RP4	1719	10	1685	10	2124	10	2195	10
R1	1640	10	1615	10	2425	10	2691	10
R2	1566	10	1526	10	2320	10	2502	10
R3	1510	4.7	1431	4.7	2206	4.7	2423	4.7
R4	1640	4.7	1615	4.7	2425	4.7	2691	4.7
R5	1566	10	1526	10	2320	10	2502	10
R6	1510	4.7	1431	4.7	2206	4.7	2423	4.7

Table D.2: Short circuit data for PV based DG sources with a microgrid in islanded mode.

Fault Type	Three-Phase		Line-to-Line		Line-to-Ground		Line-to-Line-to-Ground	
Relay	I_{fmax}	I_{load}	I_{fmax}	I_{load}	I_{fmax}	I_{load}	I_{fmax}	I_{load}
RUM	55	8.59	65	8.59	89.3	8.59	96.1	8.59
RP1	28	4.3	32	4.3	45	4.3	47	4.3
RP4	28	4.3	32	4.3	45	4.3	47	4.3
R1	53.6	9.3	63	9.3	89.15	9.3	94.14	9.3
R2	53.6	9.3	63	9.3	89.13	9.3	93.98	9.3
R3	53.5	4.65	60	4.65	89.2	4.65	93.67	4.65
R4	53.6	9.3	63	9.3	89.15	9.3	94.14	9.3
R5	53.6	9.3	63	9.3	89.13	9.3	93.98	9.3
R6	53.5	4.65	60	4.65	89.2	4.65	93.67	4.65

Table D.3: Short circuit data for synchronous machine based DG sources with a microgrid in grid connected mode.

Fault Type	Three-Phase		Line-to-Line		Line-to-Ground		Line-to-Line-to-Ground	
Relay	I_{fmax}	I_{load}	I_{fmax}	I_{load}	I_{fmax}	I_{load}	I_{fmax}	I_{load}
RUM	1729	9.76	1755	9.76	1917	9.76	1864	9.76
RP1	1845	4.86	1798	4.86	2023	4.86	1954	4.86
RP4	1845	4.88	1798	4.88	2023	4.88	1954	4.88
R1	1902	9.3	1844	9.3	2051	9.3	2057	9.3
R2	1815	9.3	1737	9.3	1884	9.3	1992	9.3
R3	1733	4.65	1619	4.65	1731	4.65	1886	4.65
R4	1902	9.3	1844	9.3	2051	9.3	2057	9.3
R5	1815	9.3	1737	9.3	1884	9.3	1992	9.3
R6	1733	4.65	1619	4.65	1731	4.65	1886	4.65

Table D.4: Short circuit data for synchronous machine based DG sources with a microgrid in islanded mode.

Fault Type	Three-Phase		Line-to-Line		Line-to-Ground		Line-to-Line-to-Ground	
Relay	I_{fmax}	I_{load}	I_{fmax}	I_{load}	I_{fmax}	I_{load}	I_{fmax}	I_{load}
RUM	293	9.76	302	9.76	345	9.76	302	9.76
RP1	148	4.86	150	4.86	176	4.86	152	4.86
RP4	148	4.88	150	4.88	176	4.88	152	4.88
R1	293	9.3	300	9.3	352	9.3	351	9.3
R2	293	9.3	300	9.3	352	9.3	351	9.3
R3	292	4.65	299	4.65	351	4.65	350	4.65
R4	293	9.3	300	9.3	352	9.3	351	9.3
R5	293	9.3	300	9.3	352	9.3	351	9.3
R6	292	4.65	299	4.65	351	4.65	350	4.65

In every case, there were no false tripping instances and the correct protective device (differential or adaptive overcurrent relay) operated when faults occurred.

APPENDIX E

TRAINING AND ANAYLSIS DATA FOR POWER PLANTS USED IN THE PARTICLE SWARM OPTIMIZATION SCHEME

E.1 Wind Plant 2 Training Data

Table E.1: Training Data for Generation Plant 2 when no other plants are operating.

	Wind Speed (m/s)	11.24	11	10	9	8	7	6
	Rating (%)	100.00	97.86	88.97	80.07	71.17	62.28	53.38
Fault Current/ Fault Type (A)	Three-Phase	301	297	287	282	280	278	275
	Line-to-Line	325	316	294	277	265	255	247
	Line-to-Line-to-Ground	831	832	833	835	843	849	863
	Line-to-Ground	1064	1061	1055	1048	1040	1031	1025
	PEN (%)	100.00	100.00	100.00	100.00	100.00	100.00	100.00
Plant pre-fault current (A)	1	0	0	0	0	0	0	0
	2	137	131	108	92	82	78	77
	3	0	0	0	0	0	0	0
	4	0	0	0	0	0	0	0
	5	0	0	0	0	0	0	0
	6	0	0	0	0	0	0	0

Table E.2: Training Data for Generation Plant 2 when all other plants are operating at full capacity.

	Wind Speed (m/s)	11.24	11	10	9	8	7	6
	Rating (%)	100.00	97.86	88.97	80.07	71.17	62.28	53.38
Fault Current/ Fault Type (A)	Three-Phase	223	215	199	192	182	179	176
	Line-to-Line	276	271	250	229	210	199	191
	Line-to-Line-to-Ground	465	462	456	451	446	441	437
	Line-to-Ground	631	629	622	617	608	599	594
	PEN (%)	71.47	70.64	64.40	56.75	50.83	34.08	31.38
Plant pre-fault current (A)	1	42	42	42	42	42	42	42
	2	126	121	91	66	52	26	23
	3	8.3	8.3	8.3	8.3	8.3	8.3	8.3
	4	126	121	91	66	52	26	23
	5	43	43	43	43	43	43	43
	6	82	82	82	82	82	82	82

Table E.3: Training Data for Generation Plant 2 when the irradiance is 0 W/m^2 and plants 1 and 6 are operating at 80% capacity.

	Wind Speed (m/s)	11.24	11	10	9	8
	Rating (%)	100.00	97.86	88.97	80.07	71.17
Fault Current/ Fault Type (A)	Three-Phase	240	235	224	217	214
	Line-to-Line	296	288	264	244	226
	Line-to-Line-to-Ground	484	488	485	490	492
	Line-to-Ground	659	657	648	641	631
	PEN (%)	78.26	77.56	72.22	65.35	59.77
Plant pre-fault current (A)	1	35	35	35	35	35
	2	126	121	91	66	52
	3	0	0	0	0	0
	4	126	121	91	66	52
	5	0	0	0	0	0
	6	55	55	55	55	55

Table E.4: Training Data for Generation Plant 2 when the irradiance is 0 W/m^2 and plants 1 and 6 are operating at 60% capacity.

	Wind Speed (m/s)	11.24	11	10	9	8
	Rating (%)	100.00	97.86	88.97	80.07	71.17
Fault Current/ Fault Type (A)	Three-Phase	245	241	229	222	219
	Line-to-Line	298	289	265	245	226
	Line-to-Line-to-Ground	491	489	490	491	492
	Line-to-Ground	660	659	650	642	631
	PEN (%)	82.89	82.31	77.78	71.74	66.67
Plant pre-fault current (A)	1	26	26	26	26	26
	2	126	121	91	66	52
	3	0	0	0	0	0
	4	126	121	91	66	52
	5	0	0	0	0	0
	6	32	32	32	32	32

E.2 Wind Plant 4 Training Data

Table E.5: Training Data for Generation Plant 4 when no other plants are operating.

	Wind Speed (m/s)	11.24	11	10	9	8	7	6
	Rating (%)	100.00	97.86	88.97	80.07	71.17	62.28	53.38
Fault Current/ Fault Type (A)	Three-Phase	305	302	291	285	283	281	277
	Line-to-Line	327	321	297	281	267	257	250
	Line-to-Line-to-Ground	942	945	951	956	961	967	985
	Line-to-Ground	1191	1189	1182	1176	1169	1161	1155
	PEN (%)	100.00	100.00	100.00	100.00	100.00	100.00	100.00
Plant pre-fault current (A)	1	0	0	0	0	0	0	0
	2	0	0	0	0	0	0	0
	3	0	0	0	0	0	0	0
	4	138	132	109	92	83	78	77
	5	0	0	0	0	0	0	0
	6	0	0	0	0	0	0	0

Table E.6: Training Data for Generation Plant 4 when all other plants are operating at full capacity.

	Wind Speed (m/s)	11.24	11	10	9	8	7	6
	Rating (%)	100.00	97.86	88.97	80.07	71.17	62.28	53.38
Fault Current/ Fault Type (A)	Three-Phase	214	210	195	185	180	171	170
	Line-to-Line	288	282	256	239	223	210	198
	Line-to-Line-to-Ground	532	530	528	525	523	520	515
	Line-to-Ground	856	854	848	845	843	826	820
	PEN (%)	50.20	48.98	41.86	34.21	28.57	20.38	13.79
Plant pre-fault current (A)	1	42	42	42	42	42	42	42
	2	126	120	90	65	50	32	20
	3	8.3	8.3	8.3	8.3	8.3	8.3	8.3
	4	126	120	90	65	50	32	20
	5	43	43	43	43	43	43	43
	6	82	82	82	82	82	82	82

Table E.7: Training Data for Generation Plant 4 when the irradiance is 0 W/m^2 and plants 1 and 6 are operating at 80% capacity.

	Wind Speed (m/s)	11.24	11	10	9	8
	Rating (%)	100.00	97.86	88.97	80.07	71.17
Fault Current/ Fault Type (A)	Three-Phase	228	226	216	211	209
	Line-to-Line	291	285	264	247	231
	Line-to-Line-to-Ground	640	642	645	648	653
	Line-to-Ground	902	900	892	886	879
	PEN (%)	69.61	68.75	62.33	54.55	48.60
Plant pre-fault current (A)	1	35	35	35	35	35
	2	126	121	91	66	52
	3	0	0	0	0	0
	4	126	121	91	66	52
	5	0	0	0	0	0
	6	55	55	55	55	55

Table E.8: Training Data for Generation Plant 4 when the irradiance is 0 W/m^2 and plants 1 and 6 are operating at 60% capacity.

	Wind Speed (m/s)	11.24	11	10	9	8
	Rating (%)	100.00	97.86	88.97	80.07	71.17
Fault Current/ Fault Type (A)	Three-Phase	234	233	223	217	216
	Line-to-Line	294	288	267	247	235
	Line-to-Line-to-Ground	645	647	650	653	658
	Line-to-Ground	904	902	892	890	883
	PEN (%)	79.75	79.08	73.98	67.35	61.90
Plant pre-fault current (A)	1	26	26	26	26	26
	2	126	121	91	66	52
	3	0	0	0	0	0
	4	126	121	91	66	52
	5	0	0	0	0	0
	6	32	32	32	32	32

E.3 Biogas Plant 1 Training Data

Table E.9: Training Data for Generation Plant 1 when no other plants are operating.

	Rating (%)	100	90	80	70	60	50	40
Fault Current/ Fault Type (A)	Three-Phase	207	205	204	201	200	198	196
	Line-to-Line	212	209	206	203	200	197	193
	Line-to-Line-to-Ground	607	594	590	589	588	587	585
	Line-to-Ground	629	617	611	610	607	597	594
	PEN (%)	100.00	100.00	100.00	100.00	100.00	100.00	100.00
Plant pre-fault current (A)	1	42	39	35	31	26	22	17
	2	0	0	0	0	0	0	0
	3	0	0	0	0	0	0	0
	4	0	0	0	0	0	0	0
	5	0	0	0	0	0	0	0
	6	0	0	0	0	0	0	0

Table E.10: Training Data for Generation Plant 1 when all other plants are operating at full capacity.

	Rating (%)	100	90	80	70	60	50	40
Fault Current/ Fault Type (A)	Three-Phase	177	175	172	169	168	165	162
	Line-to-Line	194	187	186	183	180	174	170
	Line-to-Line-to-Ground	191	190	188	187	185	184	183
	Line-to-Ground	268	268	264	263	263	261	261
	PEN (%)	23.82	22.50	20.67	18.75	16.22	14.08	10.05
Plant pre-fault current (A)	1	42	39	35	31	26	22	15
	2	126	126	126	126	126	126	126
	3	8.3	8.3	8.3	8.3	8.3	8.3	8.3
	4	126	126	126	126	126	126	126
	5	43	43	43	43	43	43	43
	6	82	82	82	82	82	82	82

Table E.11: Training Data for Generation Plant 1 when the irradiance is 0 W/m^2 and wind speed is 10 m/s.

	Rating (%)	100	90	80	70	60
Fault Current/ Fault Type (A)	Three-Phase	188	184	180	176	174
	Line-to-Line	199	191	189	184	182
	Line-to-Line-to-Ground	196	193	191	190	188
	Line-to-Ground	272	271	269	268	266
	PEN (%)	31.58	30.00	27.78	25.41	22.22
Plant pre-fault current (A)	1	42	39	35	31	26
	2	91	91	91	91	91
	3	0	0	0	0	0
	4	91	91	91	91	91
	5	0	0	0	0	0
	6	82	82	82	82	82

Table E.12: Training Data for Generation Plant 1 when the irradiance is 0 W/m^2 and wind speed is 10 m/s with plants 2 and 4 having one generator disconnected.

	Rating (%)	100	90	80	70	60
Fault Current/ Fault Type (A)	Three-Phase	201	195	193	185	182
	Line-to-Line	204	201	196	189	187
	Line-to-Line-to-Ground	205	204	202	201	200
	Line-to-Ground	277	276	275	273	272
	PEN (%)	47.73	45.88	43.21	40.26	36.11
Plant pre-fault current (A)	1	42	39	35	31	26
	2	46	46	46	46	46
	3	0	0	0	0	0
	4	47	47	47	47	47
	5	0	0	0	0	0
	6	82	82	82	82	82

E.4 Biogas Plant 6 Training Data

Table E.13: Training Data for Generation Plant 6 when no other plants are operating.

	Rating (%)	100	90	80	70	60	50	40
Fault Current/ Fault Type (A)	Three-Phase	368	361	352	344	340	334	332
	Line-to-Line	357	345	335	327	319	314	310
	Line-to-Line-to-Ground	607	603	597	591	584	574	570
	Line-to-Ground	646	634	625	616	609	601	597
	PEN (%)	100.00	100.00	100.00	100.00	100.00	100.00	100.00
Plant pre-fault current (A)	1	0	0	0	0	0	0	0
	2	0	0	0	0	0	0	0
	3	0	0	0	0	0	0	0
	4	0	0	0	0	0	0	0
	5	0	0	0	0	0	0	0
	6	82	69	55	43	32	22	16

Table E.14: Training Data for Generation Plant 6 when all other plants are operating at full capacity.

	Rating (%)	100	90	80	70	60	50	40
Fault Current/ Fault Type (A)	Three-Phase	344	335	327	321	315	311	308
	Line-to-Line	356	342	332	321	312	310	302
	Line-to-Line-to-Ground	357	343	333	321	316	312	303
	Line-to-Ground	311	311	311	308	308	308	308
	PEN (%)	32.67	28.99	24.55	20.28	15.92	11.52	8.65
Plant pre-fault current (A)	1	42	42	42	42	42	42	42
	2	126	126	126	126	126	126	126
	3	8.3	8.3	8.3	8.3	8.3	8.3	8.3
	4	126	126	126	126	126	126	126
	5	43	43	43	43	43	43	43
	6	82	69	55	43	32	22	16

Table E.15: Training Data for Generation Plant 6 when the irradiance is 0 W/m^2 and wind speed is 10 m/s.

	Rating (%)	100	90	80	70	60
Fault Current/ Fault Type (A)	Three-Phase	347	339	330	324	318
	Line-to-Line	357	344	333	325	319
	Line-to-Line-to-Ground	361	345	336	328	318
	Line-to-Ground	312	311	311	311	311
	PEN (%)	47.40	43.13	37.67	32.09	26.02
Plant pre-fault current (A)	1	42	42	42	42	42
	2	91	91	91	91	91
	3	0	0	0	0	0
	4	91	91	91	91	91
	5	0	0	0	0	0
	6	82	69	55	43	32

Table E.16: Training Data for Generation Plant 6 when the irradiance is 0 W/m^2 and wind speed is 10 m/s with plants 2 and 4 having one generator disconnected.

	Rating (%)	100	90	80	70	60
Fault Current/ Fault Type (A)	Three-Phase	353	347	339	332	326
	Line-to-Line	357	344	334	326	319
	Line-to-Line-to-Ground	366	354	343	333	324
	Line-to-Ground	317	318	318	318	317
	PEN (%)	63.57	59.48	53.92	47.78	40.51
Plant pre-fault current (A)	1	42	42	42	42	42
	2	46	46	46	46	46
	3	0	0	0	0	0
	4	47	47	47	47	47
	5	0	0	0	0	0
	6	82	69	55	43	32

E.5 Wind Plant 2 Regression Analysis

As a result of the data presented in Appendix E.1 the following maximum and minimum short circuit current in relation to percentage rating graphs are obtained for each type of fault:

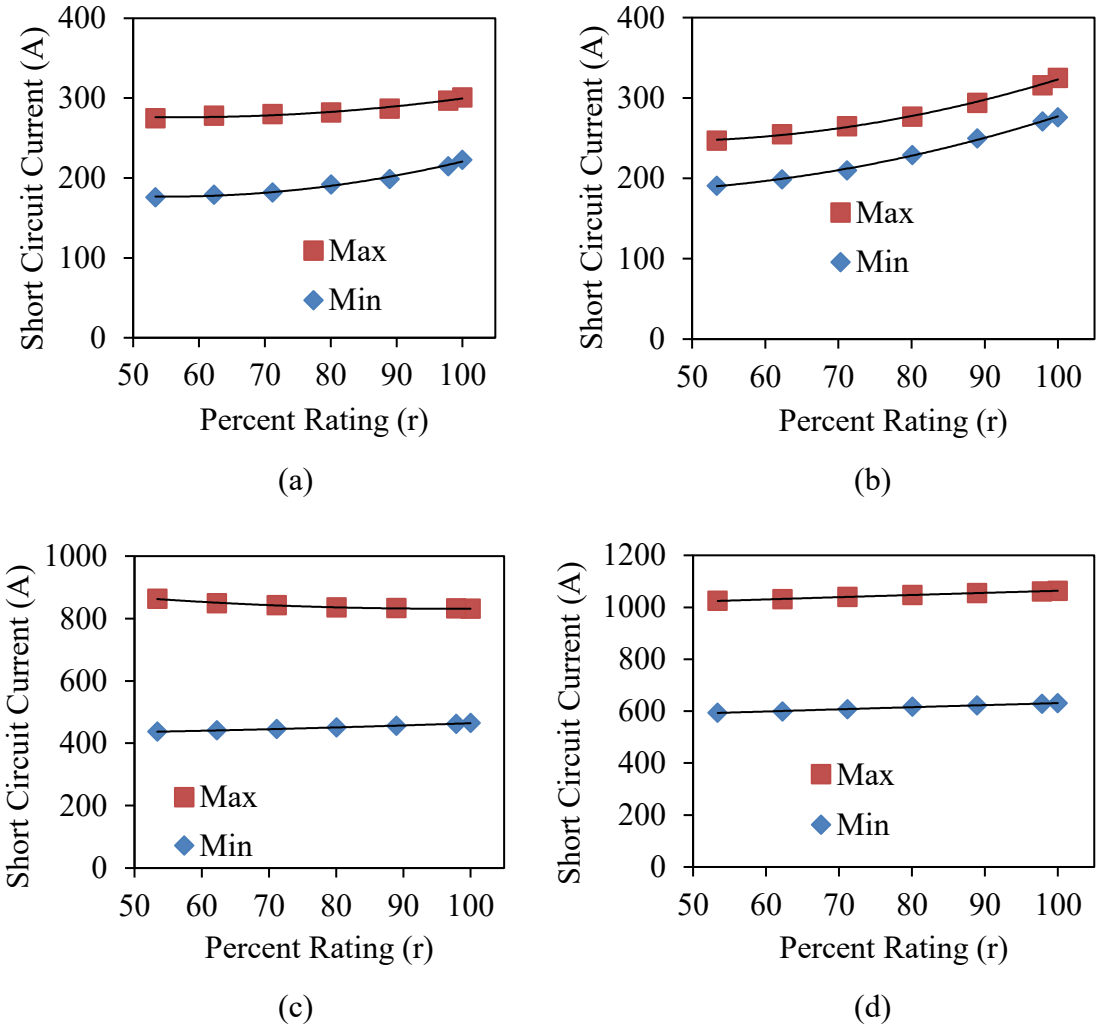

Figure E.1: Plant 2 short circuit current versus percentage rating for maximum and minimum cases for a: (a) three- phase fault, (b) line-to-line fault, (c) line-to-line-to-ground fault, (d) line-to-ground fault.

This gives the following maximum predicted short circuit currents:

$$I_{fr3PDG2} = 0.0128(r_{DG2})^2 - 1.469(r_{DG2}) + 318.16$$

$$I_{frLLDG2} = 0.0251(r_{DG2})^2 - 2.243(r_{DG2}) + 296.17$$

$$I_{frLLGDG2} = 0.0171(r_{DG2})^2 - 3.278(r_{DG2}) + 988.50$$

$$I_{frLGDG2} = -0.0011(r_{DG2})^2 + 1.011(r_{DG2}) + 973.59$$

As specified in Section 6.3.2, the fault ratio is required to be plotted against the percentage penetration for each percentage rating. This gives the following plots:

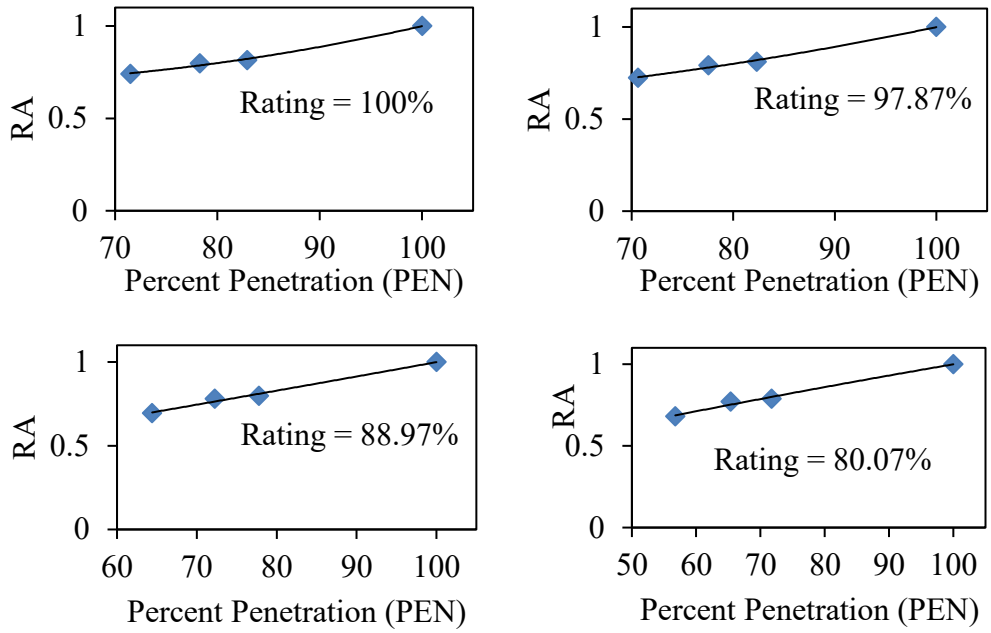

Figure E.2: Plant 2 three-phase short circuit ratios versus percentage penetration operating at various percentages of rated output.

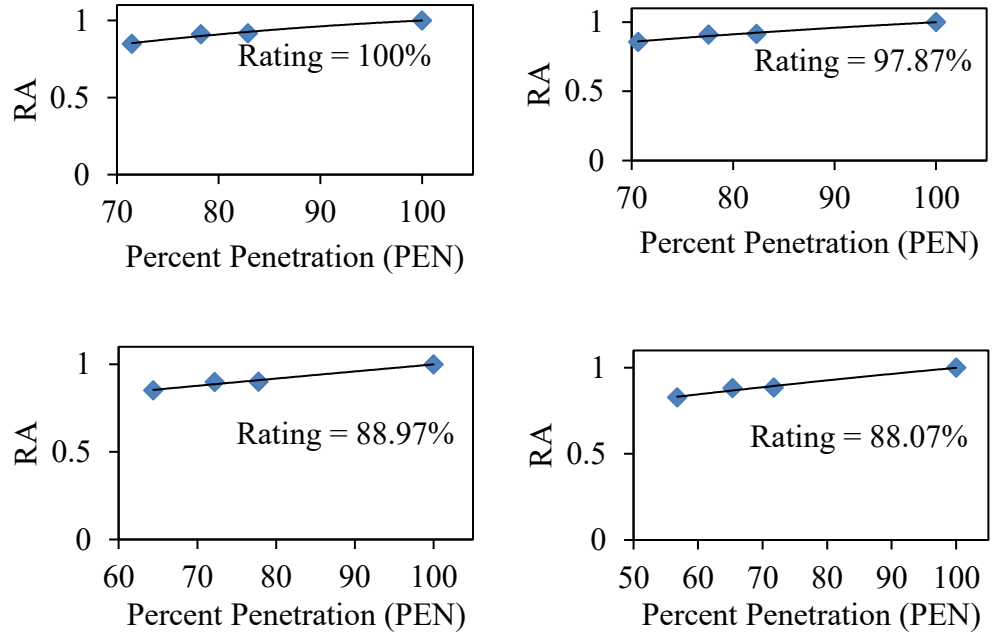

Figure E.3: Plant 2 line-to-line short circuit ratios versus percentage penetration operating at various percentages of rated output.

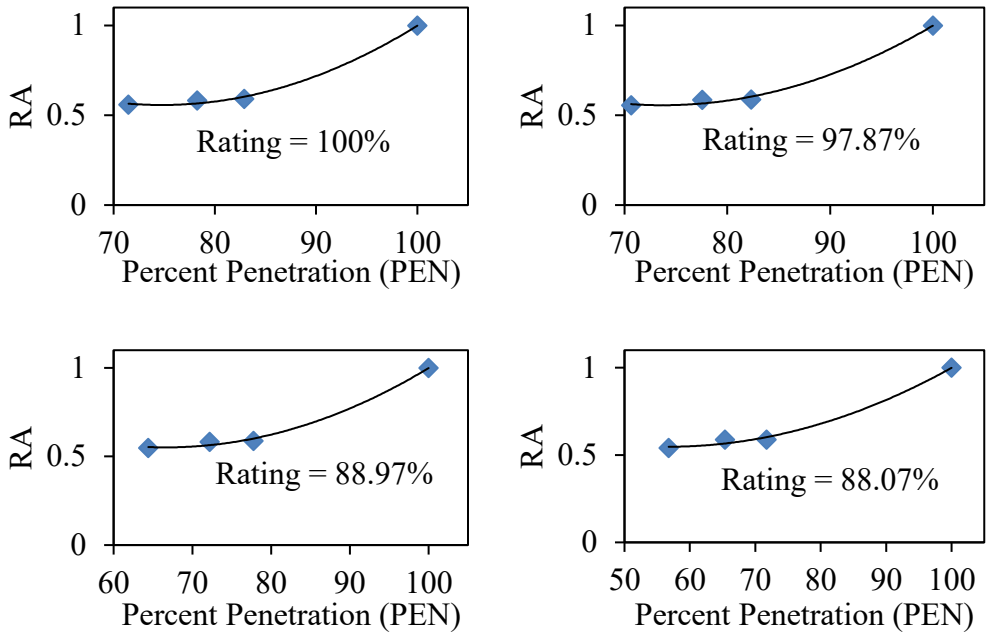

Figure E.4: Plant 2 line-to-line-to-ground short circuit ratios versus percentage penetration operating at various percentages of rated output.

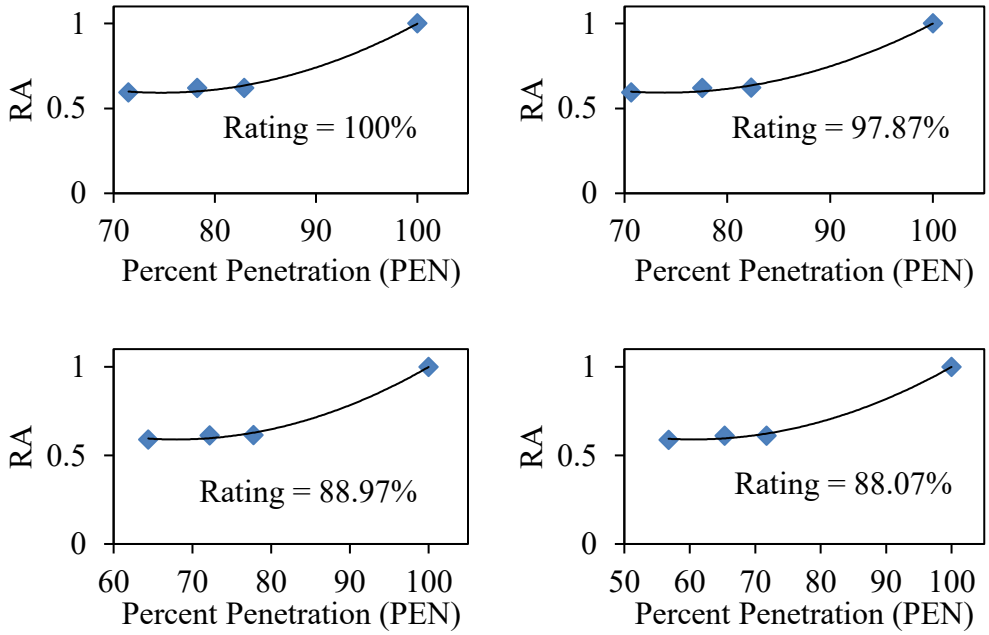

Figure E.5: Plant 2 line-to-ground short circuit ratios versus percentage penetration operating at various percentages of rated output.

These are expressed generically in the form given in Equation 6.19:

$$RA_{prtDGi} = \tau_{rtDGi}(PEN_{rDGi})^2 + \gamma_{rtDGi}(PEN_{rDGi}) + \varepsilon_{rtDGi}$$

This gives the coefficients of Equation 6.19 for each percentage rating and fault type:

Table E.17: Ratio scaling coefficients for Plant 2 for a three-phase fault.

Percentage Rating (r)	τ	γ	ε
100.00	1.242E-04	-0.01235	0.99273
97.86	7.523E-05	-0.00358	0.60486
88.97	4.936E-06	0.00762	0.18739
80.07	-1.046E-05	0.00886	0.21754
71.17	-5.690E-05	0.01551	0.01687

Table E.18: Ratio scaling coefficients for Plant 2 for a line-to-line fault.

Percentage Rating (r)	τ	γ	ε
100.00	-7.416E-05	0.01784	-0.04348
97.86	-3.584E-05	0.01081	0.27636
88.97	-3.331E-06	0.00463	0.56954
80.07	-1.004E-05	0.00546	0.55356
71.17	-2.288E-06	0.00443	0.57923

Table E.19: Ratio scaling coefficients for Plant 2 for a line-to-line-to-ground fault.

Percentage Rating (r)	τ	γ	ε
100.00	6.919E-04	-0.10343	4.42211
97.86	6.391E-04	-0.09418	4.02529
88.97	4.012E-04	-0.05344	2.33096
80.07	2.387E-04	-0.02697	1.30921
71.17	1.651E-04	-0.01550	0.89823

Table E.20: Ratio scaling coefficients for Plant 2 for a line-to-ground fault.

Percentage Rating (r)	τ	γ	ε
100.00	6.360E-04	-0.09505	4.14324
97.86	5.941E-04	-0.08774	3.83198
88.97	3.983E-04	-0.05413	2.42910
80.07	2.623E-04	-0.03174	1.55065
71.17	1.994E-04	-0.02174	1.17942

The coefficients are plotted as such:

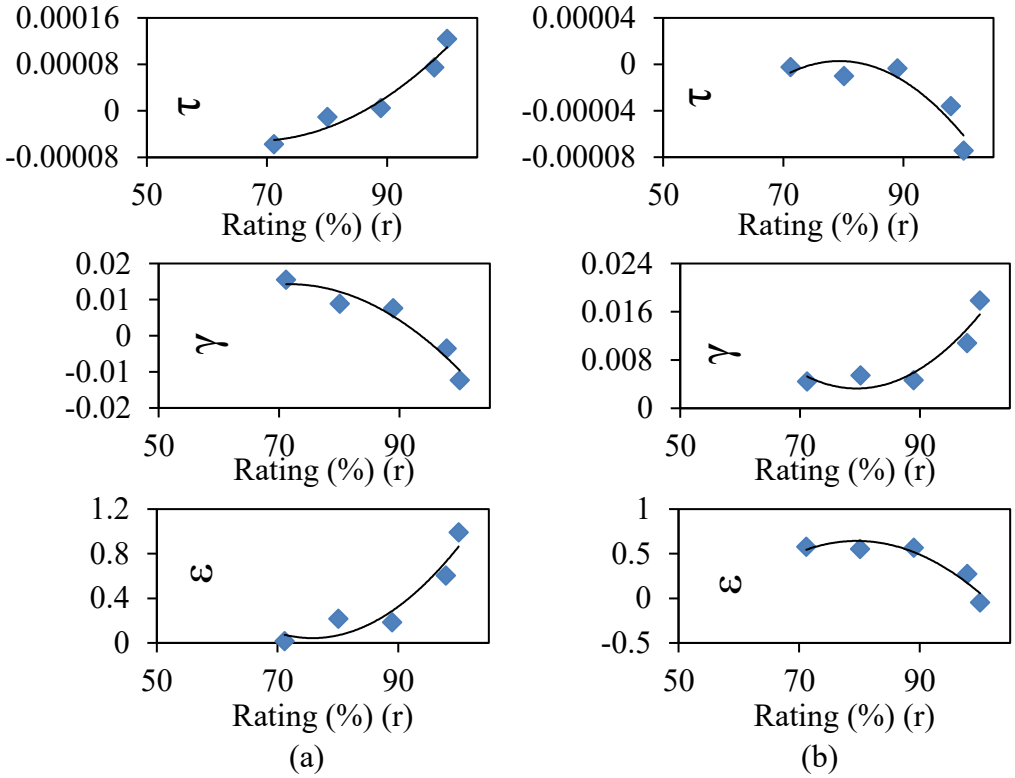

Figure E.6: Plant 2 coefficients for (a) three-phase and (b) line-to-line faults.

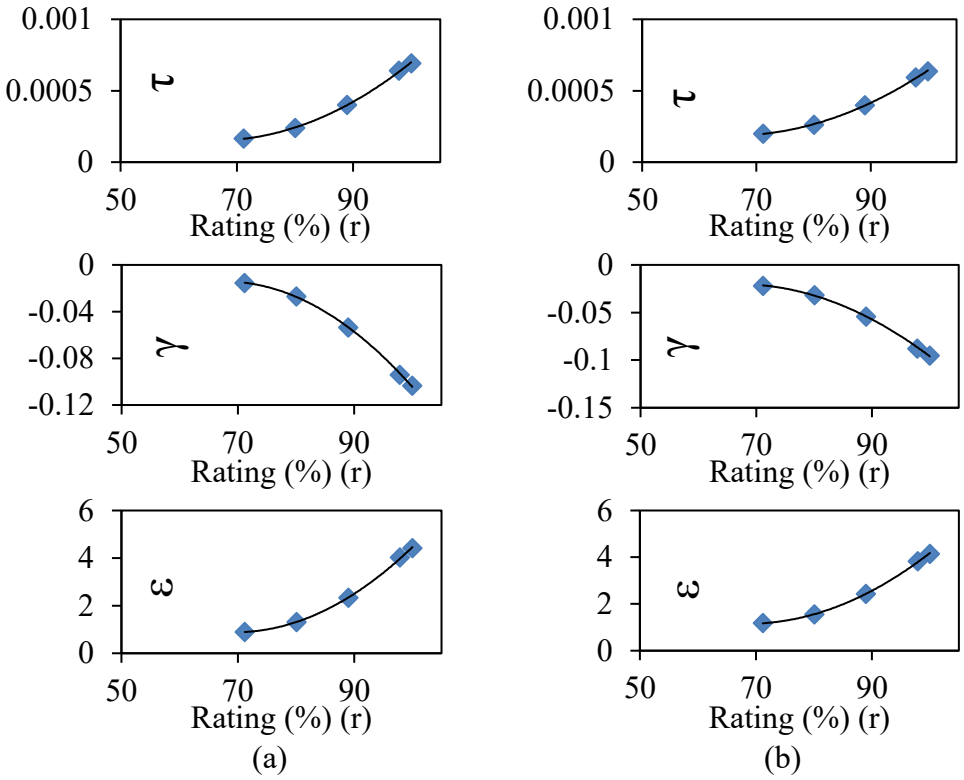

Figure E.7: Plant 2 coefficients for (a) line-to-line-to-ground and (b) line-to-ground faults.

This gives the following correction coefficient equations given in the form:

$$\tau_{crtDGi} = a_{rtDGi}(r_{DGi})^2 + b_{rtDGi}(r_{DGi}) + c_{rtDGi}$$

$$\gamma_{crtDGi} = d_{rtDGi}(r_{DGi})^2 + f_{rtDGi}(r_{DGi}) + g_{rtDGi}$$

$$\varepsilon_{crtDGi} = h_{rtDGi}(r_{DGi})^2 + k_{rtDGi}(r_{DGi}) + m_{rtDGi}$$

The corresponding coefficients for the correction coefficient equations are:

Table E.21: Coefficients for correction coefficient equations for Plant 2.

Fault Type	Three-Phase	Line-to-Line	Line-to-Line-to-Ground	Line-to-Ground
a	1.5756E-07	-1.5021E-07	4.8098E-07	3.8523E-07
b	-2.1432E-05	2.3834E-05	-6.3758E-05	-5.0521E-05
c	6.7719E-04	-9.4261E-04	2.2646E-03	1.8419E-03
d	-2.9774E-05	2.9067E-05	-8.6526E-05	-6.8977E-05
f	4.2680E-03	-4.6184E-03	1.1717E-02	9.2214E-03
g	-1.3867E-01	1.8673E-01	-4.1090E-01	-3.2841E-01
h	1.4022E-03	-1.4051E-03	3.8428E-03	3.0451E-03
k	-2.1253E-01	2.2358E-01	3.8428E-03	-4.1691E-01
m	8.0967E+00	-8.2509E+00	3.8428E-03	1.5421E+01

These corrected coefficient equations are utilized in Equation 6.23 which is expressed as:

$$RA_{cprtDGi} = \tau_{crtDGi}(PEN_{rDGi})^2 + \gamma_{crtDGi}(PEN_{rDGi}) + \varepsilon_{crtDGi}$$

This gives a predicted short circuit current equation in the form:

$$I_{fprtDGi} = I_{frtDGi} \times RA_{cprtDGi}$$

E.6 Wind Plant 4 Regression Analysis

As a result of the data presented in Appendix E.2 the following maximum and minimum short circuit current in relation to percentage rating graphs are obtained for each type of fault:

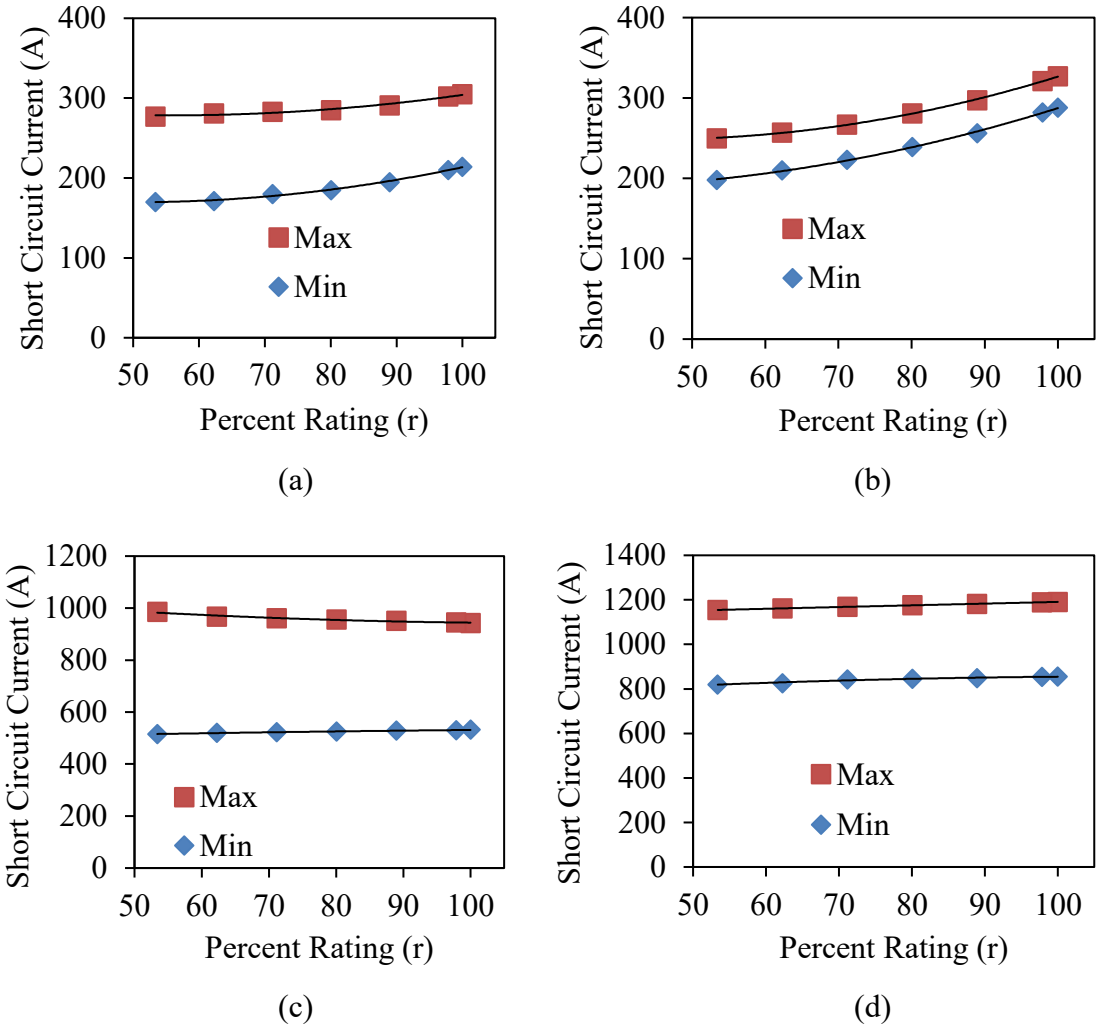

Figure E.8: Plant 4 short circuit current versus percentage rating for maximum and minimum cases for a: (a) three- phase fault, (b) line-to-line fault, (c) line-to-line-to-ground fault, (d) line-to-ground fault.

This gives the following maximum predicted short circuit currents:

$$I_{fr3PDG4} = 0.0130(r_{DG4})^2 - 1.440(r_{DG4}) + 318.43$$

$$I_{frLLDG4} = 0.0253(r_{DG4})^2 - 2.244(r_{DG4}) + 298.26$$

$$I_{frLLGDG4} = 0.0114(r_{DG4})^2 - 2.566(r_{DG4}) + 1086.95$$

$$I_{frLGDG4} = -0.0003(r_{DG4})^2 + 0.827(r_{DG4}) + 1111.56$$

As specified in Section 6.3.2, the fault ratio is required to be plotted against the percentage penetration for each percentage rating. This gives the following plots:

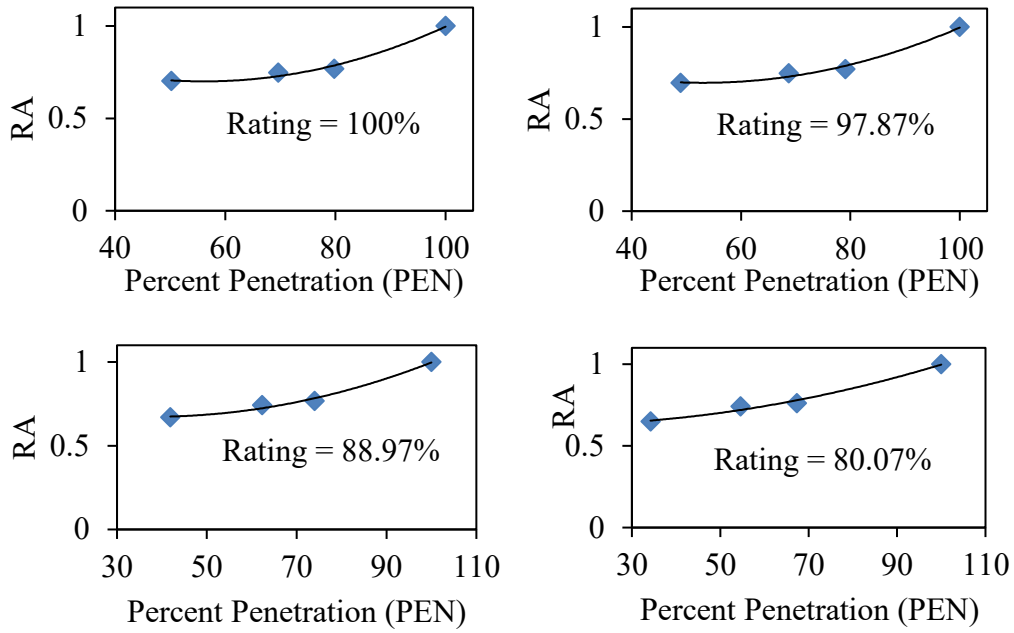

Figure E.9: Plant 4 three-phase short circuit ratios versus percentage penetration operating at various percentages of rated output.

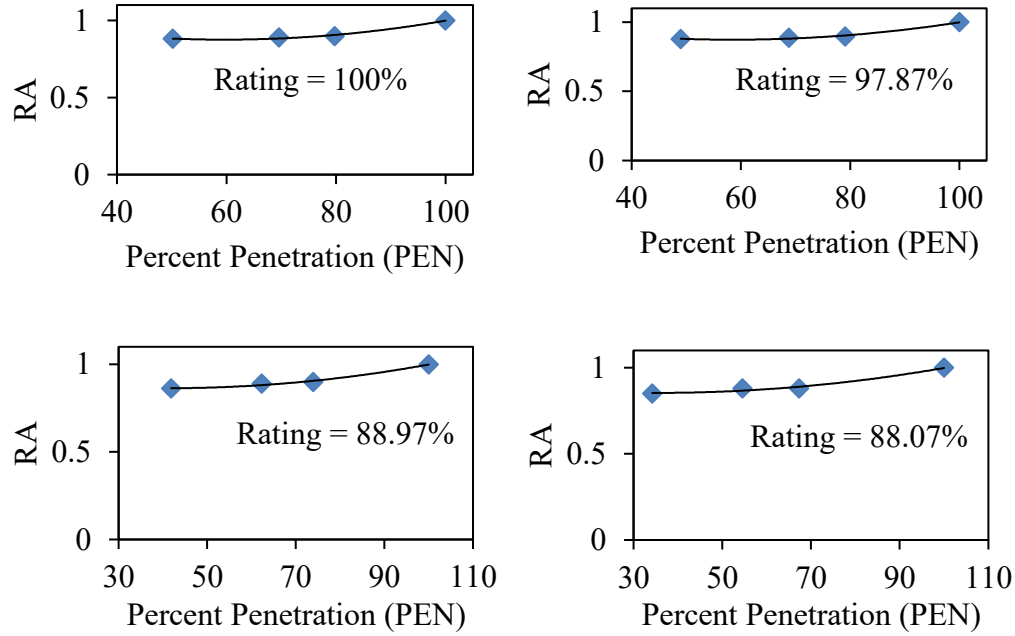

Figure E.10: Plant 4 line-to-line short circuit ratios versus percentage penetration operating at various percentages of rated output.

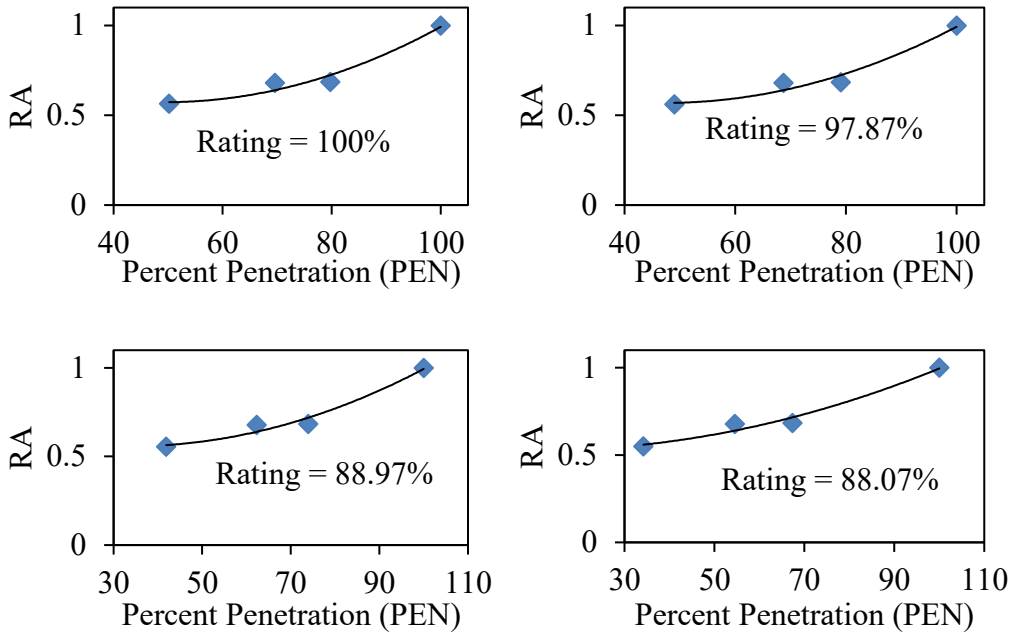

Figure E.11: Plant 4 line-to-line-to-ground short circuit ratios versus percentage penetration operating at various percentages of rated output.

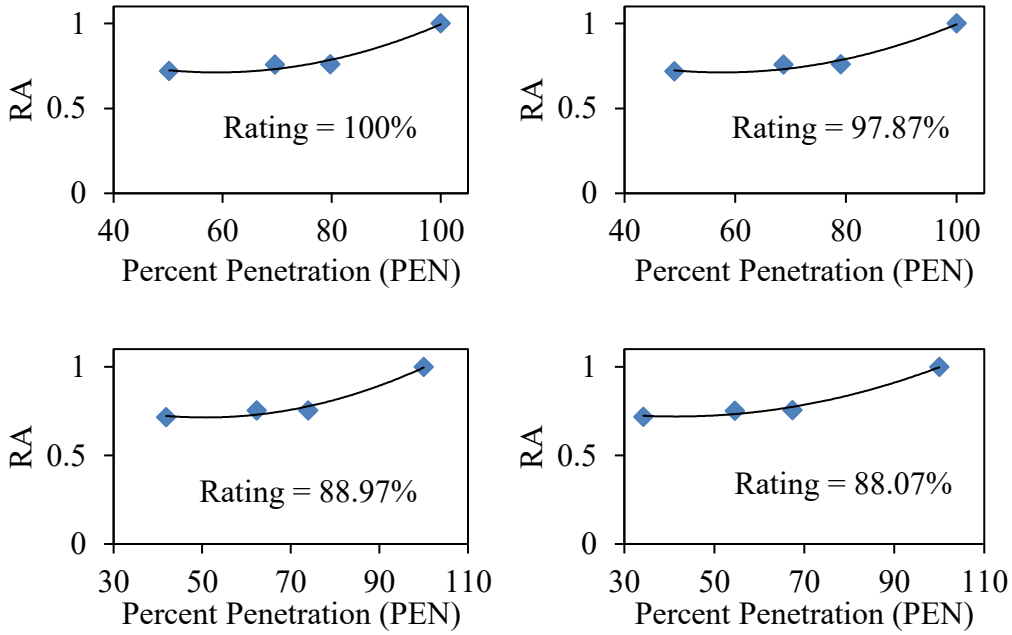

Figure E.12: Plant 4 line-to-ground short circuit ratios versus percentage penetration operating at various percentages of rated output.

These are expressed generically in the form given in Equation 6.19:

$$RA_{prtDGi} = \tau_{rtDGi}(PEN_{rDGi})^2 + \gamma_{rtDGi}(PEN_{rDGi}) + \varepsilon_{rtDGi}$$

This gives the following coefficients of Equation 6.19 for each percentage rating and fault type:

Table E.22: Ratio scaling coefficients for Plant 4 for a three-phase fault.

Percentage Rating (r)	τ	γ	ε
100.00	1.536E-04	-0.01724	1.18381
97.86	1.359E-04	-0.01441	1.07907
88.97	8.312E-05	-0.00624	0.79002
80.07	4.449E-05	-0.00076	0.62863
71.17	2.250E-05	0.00209	0.56358

Table E.23: Ratio scaling coefficients for Plant 4 for a line-to-line fault.

Percentage Rating (r)	τ	γ	ε
100.00	7.572E-05	-0.00903	1.14492
97.86	7.299E-05	-0.00855	1.12355
88.97	3.880E-05	-0.00318	0.92889
80.07	3.439E-05	-0.00242	0.89622
71.17	2.211E-05	-0.00057	0.83489

Table E.24: Ratio scaling coefficients for Plant 4 for a line-to-line-to-ground fault.

Percentage Rating (r)	τ	γ	ε
100.00	1.638E-04	-0.01619	0.97290
97.86	1.514E-04	-0.01426	0.90429
88.97	9.863E-05	-0.00660	0.66790
80.07	5.866E-05	-0.00124	0.53320
71.17	3.597E-05	0.00155	0.48134

Table E.25: Ratio scaling coefficients for Plant 4 for a line-to-ground fault.

Percentage Rating (r)	τ	γ	ε
100.00	1.671E-04	-0.01966	1.29000
97.86	1.584E-04	-0.01828	1.23899
88.97	1.157E-04	-0.01172	1.01096
80.07	8.120E-05	-0.00674	0.85933
71.17	6.593E-05	-0.00467	0.80560

The coefficients are plotted as such:

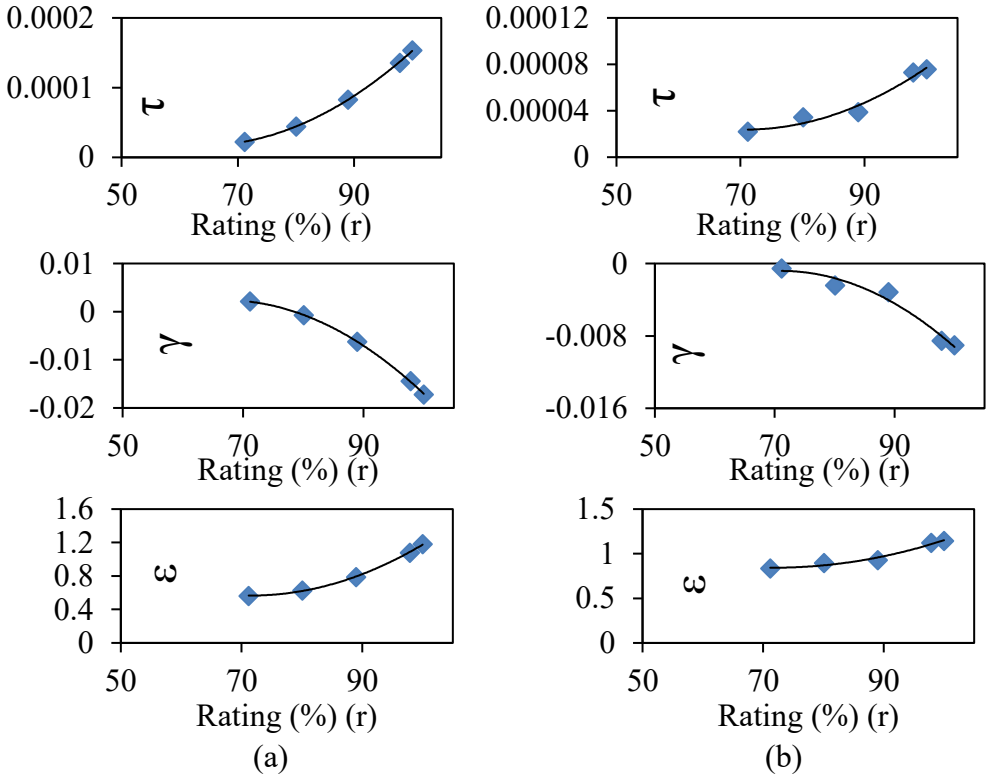

Figure E.13: Plant 4 coefficients for (a) three-phase and (b) line-to-line faults.

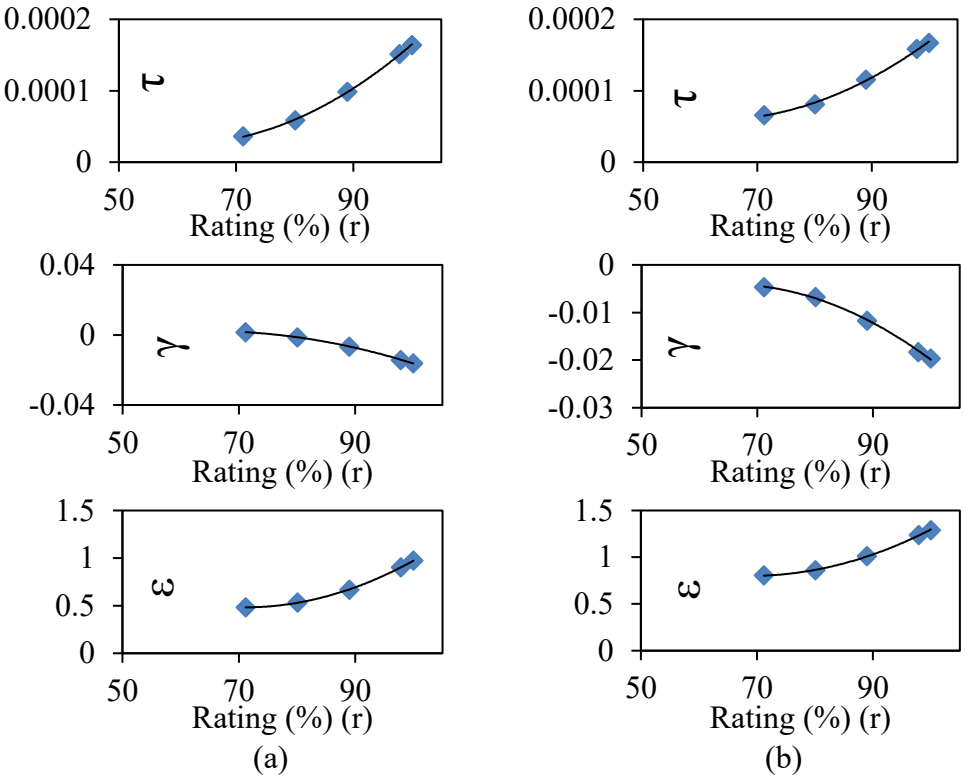

Figure E.14: Plant 4 coefficients for (a) line-to-line-to-ground and (b) line-to-ground faults.

This gives the following correction coefficient equations given in the form:

$$\tau_{crtDGi} = a_{rtDGi}(r_{DGi})^2 + b_{rtDGi}(r_{DGi}) + c_{rtDGi}$$

$$\gamma_{crtDGi} = d_{rtDGi}(r_{DGi})^2 + f_{rtDGi}(r_{DGi}) + g_{rtDGi}$$

$$\varepsilon_{crtDGi} = h_{rtDGi}(r_{DGi})^2 + k_{rtDGi}(r_{DGi}) + m_{rtDGi}$$

The corresponding coefficients for the correction coefficient equations are:

Table E.26: Coefficients for correction coefficient equations for Plant 4.

Fault Type	Three-Phase	Line-to-Line	Line-to-Line-to-Ground	Line-to-Ground
a	1.0254E-07	-1.5021E-07	4.8098E-07	3.8523E-07
b	-1.3039E-05	2.3834E-05	-6.3758E-05	-5.0521E-05
c	4.3112E-04	-9.4261E-04	2.2646E-03	1.8419E-03
d	-1.7795E-05	2.9067E-05	-8.6526E-05	-6.8977E-05
f	2.3828E-03	-4.6184E-03	1.1717E-02	9.2214E-03
g	-7.7390E-02	1.8673E-01	-4.1090E-01	-3.2841E-01
h	7.5369E-04	-1.4051E-03	3.8428E-03	3.0451E-03
k	-1.0788E-01	2.2358E-01	3.8428E-03	-4.1691E-01
m	4.4271E+00	-8.2509E+00	3.8428E-03	1.5421E+01

These corrected coefficient equations are utilized in Equation 6.23 which is expressed as:

$$RA_{cprtDGi} = \tau_{crtDGi}(PEN_{rDGi})^2 + \gamma_{crtDGi}(PEN_{rDGi}) + \varepsilon_{crtDGi}$$

This gives a predicted short circuit current equation in the form:

$$I_{fprtDGi} = I_{frtDGi} \times RA_{cprtDGi}$$

E.7 Biogas Plant 1 Regression Analysis

As a result of the data presented in Appendix E.3 the following maximum and minimum short circuit current in relation to percentage rating graphs are obtained for each type of fault:

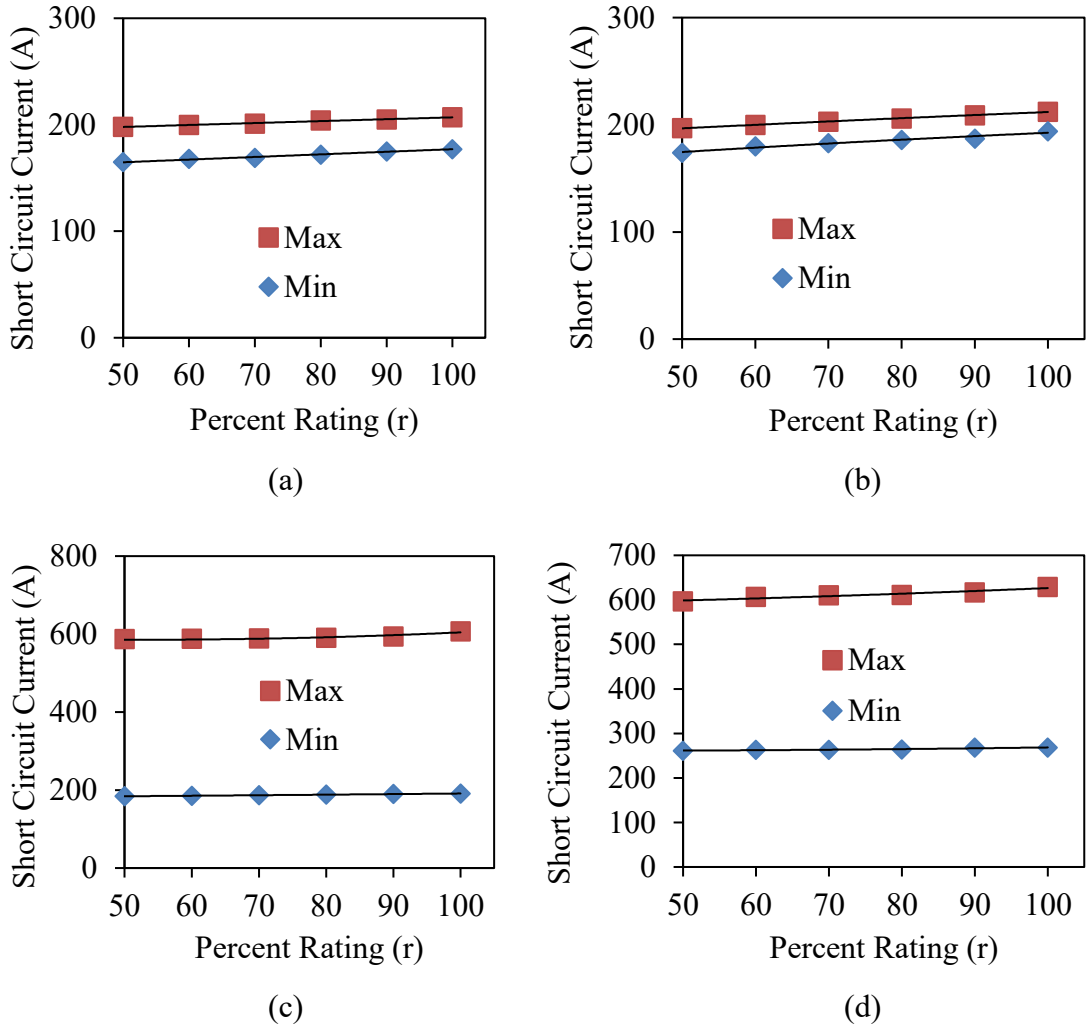

Figure E.15: Plant 1 short circuit current versus percentage rating for maximum and minimum cases for a: (a) three- phase fault, (b) line-to-line fault, (c) line-to-line-to-ground fault, (d) line-to-ground fault.

This gives the following maximum predicted short circuit currents:

$$I_{fr3PDG1} = -0.00012(r_{DG1})^2 + 0.199(r_{DG1}) + 188.29$$

$$I_{frLLDG1} = -0.0006(r_{DG1})^2 + 0.394(r_{DG1}) + 178.43$$

$$I_{frLLGDG1} = 0.0083(r_{DG1})^2 - 0.874(r_{DG1}) + 608.43$$

$$I_{frLGDG1} = 0.0025(r_{DG1})^2 + 0.182(r_{DG1}) + 583.29$$

As specified in Section 6.3.2, the fault ratio is required to be plotted against the percentage penetration for each percentage rating. This gives the following plots:

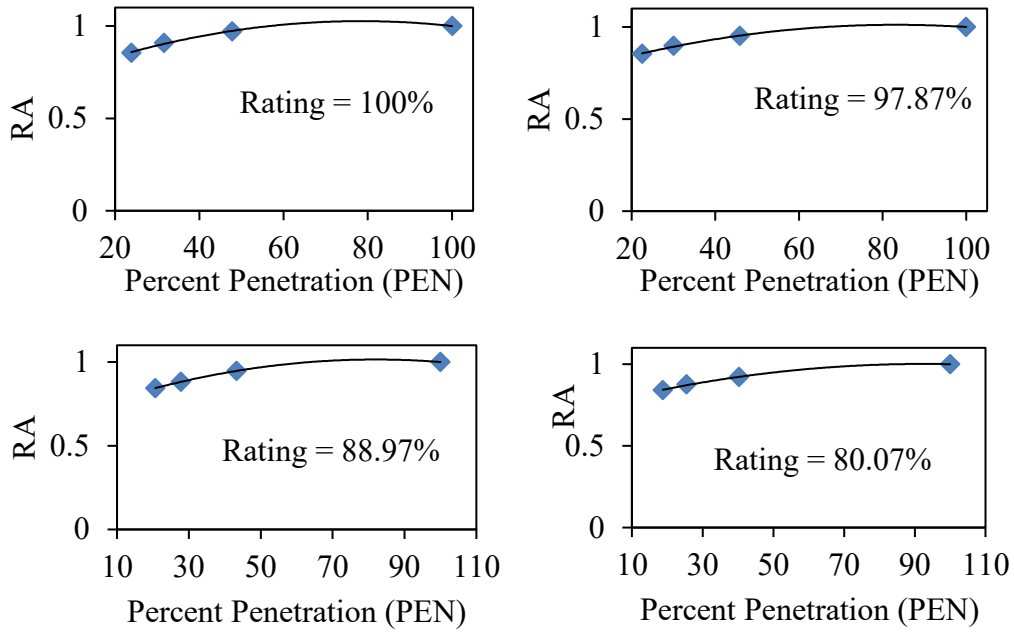

Figure E.16: Plant 1 three-phase short circuit ratios versus percentage penetration operating at various percentages of rated output.

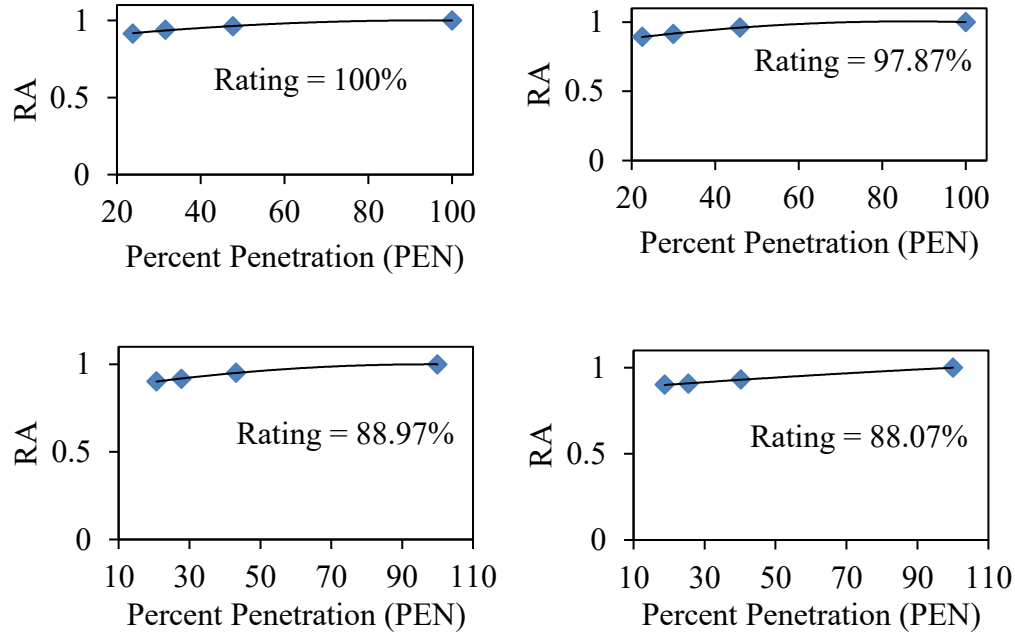

Figure E.17: Plant 1 line-to-line short circuit ratios versus percentage penetration operating at various percentages of rated output.

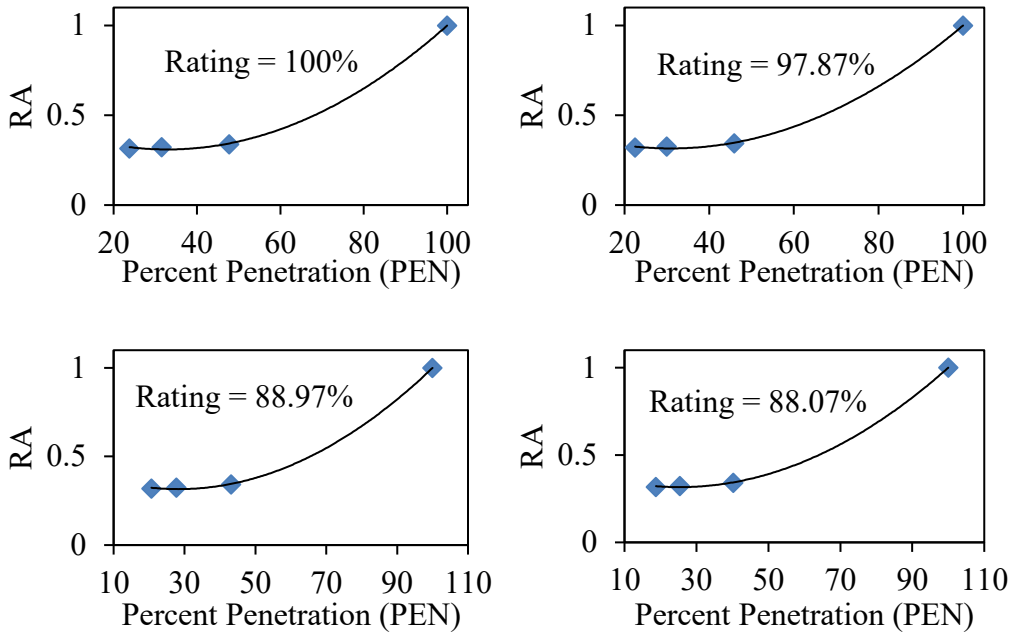

Figure E.18: Plant 1 line-to-line-to-ground short circuit ratios versus percentage penetration operating at various percentages of rated output.

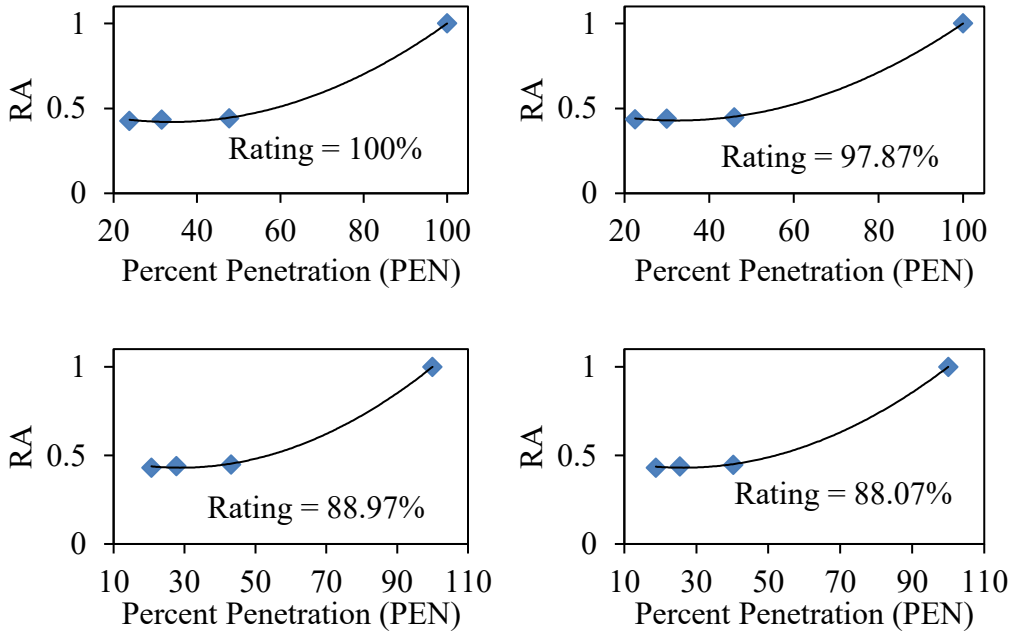

Figure E.19: Plant 1 line-to-ground short circuit ratios versus percentage penetration operating at various percentages of rated output.

These are expressed generically in the form given in Equation 6.19:

$$RA_{prtDGi} = \tau_{rtDGi}(PEN_{rDGi})^2 + \gamma_{rtDGi}(PEN_{rDGi}) + \varepsilon_{rtDGi}$$

This gives the coefficients of Equation 6.19 for each percentage rating and fault type:

Table E.27: Ratio scaling coefficients for Plant1 for a three-phase fault.

Percentage Rating (r)	τ	γ	ε
100.00	1.242E-04	-0.01235	0.99273
97.86	7.523E-05	-0.00358	0.60486
88.97	4.936E-06	0.00762	0.18739
80.07	-1.046E-05	0.00886	0.21754
71.17	-5.690E-05	0.01551	0.01687

Table E.28: Ratio scaling coefficients for Plant 1 for a line-to-line fault.

Percentage Rating (r)	τ	γ	ε
100.00	-1.649E-05	0.00312	0.85251
90.00	-2.786E-05	0.00480	0.79855
80.00	-1.643E-05	0.00322	0.84235
70.00	-2.874E-06	0.00158	0.87107
60.00	-8.939E-06	0.00224	0.86549

Table E.29: Ratio scaling coefficients for Plant 1 for a line-to-line-to-ground fault.

Percentage Rating (r)	τ	γ	ε
100.00	1.535E-04	-0.01011	0.47634
90.00	1.436E-04	-0.00889	0.45301
80.00	1.329E-04	-0.00752	0.42212
70.00	1.225E-04	-0.00620	0.39461
60.00	1.084E-04	-0.00445	0.36091

Table E.30: Ratio scaling coefficients for Plant 1 for a line-to-ground fault.

Percentage Rating (r)	τ	γ	ε
100.00	1.325E-04	-0.00897	0.57180
90.00	1.247E-04	-0.00806	0.55868
80.00	1.123E-04	-0.00647	0.52376
70.00	1.049E-04	-0.00553	0.50345
60.00	9.473E-05	-0.00429	0.48137

The coefficients are plotted as such:

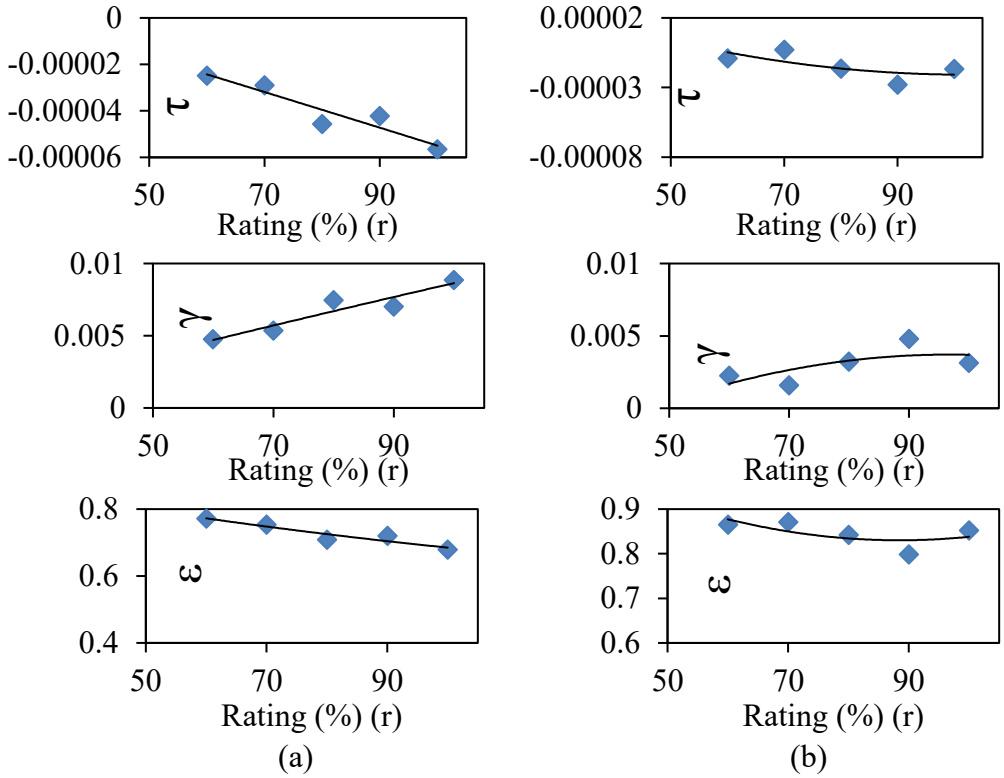

Figure E.20: Plant 1 coefficients for (a) three-phase and (b) line-to-line faults.

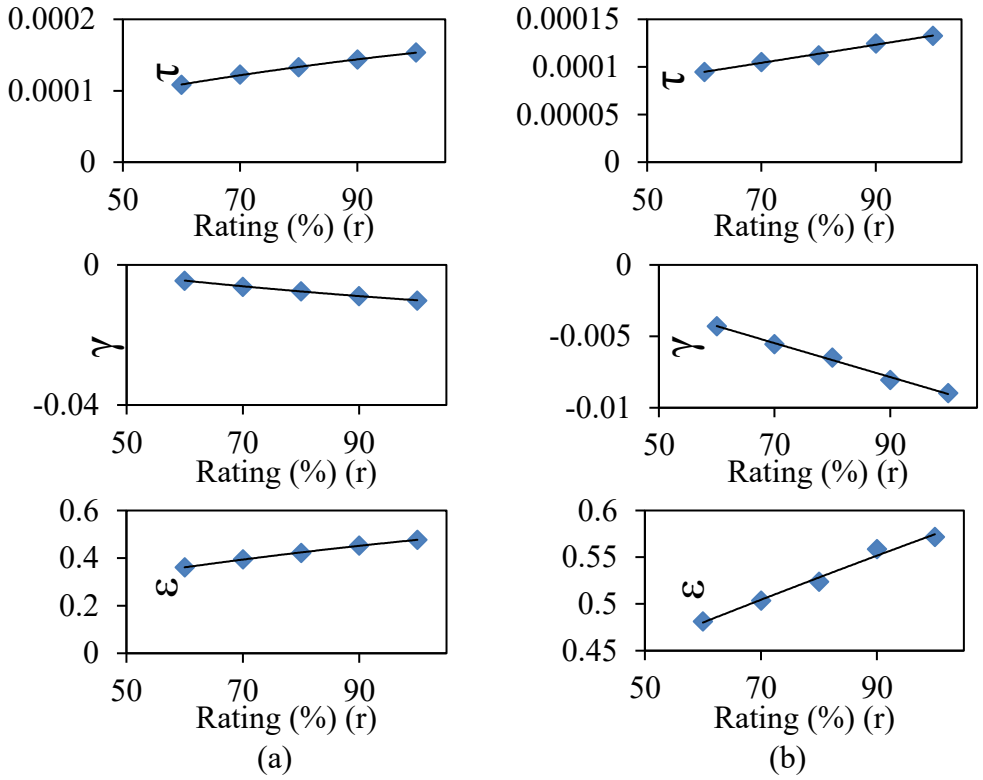

Figure E.21: Plant 1 coefficients for (a) line-to-line-to-ground and (b) line-to-ground faults.

This gives the following correction coefficient equations given in the form:

$$\tau_{crtDGi} = a_{rtDGi}(r_{DGi})^2 + b_{rtDGi}(r_{DGi}) + c_{rtDGi}$$

$$\gamma_{crtDGi} = d_{rtDGi}(r_{DGi})^2 + f_{rtDGi}(r_{DGi}) + g_{rtDGi}$$

$$\varepsilon_{crtDGi} = h_{rtDGi}(r_{DGi})^2 + k_{rtDGi}(r_{DGi}) + m_{rtDGi}$$

The corresponding coefficients for the correction coefficient equations are:

Table E.31: Coefficients for correction coefficient equations for Plant 1.

Fault Type	Three-Phase	Line-to-Line	Line-to-Line-to-Ground	Line-to-Ground
a	-1.6939E-10	-1.5021E-07	4.8098E-07	3.8523E-07
b	-7.4012E-07	2.3834E-05	-6.3758E-05	-5.0521E-05
c	2.0748E-05	-9.4261E-04	2.2646E-03	1.8419E-03
d	-7.1212E-08	2.9067E-05	-8.6526E-05	-6.8977E-05
f	1.0996E-04	-4.6184E-03	1.1717E-02	9.2214E-03
g	-1.6388E-03	1.8673E-01	-4.1090E-01	-3.2841E-01
h	8.6804E-06	-1.4051E-03	3.8428E-03	3.0451E-03
k	-3.5758E-03	2.2358E-01	3.8428E-03	-4.1691E-01
m	9.5567E-01	-8.2509E+00	3.8428E-03	1.5421E+01

These corrected coefficient equations are utilized in Equation 6.23 which is expressed as:

$$RA_{cprtDGi} = \tau_{crtDGi}(PEN_{rDGi})^2 + \gamma_{crtDGi}(PEN_{rDGi}) + \varepsilon_{crtDGi}$$

This gives a predicted short circuit current equation in the form:

$$I_{fprtDGi} = I_{frtDGi} \times RA_{cprtDGi}$$

E.8 Biogas Plant 6 Regression Analysis

As a result of the data presented in Appendix E.4 the following maximum and minimum short circuit current in relation to percentage rating graphs are obtained for each type of fault:

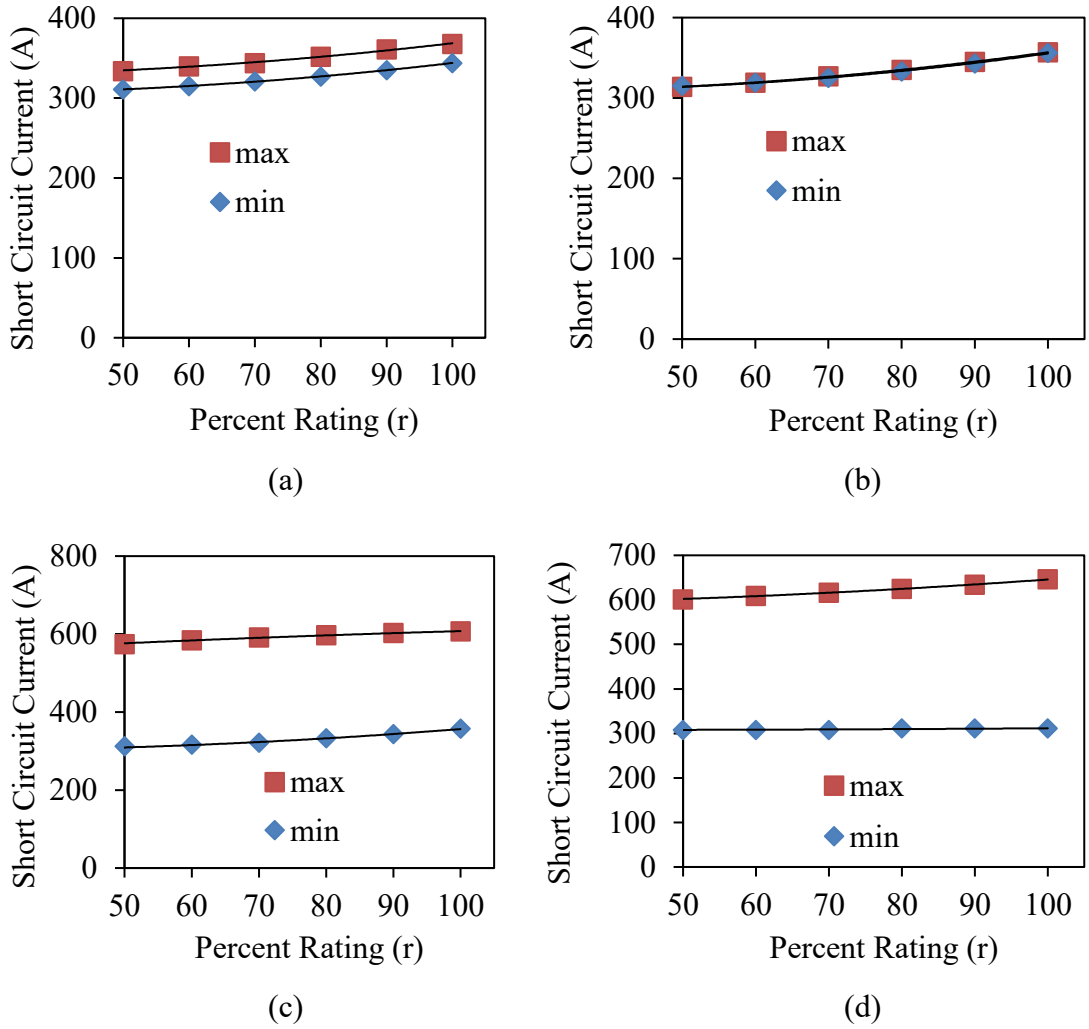

Figure E.22: Plant 6 short circuit current versus percentage rating for maximum and minimum cases for a: (a) three- phase fault, (b) line-to-line fault, (c) line-to-line-to-ground fault, (d) line-to-ground fault.

This gives the following maximum predicted short circuit currents:

$$I_{fr3PDG6} = 0.0057(r_{DG6})^2 - 0.179(r_{DG6}) + 329.50$$

$$I_{frLLDG6} = 0.0077(r_{DG6})^2 - 0.302(r_{DG6}) + 309.64$$

$$I_{frLLGDG6} = -0.0026(r_{DG6})^2 + 1.017(r_{DG6}) + 532.14$$

$$I_{frLGDG6} = 0.0058(r_{DG6})^2 + 0.001(r_{DG6}) + 587.29$$

As specified in Section 6.3.2, the fault ratio is required to be plotted against the percentage penetration for each percentage rating. This gives the following plots:

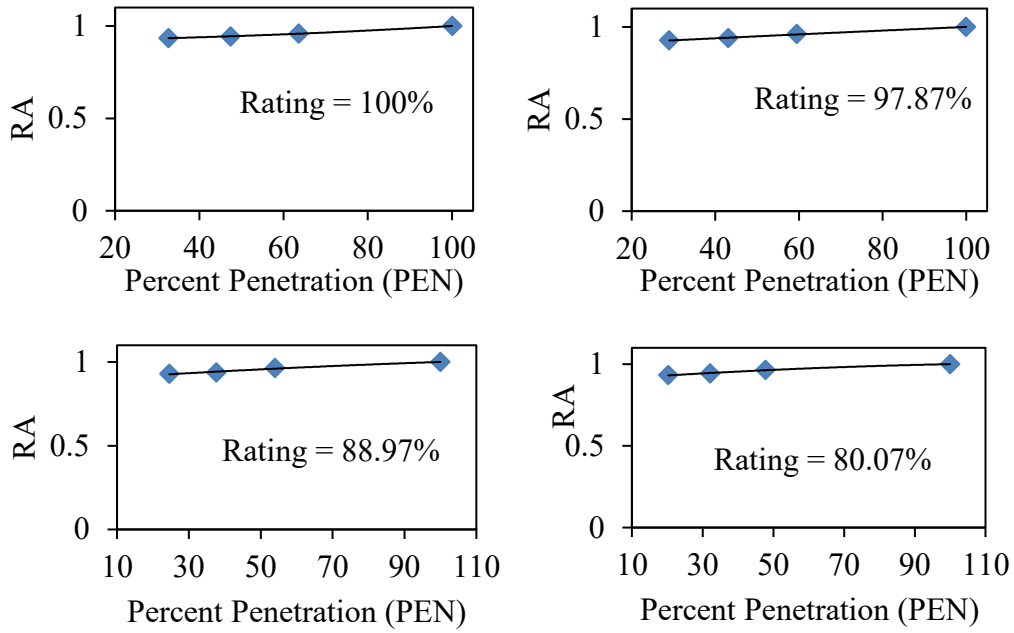

Figure E.23: Plant 6 three-phase short circuit ratios versus percentage penetration operating at various percentages of rated output.

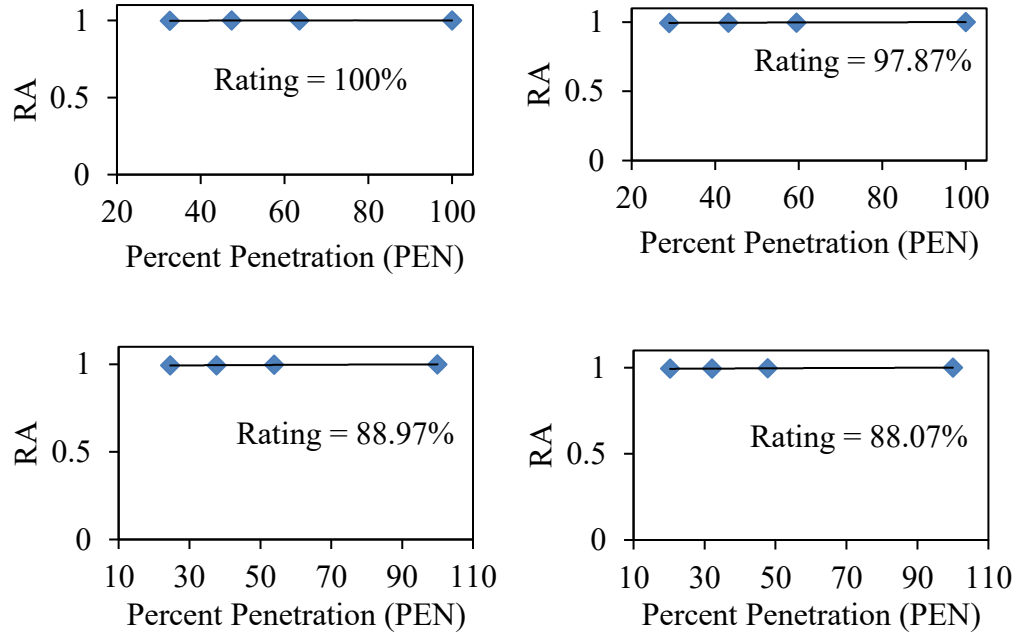

Figure E.24: Plant 6 line-to-line short circuit ratios versus percentage penetration operating at various percentages of rated output.

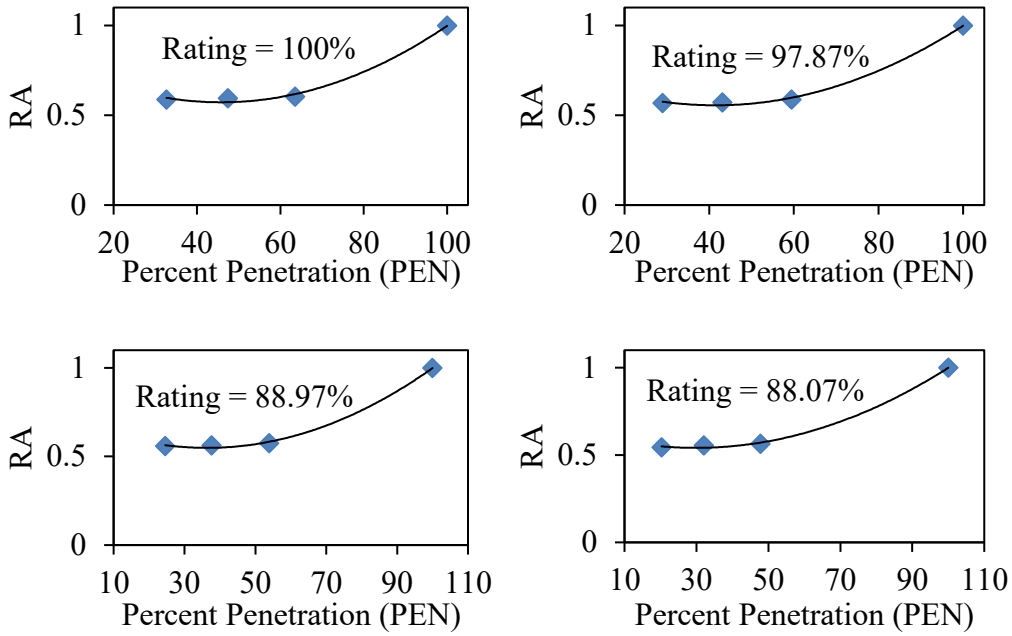

Figure E.25: Plant 6 line-to-line-to-ground short circuit ratios versus percentage penetration operating at various percentages of rated output.

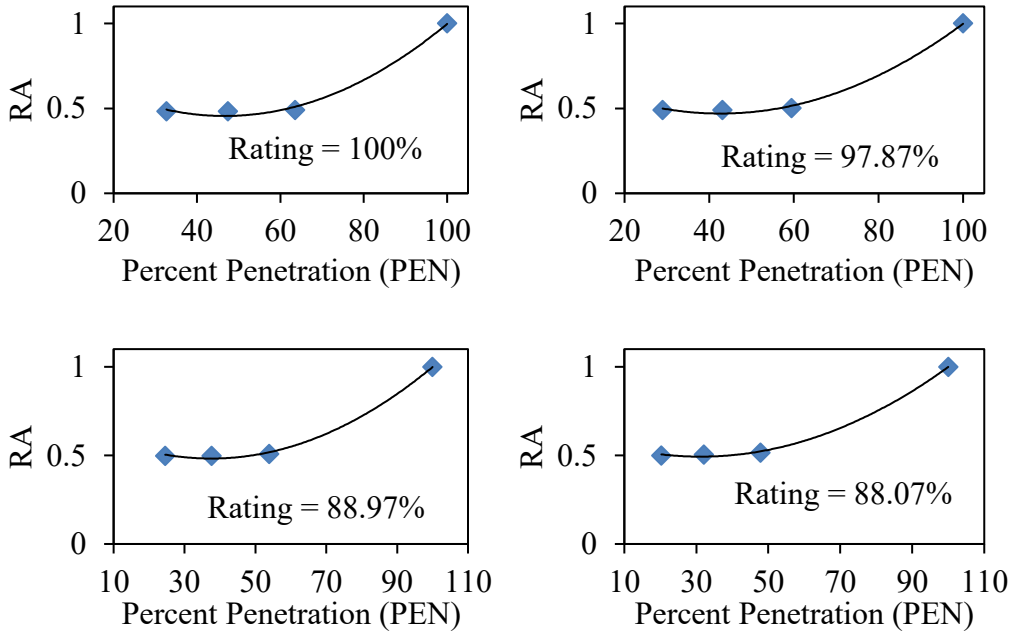

Figure E.26: Plant 6 line-to-ground short circuit ratios versus percentage penetration operating at various percentages of rated output.

These are expressed generically in the form given in Equation 6.19:

$$RA_{prtDGi} = \tau_{rtDGi}(PEN_{rDGi})^2 + \gamma_{rtDGi}(PEN_{rDGi}) + \varepsilon_{rtDGi}$$

This gives the following coefficients of Equation 6.19 for each percentage rating and fault type:

Table E.32: Ratio scaling coefficients for Plant 6 for a three-phase fault.

Percentage Rating (r)	τ	γ	ε
100.00	5.507E-06	0.00025	0.92020
90.00	-8.233E-07	0.00114	0.89430
80.00	-3.501E-06	0.00141	0.89420
70.00	-5.503E-06	0.00153	0.90250
60.00	-7.042E-06	0.00171	0.89908

Table E.33: Ratio scaling coefficients for Plant 6 for a line-to-line fault.

Percentage Rating (r)	τ	γ	ε
100.00	-1.662E-06	0.00026	0.99086
90.00	-6.574E-07	0.00016	0.99051
80.00	-2.537E-07	0.00012	0.99089
70.00	-4.960E-07	0.00014	0.99075
60.00	0.000E+00	0.00000	1.00000

Table E.34: Ratio scaling coefficients for Plant 6 for a line-to-line-to-ground fault.

Percentage Rating (r)	τ	γ	ε
100.00	1.447E-04	-0.01325	0.87546
90.00	1.293E-04	-0.01073	0.77808
80.00	1.112E-04	-0.00809	0.69571
70.00	9.321E-05	-0.00557	0.62431
60.00	8.171E-05	-0.00406	0.58829

Table E.35: Ratio scaling coefficients for Plant 6 for a line-to-ground fault.

Percentage Rating (r)	τ	γ	ε
100.00	1.906E-04	-0.01779	0.87056
90.00	1.607E-04	-0.01370	0.76175
80.00	1.323E-04	-0.00993	0.66850
70.00	1.067E-04	-0.00664	0.59649
60.00	8.790E-05	-0.00436	0.55691

The coefficients are plotted as such:

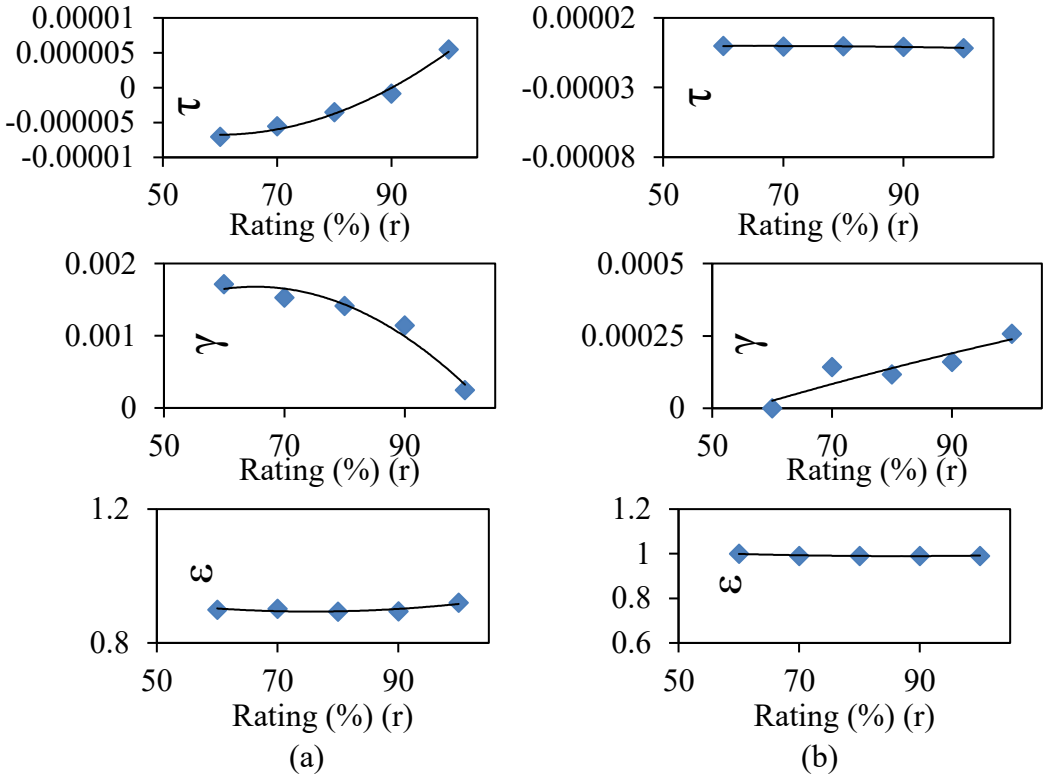

Figure E.27: Plant 6 coefficients for (a) three-phase and (b) line-to-line faults.

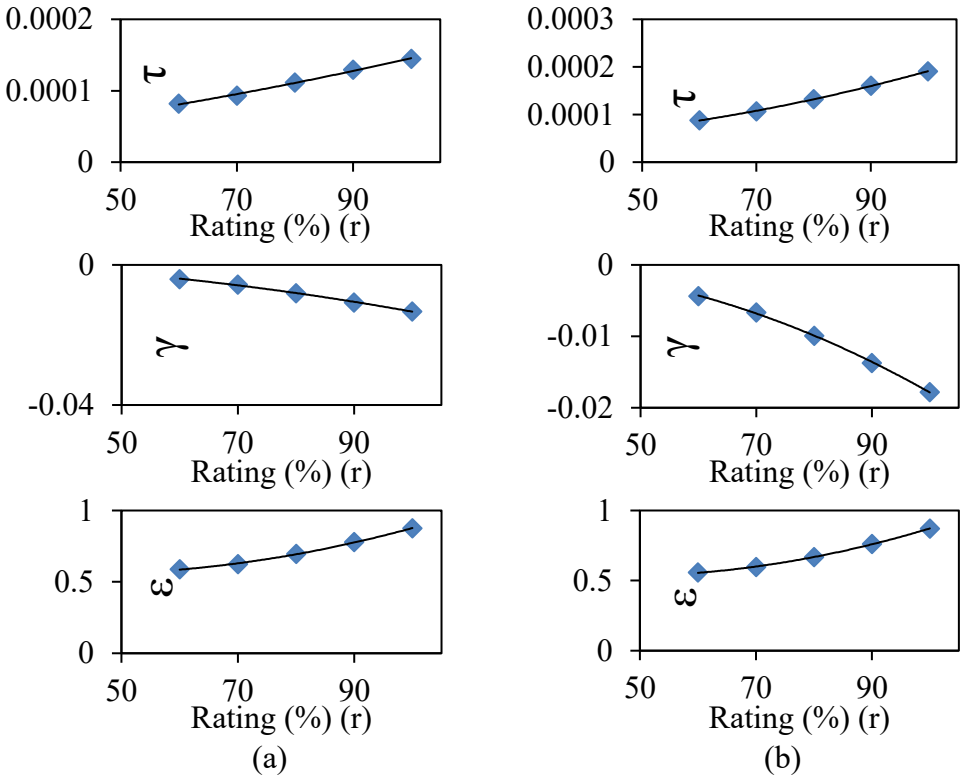

Figure E.28: Plant 6 coefficients for (a) line-to-line-to-ground and (b) line-to-ground faults.

This gives the following correction coefficient equations given in the form:

$$\tau_{crtDGi} = a_{rtDGi}(r_{DGi})^2 + b_{rtDGi}(r_{DGi}) + c_{rtDGi}$$

$$\gamma_{crtDGi} = d_{rtDGi}(r_{DGi})^2 + f_{rtDGi}(r_{DGi}) + g_{rtDGi}$$

$$\varepsilon_{crtDGi} = h_{rtDGi}(r_{DGi})^2 + k_{rtDGi}(r_{DGi}) + m_{rtDGi}$$

The corresponding coefficients for the correction coefficient equations are:

Table E.36: Coefficients for correction coefficient equations for Plant 6.

Fault Type	Three-Phase	Line-to-Line	Line-to-Line-to-Ground	Line-to-Ground
a	7.3274E-09	-1.5021E-07	4.8098E-07	3.8523E-07
b	-8.7461E-07	2.3834E-05	-6.3758E-05	-5.0521E-05
c	1.9336E-05	-9.4261E-04	2.2646E-03	1.8419E-03
d	-1.1175E-06	2.9067E-05	-8.6526E-05	-6.8977E-05
f	1.4564E-04	-4.6184E-03	1.1717E-02	9.2214E-03
g	-3.0666E-03	1.8673E-01	-4.1090E-01	-3.2841E-01
h	3.8104E-05	-1.4051E-03	3.8428E-03	3.0451E-03
k	-5.7563E-03	2.2358E-01	3.8428E-03	-4.1691E-01
m	7.3274E-09	-1.5021E-07	4.8098E-07	3.8523E-07

These corrected coefficient equations are utilized in Equation 6.23 which is expressed as:

$$RA_{cprtDGi} = \tau_{crtDGi}(PEN_{rDGi})^2 + \gamma_{crtDGi}(PEN_{rDGi}) + \varepsilon_{crtDGi}$$

This gives a predicted short circuit current equation in the form:

$$I_{fprtDGi} = I_{frtDGi} \times RA_{cprtDGi}$$

APPENDIX F

RESULTS FOR USE OF THE PARTICLE SWARM OPTIMIZATION SCHEME WITH VARYING MICROGRID CONDITIONS

F.1 Grid Condition 1 Results

Table F.1: PSO inputs for grid condition 1.

Generation Plant	1	2	3	4	5	6
PEN (%)	23.82	71.47	4.71	50.20	17.13	32.67
Rating (%)	100	100	100	100	100	100
Irradiance (W/m^2)	1000					
Wind speed (m/s)	11.24					

Table F.2: Predicted and actual fault currents for grid condition 1.

Generation Plant		Fault currents (A)			
		Three-Phase	Line-to-Line	Line-to-Line-to-Ground	Line-to-Ground
1	Predicted	178	194	195	272
	Actual	177	195	191	268
2	Predicted	221	276	467	635
	Actual	215	271	462	631
3	Predicted	20	23	45	50
	Actual	20	24	46	48
4	Predicted	214	288	538	861
	Actual	214	288	532	853
5	Predicted	83	60	155	165
	Actual	82	63	160	158
6	Predicted	344	356	362	318
	Actual	344	356	359	311
Overall	Predicted	1060	1197	1762	2301
	Actual	1049	1196	1800	2280

Table F.3: Predicted and actual fault currents for grid condition 1 percentage differences.

	Percentage difference (%)			
Generation Plant	Three-Phase	Line-to-Line	Line-to-Line-to-Ground	Line-to-Ground
1	0.56	0.51	2.05	1.47
2	2.71	1.81	1.07	0.62
3	0.00	4.34	2.22	4.00
4	0.00	0.00	1.11	0.92
5	1.20	5.00	3.22	4.24
6	0.00	0.00	0.82	2.20
Overall	1.03	0.08	2.15	0.91

Table F.4: Outputs from the proposed scheme's PSO for grid condition 1.

Generation Plant	1	2	3	4	5	6
Number of generators to trip (phase)	0	2	0	2	0	0
Number of generators to trip (ground)	2	2	0	2	0	2

Table F.5: Predicted and actual fault currents for grid condition 1 after tripping.

	Fault current (A)			
Fault type	Predicted	Actual	Percentage difference (%)	Coordination restored?
Three-Phase	669	672	0.45	Yes
Line-to-Line	652	651	0.15	Yes
Line-to-Line-to-Ground	623	605	2.89	Yes
Line-to-Ground	638	645	1.10	Yes

F.2 Grid Condition 2 Results

Table F.6: PSO inputs for grid condition 2.

Generation Plant	1	2	3	4	5	6
PEN (%)	100	0	0	0	0	100
Rating (%)	100	0	0	0	0	100
Irradiance (W/m^2)	0					
Wind speed (m/s)	0					

Table F.7: Predicted and actual fault currents for grid condition 2.

		Fault currents (A)			
Generation Plant		Three-Phase	Line-to-Line	Line-to-Line-to-Ground	Line-to-Ground
1	Predicted	207	212	604	627
	Actual	200	204	582	599
2	Predicted	0	0	0	0
	Actual	0	0	0	0
3	Predicted	0	0	0	0
	Actual	0	0	0	0
4	Predicted	0	0	0	0
	Actual	0	0	0	0
5	Predicted	0	0	0	0
	Actual	0	0	0	0
6	Predicted	368	357	608	646
	Actual	362	362	595	615
Overall	Predicted	575	569	1212	1273
	Actual	559	564	1160	1240

Table F.8: Predicted and actual fault currents for grid condition 2 percentage differences.

	Percentage difference (%)			
Generation Plant	Three-Phase	Line-to-Line	Line-to-Line-to-Ground	Line-to-Ground
1	3.38	3.77	3.64	4.46
2	0.00	0.00	0.00	0.00
3	0.00	0.00	0.00	0.00
4	0.00	0.00	0.00	0.00
5	0.00	0.00	0.00	0.00
6	1.63	1.40	2.13	4.79
Overall	2.78	0.87	4.29	2.59

Table F.9: Outputs from the proposed scheme's PSO for grid condition 2.

Generation Plant	1	2	3	4	5	6
Number of generators to trip (phase)	0	0	0	0	0	0
Number of generators to trip (ground)	3	0	0	0	0	2

Table F.10: Predicted and actual fault currents for grid condition 2 after tripping.

	Fault current (A)			
Fault type	Predicted	Actual	Percentage difference (%)	Coordination restored?
Three-Phase	575	559	2.78	-
Line-to-Line	569	564	0.88	-
Line-to-Line-to-Ground	606.4	620	2.24	Yes
Line-to-Ground	638.4	645	1.03	Yes

F.3 Grid Condition 3 Results

Table F.11: PSO inputs for grid condition 3.

Generation Plant	1	2	3	4	5	6
PEN (%)	36.14	56.80	7.06	34.21	22.63	43.16
Rating (%)	100	80.07	100	80.07	100	100
Irradiance (W/m^2)	1000					
Wind speed (m/s)	9					

Table F.12: Predicted and actual fault currents for grid condition 3.

		Fault currents (A)			
Generation Plant		Three-Phase	Line-to-Line	Line-to-Line-to-Ground	Line-to-Ground
1	Predicted	192	200	189	264
	Actual	185	206	196	268
2	Predicted	189	233	450	616
	Actual	196	240	463	614
3	Predicted	20	23	45	50
	Actual	19	23	44	51
4	Predicted	186	238	530	849
	Actual	190	245	529	840
5	Predicted	83	60	155	165
	Actual	81	59	153	160
6	Predicted	347	357	348	295
	Actual	349	368	357	282
Overall	Predicted	1017	1111	1717	2239
	Actual	1010	1116	1780	2190

Table F.13: Predicted and actual fault currents for grid condition 3 percentage differences.

	Percentage difference (%)			
Generation Plant	Three-Phase	Line-to-Line	Line-to-Line-to-Ground	Line-to-Ground
1	3.64	3.00	3.70	1.51
2	3.70	3.00	2.88	0.32
3	5.00	0.00	2.22	2.00
4	2.15	2.94	0.18	1.06
5	2.40	1.66	1.29	3.03
6	0.57	3.08	2.58	4.40
Overall	0.68	0.45	3.66	2.18

Table F.14: Outputs from the proposed scheme's PSO for grid condition 3.

Generation Plant	1	2	3	4	5	6
Number of generators to trip (phase)	0	2	0	2	0	0
Number of generators to trip (ground)	2	2	0	2	0	2

Table F.15: Predicted and actual fault currents for grid condition 3 after tripping.

	Fault current (A)			
Fault type	Predicted	Actual	Percentage difference (%)	Coordination restored?
Three-Phase	669	658	1.64	Yes
Line-to-Line	652	651	0.15	Yes
Line-to-Line-to-Ground	623	610	2.09	Yes
Line-to-Ground	638	630	1.25	Yes

F.4 Grid Condition 4 Results

Table F.16: PSO inputs for grid condition 4.

Generation Plant	1	2	3	4	5	6
PEN (%)	44.68	55.32	0.00	37.88	0.00	62.12
Rating (%)	100	71.17	0.00	71.17	0.00	100
Irradiance (W/m^2)	0					
Wind speed (m/s)	8					

Table F.17: Predicted and actual fault currents for grid condition 4.

Generation Plant		Fault currents (A)			
		Three-Phase	Line-to-Line	Line-to-Line-to-Ground	Line-to-Ground
1	Predicted	199	204	200	273
	Actual	194	205	199	275
2	Predicted	198	215	462	612
	Actual	207	218	467	614
3	Predicted	0	0	0	0
	Actual	0	0	0	0
4	Predicted	192	226	571	846
	Actual	201	232	595	883
5	Predicted	0	0	0	0
	Actual	0	0	0	0
6	Predicted	353	357	371	323
	Actual	348	346	368	315
Overall	Predicted	942	1002	1604	2054
	Actual	944	1002	1655	2120

Table F.18: Predicted and actual fault currents for grid condition 4 percentage differences.

	Percentage difference (%)			
Generation Plant	Three-Phase	Line-to-Line	Line-to-Line-to-Ground	Line-to-Ground
1	2.51	0.49	0.50	0.73
2	4.54	1.39	1.08	0.32
3	0.00	0.00	0.00	0.00
4	4.68	2.65	4.20	4.37
5	0.00	0.00	0.00	0.00
6	1.41	3.08	0.80	2.47
Overall	0.21	0.00	3.17	3.21

Table F.19: Outputs from the proposed scheme's PSO for grid condition 4.

Generation Plant	1	2	3	4	5	6
Number of generators to trip (phase)	0	1	0	2	0	0
Number of generators to trip (ground)	2	2	0	2	0	3

Table F.20: Predicted and actual fault currents for grid condition 4 after tripping.

	Fault current (A)			
Fault type	Predicted	Actual	Percentage difference (%)	Coordination restored?
Three-Phase	654	649	0.76	Yes
Line-to-Line	663	670	2.00	Yes
Line-to-Line-to-Ground	605	614	1.49	Yes
Line-to-Ground	633	626	1.11	Yes

F.5 Grid Condition 5 Results

Table F.21: PSO inputs for grid condition 5.

Generation Plant	1	2	3	4	5	6
PEN (%)	22.00	71.48	6.52	55.21	26.38	18.40
Rating (%)	80	88.97	100	88.97	100	60
Irradiance (W/m^2)	1000					
Wind speed (m/s)	10					

Table F.22: Predicted and actual fault currents for grid condition 5.

		Fault currents (A)			
Generation Plant		Three-Phase	Line-to-Line	Line-to-Line-to-Ground	Line-to-Ground
1	Predicted	174	185	191	268
	Actual	174	188	190	256
2	Predicted	220	262	473	633
	Actual	210	252	488	626
3	Predicted	20	23	45	50
	Actual	19	23	47	48
4	Predicted	206	260	576	851
	Actual	209	250	568	852
5	Predicted	83	60	155	165
	Actual	80	62	160	158
6	Predicted	316	320	316	308
	Actual	311	324	318	311
Overall	Predicted	1019	1110	1756	2275
	Actual	993	1060	1802	2198

Table F.23: Predicted and actual fault currents for grid condition 5 percentage differences.

	Percentage difference (%)			
Generation Plant	Three-Phase	Line-to-Line	Line-to-Line-to-Ground	Line-to-Ground
1	0.00	1.62	0.52	4.47
2	4.54	3.81	3.17	1.10
3	5.00	0.00	4.44	4.00
4	1.45	3.84	1.38	0.11
5	3.61	3.33	3.22	4.24
6	1.58	1.25	0.63	0.97
Overall	2.55	4.50	2.61	3.38

Table F.24: Outputs from the proposed scheme's PSO for grid condition 5.

Generation Plant	1	2	3	4	5	6
Number of generators to trip (phase)	1	1	0	2	0	0
Number of generators to trip (ground)	2	2	0	2	0	2

Table F.25: Predicted and actual fault currents for grid condition 5 after tripping.

	Fault current (A)			
Fault type	Predicted	Actual	Percentage difference (%)	Coordination restored?
Three-Phase	670	664	0.90	Yes
Line-to-Line	677	662	2.22	Yes
Line-to-Line-to-Ground	572	570	0.35	Yes
Line-to-Ground	617	625	1.30	Yes